Journal of the CERAMIC SOCIETY of Japan, International Edition 第99集 第1149号 平成3年4月25日発行(毎月1回25日発行) ISSN 0912-9200

Journal of the CERAMIC SOCIETY of Japan, International Edition

Vol.99 Apr. 1991

■ 18 Papers from Nippon Seramikkusu Kyokai Gakujutsu Ronbunshi, Vol. 99 No.4 1991

NIPPON SERAMIKKUSU KYOKAI GAKUJUTSU RONBUNSHI Vol.99 1991

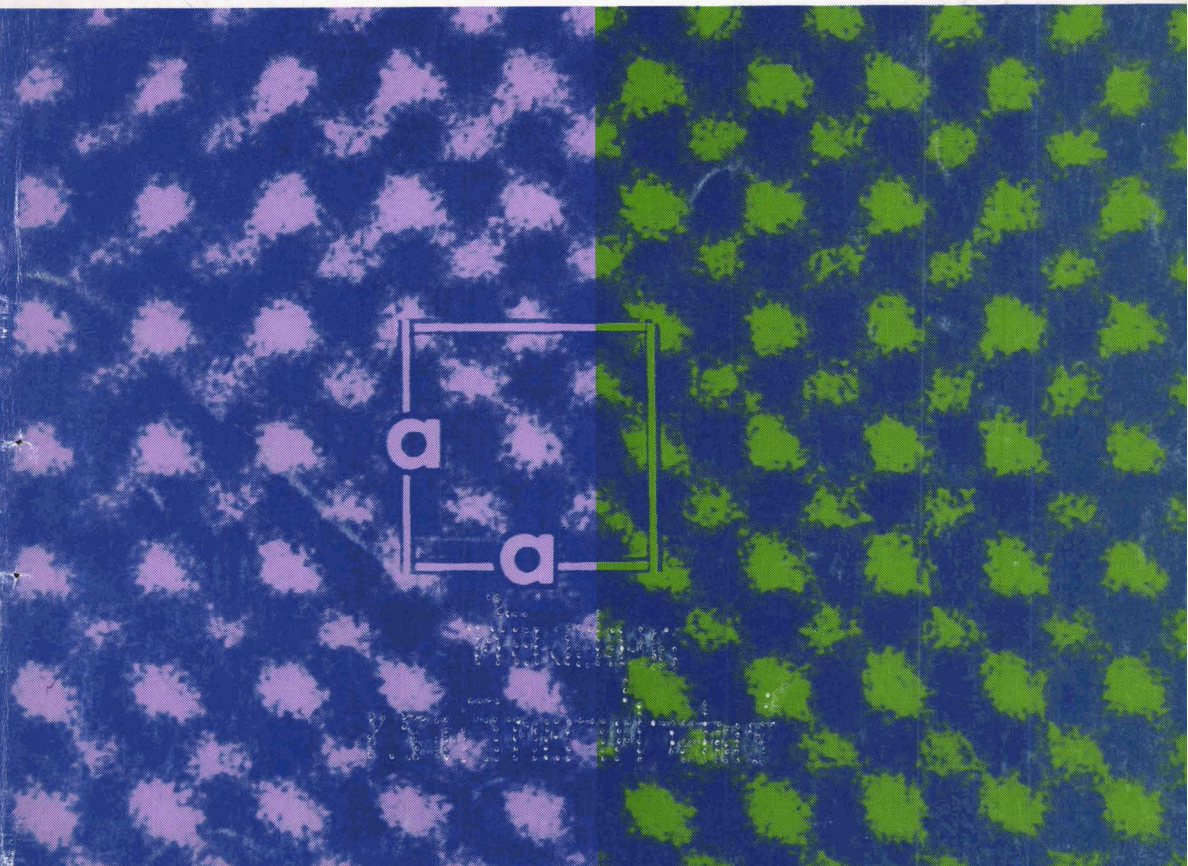

Journal of Ceramic Society of Japan, *International Edition*

Vol.99 No.4
Apr. 1991

CONTENTS

Published Monthly by
FUJI TECHNOLOGY PRESS LTD.
7F Daini Bunsei Bldg.
11-7, Toranomon 1-chome
Minato-ku, Tokyo 105, Japan
Tel:81-3-3508-0051
Fax:81-3-3592-0648

One year subscription
Air Mail ¥200,000

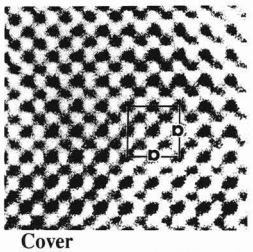

Cover

The picture shows the high-resolution structure image of zirconia (ZrO_2) projected along the a-axis of a cubic lattice (a=5.1Å). As indicated by arrowheads in the micrograph, both zirconium (Zr) and oxygen (O) atom positions are imaged as strong and weak dark dots, respectively. This is the first electron microscope data in which individual oxygen positions in inorganic compounds are directly observed as weak dark dots. The microgram was obtained by the ultra-high-resolution, high-voltage electron microscope (Model: H-1500) has been developed in 1990 as NIRIM's second high-voltage electron microscope. It achieved a resolution of 1.0Å, which is the world's best at present. In order to obtain such high resolution, maximum operating voltage of 1300kV and also maximum applicable one of 1500kV are employed. Very low spherical aberration coefficient of an objective lens (C_s = 1.85mm at 1300kV) was achieved by computer-aided designing of electron-magnetic lens systems. Owing to the success of the new machine, it has now become possible to image not only metal atoms but also light atoms such as oxygen in many inorganic materials, by means of high-resolution electron microscopy.

Tetsuo Yazawa, Hiroshi Tanaka, Kiyohisa Eguchi and Takashi Arai

Information & Communications

Papers, Letters and Notes

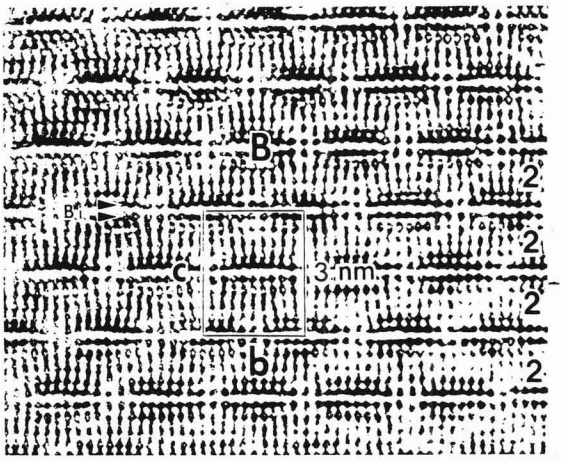

High resolution electron microscope photograph of the modulation doped structure of $Bi_2Sr_2CaCu_2O_y$ (T_c=80K) in the [100] direction. Figures at right side indicate number of copper layers, symbol B indicates bismuth rich region.

Microdesigned Interfaces: New Opportunities for Materials Science

Jürgen Rödel* and Andreas M. Glaeser

Department of Materials Science and Mineral Engineering, University of California
and Materials and Chemical Sciences Division Lawrence Berkeley Laboratory, Berkeley, CA94720
*Now at Advanced Ceramics Group, Technische Universität, Hamburg-Harburg
P.O.Box 90-10-52, D-2100 Hamburg 90, Germany
(Research supported by the Director, the Office of Energy Research, Office of Basic Energy Sciences, Materials Sciences Division of the U.S.Department of Energy under Contract No. DE-AC03-76SF00098)

A new family of lithography-based model experiments has been developed that permits the introduction of micron-scale controlled-geometry defects at internal interfaces. These microdesigned interfaces can be used to study various aspects of microstructural evolution during sintering. In addition, they can be applied to studies of mechanical behavior of porous materials and ceramic-metal composites. Research utilizing such microdesigned interfaces is reviewed, and numerous potential applications of the technique are suggested.
[Received September 22, 1990; Accepted December 14, 1990]

Key-words: Lithography, Interfaces, Microstructure, Grain growth, Pore drag, Coarsening, Crack healing, Fracture, Thermodynamics, Kinetics

1. Introduction

Most ceramics are fabricated from powders that have an average particle size between a few tenths to several microns. Particle size, particle size distribution, and particle packing play a major role in determining the pore size, pore size distribution, and pore spacing in the unfired compact. In well-packed compacts, the effective pore diameter is typically in the range of a few tenths of a micron. During the initial stages of sintering we are thus concerned with micron and submicron scale structures. Multimodal packing and the use of nanosized powders drive the size scale of interest even lower.

The pore network geometry has a strong influence on subsequent chemical and microstructural changes. The pore network is the pathway for the removal of fluids (drying). During heating, the pore network is the pathway for the redistribution and removal of organic additives (e.g., binders). The microstructural changes that occur during the transformation of an as-formed powder compact to a fired or sintered body at higher temperature reflect the relative rates of coarsening and densification. The geometry of the compact plays a major role in determining the driving forces for both coarsening and densification processes. The coupling between these topologically dictated driving forces and grain boundary, surface, and lattice diffusivities, or interfacial reaction rate constants, or both, will ultimately determine the relative fluxes associated with competing mass source-mass sink pairs, and thus will determine the dominant transport mechanism.

To simplify theoretical modelling of microstructural evolution, simple geometries, isotropy, and a single dominant process are often assumed. Real systems are generally more complex. Multiple processes interact and compete, the materials are anisotropic, and the geometries differ from those that are assumed. In modelling fracture, the situation is similar. The toughness increment due to a specific toughening mechanism can be sensitive to the local geometry of microstructural features, e.g., the size, number, and spacing of ductile ligaments in a brittle matrix.

When significant disparities develop between theoretical predictions and experimental observations, several explanations are thus possible. There may be a fundamental error in the modelling, or the disparities between the assumptions made in the model and the experimental conditions may be the cause. Studies on real materials can be inadequate to test theoretical models critically because of a limited ability to control the relevant microstructural parameters. Thus, an experimental method that provides control over the pore, flaw, or second phase geometry, and in some cases, the ability to alter the relative contributions of coarsening and densification processes, has the potential to further our understanding of both the thermodynamics and kinetics of microstructural evolution. Microdesigned samples which predetermine the geometrical characteristics of crack-interface interactions, e.g., the angle between the crack plane and the interface can have a similar beneficial impact on our understanding of fracture.

Our recent work has focussed on applying lithography to the study of microstructural evolution, both during sintering and during subsequent high-temperature use. We have developed several model experiments that closely simulate the theoretically modelled defect geometries. Using these experiments, high-temperature crack healing, pore-boundary interactions during sintering, pore coarsening, and pore elimination have been examined.

This paper has three primary objectives. These are: 1) to describe the technique, its capabilities and its limitation, 2) to review the application of the technique to a variety of research problems, and 3) to identify some additional, largely unexploited research opportunities.

2. Experimental Procedure

2.1. Process Description

2.1.1. Overview

Lithography has been used by researchers to pattern external surfaces for many years. For example, Huang et al. studied the morphological evolution of patterned sapphire surfaces at high temperature in the 1970's.[1] The method has also been applied to the fabrication of controlled-geometry internal defects. McKellar and Wardlaw used lithography to prepare two-dimensional glass micromodels of pore systems with ≥40μm pore diameters to study fluid flow in porous media.[2] Related techniques have also been developed to generate large stable void structures for various purposes. Kahn et al.[3,4] introduced patterned macrovoids (with dimensions of the order of several hundred microns) into PZT ceramics using fugitive ink and tape technology to increase the hydrostatic pressure-sensing response of the ceramic. Burger et al.[5] used photolithographic techniques to introduce flaws into Nb/Al_2O_3 interfaces, which were 5 to 200μm wide and 2μm deep. The flaw morphology did not change during a 2h anneal at 1700°C. Refinements of the basic lithographic method have made micron and submicron scale structures accessible, and studies of their evolution feasible.[6,7]

The combination of photolithographic methods, ion beam etching, and hot pressing provides the ability to define and introduce surface features with a controlled geometry and location, and to subsequently transform these surface features into internal flaws. **Figure 1** illustrates the basic processing steps. A wide range of interfacial structures can be simulated by controlled modification of the surface features and the bonding configuration. In principle, intragranular defects can be produced. Microdesigned intergranular defect structures can be produced in bicrystals in which both grain boundary misorientation and interface chemistry can be systematically varied. Identical defect structures can be introduced at single crystal/polycrystal and polycrystal/polycrystal interfaces.

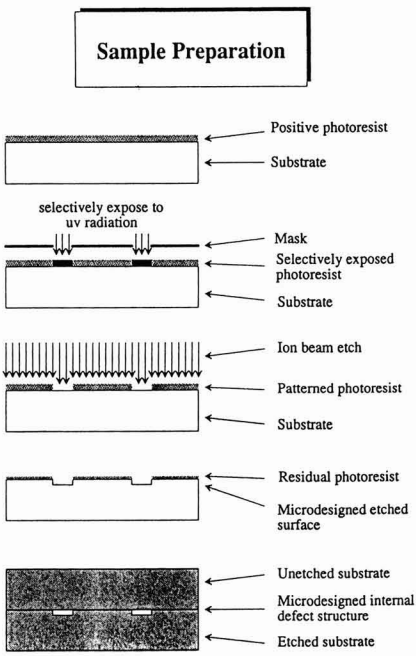

Fig. 1. Schematic illustration of procedure used to generate controlled interfacial pore structures: a) photoresist-coated substrate, b) selective exposure through a mask, c) ion beam etching of substrate and patterned photoresist, d) etched photoresist and substrate, and e) bonding.

To date, studies have focussed on alumina, and most of the defect structures produced have consisted of isolated voids (pores). In principle, the method is applicable to any material that can be etched and bonded. The production of microdesigned interphase interfaces, specifically ceramic-metal interfaces, is possible. Deposition and infiltration techniques provide the means of creating a broader spectrum of two-phase interfacial structures. The primary use of the method has been to study the morphological evolution of pores and cracklike defects, and thereby improve our understanding of the thermodynamic and kinetic properties of surfaces and interfaces at high temperatures. The use of such structures in fundamental studies of fracture is just beginning. Continuous micron scale pore structures have now been generated[8], and offer new opportunities for studying additive redistribution, binder burnout, infiltration, as well as pore network evolution during firing. In the following sections, the processing steps used in preparing microdesigned interfaces in sapphire will be described.

2.1.2. Mask Preparation

Masks provide the vehicle for transferring the desired pattern, which is generated using a computer aided layout system, to a sample surface. Chrome oxide coated glass disks are coated with a photoresist layer. The masks are prepared from these disks using a pattern generator*1 that selectively exposes the photoresist through a rectangular aperture. The aperture size adjusts to reflect the information generated by the CAD program. The photoresist is developed, and the exposed oxide is removed by chemical etching. The resulting patterned mask is used to expose photoresist-coated substrates selectively.

The smallest features that can be generated on the mask are 2μm×2μm squares. All other features are created by combining rectangular elements (boxes) with edge lengths that are multiples of 2μm. As an example, approximately 200 adjacent boxes must be exposed to generate a nearly perfectly circular feature (see 3.1.2) with a diameter of 800μm on the mask.

2.1.3. Photolithography

All processing of surfaces described herein was performed in Class 100 (less than 100 particles 0.5μm in diameter per cubic foot of air space) in the Microfabrication Laboratory at the University of California at Berkeley. Wafer surfaces were first ultrasonically cleaned with a solution of 1 part NH_4OH, 1 part H_2O_2, and 5 parts H_2O (hereafter called SC1) to remove organic residue from the surface, and 1 part HCl, 1 part H_2O_2 and 6 parts H_2O(SC2) to remove trace metals. Wafers were then rinsed in purified

*1 Pattern generator, GCA Corporation, Bedford, MA, U.S.A.

water and baked out at 150°C for 20min. Any remaining dust particles were blown off with a nitrogen gun. A drop of positive photoresist[*2] was placed onto the wafer (typically 12mm×10mm×0.7mm), which was then spun at 5000rpm for 30sec to produce a uniform 1.8μm thick photoresist layer. Subsequently, wafers were baked out at 90°C for 20 min on a hot plate. A hot plate is preferable to a conventional furnace because it promotes drying from the sapphire-photoresist interface. The purpose of the pre-exposure bake-out is to dry the resist film, prevent tackiness, and improve adhesion to the substrate.

The resist thickness can be varied within limits. A thin layer, e.g., 1.3μm thick at 6000rpm, is preferred if high resolution and small etch depths are the goals. If a deep etch is desired, and an etching technique that attacks both the resist and the substrate is used, a thicker photoresist layer is necessary. At 2000rpm, a uniform 2.6μm thick coating is obtained using the Shipley photoresist. Lower spin rates result in breakup of the resist layer. With special photoresists,[*3] a thickness of up to 30μm can be achieved, but the resolution of small features deteriorates with increasing thickness due to focussing problems during exposure and light scattering in the photoresist layer.

In the next processing step, the mask pattern is transferred to the photoresist-coated wafer by exposure with 436nm radiation. This produces photochemical changes in the resist that result in differential solubility. For all the work described in 3.1 and 3.2, the material used was sapphire, and the exposure was performed using a 4:1 projection printer[*4] that reduces the size of features in the mask by a factor 4; this reduction must be considered in the mask design. The examples given in 3.3 were produced using a contact printer to expose either glass samples (3.3.3) or metal/ceramic bend bars (3.3.4). The exposure time and focus that yield optimum resolution must be determined in advance.

In the final step prior to etching, the photoresist is developed for 1 min, rinsed with water for 1 min, blown dry with a nitrogen gun, and given a post-bake at 95°C for 10 min. The developer and post-bake conditions depend upon the specific photoresist used, and the values given are appropriate for the Shipley photoresist.

2.1.4. Etching

Although elegant crystallographically selective wet etching procedures for silicon are documented[9], many ceramics are more resistant to chemical attack, and dry etching is necessary. For sapphire, etching was performed with an argon ion beam in an ion mill[*5] under perpendicular incidence. To remove heat generated during ion bombardment, the sapphire wafers were placed upon a water-cooled aluminum substrate coated with an emulsion of polyphenylether (a low vapor pressure oil) and colloidal silver. A heat shield limits the exposure to a 5cm×5cm area. These measures are necessary to prevent photoresist deterioration during etching. The ion mill chamber is evacuated to≈1.3×10^{-4}Pa, and subsequently, argon is injected to establish an argon pressure of≈1.3×10^{-2}Pa. The substrate is rotated continuously during etching.

The ion beam is uniform over a diameter of≈7cm (in the absence of the heat shield). Thus, several samples can be etched concurrently under uniform conditions. At an accelerating voltage of 1 kV, the current density was 0.5mA/cm^2, and the etch rate was ≈0.6μm/h for basal plane sapphire.[*6] A surface profilometer[*7] can be used to measure the depth of features > 5μm wide. Feature depths were constant for all structures within the 25cm^2 bombarded area.

After etching, the residual photoresist was removed with acetone, and the sapphire wafer was cleaned with purified water. To remove all organic residue (from both the bombarded photoresist and the emulsion oil), wafers were cleaned with solutions SC1, SC2, heat-treated for 2h in air at 1200°C, and then cleaned again with SC1 and SC2.

The flexibility and reproducibility of the method is apparent in **Fig.2**, which depicts pore structures intended for several different studies. The structure illustrated in Figure 2a is suitable for studies of pore drag and pore separation (3.1.1) or pore elimination (3.1.5). A bimodal pore array in which the finer pores have submicron width is shown in Figure 2b, and is suitable for pore coarsening (3.1.4)or pore elimination (3.1.5) studies. Pore channel break-up (3.1.3), cavitational creep (3.1.6), the development of equilibrium pore shapes (3.2.1), fracture of porous solids (3.3.1)and composite structures (3.3.2,3.3.3), as well as dielectric breakdown (3.3.5). The morphological evolution of tailored nonequilibrium pore shapes, such as the chevrons in Figure 2d, can be examined to probe the development of metastable pore structures (3.2.2).

2.1.5. Hot Pressing

Prior to pressure bonding, samples should be checked for attached surface particles. These can be removed using either a nitrogen gun or clean room compatible paper.[*8] Failure to do so can contribute to poorly bonded interfaces, unwanted contamination, or both.

For hot pressing, the etched sapphire wafer was placed on top of either an untreated sapphire wafer, or a polished dense polycrystalline alumina substrate. The ensemble is placed between two hot-pressed boron nitride spacers,[*9] and then loaded into a high-purity graphite die.[*10] Typical sample dimensions were 12mm×10mm×0.7mm. Alignment inside the die was assured by having both sapphire disks butted against a third intermediate pre-cut boron nitride spacer.

Samples were subsequently heated to 1370°C at a rate of≈7°C/min. A stress of 15 MPa was sustained for 1h while a vacuum of≈2.6×10^{-3}Pa was maintained. The assemblies were continuously bonded, and defect structures reflecting the etched surface structures were obtained.

2.2. Modes of Observation

Once a microdesigned interfacial structure has been pro-

*2 Shipley 1400:13, GCA Corporation, bedford, MA, U.S.A.

*3 AZ 4303 Photoresist, American Hoechst Corporation, Sommerville, NJ, U.S.A.

*4 Canon, Santa Clara, CA, U.S.A.

*5 Veeco Microetch System, Veeco Instruments Inc., New UYork, NY, U.S.A.

*6 Adolf Meller Company, Providence, RI, U.S.A.

*7 Alphastep 200, Tencor Instruments, Mountain View, CA, U.S.A.

*8 Techni-Cloth, The Texwipe Company, Upper Saddle River, NJ, U.S.A.

*9 Union Carbide Corporation, Cleveland, OH, U.S.A.

*10 Poco Graphite, Inc., Decatur, TX, U.S.A.

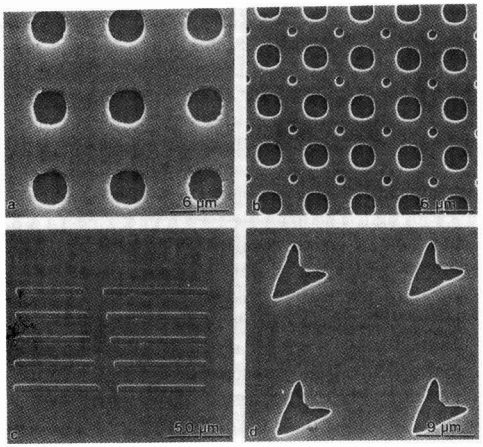

Fig. 2. SEM micrographs of accessible surface structures: a) monomodal pore array (see 3.1.1,3.1.5), b) bimodal pore structures (see 3.1.4), c) pore channels (see 3.1.3, 3.1.6, 3.2.1, 3.3.1, 3.3.2, 3.3.3 and 3.3.5) and d) chevrons (see 3.2.2).

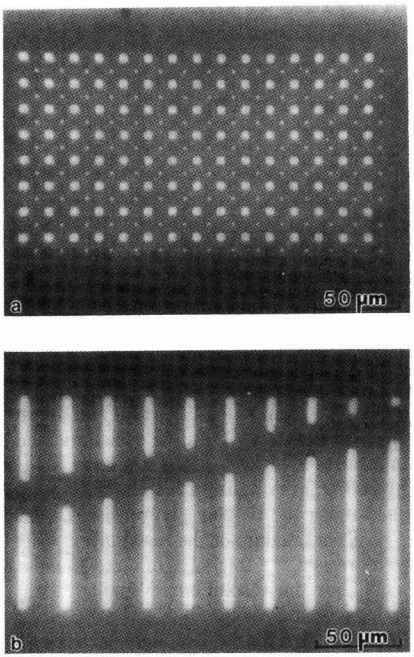

Fig. 3. Optical micrographs of internal pore structures: a) bimodal pore size distribution and b) pore structures with varying aspect ratio.

duced, monitoring the morphological evolution of the features is generally of interest. Three different methods of studying the evolution have been employed.

When one (or both) of the bonded wafers is optically transparent, optical microscopy provides a rapid, non-destructive means of evaluating the interfacial structure of the entire bonded assembly. The quality and continuity of the interfacial bond achieved during hot pressing can be assessed conveniently. Individual features can be examined also. Figure 3a illustrates internal arrays of pores with a bimodal size distribution, whereas Figure 3b shows internal features of varying aspect ratio. Optical microscopy is also a valuable tool for studying the evolution of morphologically unstable internal defects, such as cracks (3.1.2) and pore channels (3.1.3). Each microstructural element in the interfacial structure matrix can be catalogued, and the evolution of these features can be assessed by repeated heat treatment and microscopy.

Alternatively, as-bonded samples can be cut perpendicular to the bonded interface, polished, thermally etched, and then examined using scanning electron microscopy. This method allows scrutiny of the continuity of the interfacial bond, but also serves a key role in certain types of experiments. **Figures 4a** and **4b** illustrate the application of this method to the study of pores at single-crystal sapphire/polycrystalline alumina interfaces. The etched features were introduced into the sapphire (top), and the defects have not yet achieved equilibrium shapes; the pores are not symmetric about the interface. With further annealing, additional contraction parallel to and expansion perpendicular to the boundary is expected. SEM observations have been used extensively in studying pore-boundary interactions, and identifying pore-boundary separation conditions (3.1.1). Such observations also allow accurate measurements of the morphological evolution of pores in low misorientation bicrystals in materials exhibiting surface energy anisotropy. In these cases, the deviations from a circular cross section are of interest (3.1.2,3.1.2,and 3.2.2).

If the interface can be fractured, a second mode of high resolution SEM observation becomes possible, as illustrated in **Fig.5**. This technique is destructive, but the results supplement the observations provided by optical microscopy, and are particularly valuable when precise measurements

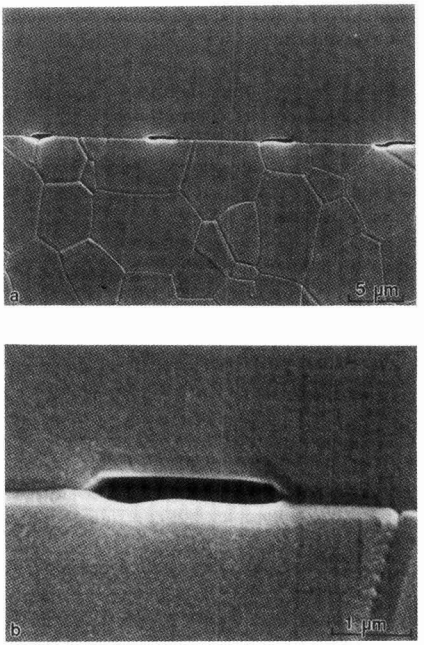

Fig. 4. Pores in single crystal-polycrystal interface: a) pore array, and b) high magnification of single pore.

(3.1.4 and 3.1.5) or detailed observations (3.1.2,3.1.3,3.2.1 and 3.2.2), or both, are required.

In principle, transmission electron microscopy can be applied also. Replicas of fracture surfaces can be produced and examined using TEM. Preparation of foils has been difficult, particularly when the interface contains many fine, closely spaced defects. The resulting foils are extremely delicate. Moreover, preferential attack of pore surfaces, and thus pore distortion may occur during ion beam milling. This can be prevented, or at least reduced, by using shallow incidence angles and lower voltage ion milling.

2.3. Limitations

Lithography has many advantages. Hundreds of data points can be collected from a single sample. Several different experiments can be conducted simultaneously. There is great flexibility in designing a pattern, and features of almost any size, shape, and spacing can be transferred to an internal interface. There are, however, several limitations and pattern design considerations that merit elaboration.

The number of features that can be produced at an interface is limited, and is related to the number of features that can be placed onto the mask. This number in turn depends upon the capabilities and limitations of the specific pattern generator used. It is possible to generate≈200,000 features on a high resolution mask. The mask can be used to expose several different regions on the wafer. Using a Canon mask aligner, the pattern can be repeated up to nine times with the lateral displacement of the pattern accurate to within 0.75μm. Thus, well in excess of 10^6 features can be introduced. This "limitation" on the number of features should not constrain most studies. Only pore elimination studies (3.1.5) require a large number of features.

Several limitations acting in tandem constrain the volume of the internal features that can be created. Since other techniques can produce large controlled-geometry defects, the primary sources of concern are the minimum feature volume, and the maximum feature depth.

The minimum feature depth and width determine the minimum feature volume. The lower limit on feature depth arises because one wants mask features, not intrinsic surface features/defects, to determine the final interfacial defect structure. Thus, the minimum feature depth must exceed the scale of the surface roughness. Sapphire single crystals can be obtained readily with a surface finish of 0.025μm, and features with depths as low as 0.09μm have been introduced and resolved.[10] If the defects are to be introduced in a polycrystalline sample, the surface must be well-polished.

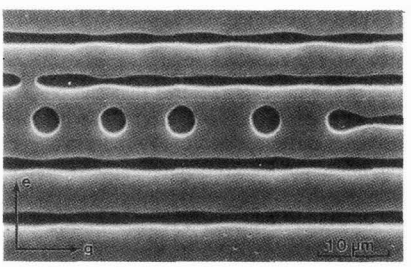

Fig. 5. SEM micrograph of bicrystal fracture surface (basal plane sapphire) with array of 5 channels of varying size. Sample had been heat treated for 25 hours at 1800°C; The directions e and g are [11$\bar{2}$0] and [1$\bar{1}$00], respectively.

The minimum feature width depends upon the wavelength of the radiation used to expose the photoresist. Using 436nm wavelength radiation, feature widths as small as≈1μm can be produced as illustrated by the smaller features in **Fig.2b**. (The minimum edge-to-edge feature separation is also of the order of 1μm.) This feature size in conjunction with the limitation imposed by surface roughness establishes a minimum accessible pore volume approximately equal to that of a spherical pore with a radius of 0.3μm.

The upper limit on the etch depth arises because both the photoresist and substrate are attacked during dry etching processes such as ion beam milling. The relative etch rates of the photoresist and substrate can vary considerably. The etch rate of sapphire is approximately one-third that of the photoresist under the etching conditions previously described. Thus, using the Shipley photoresist, the maximum etch depth is≈0.8μm. The etch rate of lithium fluoride is roughly equal to that of the photoresist under similar etching conditions, and thus, much deeper features can be produced.[11] Chemical etching is also possible for some materials. If less than optimum resolution is acceptable, thicker photoresist layers can be applied, and the etch depth can be increased to several microns. For many applications of interest, the accessible range of etch depths is adequate, and thus, the limitations are not of major concern.

If noncubic materials or dissimilar materials are to be bonded, thermal expansion mismatch induced cracking becomes a factor. This is a particular concern in alumina, where thermal expansion coefficients along the a-axis and c-axis differ by as much as 10%.[12] A full range of basal plane twist boundaries can be produced, but the range of misorientations accessible when prismatic plane crystals are to be bonded is much more restricted. Symmetric tilt boundaries are of course possible.

Finally, preserving the interfacial defect structure requires consideration of the overall arrangement of the surface structures on the substrate. If closely spaced etch pits are distributed uniformly over the entire surface, all pores may vanish during hot pressing because of vacancy condensation along the interface. Uniform vacancy condensation requires a vacancy flux that increases linearly with distance from the midpoint between two equisized pores. This in turn requires a parabolic vacancy concentration profile between the two pores if the concentration gradient is the driving force for the vacancy flux. To reduce the vacancy flux, and therefore the pore shrinkage rates, the interpore spacing must be increased. Fortunately, this need not be done uniformly and throughout the sample; isolating arrays of specific pore size and spacing with pore-free regions several hundred microns wide is sufficient to reduce pore shrinkage during both hot pressing/bonding and subsequent annealing significantly. This geometry equilibrates local stresses between points adjacent to the pore surface and at the midpoint between pores by a flow of vacancies from the pores to the grain boundaries. This relaxation of local stresses reduces the transport of matter within the pore arrays and causes the pore-free ligaments alone to support the compressive stress applied during hot pressing.

2.4. Refinements and Developments

Efforts to refine the technique further focus on three major areas. The first deals with increasing the geometric complexity and interconnectivity of the pattern. The fea-

tures studied to date have included simple equiaxed pore structures (3.1.1,3.1.4 and 3.1.5), features with varying aspect ratio (3.1.2 and 3.1.3), and very complex features generated with more elaborate computer programs (3.2.2). Features with a higher degree of connectivity have been generated.[8,13] The closure of continuous networks during high temperature annealing is being studied to improve our understanding of the transition from intermediate to final stage sintering.

There is a parallel interest in increasing the chemical complexity of the interfacial structures. Film deposition techniques are well developed in the semiconductor processing industry. The adaptation of these methods to the "filling" of etched surface features provides an opportunity to microdesign ceramic-metal composite interfaces. If features are continuous, infiltration by a metal, ceramic slurry, or a ceramic polymer precursor can potentially be explored to produce complex but controlled interfacial microstructures.

A growing interest in nanoscale materials is driving an effort to extend the accessible feature size downward to the nanoscale range. E-beam lithography provides this capability, and the National Nanofabrication Facility at Cornell has facilities that provide 25nm resolution.[14] Thus, the fabrication of nanoscale interfacial structures is possible, if substrates of sufficiently high surface quality can be prepared. Very recent developments have significantly reduced the cost of a high-resolution lithography capability. McIntyre et al. report that by interfacing a personal computer with an SEM, a system allowing the fabrication of e-beam lithography resolution features can be assembled for under $90,000.[15] The interface system in essence converts images drawn using graphics software to an instruction set that controls the movement of the SEM's electron beam. The possibility of fabricating 5 nm features is suggested. With features of this size, the temperature range over which the evolution of structures could be studied would be extended significantly. However, detection of the defects will be more challenging.

3. Applications

3.1. Kinetic Studies of Defect Evolution

3.1.1. Pore Drag and Pore-boundary Separation

Using lithographically introduced pore arrays, measurements of the maximum attainable velocity of a pore in a given material are possible. Moreover, the dependence of this so-called peak pore velocity on pore size, temperature, and impurity content can be determined. The peak pore velocity, specifically its value relative to the grain boundary velocity, has a critical effect on microstructural evolution in ceramics. During densification, pores at grain boundaries exert a drag force on migrating boundaries, and thus affect the grain boundary velocity. Simultaneously, the pores continue to shrink. If the pore velocity falls below the grain boundary velocity, pore-boundary separation ensues, and pore shrinkage effectively ceases. The peak pore velocity therefore has an impact on both of the major component processes during sintering, grain growth and densification.

Sample preparation entails the introduction of controlled-geometry pore arrays such as in **Fig.2a**, at the interface between a single crystal seed and a polycrystal (**Fig.4**). During subsequent heat treatment, the single crystal will consume the polycrystalline material. The migration rate of the single-crystal/polycrystal interface is affected by the drag force exerted by the pores (**Fig.6**). If pores remain attached to the grain boundaries, the grain boundary velocity has not exceeded the peak pore velocity. If in contrast, pore-boundary separation occurs, as illustrated in **Fig.7**, the interface (and therefore pore) velocity approached the peak pore velocity just prior to separation, and then exceeded it. Studies of pore drag and quantification of pore-boundary separation conditions in alumina have recently been completed [16,17]. Besides providing valuable new insights, a framework for analogous studies of pore drag in other systems has been established.

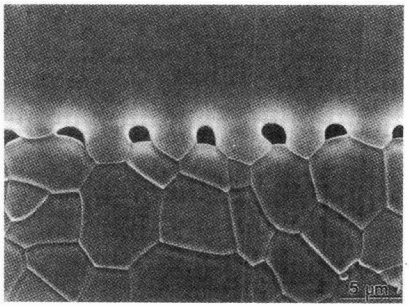

Fig. 6. Example of pore drag at interface between prismatic plane sapphire and MgO-doped alumina after 5h at 1600°C.

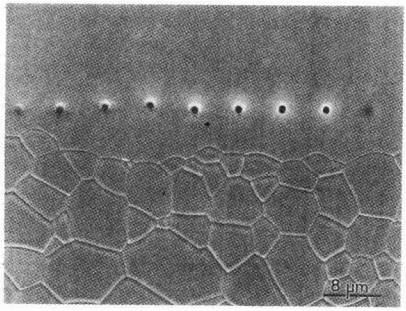

Fig. 7. Example of pore-boundary separation at interface between prismatic plane sapphire and MgO-doped alumina after 5h at 1600°C.

3.1.2. High-temperature crack healing

Crack healing is studied by introducing controlled-geometry cracklike defects into an interface using lithography, and then monitoring the evolution of the crack during high temperature annealing. The complementary nature of the different modes of observation was particularly valuable in this study. Optical microscopy provides a means of studying the evolution of individual cracks. The sequence of optical micrographs in **Fig.8** illustrates the healing of two specific circular cracks oriented parallel to the basal plane in a sapphire bicrystal after incremental anneals at 1800°C. Cross sections of cracks provided a means of assessing the effects of facetting and surface energy anisotropy on the healing characteristics.[18] High resolution SEM

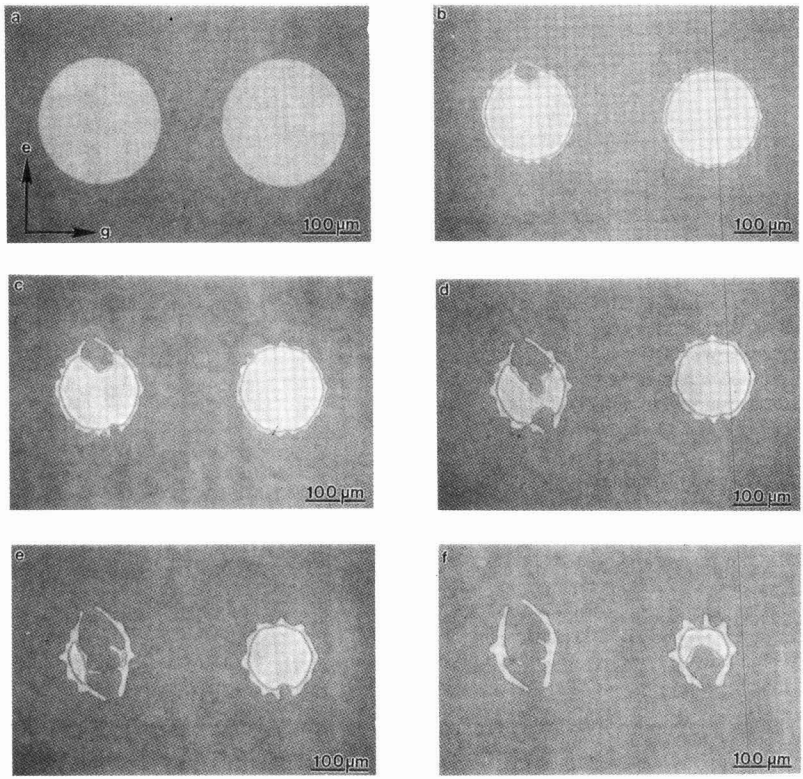

Fig. 8. Optical micrographs of circular cracks in basal plane sapphire after a) 0h, b) 4h, c) 8h, d) 14h, e) 22h,and f) 35h at 1800°C.

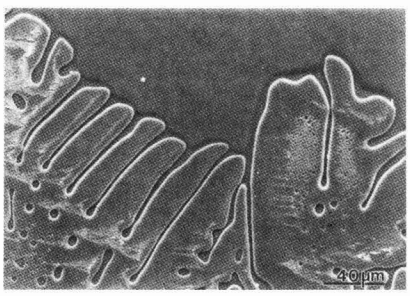

Fig. 9. SEM micrograph of bicrystal fracture surface (basal plane sapphire) of sample annealed for 5.5h at 1800°C. The partially healed crack was the result of incomplete bonding during hot pressing.

micrographs of fracture surfaces allow a more detailed view. **Figure 9** shows a partially healed basal plane crack that resulted from incomplete bonding. Cylinderization and breakup of cylindrical ligaments into spherical pores is evident.

Using lithography, both crack face and crack edge crystallography can be controlled, and thus, their effect on the morphological evolution of cracks can be assessed.[18] The observations have revealed that both crack face crystallography and crack edge orientation have a major impact on the healing process. Cracks oriented parallel to the basal, prismatic, and rhombohedral planes exhibit distinct healing

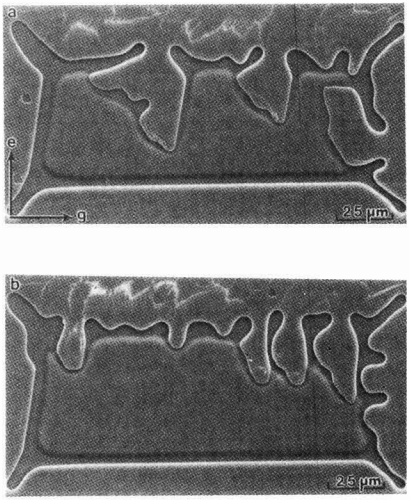

Fig. 10. SEM micrographs of bicrystal fracture surface (basal plane sapphire) of controlled-geometry cracks after heat treatment for 16h at 1800°C.

patterns.[10,18] The effect of crack edge orientation on crack healing is clearly evident in **Fig.10**. When the crack edges consist of energetically favorable planes (cusp orientations) edge perturbation and breakup are inhibited. More recent

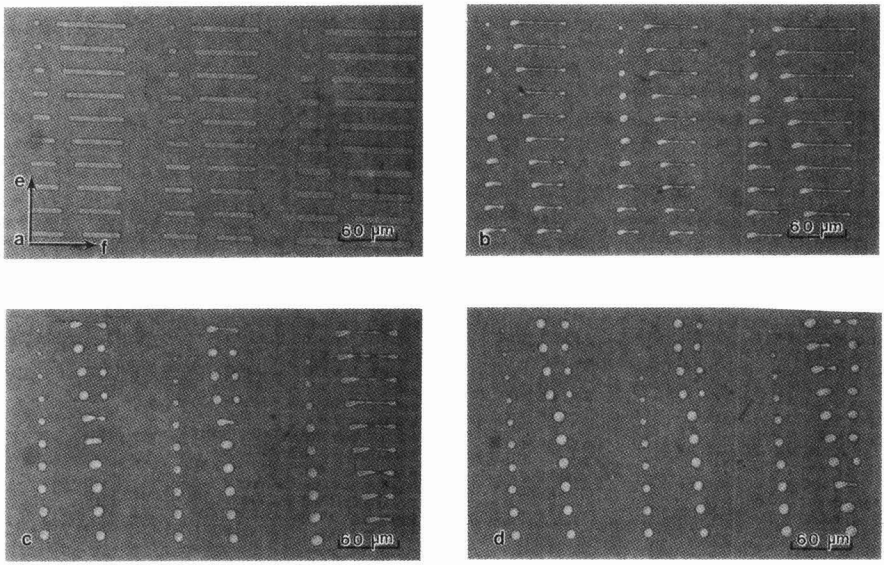

Fig. 11. Optical micrographs showing evolution of pore channels in basal plane sapphire bicrystals after heat treatments of a) 0h, b) 30h, c) 120h, and d) 180h at 1600°C; e=[11$\bar{2}$0] and f=[1$\bar{1}$00].

experiments, in which rectangular cracks have been rotated progressively within a fixed plane, indicate a systematic change in the stability of the edges to breakdown as the edge orientation is changed.[10] Surface energy anisotropy has less effect on the evolution of circular and accidentally introduced flaws, presumably because they sample a broader crystallographic spectrum along their edges.

Efforts to date have focussed on crack healing in undoped sapphire. Experiments utilizing doped and possibly co-doped sapphire are planned. Studies of crack healing in glass are in progress, and will ultimately address crack healing in glass-bonded and non-oxide ceramics. Elimination of defects at ceramic/ceramic and ceramic/metal interfaces is an essential aspect of diffusion bonding. The effects of flaw and surface characteristics (flaw width and depth and surface roughness) as well as of impurities in the adjoining materials in defect elimination rates can now be assessed readily.

3.1.3. Pore Channel Instability

High aspect ratio pore channels are subject to Rayleigh instabilities, and thus, kinetics permitting, will evolve into a string of isolated pores (Figure 5). During the intermediate stage of sintering, pore channels along three-grain junctions undergo breakdown and evolve into isolated pores. Similar morphological changes have been observed during the late stages of crack healing.[18]

Using lithography, pore channels of varying aspect ratio can be produced, and their breakdown can be studied [19]. **Figure 11** illustrates the use of optical microscopy and sequential heat treatments for studying pore channel breakdown. For pore channels in low misorientation angle bicrystals, the perturbation wavelengths and pore-pore spacings suggest strong effects of surface energy anisotropy. Neither crack face and crack edge crystallography, nor grain boundary misorientation were subject to control in previous experimental studies. Variations in these parameters may contribute significantly to the wide disparity in the surface diffusivities inferred from rates of pore channel breakup.

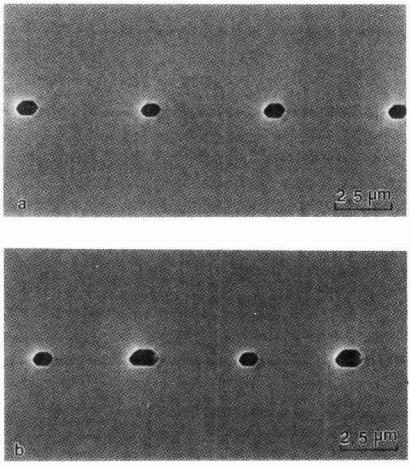

Fig. 12. Monomodal (a) and bimodal (b) pore size distributions in basal plane sapphire viewed edge on.

3.1.4. Pore Coarsening

This application of microdesigned interfaces has been described in detail,[20] but investigations of pore coarsening have not advanced beyond feasibility studies.[7,21] Pore coarsening reflects the transfer of vacancies between pores of differing size. To simplify the study (and analysis) of this phenomenon, bimodal surface structures exhibiting a high degree of symmetry (Fig. 2b) are created. After bonding, pore structures such as those illustrated in **Fig.12a** are obtained. During heat treatment, the growth of larger pores at the expense of smaller pores is monitored. The evolution of the arrays can be monitored continuously using optical microscopy, or by studies of fracture surfaces. By varying

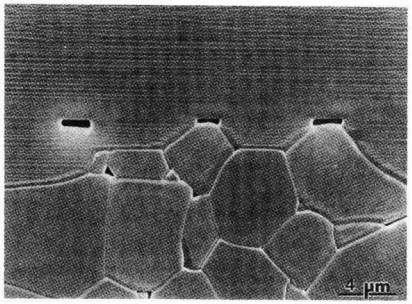

Fig. 13. SEM micrographs showing ensuing pore channel-boundary separation at interface between basal plane sapphire and polycrystalline alumina after heat treatment for 5h at 1800°C.

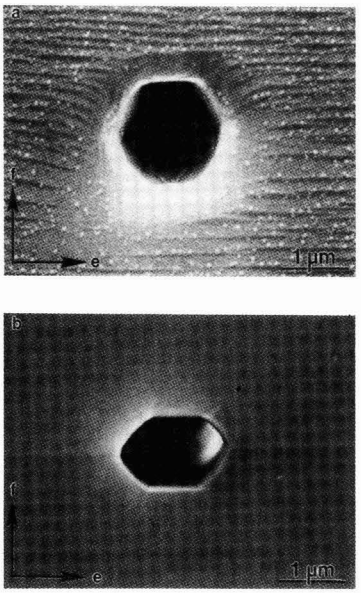

Fig. 14. Cross sections of pore channels a) in lattice and b) at grain boundary of basal plane sapphire bicrystal after heat treatment for a) 1.5h and b) 4h at 1800°C.

the grain boundary misorientation, it should be possible to separate the contributions of lattice and grain boundary transport to coarsening. In addition, strong effects of dopant additions on grain boundary transport rates should be discernable.

3.1.5. Pore Elimination

Pore elimination is the result of transfer of vacancies from the pore surface to the grain boundary. Monomodal structures, as illustrated in Figs.2a and 12b, simplify the analysis. Such controlled-geometry arrays are introduced at an interface, and then the wide pore-free regions that suppress pore elimination during hot pressing (see 2.3) are removed. During anneals, there will always be a contribution from diffusive transport of vacancies through the lattice. The bicrystal misorientation can be varied to modify the relative contribution from transport along the grain boundary.

To date, experiments have been limited to feasibility studies.[20,21] Although no external stress was applied in these experiments, a compressive or tensile stress could be applied. The densification rate could be examined as a function of applied stress. The densification potential can be determined by identifying the magnitude of the applied tensile stress that prevents densification.[22,23]

3.1.6. Cavitational Creep

This application has been suggested by many colleagues [24], but has not yet been pursued. It is a direct extension of the pore elimination studies. A sample containing the desired pore structure is subjected to tensile stresses that exceed the magnitude of the densification potential (also called the zero-creep stress[25]) at elevated temperature. Existing cavities (either naturally occurring or lithographically introduced) will grow and cause extension of the sample in the direction of the applied stress. This process plays a critical role in high temperature failure. [26] The mathematical formulation, in particular, the prediction of the crack propagation rate as a function of load and temperature, has been worked out in great detail.[27,28] Experimental verification has been attempted.[29] The ability to measure surface and grain boundary diffusivities accurately is as yet undemonstrated.

3.2. Thermodynamic Studies

3.2.1. Equilibrium Pore Structures

Lithographically introduced pores are well suited to determining equilibrium pore shapes.[30,31] Measurements of equilibrium pore shapes provide a means of determining certain aspects of the surface energy γ versus surface orientation (as characterized by an angle θ) plot.

Information on the form of the so-called γ-plot can be obtained by generating intragranular pore channels and determining the equilibrium cross section. Samples containing controlled orientation pore channels at a single-crystal/polycrystal interface can be produced. The interfaces can be designed such that pore channel-boundary separation (3.1.1) occurs (**Fig.13**) prior to any significant longitudinal instability (3.1.3). High resolution micrographs, as illustrated in **Fig.14a**, provide the equilibrium cross section for a pore channel of known orientation. If the pore channels are introduced at grain boundaries, a rule of truncation applies.[32] The effect of an intersecting grain boundary can be seen by comparing the channel cross sections in Fig.14a and 14b. The amount of truncation provides a measure of the grain boundary energy for the particular interface. By using crystals of differing orientations, or bicrystals of differing misorientation, or both, equilibrium pore channel cross sections along different crystallographic axes can be determined (**Fig.15**). By combining these, the inner envelop of the Wulff plot can be constructed.

3.2.2. Metastable Pore Structures

This preliminary investigation was prompted by the development of metastable pear-like pore shapes (**Fig.16**) during the morphological evolution of bimodal pore structures.[33] Pore shapes based primarily on six-fold and three-fold symmetry (**Fig.17**) were created. The pores were progressively rotated, **Fig.18**, to produce pore edges of differing orientation, and then annealed at 1800°C. Figure 18 shows the evolution of these structures. The outer and inner

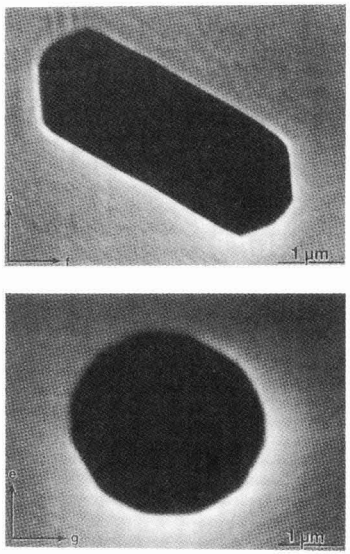

Fig. 15. Comparison of cross sections of pore channels in different grain boundaries after 48h at 1800°C.

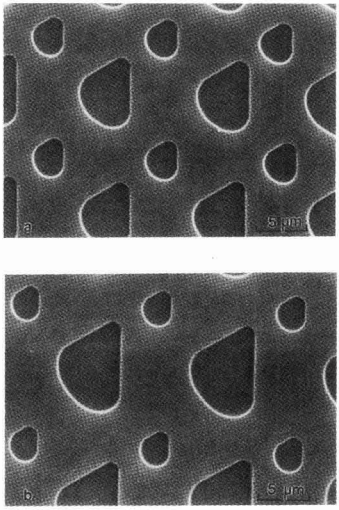

Fig. 16. SEM micrographs of bimodal distributions of pear-like pore structures.

perimeters appear to be round. As expected matter flows from the inner perimeter, which has one positive and one negative radius of curvature, to the outer perimeter, which has two negative radii of curvature. After dissolution of the inner joined region is complete, there is some indication of the formation of facets. Further work, using fracture surfaces and cross sections or both will hopefully provide additional useful information. Since surface diffusion is thought to dominate mass transport under the conditions used, experiments of this design can be used to assess the directional dependence of surface diffusion.

3.3. Fracture and Instabilities of Microdesigned Interfaces

3.3.1. Fracture of Porous Materials

Ryshkewitch investigated the effect of the volume fraction of porosity on fracture strength forty years ago.[34] The strength of alumina and zirconia decreased exponentially with increasing porosity. More recent studies, e.g., by Kendall et al.,[35] demonstrate the large increases in strength that are possible if large pores in the body are eliminated. By using test specimens with lithographically introduced defects, the size and relative location of flaws, and thereby the level of flaw-flaw interaction, could be controlled. Fracture experiments using a range of microdesigned defect structures thus could be useful in testing and improving our theoretical understanding of this fracture mechanics problem.

3.2.2. Fracture of Controlled-Geometry Composites

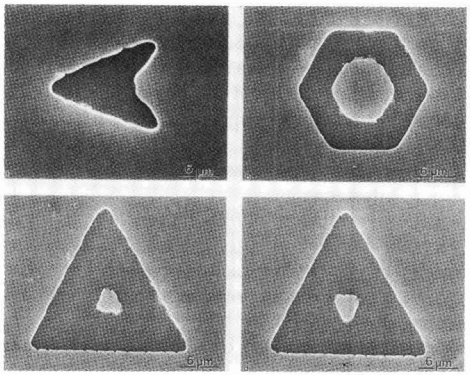

Fig. 17. High-complexity surface structures for studying the evolution and stability of metastable pore structures in sapphire.

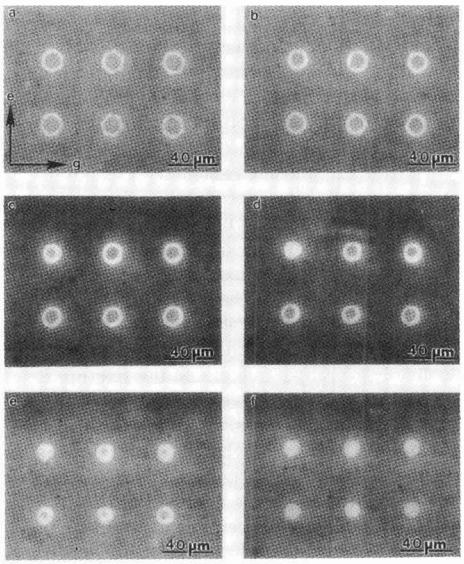

Fig. 18. Optical micrographs showing evolution of hexagonal pore annulus with varying orientation after a) 0h, b) 1h, c) 2h, d) 4h, e) 8h, and f) 16h at 1800°C.

Fracture of controlled-geometry composites can be investigated using procedures analogous to those for studying the fracture of porous ceramics. These composites can be produced by infiltration of microdesigned pore channels with a second phase, e.g., a metal. Samples can then be tested using configurations like those illustrated in **Fig.19**.

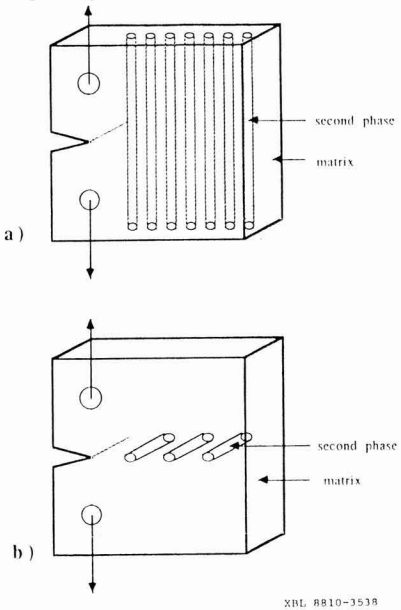

Fig. 19. Schematics outlining possible geometries for 2-dimensional controlled-geometry composites; a) rod-shaped second phase aligned perpendicular to the crack plane, and b) in the crack

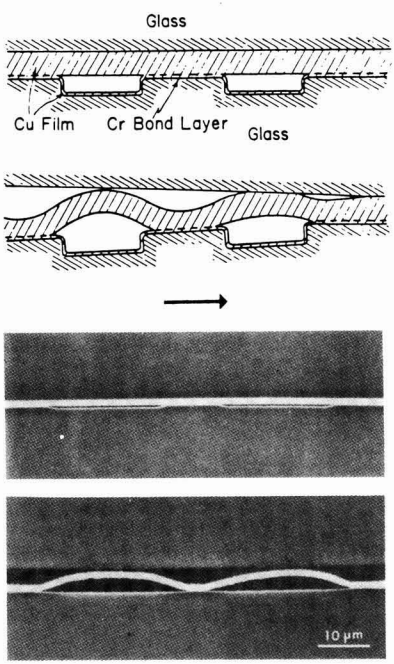

Fig. 20. Schematics and micrographs illustrating crack bridging for as-fabricated and cracked but still partially bridged interface.

This approach has the potential to isolate and determine the effects of several parameters on the fracture toughness of metal-reinforced composites. These parameters include the size (cross-sectional area), spacing, and debonding characteristics [36] of the second phase. The results of controlled experiments can then be used to guide the microstructural design of metal-infiltrated porous ceramic compacts.

3.3.3. Toughening of Ceramic-Metal Interfaces

Oh and co-workers have extended the lithographic technique and introduced controlled geometry near-interfacial cracklike defects in a ceramic-metal interface.[37,38] Specifically, cracklike defects were produced within a copper layer lying between two glass plates. The response of such samples, configured as double-cantilever beam test specimens, to an applied tensile stress was monitored. The fracture toughness of the patterned interfaces exhibited resistance curve (R-curve) behavior. Notably, the fracture toughness was 4×-9× that of a more conventional "planar" interface. The toughness increase was attributed to the formation of metal ligaments in the crack wake that bridged the crack faces and absorbed energy by plastic stretching. **Figure 20** illustrates the sample configuration and provides micrographs of cross sections before and after the application of a stress.

3.3.4. The Fracture Resistance of Non-Planar Interfaces

Evans and Hutchinson[39] suggest that interfacial roughness, particularly the height of interfacial steps, can have a strong effect on the interfacial fracture energy. This proposition can be tested by producing interfacial geometries with varying interfacial step heights. In contrast to the other applications that have been described, the method is used here to focus on interfacial geometries as opposed to pore-related geometries.

The effects of interfacial roughness on metal deformation (and therefore energy absorption) is shown in **Fig.21**. It depicts the front face of a bend bar, consisting of an $Al_2O_3/Pt/Al_2O_3$ sandwich. The reference lines were etched across the interface to permit better resolution in regions close to the interface where metal deformation is the focal point of observation.[40]

3.3.5. Dielectric Breakdown

Garboczi has analyzed dielectric breakdown [41] in a manner analogous to that used to analyze fracture. Energy balance calculations that treat dielectric breakdown via a

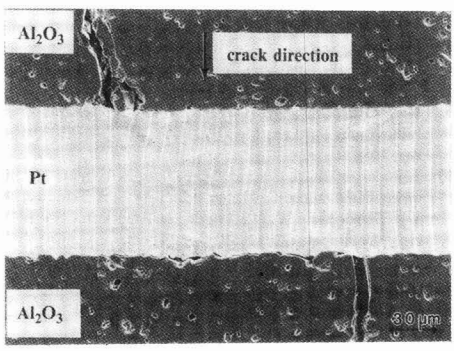

Fig. 21. Bend bar of Al_2O_3/Pt composite outlining crack path and metal deformation at the interface.

conducting crack embedded in an isotropic linear dielectric medium subjected to a uniform electric field can be performed. The results rationalize the observation that most materials show a dielectric breakdown strength much lower than the intrinsic strength. Although this analysis suggests a direction for developing improved dielectrics, its predictions have not been tested experimentally. Measurements of the dielectric strength of bicrystals containing controlled-geometry cracklike flaws or a distribution of second phase particles could either validate or disprove the modelling assumptions. The results also may provide guidance in the design of materials with higher dielectric strength.

3.3.6. Standards for Non-Destructive Testing

The ability to produce controlled-geometry cracklike defects at an internal interface is ideally suited to the production of calibration and resolution targets for non-destructive testing. The resolution limits of competing test methods[42] can be evaluated, and procedures that exploit the strengths of each can be developed. If multiple instruments of the same design are used, the target can serve as a calibration standard. Internal voids have been produced in ceramics by the burnout of embedded plastic spheres from a powder compact prior to densification.[43] Using lithography, cracklike defects of known depth, width, shape, relative location in the interface, and depth below the external surface can be produced. All of these parameters can be varied in one well-designed standard. In addition, the pattern can be reproduced precisely, and introduced into a broad range of materials. Efforts to produce such resolution targets have been initiated.

3.4. Pathway for Mass Transport

In the previous sections, the kinetics or thermodynamics of shape changes of defects, or the effects of a defect on a property were of interest. In the following applications, the defects provide a pathway for mass transport.

3.4.1. Binder Burnout

As a result of their limited plasticity, ceramics are typically formed from powders. Particulate-based forming techniques often involve the use of a liquid or organics (or both) to provide proper deformation and flow characteristics. The organics must be completely removed before sintering and pore closure.

Lewis and Cima have examined binder redistribution within, and removal of binder from, lithographically introduced pore networks in glass.[44] The channels were filled with a binder, a top cover was placed onto the filled channels, and optical hot stage microscopy was used to examine the binder redistribution. Two limitations of this study, a minimum accessible channel width of 20μm and the use of rectangles to approximate particles, have now been overcome.[8] It is now possible to simulate micron scale particles, and both well-packed and low-density regions of a compact.[13] These controlled-geometry network structures provide the basis for both binder redistribution, binder removal, and drying studies.

3.4.2. Liquid Metal and Vapor Infiltration

There are also several processing approaches in which the infiltration characteristics of porous media are of interest. Glass et al. have investigated the complete and partial infiltration of porous compacts and subsequent heat treatment for producing composites.[45] Hama et al.[46] have investigated the infiltration of porous alumina with polymer precursors to reduce the sintering temperature of alumina. Ceramic and other preforms can be infiltrated with liquid metal to fabricate ceramic-metal composites.[47] Stinton et al. have explored the use of thermal-gradient and pressure-gradient assisted vapor infiltration to produce SiC-SiC composites.[48]

Porous networks with controlled reproducible geometries can be produced using lithography. These networks are two-dimensional, and lack certain topological characteristics found in three dimensionally interconnected networks.[2] Still, these networks are more realistic representations of pore networks than parallel arrays of capillaries. Microstructures with different pore sizes and network structures can be simulated, and the effects of these variables can be assessed; the need for such measurements is suggested by the recent work of Toy and Scott.[49] Effects of changes in other microstructural or processing variables may be more readily apparent in experiments utilizing controlled-geometry networks. Modelling of flow processes in two-dimensional networks will be simpler than modelling of three-dimensional flow. Opportunities for direct comparison between results of computer simulations and experiment suggest themselves.

4. Conclusions

Lithographically produced microdesigned interfaces have provided a valuable new tool for studying the kinetics of pore-boundary interactions during sintering, high-temperature crack healing, pore coarsening and pore elimination. Thermodynamic studies of surfaces that provide information on the form of the γ-plot and its sensitivity to temperature and impurity additions are possible. Experiments can be designed to isolate a particular phenomenon, but also can be modified to allow the simultaneous occurrence of several processes.

Many opportunities exist for fundamental studies of fracture and flaw detection using lithographically prepared interfaces. Flow processes in porous media are also candidates for future studies. The technique is sufficiently flexible, that its application to the study of many other properties and phenomena should be possible.

Acknowledgements

We are indebted to Craig Carter for his assistance in the development of complex pore structures, and to Phil Guillory for technical assistance in the Microfabrication Laboratory in the Department of Electrical Engineering and Computer Science.

References:

1) F.H. Huang, R.A. Henrichsen and Che-Yu Li, "A Study of Capillarity and Mass Transport on the Al_2O_3 Surface," pp.173-86 in Mat. Sci. Res., Vol. 10, Sintering and Catalysis, Edited by G.C. Kuczynski, Plenum Press, New York, 1975.
2) M. McKellar and N.C. Wardlaw, "A Method of Making Two-Dimensional Glass Micromodels of Pore Systems," J. Can. Petr. Technol., 21,[4], 39-41 (1982).
3) M. Kahn and B. Kriese, "Patterned Macrovoids for Dielectric Constant Control of High Frequency Circuit Substrates,"in Electronic Packaging Materials Science, Mat. Res. Soc.,72,35-40(1986).
4) M. Kahn, A. Dalzell and B. Kovel, "PZT-Air Composites for Hydrostatic Sensing," Adv. Ceram. Mat., 2,[4],836-40(1987).

5) K. Burger, W. Mader and M. Rühle, "Structure, Chemistry and Diffusion Bonding of Metal/Ceramic Interfaces," Ultramicroscopy, 22, [1], 1-14(1987).
6) J. Rödel and A.M. Glaeser, "Production of Controlled-Morphology Pore Arrays: Implications and Opportunities," J. Am. Ceram. Soc., 70, [8], c172-c175 (1987).
7) J. Rödel, "Applications of Controlled Interfacial Pore Structures to Pore Perturbation and Pore Drag in Alumina," Ph.D. thesis, University of California, Berkeley (1988).
8) K. Johnson and A.M. Glaeser, unpublished research (1989).
9) R.A. Colclaser, MICROELECTRONICS: PROCESSING AND DEVICE DESIGN, John Wiley and Son, New York, New York (1980).
10) A. Nickles, J. Powers and A.M. Glaeser, unpublished research (1990).
11) J. Bullard, "Morphological Studies of Lithium Fluoride Surfaces," MS thesis, University of California, Berkeley (1990).
12) E. Dörre and H. Hübner, ALUMINA, Springer Verlag, Berlin 1984.
13) A.M. Glaeser, "Application of Microdesigned Interfaces to Studies of Ceramic Processing," to be published in Proceedings of Third International Conference on Ceramic Powder Processing Science, edited by G. Messing, H. Hausner, and S. Hirano, The American Ceramic Society, Westerville, OH.
14) G. Galvin, "Up Close: National Nanofabrication Facility at Cornell University," MRS Bull., 13, (7), 31-34 (1988).
15) B. McIntyre, R. Perman, and B. Gold, "Million Dollar Lithography For Less Than $90,000," R&D, 44-48, (December, 1989).
16) J. Rödel and A.M. Glaeser, "Pore Drag in Alumina," pp.280-95 in Sintering of Advanced Ceramics, Edited by C.A. Handwerker, J.E. Blendell and W.A. Kaysser, The American Ceramic Society, Columbus, OH (1990).
17) J. Rödel and A.M. Glaeser, "Pore Drag and Pore-Boundary Separation in Alumina," J. Am. Ceram. Soc.. 73[11]3302-12 (1990).
18) J. Rödel and A.M. Glaeser, "High Temperature Healing of Lithographically Introduced Cracks In Sapphire," J. Am. Ceram. Soc., 73,[3], 592-601 (1990).
19) J. Rödel and A.M. Glaeser, "Morphological Evolution of Pore Channels in Alumina," pp.243-57 in Sintering of Advanced Ceramics, Edited by C.A. Handwerker, J.E. Blendell and W.A. Kaysser, The American Ceramic Society, Columbus, OH (1990).
20) J. Rödel and A.M. Glaeser, "A Technique for Investigating the Elimination and Coarsening of Model Pore Arrays," Materials Letters, 6, [10], 351-355 (1988).
21) J. Bierach and A.W. Searcy, "Pore Coarsening and Pore Elimination in LiF," unpublished research.
22) R.M. Cannon and W.C. Carter, "Interplay of Sintering Microstructures, Driving Forces and Mass Transport Mechanisms," J. Am. Ceram. Soc., 72, [8], 1550-55 (1989).
23) W.C. Carter and R.M. Cannon, "Sintering Microstructures: Instabilities and the Interdependence of Mass Transport Mechanisms,"pp.137-63 in Sintering of Advanced Ceramics, Edited by C.A. Handwerker, J.E. Blendell and W.A. Kaysser, The American Ceramic society, Columbus, OH (1990)
24) M.D. Drory, J.Schneibel, G.H.Pharr, T.J. Chuang, A.Chokshi, private communications.
25) H. Udin, A.J. Shaler, J.Wulff, "The Surface Tension of Copper," Trans. AIME,186, [2], 186-90 (1949).
26) L.E. Svensson and G.L. Dunlop, "Growth of Intergranular Creep Cavities," Int. Met. Rev. 26, 109-32 (1981).
27) T.J. Chuang and J.R. Rice, "The Shape of Intergranular Creep Cracks Growing by Surface Diffusion," Acta Metall., 21,[12] 1625-28 (1973).
28) T.J. Chuang, "A Diffusive Crack-Growth Model for Creep Fracture," J. Am. Ceram. Soc. 65, [2], 93-103 (1982).
29) T.J. Chuang and N.J. Tighe, "Diffusional Crack Growth in Alumina," Proc. 3rd Int. Conf. Fund. Fract., Ed. P.Neumann, Schwaebische Bildungsgemeinde, Irrsee, West Germany, 129 (1989).
30) C.Herring, "Some Theorems on the Free Energies of Crystal Surfaces," Phys. Rev., 82, [1], 87-93 (1951).
31) C. Herring, "The Use of Classical Macroscopic Concepts in Surface-Energy Problems," pp.5-81 in STRUCTURE AND PROPERTIES OF SOLID SURFACES, ed. by R.Gomer and C.S. Smith, The University of Chicago Press, Chicago 1953.
32) J.W. Cahn and D.W. Hoffman, "A Vector Thermodynamics for Anisotropic Surfaces. Curved and Faceted Surfaces," Acta Metall., 22, [10], 1205-14 (1974).
33) J. Rödel and A.M. Glaeser, "Application of controlled interfacial pore structures to kinetic studies in alumina," in INTERFACIAL STRUCTURES, PROPERTIES AND DESIGN, edited by M.H. Yoo, W.A. T. Clark, and C.L. Braint (Mater. Res. Soc. Proc., 122, Pittsburgh, PA 1988); pp.485-90.
34) E. Ryshkewitch, "Compression Strength of Porous Sintered Alumina and Zirconia," J. Am. Ceram. Soc., 36, [2], 65-68 (1953).
35) N. McN. Alford, J.D. Birchall and K. Kendall, "High-Strength Ceramics through Colloidal Control to Remove Defects," Nature, 330, [6143], 51-53 (1987).
36) L.S. Sigl, P.A. Mataga, B.J. Dalgleish, R.M. McMeeking and A.G. Evans, "On the Toughness of Brittle Materials Reinforced with a Ductile Phase," Acta Metall., 36, [4], 945-53 (1988).
37) T.S. Oh, "Critical and Subcritical Crack-Growth Behavior along Toughened Ceramic/Metal Interfaces," Ph.D. Thesis, University of California, Berkeley, (1988).
38) T.S. Oh, J.Rödel, R.M. Cannon and R.O. Ritchie, "Ceramic/Metal Interfacial Crack Growth: Toughening by Controlled Microcracks and Interfacial Geometries," Acta Metall., 36, [8], 2083-93 (1988).
39) A.G. Evans and J.W. Hutchinson, "Effects of Non-Planarity on the Mixed Mode Fracture Resistance of Bimaterial Interfaces," Acta Metall., 37, [3] 909-16 (1989).
40) B. Dalgleish, J. Rödel and A.G. Evans, unpublished research.
41) E.J. Garboczi, "Linear Dielectric-Breakdown Electrostatics," Phys. Rev. B., 38, [13], 9005-10 (1988).
42) M.C. Bhardwaj, "Principles and Methods of Ultrasonic Characterization of Materials," Adv. Ceram. Mat., 1, [4], 311-24 (1986).
43) D.J. Roth and G.Y. Baaklini, "Reliability of Scanning Laser Acoustic Microscopy for Detecting Internal Voids in Structural Ceramics," Adv. Ceram. Mat., 1, [3], 252-58 (1986).
44) J. Lewis and M. Cima, "Binder Distibution Processes During Thermolysis from Ceramic Greenware," Paper 29-SIV-89, presented at 91st Annual Meeting of the American Ceramic Society, April 26, 1989; Indianapolis, IN.
45) S.J. Glass and D.J. Green, "Fabrication of Multiphase Ceramics by Infiltration into Powder Compacts," pp.784-91 in CERAMIC POWDER SCIENCE B, Ceramic Transactions, Vol. 1, Edited by G.L. Messing, E.R. Fuller Jr. and H.Hausner, The American Ceramic Society (1988).
46) Maasaki Hama, D.M. Dabbs, and I.A. Aksay, "Low Temperature Sintering of Ceramic Materials,"U.S. Application Number 109485
47) W.B. Hillig, "Melt Infiltration Approach to Ceramic-Matrix Composites," J. Am. Ceram. Soc., 71, [2], C96-C99 (1988).
48) D.P. Stinton, A.J. Caputo and R.A. Lowden, "Synthesis of Fiber-Reinforced SiC Composites by Chemical Vapor Infiltration," Am. Ceram. Soc. Bull., 65, [2], 347-50 (1986).
49) C.Toy and W.D. Scott, "Ceramic-Metal Composite Produced by Melt Infiltration," J. Am. Ceram. Soc, 73, [1], 97-101 (1990).

This article appeared in English in Nippon Seramikkusu Kyokai Gakujutsu Ronbunshi (Japanese version), Vol.99, No.4, 1991.

Preparation and Optical Properties of CuCl-Doped Na_2O-B_2O_3-SiO_2 Glasses

Hiroyuki Nasu, Shoji Kaneko, Keiji Tsunetomo* and Kanichi Kamiya

Department of Chemistry for Materials, Faculty of Engineering, Mie University, Kamihama, Tsu 514, Japan
* Department of Electrical Engineering, Faculty of Engineering, Hiroshima University, Saijo, Higashi-Hiroshima 724, Japan

CuCl-doped Na_2O-B_2O_3-SiO_2 glasses were successfully obtained by the conventional melt-quenching method. Complete glassy bodies were obtainable up to 2mol% CuCl. The CuCl microcrystals grew by heat-treatment at 450°C or 500°C, and the mean radius of the microcrystals was proportional to one third power of heating duration. The exciton peaks were observable even at room temperature and the temperature dependence of the peak shift implied the significant influence of volume effect. Homogeneous and inhomogeneous widths of the exciton peaks were evaluated from the temperature dependence of Z_3 peak line width. The large inhomogeneous distribution seems to result from the random structure of the matrix glasses and large microcrystal size distribution.
[Received February 26, 1990; Accepted January 24, 1991]

Key-words: CuCl-doped glasses, Optical properties, Microcrystal, Exciton, Coherent length

1. Introduction

The recent and remarkable development of optical, communication and processing technologies has stimulated the research and development of new materials for very fast optical systems. Materials with large optical nonlinearity are powerful candidates for the systems. Nonlinear polarizability of a material (P_{NL}) is expressed as

$$P_{NL} = \chi^{(2)}E^2 + \chi^{(3)}E^3 + \cdots \quad \ldots\ldots\ldots\ldots (1)$$

where E is electric field, and $\chi^{(2)}$ and $\chi^{(3)}$ are second- and third-order nonlinear susceptibility. For all-optical or optoelectronic communication systems, the optical Kerr effect, and optical bistability, in particular, caused by $\chi^{(3)}$ are quite significant. To obtain effective functions, large $\chi^{(3)}$ is naturally preferable. The studies of developing materials with large $\chi^{(3)}$ can be divided into two categories. One is the study of large homogeneous $\chi^{(3)}$ glasses, such as high-index glasses,[1-3] and the other is that of the glasses containing metal or semiconductor microcrystals.[4-7] Although nonresonant-type $\chi^{(3)}$ of homogeneous glasses has been no more than 10^{-10} (esu), that of resonant-type CdS_xSe_{1-x}-doped glasses are on the order of 10^{-8} to 10^{-9} (esu)[4] in the visible region. In particular, $\chi^{(3)}$ caused by excitons are predicted to be much larger than that of CdS_xSe_{1-x}-doped glasses.[8] Although the radius of exciton of the semiconductors is commonly larger than the microcrystals doped in glasses as quantum dots, excitons of some halides such as CuCl or CuBr seem to be formable due to the small exciton radius, even in quantum dots. Ekimov et al.[9,10,11] prepared CuCl or CuBr-doped glasses and found exciton peaks at 4.2K. Further, they confirmed the existence of the quantum size effect of the doped microcrystals. However, detailed information important for practical use such as the composition of the matrix glasses, temperature dependence of exciton peaks and the influences of glass matrix compared to crystal matrix, has not been sufficiently provided. Therefore, this work reports preparation and temperature dependence of exciton-peaks of CuCl-doped Na_2O-B_2O_3-SiO_2 glasses and influences of matrix on optical properties.

2. Experimental Procedure

Commercially available analytical grade, Na_2CO_3, B_2O_3, SiO_2 and CuCl were used as raw materials. The Na_2CO_3, B_2O_3 and SiO_2 powders were weighed to be $13Na_2O{\cdot}54B_2O_3{\cdot}33SiO_2$ in mol%, and after mixed well, the batch was put into a platinum crucible and decarbonated at 800°C for 30 min in air. Subsequently, the batches were melted at 1100°C for 1h in air, and the melts were quenched between stainless steel plates. The quenched bodies were completely transparent and glassy. Then, the bodies were crushed by stainless steel dye and milled by alumina pestle and motor. After milled, the powders passing through 60 mesh were used as raw matrix powders. Then, CuCl was weighed and mixed with the powder. The concentration of CuCl was varied from 0.5 to 15mol% to the matrix glasses, but no microcrystals could be formed below 1mol% CuCl even after heat-treatment. The mixed batches were melted using platinum crucibles from 1350°C to 1450°C for 5 min with covers of platinum, and then the melts were quenched between stainless steel plates. The quenched bodies containing CuCl less than 2mol% were transparent and completely glassy.

The glass samples were annealed at 450°C or 500°C for various duration, so as to form microcrystals. After annealed, the glasses were polished and optical spectra were measured with an optical spectrometer (Cary 14) from liquid nitrogen temperature to room temperature. The CuCl films were prepared by vacuum evaporation for comparison.

3. Results and Discussion

Glass forming region as a function of the concentration of CuCl is tabulated in **Table 1** with final melting temperature. Complete homogeneous glasses were obtained to 2mol% CuCl in the nominal composition as seen in the table, while the quenched bodies containing over 2mol% CuCl were opaque, and CuCl large crystals precipitated,

those identified from the X-ray diffraction pattern.

Figure 1 shows the exciton peaks of CuCl polycrystalline film at 77K for comparison. The peak at nearly 375nm and that at nearly 383nm are ascribed to $Z_{1,2}$ and Z_3 peaks, respectively. Both peaks were quite sharp and the position of the each was quite similar to those in literature.[9,10,11] The dependence of growth of exciton peaks of CuCl in the glass on annealing conditions measured at 77K are shown in **Figs.2(a)** and **(b)**. The annealing temperatures were 500°C and 450°C and the time was from 3h to 18h. In Fig.2(a), the shoulder assignable to Z_3 peak could be seen even for 10 min heat-treatment, and the peak became sharper with increasing heating time. Both $Z_{1,2}$ and Z_3 peaks shifted to longer wavelength as annealing time increased, the shift resulting from the increase of mean diameter of the microcrystals. On the other hand, the effect of annealing was not relatively effective at 450°C. Even after 3h treatment, no Z_3 peak was detectable, and the 84h's treatment was necessary to obtain clear Z_3 peak. With respect to the red shift, both peaks likewise shifted to longer wavelength, resulting from the increase of microcrystal diameter as will be discussed below. After vert long annealing enough to form CuCl crystals without quantum size effect, no difference in the peak positions of the exciton could be seen in CuCl films and in glass matrix. It is interpreted that theoretically, the exciton absorption energy is mainly influenced by the mass of excitons and crystal radius, and that the energy is insensitive with small amounts of impurities.

Table 1. Glass forming region of xCuCl (1-x)($13Na_2O \cdot 53B_2O_3 \cdot 33SiO_2$) (mol%) glasses as a function of x.

x	melting temperature	state of quenched bodies
1	1350℃, 1450℃	glass
2	1350℃, 1450℃	glass
3	1450℃	glass + partially crystal
5	1450℃	partially glass + crystal
7	1450℃	crystal
9	1450℃	crystal
10	1450℃	crystal
15	1450℃	crystal

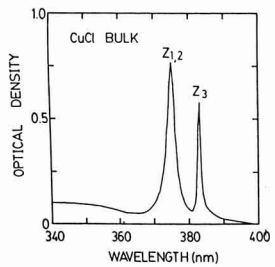

Fig. 1. Exciton peaks of bulk CuCl at 77K.

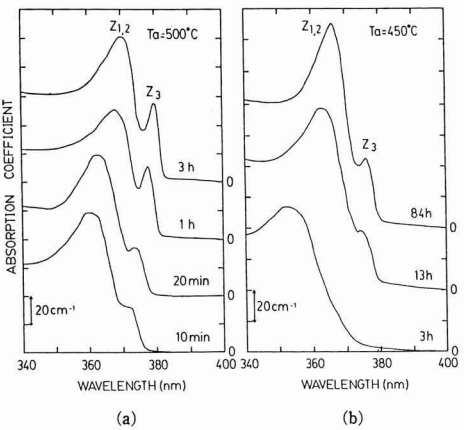

Fig. 2. Annealing time dependence of exciton peaks when annealed at 500°C (a) and 450°C (b), measured at 77K.

Figure 3 depicts dependence of energies of the exciton peaks on the temperature of measurements for the sample annealed at 500°C for 3h. As temperature increases, the Z_3 peak became broader, but, even at 249K and at room temperature, the exciton peaks were observable. That is quite important for the future practical use of the materials as an exciton device at room temperature.

The mean diameter of the microcrystals was evaluated by the following. The observed blue shift (ΔE) at constant temperature is theoretically proportional to the reciprocal of square diameter of microcrystals as $\Delta E \propto 1/d^2$. [9] Therefore, by fitting the blue shift of this work for $Z_{1,2}$ and Z_3, one can evaluate mean diameter of the microcrystals in the present glasses. Specifically, $d\Delta E_{Z1,2}/d(1/R)^2$ is evaluated from ref.11 as 19.9, and the average microcrystal diameter (d) is calculated from

$$d = \frac{4.464}{(\Delta E_{Z1,2} - \Delta E_{77K})^{1/2}} \quad \cdots\cdots\cdots\cdots (2)$$

When the crystallization process undergoes in supersaturated melts and crystals grow at the expense of small crystalline particles, the mean radius of crystals depends on $t^{1/3}$, where t is annealing time (Lifshitz-Slyozov model[13]). The radius of CuCl is plotted against $t^{1/3}$ in **Fig.4**. One can point out that the growth mechanism of CuCl microcrystals can be interpreted by Lifshitz-Slyozov model at 500°C and 450°C, and the growth rate at 500°C is rather faster than that at 450°C.

Figures 5(a) and **(b)** show the temperature dependence of peak energies of $Z_{1,2}$ and Z_3, respectively, for the samples annealed at 500°C. As pointed out above, the crystal radius is dependent on one third of annealing time, and thus crystal diameter increases as annealing time increases. The red

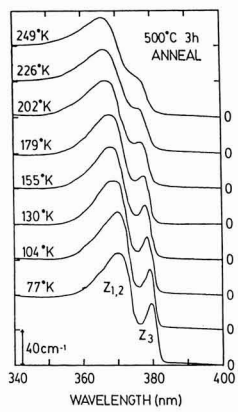

Fig. 3. Temperature dependence of exciton peaks for the sample annealed at 500°C for 3h.

shift of peaks due to annealing can be interpreted by the increase of crystal diameter. As temperature increases, the peaks show blue shift. From the linear relationship between temperature and the blue shift (ΔE), one can calculate temperature coefficient of the shift. For bulk CuCl, $d\Delta E/dT = 1.3\times10^{-4}$eV/K, and no obvious dependence on the diameter can be seen. The value for bulk CuCl can be considered as temperature dependence of band gap and the present value seem to contain those of band gap and quantum size effect. Assuming that the band gap of microcrystals is the same as bulk, temperature dependence of quantum size effect is calculated as 0.8 to 1.3×10^{-4}eV/K. According to Cordona[14], $d\Delta E/dT$ is caused by two factors. One is volume effect, resulting from thermal expansion of lattice, and the other is the explicit temperature effect, resulting from electron-phonon interaction. Volume effect should positively influence $d\Delta E/dT$, but the other should yield negative $d\Delta E/dT$. The observed $d\Delta E/dT$ is positive and similar to that of the band gap. Thus, the positive temperature dependence of the quantum size effect can be attributed to the volume effect.

Figure 6 shows temperature dependence of the linewidth (Γ) of Z_3 peak. The line width can be expressed as

$$\Gamma = \Gamma_{inh} + \Gamma_h = \Gamma_{inh} + A/[\exp(B/k_BT) - 1] \quad (3)$$

where Γ_{inh} and Γ_h are inhomogeneous and homogeneous linewidth, respectively, and A and B are constants. By fitting this equation with the experimental values in Fig.6, Γ_{inh}, A and B are estimated as 23.4meV, 502meV and 58.0meV, respectively. Compared to the values for CuCl microcrystal in NaCl matrix,[15] Γ_{inh} in glasses (23.4meV) is far larger than that in NaCl matrix (8.0meV). That seems to result from the random structure of glass matrix and larger distribution of microcrystal size. 58.0meV for B is very close to that in NaCl matrix, and thus the excitation process seems to be quite similar to the CuCl microcrystals in NaCl matrix.

Figure 7 depicts $\Delta E(Z_{1,2}\text{-}Z_3)$ as a function of temperature for the samples annealed at 500°C. Although some fluctuation can be seen, it can be said that $\Delta E(Z_{1,2}\text{-}Z_3)$ is almost independent of temperature. $\Delta E(Z_{1,2}\text{-}Z_3)$ is plotted against $1/R^2$ in **Fig.8** with the data in literature[9] for comparison. The deviation between solid and broken lines is due to the difference of the temperature. According to Ekimov et al.,[9] the spectral position of Z_3 can be expressed as

$$h\omega_{Z_3} = E_q - E_{ex} + 0.67\frac{h^2}{2M_3a}\pi^2 \quad \ldots\ldots\ldots (4)$$

where E_q and E_{ex} are energy gap and exciton energy, respec-

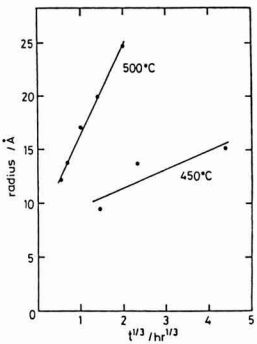

Fig. 4. Radius of CuCl microcrystals as a function of one third power of annealing time.

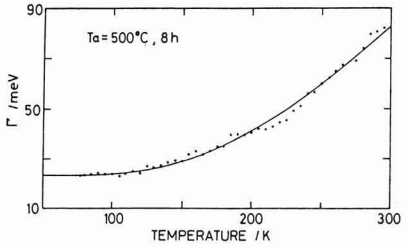

Fig. 6. Temperature dependence of the linewidth of Z_3 peak for the samples annealed at 500°C for 8h. The line was drawn by the least square fitting.

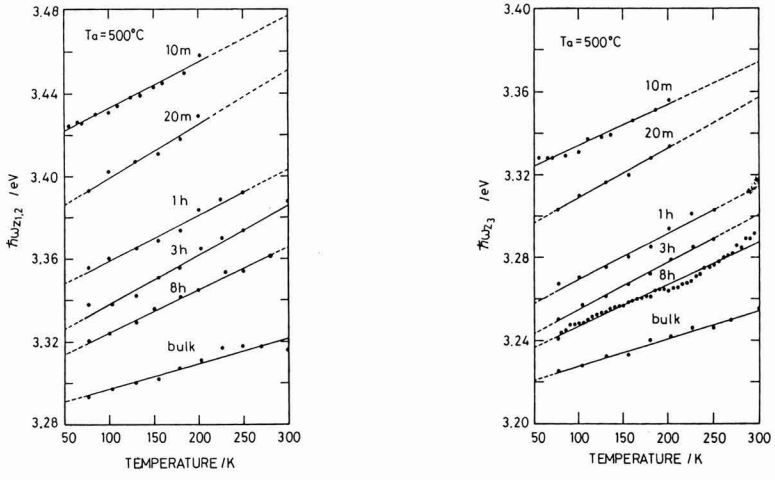

Fig. 5. Temperature dependence of spectral $Z_{1,2}$ (a) and Z_3 (b) peak positions for the samples annealed at 500°C. Annealing times are denoted besides each line.

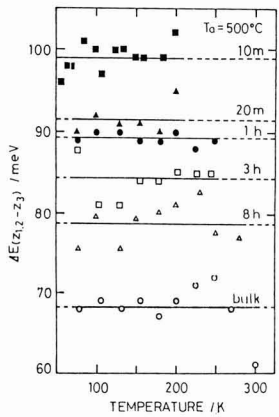

Fig. 7. The energy difference of $Z_{1,2}$ and Z_3 peaks, $\Delta E(Z_{1,2}-Z_3)$, as a function of temperature for the samples annealed at 500°C. Annealing times were denoted beside each line.

tively, M_s is the exciton translational mass, and a is mean radius of microcrystals. On the other hand, that of $Z_{1,2}$ is given by

$$h\omega_{Z_{1,2}} = E_q - E_{ex} + 0.67\frac{h^2}{2M_h a}[\psi(M_l/M_h)]^2 \quad . . (5)$$

where M_h and M_l are the mass of the heavy and light excitons, respectively, and $\psi(M_l/M_h)$ is a root of the transcendental equation cited in Ref.16). Thus, $\Delta E(Z_{1,2}-Z_3)$ can be expressed as

$$\Delta E(Z_{1,2}-Z_3) = \frac{0.67}{a}\left(\frac{h^2}{2M_h}[\psi(M_l/M_h)]^2 - \frac{h^2\pi^2}{2M_s}\right) \quad \ldots\ldots (6)$$

Thus, when the masses of excitons are independent of the diameter, $\Delta E(Z_{1,2}-Z_3)$ could be linearly proportional to $1/a^2$. Above a=15A, $\Delta E(Z_{1,2}-Z_3)$ is linearly proportional to $1/a^2$ as expected when the masses are constant. However, below 15A, the experimental points deviated from the line. Ultimate interpretation on the deviation is so far difficult, but one may presume that the basic parameters of exciton are influenced by the microcrystal size, or that the quantum size effect changes to the relative motion of electrons and holes from center-of-mass motion when the size comes to be close to the Bohr radius of CuCl exciton (13.6A in diameter).[12]

4. Conclusion

CuCl-doped Na_2O-B_2O_3-SiO_2 glasses were successfully prepared by the conventional melt-quenching technique. The maximum content of CuCl to obtain complete homogeneous glasses is 2mol%. The exciton peaks are observed at 77K and even at room temperature. The microcrystal radius is dependent on one third power of annealing time, which clears the crystal growth process. The spectral exciton positions $Z_{1,2}$ and Z_3 are dependent on microcrystal size, and it proves the existence of quantum size effect. The temperature dependence of peak position is attributed to mainly volume effect. From the temperature dependence of Z_3 linewidth, inhomogeneous term is much larger than that of CuCl in NaCl matrix, presumably resulting from the random structure of glass matrix and larger crystal size distribution. Coherent length of CuCl is evaluated to cover whole microcrystals from homogeneous term. The energy difference of $Z_{1,2}$ and Z_3 peak was linearly proportional to the reciprocal of square diameter of microcrystals ($1/a^2$), when a is larger than 15A. However, obvious deviation is noticed below a=15A, perhaps attributable to the change of exciton type.

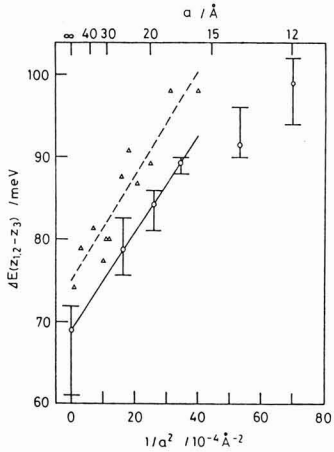

Fig. 8. $\Delta E(Z_{1,2}-Z_3)$ as a function of the reciprocal of square mean diameter of microcrystals, $1/a^2$.

References:

1) D.W. Hall, M.A. Newhouse, N.F. Borrelli, W.H. Dumbaugh and D.L. Weidman, Appl. Phys. Lett. 54 (1989) 1293-1295.
2) H. Nasu, Y. Ibara and K. Kubodera, J. Non-Cryst. Solids 110 (1989) 229-234.
3) H. Nasu, M. Nakamura, K. Kamiya, M. Kobayashi and K. Kubodera, J. Amer. Ceram. Soc., in press.
4) R.K. Jain and R.C. Lind, J. Opt. Soc. Am. 73 (1983) 647-653.
5) J. Yumoto, S. Fukushima and K. Kubodera, Opt. Lett. 12 (1987) 832-834.
6) H. Nasu, K. Tsunetomo, Y. Tokumitsu and Y. Osaka, Jpn. J. Appl. Phys. 28 (1989) L862-864.
7) K. Tsunetomo, H. Nasu, H. Kitayama, A. Kawabuchi and Y. Osaka, Jpn. J. Appl. Phys. 28 (1989) 1928-1933.
8) E. Hanamura, Phys. Rev. B 37 (1988) 1273-1279.
9) A.I. Ekimov, Al. L. Efros and A.A. Onushchenko, Solid. St. Comm. 56 (1985) 921-924.
10) A.I. Ekimov, A.A. Onushchenko, A.G. Plyukhin and Al. L. Efros, Sov. Phys. JETP 61 (1985) 891-897.
11) A.I. Ekimov, Al. L.Efros, M.G. Ivonov, A.A. Onushchenko and S.K. Shumilov, Solid St. Comm. 69 (1989) 565-568.
12) T. Itoh, Y. Iwabuchi and T. Kirihara, Phys. Stat. Sol. (b) 146 (1988) 531-543.
13) I.M. Lifshtz and V.V. Slesov, Zh. Eksp. Theor. Fiz. 35 (1958) 479.
14) M. Cardona, Phys. Rev. 129 (1963) 69-78.
15) Y. Masumoto, Kotai Butsuri 24 (1989) 937-940.
16) A.I. Ekimov, A.A. Onushchenko, A.G. Pluhin and Al.L. Efros, Sov. Phys. JETP 61 (9185) 891-897.
17) Y. Kayanuma, Kotai Butsuri 24 (1989) 551-558.

This article appeared in English in Nippon Seramikkusu Kyokai Gakujutsu Ronbunshi (Japanese version), Vol.99, No.4, 1991.

Preparation and Sinterability of Zirconia-Toughened-Alumina Composite Powder

Chii-Shyang HWANG and Wen-Haur LIN

Department of Materials Engineering, National Cheng-Kung University, Tainan, Taiwan, R.O.C.

To improve the properties of zirconia-toughened-alumina(ZTA) ceramics, a technique which involves hydrolysis of $Zr(OC_3H_7)_4$ in an Al_2O_3 slurry to form an Al_2O_3 powder with uniformly distributed ZrO_2 is described. The addition of TiO_2 within its solubility limit in ZTA enhanced the sinterability of the ZTA powder. A relative density of 98% for ZTA bodies can be obtained by firing at 1500°C for 2hr. It is shown that the presence of TiO_2 promotes the grain growth of Al_2O_3 and ZrO_2, and contributes to the retention of tetragonal-ZrO_2 in the sintered ZTA body.

[Received September 17, 1990; Accepted January 24, 1991]

Key-words: Al_2O_3-ZrO_2 system, TiO_2 addition, Sintering, Phase transformation, Microstructure

1. Introduction

To enhance the mechanical properties of alumina ceramics, it is known that dispersed ZrO_2 particles in Al_2O_3 matrix play an important role. The so-called zirconia-toughened-alumina (ZTA) ceramics has many applications in which high wear resistance and mechanical strength are required.[1,2] It is believed that the mechanical properties of ZTA composite depend mainly on the ZrO_2 content, the size of ZrO_2 grains and the relative content of tetragonal-ZrO_2. Two important mechanisms, i.e., stress induced transformation toughening and microcrack toughening have been proposed to explain the increased toughness of ZTA composite.[3,4] The transformation of t-ZrO_2 to m-ZrO_2 depends on the critical size[5] which in turn is related to Young's modulus of the matrix, the shape of ZrO_2 particle (polymorph or round), the location of ZrO_2 particle (intergranular or intragranular) and the variety of stabilizers (CaO, MgO, Y_2O_3 etc.).[6]

In order to improve the properties of ZTA ceramics, various approaches, such as mechanical mixing of powders,[7] reactive sintering,[7] sol-gel synthesis,[7,8] evaporative decomposition of slurry,[9] spray-ICP technique[10] and optimized ZrO_2 particle size and size distributions[7] have been reported. However, there are still many unsolved problems such as non-homogeneity, difficult sintering and retention of t-ZrO_2 in the sintered ZTA body, etc[11,12] which need to be investigated. In this study, a technique which involves hydrolysis of Zr-alkoxide in Al_2O_3 slurry for the preparation of Al_2O_3-ZrO_2 powders is described. The effect of a small amount of TiO_2 additives on the sintering temperature of ZTA ceramics and the retention of tetragonal ZrO_2 in the sintered ZTA body was investigated.

2. Experimental Procedure

The starting materials were high purity alumina (α-Al_2O_3, AKP-20, Sumitomo Chemical Co., Ltd.) and zirconium (IV) propoxide (Fluka Co., Ltd.) which used to synthesize ZTA powders. Tetraisopropyl orthotitanate(TPT, Tokyo Kasei Co., Ltd.) was used to synthesize the additive of TiO_2. The amount of TPT was adjusted so as to provide 2.5 mole% TiO_2 in the final mixed powder. The concentration of TiO_2 was kept below the total solubility limit in Al_2O_3 and ZrO_2.[13,14] The amount of Zr-alkoxide and/or TPT were adjusted in order to yield the desired amount of ZrO_2 and TiO_2. The molar ratio of ZrO_2 and/or TiO_2 to water was kept at 1/24. Powders of Al_2O_3 were thoroughly mixed with a predetermined amount of Zr-alkoxide and TPT in 2-methoxyethanol for 4.5hr, then hydrolyzed by the addition of a 12M water/2-methoxyethanol solution. After mixing for 5hr, the solution was removed by centrifugation. The mixed powder product was dried at 110°C. After calcining at 850°C for 1hr, the powders were die-pressed at 25MPa uniaxially and then isostatically pressed at 98MPa to obtain bars with a dimension of 5x5x40 mm. These bars were sintered at 1450-1550°C in air. Linear shrinkage was measured by using a non-loading dilatometer. The heating rate was kept at 6°C/min. The crystalline phases were identified using an X-ray diffractometer (Rigaku Co., Ltd. 35KV, 20mA). The percentage of ZrO_2 in the tetragonal phase was determined as follows:[12]

$$Xt = \frac{0.6\, I_{t\,(111)}}{0.6 I_{t\,(111)} + I_{m\,(111)}} \times 100\%$$

I(111): intensity of (111) plane
m: monoclinic phase
t: tetragonal phase
Xt: percentage of ZrO_2 in tetragonal phase

Specific surface area was measured by the multipoint BET method using N_2 gas as adsorbent. The particle size distribution was measured using a Coulter particle size analyzer (Coulter Electronics N4Sd). The density of sintered specimen was determined by Archimedes' method, and was expressed in a relative scale as the ratio of actual density to theoretical density. The theoretical densities of ZTA composites were determined by

$$d_{th,ZTA} = V_{Al_2O_3} d_{Al_2O_3} + V_{TiO_2} d_{TiO_2} + V_{ZrO_2} d_{ZrO_2}$$

where
$d_{Al_2O_3}$ = 3.987g/cm^3 for α-Al_2O_3
d_{TiO_2} = 4.25g/cm^3 for rutile phase TiO_2
d_{ZrO_2} = 6.097g/cm^3 for tetergonal phase ZrO_2
V: volume ratio

The microstructure was characterized by scanning elec-

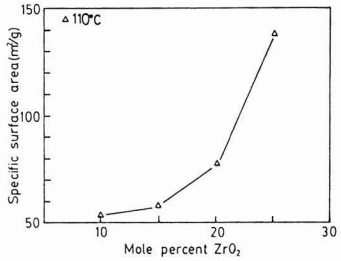

Fig. 1. Specific surface area of the AZ powders dried at 110°C with amount of ZrO_2 addition.

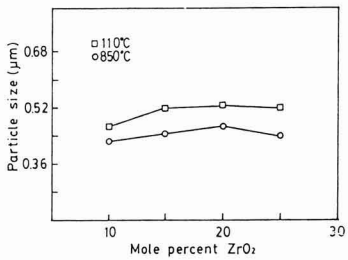

Fig. 2. Average particle size of the AZ powders dried at 110°C, and calcined at 850°C.

tron microscopy (SEM, JOEL JSM-35) and Transmission electron microscopy (TEM, Hitachi-200).

Two symbols, AZx and ATZx were used to represent the composition of ZTA with the former containing x mole% ZrO_2 and the latter containing x mole% ZrO_2 and 2.5 mole% TiO_2.

3. Results and Discussion

1)Characteristics of ZTA powder

Figure 1 shows the surface area of AZ powders of different ZrO_2 content dried at 110°C. The surface area of the AZ powder increases with increasing concentration of ZrO_2, and ranges from 52.6m^2/g to 137.2m^2/g. The mean particle size change of AZ powders with various ZrO_2 content dried at 110°C and calcined at 850°C is shown in **Fig.2.** The mean particle size of all powders calcined at 850°C is smaller than that of the powders dried at 110°C. The TEM micrographs of ATZ10 powder are shown in **Fig.3.** The micrographs clearly show that ZrO_2 gel has been coated uniformly on each individual Al_2O_3 particle. It is interesting to note that before calcination the Al_2O_3 particle was coated with "fluffy" ZrO_2 gel, however, after calcination fluffy ZrO_2 gel has condensed into round and ultrafine particles.

The behavior of surface area change shown in Fig.1 is similar to the results reported by B. Fegley et al.[15] Considering surface area measurements and particle size measurements simultaneously, it is reasonable that the ZrO_2 coating on Al_2O_3 particles would be thicker with increasing amount of ZrO_2 added, leading to both the larger surface area and particle size. Nevertheless, if the ZrO_2 content exceeds the limit of maximum absorption of Al_2O_3 particles the remaining ZrO_2 would separate from Al_2O_3 particles to form small aggregates, thus, resulting in the decreasing mean particle size as shown in Fig.2.

The relationship between the fraction of t-ZrO_2 (abbreviated as Xt) in ZTA powders calcined at 850°C and its ZrO_2 content is shown in **Fig.4.** The content of t-ZrO_2 decreases with increasing amount of ZrO_2 for specimens in which ZrO_2 content is less than 25 mole%. In addition, ATZ specimens have more Xt content than that of AZ specimens, i.e., the addition of TiO_2 appears to contribute to the retention of t-ZrO_2 in the calcined ZTA powder. The green densities, about 52-54% for all AZ and ATZ compacts, seem not to depend on the concentration of ZrO_2 or the addition of TiO_2.

2)Sinterability of ZTA powders.

The relative linear shrinkage of AZ and ATZ compacts during sintering is given in **Fig.5.** AZ_{10} and ATZ_{10} which behaved as two extremes in these specimens began to shrink above 1100°C. The relative shrinkage of AZ_{10} is only 5% at 1500°C, and continues to shrink during the subsequent isothermal treatment. After 2hrs of soaking at 1500°C, the relative shrinkage of AZ_{10} is about 13.5%. On the other hand, the relative shrinkage of ATZ_{10} is up to 14.5% at 1500°C, and there is only tiny shrinkage during the isothermal treatment. The other AZ and ATZ specimens have similar intermediate linear shrinkage curves. It is shown quite clearly that the shrinkage rates of the ATZ specimens are generally larger than that of the AZ specimens. The difference suggests that TiO_2 has substantially enhanced the sintering of ZTA composite powders.

The relative density changes of sintered bodies with soaking time are shown in **Fig.6.** For specimens AZ_{15}, AZ_{20}, AZ_{25}, the density change is generally not large when soaked for the same time. However, the AZ_{10} specimen sintered at 1500°C for 2hr has much lower relative density (only 90%) than the others. On the other hand, the relative densities of ATZ specimens decrease with increasing ZrO_2 content, and

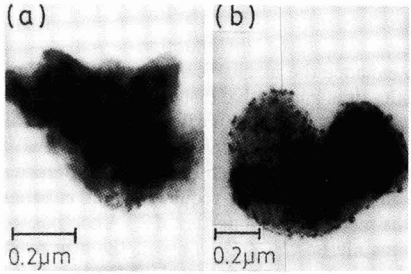

Fig. 3. Transmission electron micrographs of the ATZ_{10} powders, (a) dried at 110°C, showing Al_2O_3 particle coated with fluffy ZrO_2 gel, (b) calcined at 850°C, showing Al_2O_3 particle coated with fine ZrO_2 particles condensed from ZrO_2 gel.

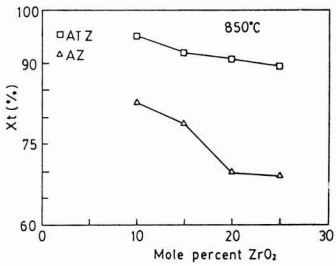

Fig. 4. Fraction of tetragonal-ZrO_2 in the AZ and ATZ powders calcined at 850°C.

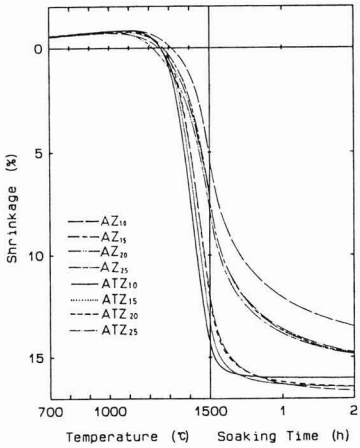

Fig. 5. Thermal expansion and shrinkage curves of AZ and ATZ specimens.

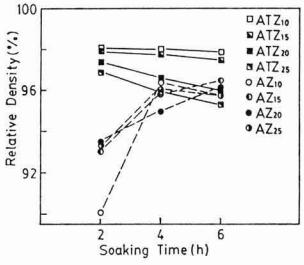

Fig. 6. Relative densities of the AZ and ATZ specimens sintered at 1500°C for 2-6 h.

also decreases with soaking time. The relative density of ATZ_{10} can reach as high as 98%. Comparing the relative densities of these two groups of specimens, the beneficial effect of TiO_2 on the sintering can be further approved.

In general, the densified ZTA composite is obtained by the hot-pressing method. For normal pressure sintering in air, there have been reports[16,17] that densified ZTA composite (density > 98% of theoretical value) can be achieved after sintered at 1600°C for 2h. However, in our study, by the addition of TiO_2 and sinting at 1500°C for 2h, the ZTA can achieve the same theoretical density.

It is shown in Fig.5 that the shrinkage percentage of the AZ10 sintered at 1500°C for 2hr is the smallest among all specimens. However, according to the trend of the shrinkage curve, it is quite possible that the shrinkage may continue with increasing isothermal soaking. This is the reason why relative density of AZ10 sintered at 1500°C for 2hr is lower than that sintered for 4hr. Because the amount of TiO_2 content is constant (2.5 mole%) for the ATZ series, it is possible that the decrease in relative density with increasing ZrO_2 content is due to the decreasing amount of TiO_2 in alumina and zirconia. During sintering, two important phenomena may occur with prolonged soaking time.

(I) Offering the energy for sintering and enhancing the densification of the compact.

(II) Promoting the grain growth of ZrO_2, causing a t→m phase transformation which is accompanied by the formation of microcracks due to volume increase of ZrO_2 grains above the critical size.[18,19]

The influence of soaking on the sintering behavior is discussed below. If the specimen has low relative density or low ZrO_2 content, the relative density of the compact will increase during prolonged isothermal process, i.e., the sintering behavior is dominated by phenomenon (I). On the other hand, if the specimen has high relative density or large ZrO_2 content, the relative density decreases and the grain growth of ZrO_2 is continued during prolonged isothermal process, i.e., the sintering behavior is dominated by phenomenon(II). As indicated in Fig.6, the relative densities of ATZ specimens decrease with prolonged isothermal soaking due to phenomenon(II) which is caused by the addition of TiO_2.

3) Microstructure

Figure 7 shows the fractured surfaces of AZ and ATZ specimens sintered at 1500°C for 2hr. Except for a few intragranular fractures, most of the fractures are intergranular. The microsturcture of polished and thermally etched AZ and ATZ specimens sintered at 1500°C for 2hr are shown in **Fig.8.** It can be seen that the Al_2O_3 grain size decreases and the ZrO_2 grain size increases with increasing ZrO_2 content. Comparing AZ_{10} and ATZ_{10}, it is found that ATZ_{10} has larger grain size and higher relative density than that of AZ_{10}. In other words, the addition of TiO_2 promotes the densification

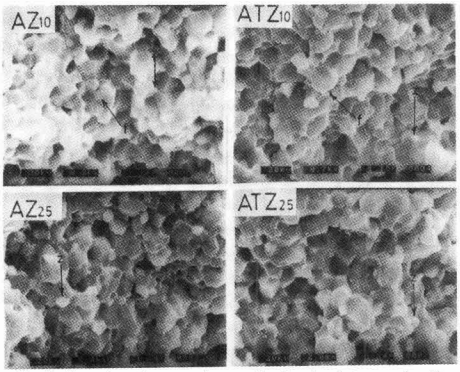

Fig. 7. Scanning electron micrographs showing intragranular (denoted by f) and intergranular fractures of zirconia-toughened-alumina sintered at 1500°C for 2h. The zirconia grains are denoted by z.

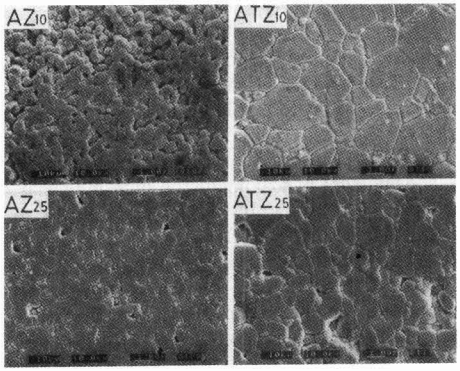

Fig. 8. Scanning electron micrographs of polished and thermally etched surfaces of zirconia-toughened-alumina sintered at 1500°C for 2h.

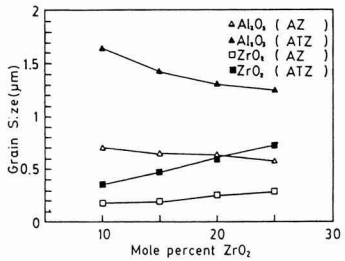

Fig. 9. Grain size of Al_2O_3 and ZrO_2 in zirconia-toughened-alumina sintered at 1500°C for 2h.

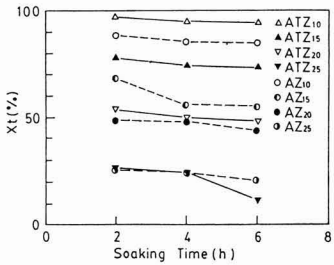

Fig. 10. Fraction of tetragonal-ZrO_2 on the surface of zirconia-toughened-alumina sintered at 1500°C for 2h.

of compact and enhances the grain growth of sintered bodies. The average grain size of Al_2O_3 and ZrO_2 are estimated by the line-intercept method. The results are shown in **Fig.9.** The Al_2O_3 grain size drops from 1.65μm to 1.2μm with increasing ZrO_2 content, and the ZrO_2 grain size increases from 0.35μm to 0.72μm for the ATZ series. For the AZ series, the grain size of Al_2O_3 decreases from 0.71μm to 0.58μm, and ZrO_2 increases from 0.18μm to 0.28μm.

In summary, intergranular and intragranular fractures were both found from microstructure observations, although with improportional ratios. The ZrO_2 grains, being almost intergranular, could inhibit the grain growth of Al_2O_3[20,21] and the coalescence of ZrO_2.[22] Lange[23] has reported that abnormal grain growth control can be achieved from compositions containing ZrO_2 larger than 5vol%. In our investigation, ZrO_2 content is larger than 5vol%, and the grain size of Al_2O_3 did decrease with increasing ZrO_2 content. Unfortunately, the distances of ZrO_2 particles are also shortened, leading to some coalescence.

4) Relative t-ZrO_2 content

The relative t-ZrO_2 content of AZ and ATZ specimens is shown in **Fig.10.** The relative t-ZrO_2 content of AZ and ATZ specimens decreased with increasing ZrO_2 content or prolonged isothermal soaking. Because ZrO_2 particles coalesced during prolonged soaking, more ZrO_2 grains will be above the critical size, which in turn facilitates the t→m phase transformation. Furthermore, the decreasing t-ZrO_2 with increasing ZrO_2 content may be due to larger ZrO_2 particle size for higher ZrO_2 volume fractions, decreasing elastic modulus of the composites or decreasing constraint on ZrO_2 particles.

With the same ZrO_2 content, ATZ specimens have higher t-ZrO_2 fraction compared to AZ specimens. This result offers some evidence that the addition of TiO_2 contributes to the retention of ZrO_2 in the tetragonal form. It is believed that higher t-ZrO_2 content can efficiently improve the toughness of ZTA composite. This effect (as mentioned before), may come from phase transformation toughening or microcrack toughening, both of which must be investigated in the future.

4. Conclusions

1) ZrO_2 can be uniformly distributed in α-Al_2O_3 powder when $Zr(OC_3H_7)_4$ is added and hydrolyzed.
2) The addition of TiO_2 within its solubility limit in ZTA can enhance the sinterability of ZTA powder. A relative density of 98% for ZTA bodies can be obtained when fired at 1500°C for 2hr.
3) The addition of TiO_2 promotes the grain growth of Al_2O_3 and ZrO_2, and contributes to the retention of t-ZrO_2.

Acknowledgements

The authors are grateful to the National Science Council for financial support (under contract No. NSC 78-0405-E006-20), and to the Research Laboratory of Engineering Materials (NAKAGAWA Laboratory, Tokyo Institute of Technology) for use of the dilatometer.

References:

1) E.M. Dickson, Industrial Minerals, 209, 49-53 (1985)
2) A.J. Hathaway, Am. Ceram. Soc. Bull., 62(5), 588-89 (1985)
3) A.G. Evans and A.H. Heuer J. Am. Ceram. Soc., 63, 241-48 (1980)
4) J. Wang and R. Stevens, J. Mat. Sci., 23, 804-08 (1988)
5) R.C. Gravie, J. Phys. Chem., 69, 1238-43 (1965)
6) R.Stevens and P.A. Evans, Br. Ceram. Trans. J., 83, 28-31 (1984)
7) N.Claussen and M.Ruhle, pp.137-63 in Advance in Ceramics, vol.3, Edited by A.H. Heuer and L.W. Hobbs. The American Ceramic Society, Columbus, Ohio (1981)
8) A.H. Heuer, N.Claussen, W.M. Kriven and M.Ruhle, J. Am. Ceram. Soc., 65, 642-50 (1982)
9) D.W. Sproson and G.L. Messing, J. Am. Ceram. Soc., 67. c92-c93 (1984)
10) M.Kagawa, M.Kikuchi, Y.Syono and T.Nagae, J. Am. Ceram. Soc., 66, 751-54 (1983)
11) F.F. Lange, B.I. DAvis and I.A. Aksay, J. Am. Ceram. Soc., 66, 407-08 (1983)
12) S.R. Witek and E.P. Butler, J. Am. Ceram. Soc., 69, 523-29 (1986)
13) Michael J. Bannister, J. Am. Ceram. Soc., 69, c269-71 (1986)
14) K.Hamano, C.S. Hwang, Z.Nakagawa and Y.Ohya, Yogyo-Kyokai-Shi, 94, 505-511 (1986)
15) B.Fegley, P.White and H.K. Bowen, J. Am. Ceram. Soc., 68, c60-62 (1985)
16) F.F. Lange, J. Am. Ceram. Soc., 66, 396-98 (1983)
17) P.Cortesi & H.K. Bowen, Ceram. International, 15, 173-77 (1989)
18) H.Tomaszewski, Ceram. Inter., 14, 117-25 (1988)
19) K.Niihara, R.Morena, D.P. H. Hasselman, J. Mater. Sci. Lett., 1, 13-16 (1982)
20) B.Kibbel and A.H. Heuer, J. Am. Ceram. Soc., 69, 231-36 (1986)
21) J.T. Lin and H.Y. Lu, Ceram. International 14, 251-58 (1988)
22) B.W. Kibble and A.H. Heuer, pp.415 in "Advances in Ceramics," Vol.12, edited by N.Claussen, M.Ruhle and A.H. Heuer, The American Ceramic Society, Columbs, Ohio. (1984)
23) F.F. Lange and M.M. Hirlinger, J. Am. Ceram. Soc., 67, 164-68 (1984)

This article appeared in English in Nippon Seramikkusu Kyokai Gakujutsu Ronbunshi (Japanese version), Vol.99, No.4, 1991.

Effects of Dopants on the Electrical Properties of Sintered SiC

Kazuo Okano

Department of Electronic Devices Technology, Oyama Polytechnic College
612-1, Yokokura Mitake, Oyama-shi, Tochigi 323, Japan

The effects of dopant on the electrical conductivity of sintered SiC were investigated. SiC specimens containing B_4C, AlB_2, and BN were fired in the temperature range of 1900°–2050°C. The frequency dependence of ac conductivity and temperature dependence of dc conductivity were measured. The electrical conductivity of B_4C or BN doped specimens fired at below 1960°C was several orders of magnitude higher than that of specimens fired at above 1970°C. On the other hand, the electrical conductivity of specimens doped with AlB_2 depended slightly on the sintering temperature. The electrical conductivity of the specimens fired below 1960°C was independent of the frequency and the measurement temperature. On the other hand, the electrical conductivity of specimens fired above 1970°C depended on the frequency and temperature. The electrical conductivity of specimens fired at 2050°C depended strongly on the frequency and the temperature regardless of the dopant. The electrical conductivity of BN doped SiC depended strongly on the frequency and measurement temperature. On the other hand, the electrical conductivity of AlB_2 doped SiC depended slightly on the frequency and temperature. The experimental results were discussed using the energy band models and the equivalent circuits.
[Received May 18, 1990; Accepted December 14, 1990]

Key-words: Sintered SiC, B_4C addition, AlB_2 addition, BN addition, AC conductivity, DC conductivity

1. Introduction

Sintered silicon carbide (SiC) is an example of non-oxide ceramic semiconductors, and it is expected that wide use in various devices which operate at high temperature, such as high-temperature thermistor will be found.[1,2] Electrical properties of sintered SiC are known to be greatly dependent on process conditions, such as sintering temperature,[3] sintering time,[4] and doped impurities,[5-7] and it is necessary to fully understand the relationship between electrical properties and process conditions before the sinter is used for various electronic devices. These relationships, when established, can be used to control the electrical properties of SiC.

It is known that high-purity semiconductors generally become p-type semiconductors when doped with a trivalent element, with the impurity atoms acting as acceptors in the semiconductor. On the other hand, a pentavalent element added to a semiconductor acts as the donor, turning the semiconductor into an n-type one. It is possible to control electrical properties of semiconductors with small quantities of impurities because these acceptors and donors determine the electrical properties to a large extent.

It is also necessary to highly densify sintered SiC when it is applied to electronic devices. Boron and carbon are generally used as sintering aids in order to accelerate densification during the sintering process.[8,9]

In this study, the author has attempted to control impurity contents in sintered SiC with sintering aids, and thereby control its electrical properties, so boron carbide (B_4C), aluminum boride (AlB_2) and boron nitride (BN)[10] were added as sintering aids to investigate their effects on electrical properties. B and Al will work as the acceptor, N as the donor. Therefore, sintered SiC doped with AlB_2 will be a p-type semiconductor having a high acceptor concentration, and use of BN as the B source will make the sintered body lower in carrier concentration than those doped with B_4C or AlB_2. Furthermore, an attempt has been made to explain, qualitatively, the effects of small quantities of impurities added to sintered SiC that has high concentrations of impurities and/or other defects, using the charge distribution, energy band model and equivalent circuit model.

2. Experimental Procedure

The SiC powder as a starting material was α-SiC with an average particle size of 0.42μm (Showa Denko). It was 98.5% pure, with major impurities of aluminum (0.012wt%), iron (0.015wt%), silica (0.34wt%) and free carbon (1.09wt%). Borides and carbon were used as the sintering aids, the latter being added in the form of phenol to 2.0wt% as residual carbon content. B_4C, AlB_2 and BN were each added to 0.5wt% as boron. The three types of sintering aid mixtures were prepared; use of AlB_2 and BN were accompanied by addition of Al of 0.62wt% and N at 0.65wt%, respectively, in addition to B at 0.5wt%. Each mixture was milled with Teflon balls in the presence of benzene dried, and monoaxially formed under 150MPa into pellets 15mm in diameter and 2.0mm thick. The pellets were sintered in a graphite resistance furnace at 1900° to 2050°C in vacuum for 0.5h.

For observation of the microstructures, each sample was mirror-polished and etched with an aqueous solution of potassium ferricyanide and sodium hydroxide for 4min and then observed under a scanning electron microscope (SEM).

The thermo-electromotive force of the sample was determined by a potentiometer, to measure its majority carrier, and a temperature gradient of 10K was maintained across the sample width under vacuum. The sintered sample was ground with a #600 diamond wheel to a thickness of 1.5mm and then aluminum was deposited in vacuum as electrodes, because it is known that ohmic contact can be secured between a surface-blasted SiC sinter and an aluminum

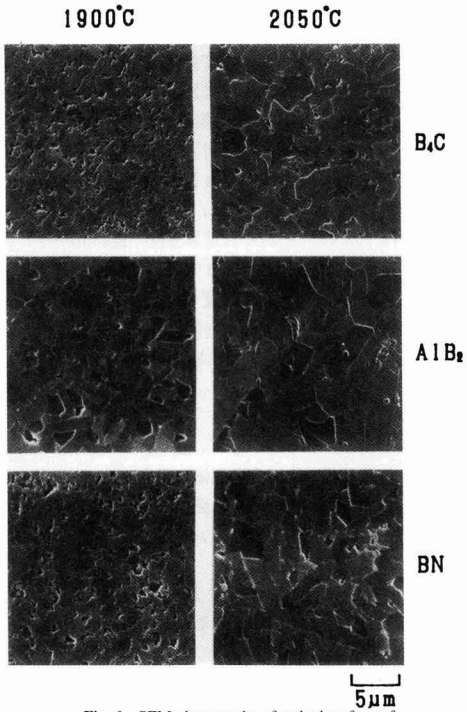

Fig. 1. SEM photographs of etched surface of sintered SiC.

electrode.[11] Electrical conductivity was determined by the fall of potential method, where a voltage of 1V was applied to the sample across its width. Dependence of dc electrical conductivity on temperature was determined in a range from 150 to 500K, and that of ac conductivity on frequency in a range from 20Hz to 200kHz. The I-V characteristics were measured by the four-probe method under a vacuum.

3. Results

The B_4C, AlB_2 and BN-doped samples, sintered at 1900° and 2050°C, were observed using SEM to compare their microstructures. The results are given in **Fig.1**. The AlB_2-doped sample which was sintered at 1900°C had an average particle size of around 3μm, whereas the B_4C- and BN-doped samples (also sintered at 1900°C) had an average particle size of 1μm or less and were more porous. The samples sintered at 2050°C were highly densified, and their average particle size varied by the sintering aids: approximately 6μm for AlB_2, 4μm for BN and 3μm for B_4C.

Analysis of thermo-electromotive force indicated that holes constituted the majority carrier in each sample. In other words, sintered SiC was judged to be an p-type semiconductor, irrespective of sintering aids used or sintering temperature.

Figure 2 shows the effects of sintering temperature on dc conductivity of the samples containing different types of sintering aids. Conductivity of the B_4C- and BN-doped sinters changed abruptly at approximately 1970°C. Conductivity of the AlB_2-doped one, on the other hand, gradually decreased as sintering temperature increased, to attain a minimum at approx. 1970°C, increasing thereafter. For the samples sintered at 2000°C or more, the AlB_2-doped sample had the highest conductivity and the BN-doped one the lowest. Dependence of electrical conductivity on frequency was measured. The conductivity of B_4C- or BN-doped sample sintered at 1960°C or less showed no dependence on frequency. Dependence on frequency of the conductivity, however, increased as the sintering temperature increased. **Figure 3** presents the samples which showed the greatest dependence on frequency i.e., those sintered at 2050°C. Conductivity of the AlB_2-doped sample, showing only a limited dependence on frequency in the low-frequency region, increased notably with frequency in the high-frequency region. It was also noted that the conductivity level was roughly two digits higher in the high-frequency region than that of the B_4C- or BN-doped sample. Conductivity of the B_4C-doped sample showed dependence from a relatively low frequency level, while that of the BN-doped sample showed dependence over the entire frequency range used in this study.

Temperature dependence of dc conductivity of each sample was also measured. The B_4C- and BN-doped sample

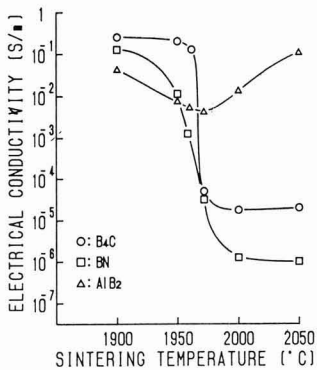

Fig. 2. DC conductivity at 300K as a function of sintering temperature.

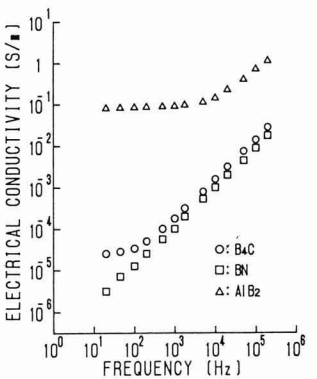

Fig. 3. Frequency dependence of electrical conductivity of SiC samples sintered at 2050°C containing B_4C, BN, and AlB_2.

sintered at 1960°C or less, showing no dependence on frequency, had a constant electrical conductivity irrespective of measurement temperature. However, conductivity of those samples sintered above 1970°C changed notably with temperature. **Figure 4** shows the effects of temperature on dc conductivity of the samples sintered at 2050°C. The AlB_2-doped sample, which showed a higher ac conductivity than any other sample as shown in Fig.3, also showed the highest dc conductivity over the entire temperature range tested. The BN-doped sample, showing a lower ac conductivity than any of the others, also showed the lowest dc conductivity. Dependence electrical condcutivity of any sample on temperature that is activation energy tended to increase as temperature increased; the activation energies of the B_4C-, AlB_2- and BN-doped samples, sintered at 2050°C, were approximately 0.5, 0.3 and 0.6eV at 500K (1000/T=2) respectively.

The I-V characteristics of each sample were measured. Nonlinear characteristics were clearly noted with those samples sintered at 2050°C whose electrical conductivity was significantly dependent on frequency and temperature. **Figure 5** shows the I-V characteristics of the samples sintered at 2050°C. The B_4C-doped sample showed Ohmic characteristics at an electric field intensity of 10^4V/m or less, however its current density increased roughly in proportion to the second power of the electric field intensity thereafter. The AlB_2- and BN-doped samples showed Ohmic characteristics in a range from 10^2 to 5×10^3V/m and from 10^2 to 7×10^3V/m, respectively, but their current density increased roughly in proportion to the second power of the electric field intensity thereafter. A voltage applied to the unit grain boundary of each sample at the electric field intensity at which the non-Ohmic characteristics started to appear was approximately 0.03V, estimated taking average particle sizes into consideration.

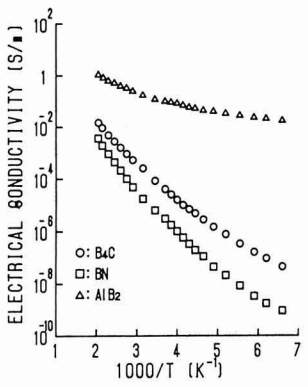

Fig. 4. Temperature dependence of electrical conductivity of SiC samples sintered at 2050°C containing B_4C, BN, and AlB_2.

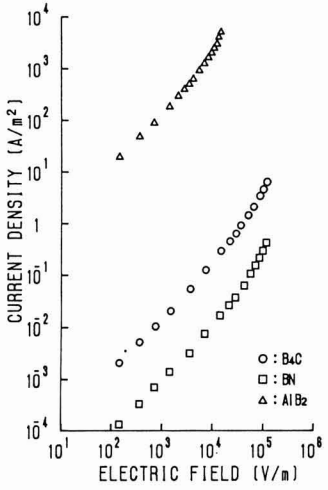

Fig. 5. I-V characteristics of 300K of SiC containing B_4C, BN, and AlB_2.

4. Discussion

These experimental results are discussed using the microstructural and energy band models. These models were developed for polycrystalline semiconductors such as those of silicon[12-20] and zinc oxide.[21-23]

Sintered SiC is a composite consisting of SiC particles and grain boundaries as show in **Fig.6(a)**, and each particle is considered to be a single-crystalline semiconductor. The grain boundary is an interface at which a particle contacts with another particle of different crystal orientation, and in which dangling bonds are present. Therefore, the grain boundary has a positive charge because the holes in each SiC particle are trapped by the dangling bonds when the particle is a P-type semiconductor. As a result, negative space charges will be distributed around the grain boundary because the acceptors around the grain boundary have negative charges. These space charge distributions create an electric field around the grain boundary, by which symmetrical Schottky barriers are formed on both sides of the grain boundary, as shown in Fig.6(b). The equivalent circuit is given in Fig.6(c), where Rg is the resistance component in the grain C_{GB} is the capacitance around the grain boundary

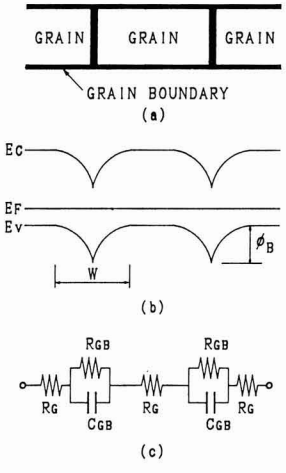

Fig. 6. Schematic models of (a) microstructure, (b) energy band, and (c) equivalent circuit.

(resulting from the space charge layer) and R_{GB} is resistance (resulting from the Schottky barrier). The current flowing through the SiC sintered body falls into two general categories, one flowing along the grain boundary (I_{GB}) and the other across the grain boundary (I_G). When the grain boundary is thick enough to form a grain boundary layer, this layer will be a semiconductor containing high concentrations of impurities, and its electrical conductivity will be very high. The height and width of the Schottky barrier vary, depending on concentrations of impurities present in the grains. **Figure 7** illustrates the space charge layer width and barrier height of the B_4C-, AlB_2-and BN-doped SiC sinters, represented by the solid, broken and chain-link lines, respectively.

Comparing the space charge layer width and barrier height of the AlB_2-doped sample with those of the B_4C-doped one, the B_4C-doped sample has an equivalent acceptor concentration N_{aB}, which is determined not only by the acceptor concentration resulting from the diffusion of B, but also by the donors, acceptors and crystal defects present in each grain. The sinter will have a higher equivalent acceptor concentration when doped with AlB_2, therefore its space charge layer width will be smaller than that of the B_4C-doped sample, as shown in Fig.7(c).

The BN-doped sample, on the other hand, will have a reduced equivalent acceptor concentration and a larger space charge layer width and barrier height than the B_4C-doped one, as shown in Fig.7.

Next, the electrical conductivity characteristics of these sintered samples are discussed while taking into consideration the varying space charge layer width and barrier height, depending on the dopants.

Electrical conductivity of the B_4C-doped sample changed abruptly at around 1960°C, as shown in Fig.2. This phenomenon could conceivably have resulted from the presence of a sufficient quantity of boron as the sintering aid in the grain boundaries to form grain boundary layers containing high concentration of B, because a sintering temperature of 1960°C or less was too low to highly densify the sample. It is known that diffusion of boron through the SiC grains is suddenly accelerated at approx. 1950°C.[24,25] It is therefore considered that boron present in the grain boundaries of the sample sintered above 1950°C is sufficiently diffuse through the grains to narrow the width of the grain boundary layers, reducing the quantity of current flowing along the grain boundaries (I_{GB}) with the result that dc electrical conductivity is sharply decreased. I_G will be much higher than I_{GB} in the sample sintered above 1950°C, and its electrical conductivity tends to be determined by the current I_G flowing across the Schottky barriers.

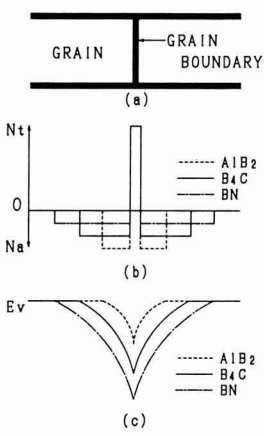

Fig. 7. Schematic models of (a) microstructure, (b) charge distribution, and (c) the Schottky barrier.

Doping AlB_2 or BN accelerates diffusion of boron as well as aluminum and nitrogen. Electrical conductivity of the samples doped with these compounds, therefore, may be determined by the effects of B diffusion to sharply decrease I_{GB} and the effects of Al or N diffusion to change the I_G level as a result of the changed Schottky barrier height. The AlB_2-doped sample sintered at high temperature will have a reduced barrier height because of B and Al diffusion. Its electrical conductivity, therefore, will be higher than that of the B_4C-doped sample. Increasing sintering temperature accelerates the diffusion of Al, which increases concentration of the acceptor in the grains and thereby decreases its barrier height and increases its electrical conductivity. The BN-doped sample, on the other hand, will have a higher electrical conductivity than the B_4C-doped sample, because of the increased barrier height as a result of the diffusion of N.

Next, the effects of frequency on ac conductivity are discussed. It was observed that electrical conductivity increased in proportion to frequency in a high frequency region, as shown in Fig.3. This meant that the C_{GB} in the equivalent circuit shown in Fig.6(c) passed a much larger quantity of current and had a much larger impedance component than the R_G. In addition, it is possible to compare the capacitance component and depletion layer width of a sample with those of another, because electrical conductivity changes in proportion to C_{GB} level in this high frequency region.

Two reasons are cited to account for the higher ac conductivity of the AlB_2-doped sample than that of other samples in the high frequency region, as shown in Fig.3: (1) the narrowed space charge layer, as shown in Fig.7(b) (broken line) and increased C_{GB} level, and (2) a decreased number of grain boundaries, or number of capacitances connected in series (per unit length), because of the larger average grain size of the AlB_2-doped SiC sinter to increase synthesized capacitance of the sample.

The BN-doped sample, on the other hand, had larger grains and a smaller capacitance than the B_4C-doped one, in spite of its decreased number of Schottky barriers per unit length, to show a lower ac conductivity, conceivably resulting from a broadened space charge layer (Fig.7(b)).

Next, dependence of dc conductivity on temperature is discussed. The doped samples, when arranged in order of ac conductivity, are AlB_2-, B_4C- and BN-doped ones, the AlB_2-doped sample being the highest. Also, the sample with higher electrical conductivity had a lower activation energy. Direct current flowing through the Schottky barriers of the sintered SiC body consists of three components: the current of carriers going over the Schottky barriers (I_E), the current of carriers hopping over the localized state within the Schottky barriers (I_H), and the current of carriers flowing through the Schottky barriers by the tunnel effect (I_T). I_E predominates in the high-temperature region while I_T does so in the low-temperature region.

Next, changes in I_E, I_H and I_T with dopant types are discussed. First, I_E tends to decrease as barrier height ϕ_B in-

creases. Therefore, the current component I_E flows in a larger quantity through the AlB_2-doped sample than in the BN-doped one, because of the former sample's lower ϕ_B level. ϕ_B represents activation energy in the high temperature region, and the model shown in Fig.7(c) will explain the descending order of the BN-, B_4C- and AlB_2-doped samples in activation energy.

Next, the current component I_H tends to increase in a sample having a high concentration of localized state. It is necessary to consider localized states density in the vicinity of the valence bands, because all of the samples used in this study are P-type semiconductors. The BN- and B_4C-doped samples will be similar to each other in localized states density around the valence bands, because their density is mainly attributable to boron. The AlB_2-doped sample, on the other hand, with levels attributable to both boron and aluminum, will have a higher localized status than the above two samples. The I_H level, therefore, will be higher in the AlB_2-doped sample than in any other sample, because of its higher localized states density.

The I_T level will increase as width of the space charge layer decreases. Therefore, the order of the samples with respect to the I_T level will be the AlB_2-, B_4C- and BN-doped samples, the AlB_2-doped one being the highest.

The dc current flowing through the sintered SiC body (I_o) is given by the following formula:

$$I_o = I_E + I_H + I_T \quad \ldots\ldots\ldots\ldots\ldots\ldots (1)$$

The AlB_2-doped sample has a higher overall dc conductivity, because it is higher than any other doped sample in I_E, I_H and I_T. Comparing the B_4C-doped sample with the BN-doped one, the former will be higher than the latter in overall conductivity, because their I_H levels are similar to each other while both the I_E and I_T levels are the lowest in the latter sample.

The observed nonlinear I-V characteristics were considered to result from height of the Schottky barrier formed around the grain boundary depending on voltage applied to the barrier. In general, dependence of current flowing the Schottky barrier on applied voltage is given by the following formula:

$$I = I_o (\exp(eV/kT) - 1) \quad \ldots\ldots\ldots\ldots (2)$$

where k is Boltzmann's constant and V is voltage applied to the Schottky barrier. The nonlinearity is more pronounced when the applied voltage is greater than kT/e, which is 0.026V at 300K. This level is in good agreement with the observed results, which indicate that the nonlinearity starts to appear when an applied voltage exceeds 0.03V for a grain boundary. In other words, the I-V characteristics observed can be explained by considering the presence of the Schottky barriers around the grain boundaries.

5. Conclusions

Electrical conductivity of the B_4C-, AlB_2- and BN-doped SiC samples, sintered at 1900° to 2050°C was investigated.

1) Electrical conductivity at room temperature of the B_4C-doped SiC sinter changed with temperature at which the sample was sintered, changing sharply at approx. 1970°C; dc conductivity of the sample sintered above 1970°C was roughly 4 digits lower than that of the sample sintered at a lower temperature.
2) DC conductivity at room temperature of the AlB_2-doped SiC sinter attained a minimum (approximately 10^{-2}S/m), when the sample was sintered at 1970°C. This compares with 10^{-1}S/m of those sintered at 1900° and 2050°C. As a whole, however, electrical conductivity of this type of sample was less sensitive to sintering temperature than the others.
3) DC conductivity at room temperature of the BN-doped SiC sinter changed with the temperature at which the sample was sintered, changing sharply at approx. 1970°C; conductivity of the sample sintered above 1970°C was roughly 5 digits lower than that of the sample sintered at a lower temperature.
4) Electrical conductivity of the B_4C- and BN-doped samples sintered at 1960°C or less showed no dependence on frequency or temperature. Its dependence on both parameters was observed for those sintered above 1970°C.
5) Activation energy was determined from dependence of Dc conductivity on temperature; 0.3, 0.5 and 0.6eV for the AlB_2-, B_4C- and BN-doped samples, respectively. The above order with respect to activation energy will be reversed for the order of height of the Schottky barrier, that of the AlB_2-doped sample being the highest.
6) DC conductivity will be in ascending order of BN-, B_4C- and AlB_2-doped samples, with that of the AlB_2-doped one being the highest. Width of the space charge layer becomes narrower in descending order of the BN-, B_4C- and AlB_2-doped samples, that of the AlB_2-doped one being the narrowest.

References:

1) K. Okano, Trans IEICE, E70, 336-38 (1987).
2) K. Okano, Yogyo Kyokai-shi, 94, 219-225 (1986).
3) K. Okano and A. Takahashi, Hyomen Kagaku, 8, 210-15 (1987).
4) K. Okano, H. Kurisaki, S. Uenouchi and H. Ito, Seramikkusu Ronbun-shi, 97, 1176-80 (1989).
5) K. Okano, S. Sakurai and T. Kato, ibid., 97, 1315-17 (1989).
6) Y. Takeda, H. Nakamura, K. Maeda and Y. Matsushita, Yogyo Kyokai-shi, 95, 860-863 (1987).
7) Y. Takeda, S. Ogiwara and K. Maeda, Seramikkusu Ronbun-shi, 96, 102-105 (1988).
8) S. Prochazka, "Special Ceramic 5," Ed. by P., Popper, Brit. Ceram. Res. Assoc., Stoke-on-Trent 171-82 (1975).
9) H. Tanaka, K. Inomata, K. Tsukuda and A. Ogimura, Yogyo Kyokai-shi, 92, 461-651 (1984).
10) K. Okano and H. Iida, Hyomen Kagaku, 9, 362-67 (1988).
11) K. Shinoe, F. Shirasaki and K. Okano, Ceramic Society of Japan, Kanto Branch Meeting Proceedings, p.28 (1985).
12) T.I. Kamins, J. Appl. Phys., 42, p.4357-65 (1971).
13) J.Y.W. Seto, J. Electrochem. Soc., 122, p.701-06 (1975).
14) M.M. Mandurah, K.C. Saraswat and C.R. Helms, J. Appl. Phys., 51, p.5755-63 (1980).
15) J.Y.W. Seto, J. Apl., Phys., 46, p.5247-65 (1975).
16) C.H. Seager and T.G. Castner, J. Appl. Phys., 49, p.3879-89 (1978).
17) M.L. Tarng, J. Appl. Phys., 49, p.4069-76 (1978).
18) G. Baccarani and B. Ricco, J. Appl. Phys., 49, p.5565-70 (1978).
19) N.C.C. Lu, L. Gerzberg, C.Y. Lu and J.D. Meindl, IEEE Electron Device Letters, 2, p.95-98 (1981).
20) J.Y.M. Lee and I.C. Cheng, J. Appl. Phys., 53, p.490-95 (1982).
21) P.R. Emtage, J. Appl. Phys., 48, 4372-84 (1977).
22) K. Mukae, K. Tsuda and I. Nagasawa, J. Appl. Phys., 50, p.4475-76 (1979).
23) K. Eda, J. Appl. Phys., 49, p.2964-72 (1978).
24) H. Suzuki and T. hase, J. Am. Ceram. Soc., Vol.63, p.349-50 (1980).

25) H. Suzuki, Seramikkusu, Vol.18, p.3-9 (1983).
26) J. Tauc, "Amorphous and Liquid Semiconductors," Plenum Press, p.231-33 (1974).

This article is a full translation of the article which appeared in Nippon Seramikkusu Kyokai Gakujutsu Ronbunshi (Japanese version), Vol.99, No.4, 1991.

Hydrothermal Synthesis of Kaolinite from Serpentinite

Katsunori Kosuge, Yoshihisa Hamada and Ryohei Otsuka*

National Research Institute for Pollution and Resources
16-3, Onogawa, Tsukuba-shi, 305, Japan
*School of Science and Engineering, Waseda University
3-4-1, Okubo, Shinjuku-ku, Tokyo, 160, Japan

This study was undertaken to obtain kaolinite from serpentinite by treating serpentinite with an $AlCl_3$ solution under various hydrothermal conditions. The serpentinite used as a starting material was from Hidaka district, Kochi Pref. Magnetite included was removed by wet magnetic separation after crushing to 280 mesh. Then, 0.4g of the purified serpentinite was sealed in an ampule together with $AlCl_3$ solution and heated in an autoclave above 150°C. When this material was treated with 0.5 ~ 1.0mol/l $AlCl_3$ solutions at 200 and 245°C for 48hrs, boehmite and/or $Al_{24}O_{11}(OH)_{44}Cl_6$ were formed together with kaolinite. Treatment with 0.5mol/l $AlCl_3$ solution yielded only boehmite in addition to kaolinite. To prevent the formation of boehmite, mixed solutions of $AlCl_3$ and HCl were used. When the concentrations of $AlCl_3$ and HCl were 0.5 and 0.3mol/l, respectively, white kaolinite with low crystallinity was obtained at 245°C for 48hrs or 200°C for 65hrs. It was found that metallic elements except Si were extracted completely from the starting material into the solutions. About 98% of Si in the starting material was converted to kaolinite. The experimental results indicate that the transformation from serpentine to kaolinite proceeds at low reaction temperature in a short duration of time. This is presumably because the kaolinization of serpentine proceeds topotaxially as a consequence of the virtually identical crystal structure of serpentine and kaolinite.

[Received on May 21, 1990 and Accepted on December 14, 1990]

Key-words: Kaolinite, Hydrothermal synthesis, Serpentinite, Topotaxial reaction

1. Introduction

Japan, though poor in mineral resources, has plenty deposit of serpentinite, an ultrabasic rock composed mainly of serpentine ($Mg_3Si_2O_5(OH)_4$), as well as limestone, zeolite, etc. Active investigation was once made on the effective utilization of serpentinite, but most focused on the utilization of MgO as magnesium sulfate and various fertilizers.[1] However, since no effective chemical methods for mass utilization have been developed to date, the rock is being used in its crushed form for aggregate, etc. or to form slag in steel industry. Thus, we have been studying methods to turn serpentinite into a more useful industrial raw material[2].

In this work, we investigated the required conditions for synthesis of kaolinite from serpentine as a single phase under hydrothermal conditions. Studies aiming at industrial mass synthesis have been launched only recently[4–6], although there were many reserches for the formayion of kaolinite from the viewpoint of phase equilibrium by using natural minerals or synthetic materials[7–9].

2. Experiment

The samples used were serpentinite supplied by Toho Olivine Industry Co., Ltd. that were mined in Hidaka district, Kochi Prefecture. These samples were crushed to under 280 mesh, and magnetic substances were removed by a hand-magnet of 1500 gauss and the purified substances were used as the starting material. The chemical composition obtained by wet analysis is shown in **Table 1**. XRD pattern (**Fig.1a**) showed the coexistence of brucite, magnetite (or chromite), uvarovite, etc. other than serpentine in the used samples. The sample of 0.4g placed in a 15ml pyrex ampule was sealed together with a solution of 8ml $AlCl_3$ in a fixed concentration or a mixed solution of $AlCl_3$ and HCl in a total of 8ml, and allowed to react in an autoclave. After the mixture was reacted at 150 ~ 245°C for a fixed period of time, the total content were filtered and then the amounts of Si, Mg and Al in the filtrate were measured by atomic-adsorption spectroscopy. The product thus obtained was dried at 50°C for 24hrs and investigated by XRD, TG-DTA and TEM.

3. Experimental Results and Discussion

3.1. Preliminary Experiment

When kaolinite was synthesized from serpentinite, black particles that could be recognized with naked eye were contained in the product obtained under any hydrothermal conditions, shown in the following sections. These particles were thought to be coexistent minerals such as magnetite (chromite), uvarovite, etc. contained in the serpentinite as shown in Fig.1(a). However, since these minerals could not be identified by XRD because of their trace amounts, the black minerals were confirmed as magnetite (chromite) only after they were concentrated with magnetic separation by XRD. Although these minerals were partially dissolved under the conditions of the current experiment, no effects were anticipated on the transformation from serpentinite to

Table 1. Chemical composition of serpentinite from Hidaka District, Kochi Pref. (wt%).

SiO_2	MgO	Fe_2O_3	Al_2O_3	CaO	NiO	Cr_2O_3	$H_2O(+)$	$H_2O(-)$	Total
41.20	39.95	2.50	1.28	0.42	0.25	0.18	13.60	0.30	99.68

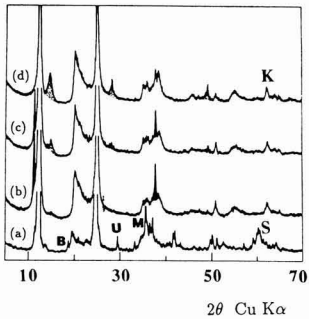

Fig. 1. X-ray diffraction patterns of the samples: (a) untreated and treated with $AlCl_3$ solutions in various concentrations: (b) 9.5mol/l, (c) 0.75mol/l and (d) 1.0mol/l. K and S indicate the (060) peaks of kaolinite and serpentine, respectively. The shadow peaks, dotted peaks, M, U and B represent $Al_{24}O_{11}(OH)_{44}Cl_6$, boehmite, magnetite, uvarovite and brucite, respectively.

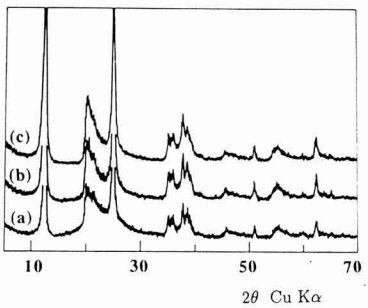

Fig. 2.. X-ray diffraction patterns of the samples treated with the mixed solutions of $AlCl_3$ (0.5mol/l) and HCl with various concentrations: (a) 0.9mol/l, (b) 0.6mol/kl and (c) 0.3mol/l.

kaolinite. Since behavior of uvarovite was not confirmed as its existence was hardly recognized, it was conceivable that kaolinization from serpentinite was hardly affected.

Thus, these coexisting minerals have to be removed by magnetic separation before synthesizing kaolite or after reactions, so that kaolinite can be synthesized from serpentinite as pure a phase as possible.

3.2. Processing by Aluminum Chloride Solution

Figure 1 shows the XRD patterns of the product after the samples were allowed to react at 245°C for 48hrs in concentrations of $AlCl_3$ solutions of 0.5, 0.75 and 1.0mol/l. Since the kaolinization from serpentinite was judged from the occurrence of the 060 reflections of serpentine and kaolinite, the peaks are expressed as S and K, respectively, in the same figure. As a result, serpentinite was mostly transformed to kaolinite, since S peak of serpentinite had disappeared and only the 060 reflection of kaolinite was recognized. However, coexistence with $Al_{24}O_{11}(OH)_{44}Cl_6$(JCPDS card 13-321) and boehmite at 1.0 and 0.75mol/l, and that with boehmite at 0.5mol/l was recognized. XRD peaks of brucite and magnetic minerals contained in the starting materials as impurities were noted to be completely absent.

Formation of boehmite was not inhibited even when the reaction temperature was decreased to 200°C and the concentration of $AlCl_3$ solutions was lowered than 0.5mol/l. Thus it was found that a single phase of kaolinite could not be obtained with treating serpentinite by $AlCl_3$ solution alone because of the crystallization of impurities such as boehmite and/or $Al_{24}O_{11}(OH)_{44}Cl_6$.

3.3. Processing with a Mixed Solution of Aluminum Chloride and Hydrochloric Acid

It is clear from Fig.1 that $Al_{24}O_{11}(OH)_{44}Cl_6$ was not formed at the concentration of 0.5mol/l – $AlCl_3$ solution, and that there was a lower amount in the formation of boehmite when the concentration of $AlCl_3$ was higher than 0.5mol/l. Thus, in order to obtain a single phase of kaolinite, an attempt was made to inhibit the formation of boehmite in a concentration area where $Al_{24}O_{11}(OH)_{44}Cl_6$ cannot be crystallized by using a mixed solutions of 0.5 mol/l - $AlCl_3$ and HCl.

Kaolinization reactions were made by changing the concentrations of HCl at 245°C for 48hrs with 0.5mol/l– $AlCl_3$ solution. As it was clear from the XRD patterns of the product thus obtained (**Fig.2**), boehmite was not formed in all cases when HCl was added to 0.5 mol/ - $AlCl_3$ solution. Although the transformation of kaolinite from serpenlinite was almost completely achieved when the concentration of HCl was 0.3mol/l. But at higher concentrations of 0.6 and 0.9mol/l HCl, decomposition of serpenlinite were acelerated and formation of an another phase, presumably amorphous silica, was recognized with kaolinite from the shape of background at 15~25°(2θ CuKα) in the XRD pattern.

As a result, it was considered necessary to carry out the procedure with the mixed solutions of $AlCl_3$ and HCl with their appropriate concentrations to obtain kaolinite from serpentinite through inhibiting the crystallization of boehmite. Thus, the concentrations of $AlCl_3$ and HCl solution were fixed to 0.5mol/l and 0.3mol/l, respectively, in their mixed solutions used for the following experiment.

3.4. Effects of Reaction Temperature and Time on the Kaolinization

Figure 3 shows the XRD patterns of the product obtained at various temperature for 48hrs by using the mixed solution adjusted to the above concentrations. The XRD pattern of the standard kaolinite sample (KGa-2; Source Clay, Kaolinite with lower crystallinity of the American Society of Clay, Warren County, Georgia, U.S.A.) was shown in (e) as reference. No transformation from serpentinite to kaolinite was recognized at 150°C from the behavior of S, K and several peaks at 30~40° (2θ CuKα). And it was found that the kaolinization started at 185°C and markedly progressed at 200°C, although the serpentinite remained.

It was clear from XRD patterns in Fig.3, serpentinite was almost transformed to kaolinite at 245°C for 48hrs. The time required for the kaolinization was investigated at a reaction temperature as low as 200°C. As a result, the changes in the XRD patterns shown in **Fig.4**, showed that serpentine was transformed to kaolinite when processed hydrothermally for about 65hrs.

And the dissolved ratios of Mg, Si and Al after 48hrs at 245°C and 65hrs at 200°C was also measured, respectively. Magnesium contained in serpentinite and also brucite showed a dissolved ratio of almost 100%. Since magnesium ion was not precipitated as a solid phase in an acid solution

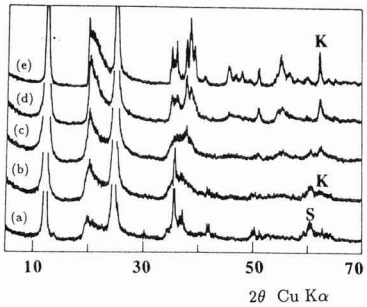

Fig. 3. X-ray diffraction patterns of the samples obtained for 48hr at various reaction temperatures: (a) 150°C, (b) 185°C, (c) 200°C, (d) 245°C; and (e) kaolinite sample (KGa-2) as reference.

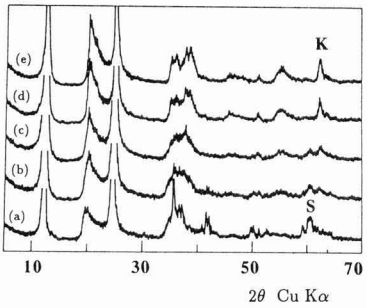

Fig. 4. X-ray diffraction patterns of the samples obtained at 200C for various reaction times; (a) 6hr, (b) 24hr, (c) 48hr, (d) 65hr and (e) 95hr.

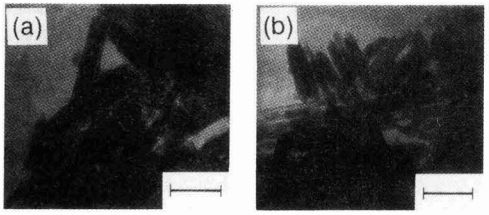

Fig. 5. TEM of serpentine (starting material) and kaolinite prepared from serpentine by hydrothermal treatment at 200°C for 65hr. Bar represents 0.25μm.

in the current experiment, its existence was apparently considered not to cause wrong effects on the kaolinization. As the dissolved ratio of SiO_2 (another major element in the serpentinite) was 2%, it may be mostly fixed in a solid phase. And approximately 70% of the added Al amount was found to be fixed in the solid phase.

3.5. Characteristics of Synthesized Kaolinite

Figure 5(b) shows the TEM of kaolinite synthesized at 200°C for 65hrs. The agglomerated particles appeared to be irregular in shape, the magnified crushed surface showed a number of tiny paper-strip shaped crystals; the product was found to be consisting of an agglomerate of these crystallized substances. The figure 5(a) reflects the micro-structure of serpentine before treatment, for it was observed that these paper-strip shape of particles remained almost unchanged before but after reactions.

When the XRD pattern of kaolinite obtained in the current experiment was compared with that of the aforementioned standard sample, KGa-2, the diffraction peaks obtained at 245°C for 48hrs and 200°C for 65hrs. (Fig.3d) and 65hrs.(Fig.4d) were broader with poor separation and thus kaolinite formed under the conditions of the current experiment could be said to have lower crystallinity. This was also clear from TG-DTA shown in **Fig.6**. When compared with the endothermic and exothermic peaks of the standard sample, KGa-2, both peaks were broader in the synthetic material, and the decomposition temperature of the latter has shifted lower by 15°C. However, weight loss was as much as 16% in the compound, while that of KGa-2 was 13% at the temperature range that from 110°C to 1000°C.

Since the crystal structure of serpentine and kaolinite was virtually identical,[11] the framework of tetrahedral layers of SiO_4 was not broken when magnesium was alleviated, and the kaolinization proceeds by a topotaxial reaction mechanism. This might be confirmed by comparison of TEM taken before and after reactions. Urabe et al.[11] pointed out the same reaction mechanism for the transformation from fluorphlogopite to kaolinite.

However, it was difficult to estimate the degree of kaolinization from XRD patterns, althogh an almost pure phase was surmised from these patterns as shown in Fig.3(d) and Fig.4(d). The weight loss obtained from TG curves was larger than that of theoretical dehydration of kaolinite; it was no doubt that amorphous silica did exist. Because of rather high acidity, amorphous silica was consequently formed under the conditions of the current experiment. Thus, hydrothermal synthetic conditions have yet to be studied in detail to obtain a pure phase of kaolinite from serpentinite.

4. Conclusion

Hydrothermal conditions for synthesizing kaolinite from serpentinite were investigated as a part of reserch for advanced utilization of serpentinite.

Either boehmite or $Al_{24}O_{11}(OH)_{44}Cl_6$ other than kaolinite coexisted when treated only with $AlCl_3$ solution (0.5 ~ 1.0mol/l) at 245°C for 48hrs. However, since boehmite alone coexisted as an impurity when the concentration of $AlCl_3$ solution was 0.5mol/l, the cyristallization was attem-

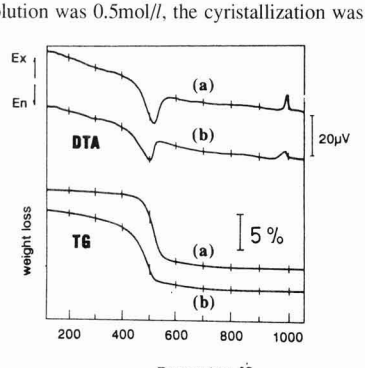

Fig. 6. TG-DTA patterns of (a) reference sample (KGa-2) and (b) synthesized kaolinite.

ped to inhibit by adding HCl to that $AlCl_3$ solution. As a result, kaolinite with lower crystallinity was obtained at 245°C for 48hrs and 200°C for 65hrs when the concentration of $AlCl_3$ solution and HCl were 0.5 and 0.3mol/*l*, respectively. Although amorphous silica coexisted under the above experimental conditions when kaolinite was formed, serpentinite was found to have been kaolinized in a relatively short period of time because of a topotaxial reaction mechanism, which made it possible for kaolinite to be formed as an agglomerate of paper-strip shaped crystals. However, it was necessary to remove impurities such as magnetite (chromite), uvarovite, etc. by magnetic separation for preparation of white kaolinite from serpentinite.

Acknowledgements

We thank Prof. N. Sakamoto, Okayama University of Sciences, and Mr. H. Koshimizu, Nihon Chemical Insdustrial Co. Ltd., for their valuable advice during this study. We also appreciate the kind guidance rendered to us by Mr. T. Tamagawa, Senior Researcher, Rare Metals Laboratory in National Research Institute for Pollution and Resources and Mr. A. Tunashima, Chief of the Siliceous Materials Laboratory of the above Institute. Finally, electron microscopic pictures kindly taken by Mr. N. Kikukawa, Senior Researcher of the same laboratory, were greatly appreciated.

References:

1) "Utilization of Ultrabasic Rocks from Hokkaido" (the materials prepared by the 3rd Study Meeting of Metallurgy), pp.228 (1962), Branch Study Meeting of Metallurgy in Hokkaido of Mining and Metallurgical Institute of Japan.
2) Annual Statistical Report on Resources, Ministry of International Trade and Industry pp.56-57 (1988).
3) R. Otsuka, K. Kosuge and H. Koshimizu, Science(Japanese Version), 6, 40-41 (1988).
4) S. Tomura, Y. Shibasaki, H. Mizuta and M,. Kitamura, Clays and Clay Minerals, 31, 413-421 (1983).
5) S. Tomura, Journal of the Japan Clay Society 25, 61-70 (1985).
6) H. Shibasaki, New Ceramics, 7, 51-57 (1989).
7) A. La Iglesia and M.C. Gastuche, Clays and Clay Minerals, 26, 397-408 (1978).
8) R. Roy and E.F. Osborn, Am. Mineral., 39, 538-85 (1954).
9) C.R. De Kimpe, M.C. Gastuche and G.W. Brindley, Am. Mineral., 49, 1-16 (1964).
10) K. Urabe, T. Ohba, H. Yamada and T. Kosaka, Yogyo Kyokaishi, 81, 486-490 (1973).
11) T. Sudo, "Nendo Kobutsugaku," Iwanami Shoten, pp.36-37 (1974).

This article is a full translation of the article which appeared in Nippon Seramikkusu Kyokai Gakujutsu Ronbunshi (Japanese version), Vol.99, No.4, 1991.

Mechanical and Electrical Properties of Hot-pressed TiN Ceramics Without Additives

Minoru Moriyama, Kiichiro Kamata* and Yoshikazu Kobayashi

Nagano National College of Technology
716, Tokuma, Nagano-shi 381, Japan
*Nagaoka University of Technology
1603-1, Kamitomioka-cho, Nagaoka-shi 940-21, Japan

Titanium nitride (TiN) ceramics without additives were fabricated by hot-pressing (HP), and their mechanical and electrical properties were investigated. Hot-pressing was performed at various sintering parameters such as sintering temperature (1800~2250°C), sintering time (30~180min), pressing pressure (2~14MPa) and ambient gas (Ar) pressure (vacuum~10atm). Densification was promoted at higher temperature, higher pressing pressure and longer sintering time. The TiN ceramics fabricated by hot-pressing at 2100°C×60min under the pressing pressure of 14MPa in the normal ambient gas pressure showed the representative properties: bulk density; 5050kgm^{-3} (relative density 92.8%), Vickers microhardness; 8.52GPa, flexural strength; 265MPa, static modulus (Young's modulus); 387GPa, dynamic modulus; 459GPa, and volume resistivity; 0.360μΩm. These properties were affected especially by the ambient gas pressure during hot-pressing. The TiN ceramics prepared in vacuum showed 30~40% augmentation, on the average, in hardness, flexural strength, Young's modulus and resistivity, compared with those prepared under normal (1atm) and higher pressures (5, 10atm). The TiN ceramics with high mechanical properties were obtained by sintering in vacuum.

[Received August 9, 1990; Accepted December 14, 1990]

Key-words: Hot-press, TiN ceramics, No additives, Mechanical property, Resistivity, Density

1. Introduction

Titanium nitride (TiN) ceramics are known for their favorable properties, high melting point (2949°C), high hardness (approximately 20GPa), metallic properties (palstically deformed at 1000°C, or more), high electrical conductivity, color (golden), high resistance to chemicals and corrosion, and superconductivity.[1-4] TiN, being a compound difficult to sinter, is generally sintered in the presence of an aid, such as Co and Ni, it become highly densified, though it is preferable not to use a sintering aid for improving resistance to grain boundary corrosion and mechanical properties at high temperatures.[5-6] These discussions, however, have been mainly based on structure and density observations, and few researchers have discussed mechanical and electrical properties. The authors have attempted to investigate the basic properties, such as mechanical and electrical, of the single-phase TiN, considering that it is a promising structural material capable of being processed by electrical discharge machining or plastic deformation at high temperature. Pure TiN powder, containing no sintering aid, was sintered by hot pressing, to investigate the effects of sintering conditions, or parameters (sintering temperature: 1800° to 2250°C, sintering time: 30 to 180min, pressing pressure: 2 to 14MPa, atmosphere pressure: 10^{-4} to 10atm) on the resultant sinter's characteristics (general, mechanical and electrical).

Yamada et al. have attempted hot pressing of TiN powder containing no sintering aid under high pressure (1.0 to 5.0GPa) using a cubic anvil to increase relative density and Vickers hardness to 95–98% or more and roughly 18GPa, respectively.[7]

Table 1. Compositions for raw TiN powders (wt%).

Ti	N	C	Fe	O
77.78	21.38	0.23	0.06	0.55

2. Experimental Procedure

2.1. Preparation of Specimens

Table 1 presents composition of the TiN powder as the starting material (Nippon Shin-Kinzoku), and **Fig.1** shows the photograph taken of the TiN by scanning electron microscope (SEM). It was of almost stoichiometric composition, and had an average particle diameter of 1.2μm. The starting powder (approximately 72g) was packed in a hot-pressing mold of graphite (60mm diameter), lined with a thin film (ca. 0.2mm thick) of sprayed BN powder as the release mold, and was placed in a hot-pressing furnace (equipped with a resistance heater unit). The furnace was

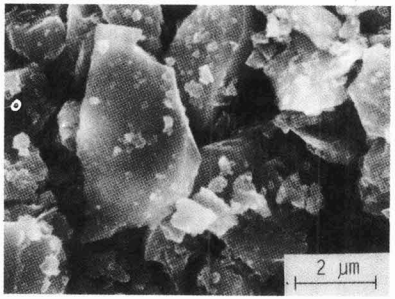

Fig. 1. SEM photograph for raw TiN powder.

purged under a vacuum (roughly 12mPa) to remove oxygen and other gases sufficiently, and the powder was treated under the conditions given in **Table 2**. Sintering temperature, time, hot-pressing pressure and ambient gas pressure as the operating parameters were changed around the standard set of conditions (temperature: 2100°C, time: 60min, hot-pressing pressure: 14MPa and atmosphere pressure: 1atm (for Specimen HP3)). The atmospheric pressure parameter was limited to that obtainable at a sintering temperature of 1950°C, which was used for the HP2 Specimen, due to the limitations set by the hot-pressing apparatus (the highest obtainable temperature was 2000°C under a vacuum). The sintering sequence; filling the apparatus with atmospheric gas (99.9995% pure inert Ar) to a set level; commencement of heating; pressing the TiN powder in the graphite mold at a given pressure as soon as temperature was increased to a given level; and holding the pressure during the sintering process. Pressing pressurization was stopped after sintering time was completed, the sinter was allowed to cool in the furnace, and was withdrawn from the furnace after it was cooled to room temperature. Many sintered bodies, however, were stuck fast to the mold on the upper and lower sides, and could not be separated readily. In such a case, the graphite mold was taken off under water by a coarse grindstone, to produce a cylindrical shape, approximately 60mm in diameter and 6mm long. It was then cut into specimen approximately 4×3×40mm by a diamond cutter for the JIS-specified bending test. The specimen for the measurement of bending strength and Young's modulus (static modulus of elasticity) could not be prepared from the sintered HP4, HP6 and HP7 sample because of several cracks running through each body. No sintering aid or other additive was used.

2.2. Analytical Procedure

Bulk and apparent densities of the sintered specimen were determined by the JIS Z8807 method (the Archimedian method for determination of the latter). TiN of the stoichiometric composition has a theoretical density of 5440kg/m^3.[3,8] The lattice parameter was determined by an X-ray diffractometer with Cu target and mixed Si powder as the internal standard. TiN's (422) plane was measured. TiN of the NaCl type structure has a lattice parameter of 0.4240nm, and the relationship between its lattice parameter and N/Ti atomic ratio is known.[1] Bending (flexural) strength was determined by the 4-point bending test method (JIS R1601) under the following conditions: crosshead speed: 0.5mm/min; upper span: 10mm; and lower span: 30mm. The 3-point bending test was also conducted for comparison, and gave higher values than the 4-point test. Hardness was determined by a Vickers microhardness tester, where the indenter was pressed against the specimen at a load of 9.8N; Young's modulus by two methods was also used; the strain gauge method determined static modulus and the ultrasonic pulse method determined dynamic modulus. Volumetric resistivity was determined, with the specimen prepared for the bending test, by the voltage drop method (4-terminal method)[9] at an amperage between 0.5 and 2.0A. Distance between the terminals was 20.25mm. For each test, a total of 10 to 30 specimens were used, except for lattice parameter test, and an average and standard deviation were reported to show the representative value and data scattering. Some of the specimens were qualitatively analyzed for their chemical compositions to confirm diffusion of carbon from the graphite mold. The quantitative analysis was not conducted for all the specimens.

Table 2. Hot-pressing conditions.

Specimen	Sintering temperature (°C)	Sintering time (min)	Pressure of pressing (MPa)*	Pressure of atmosphere (atm)**
HP1	1800	60	14	1
HP2	1950	60	14	1
HP3	2100	60	14	1
HP4	2250	60	14	1
HP5	2100	30	14	1
HP6	2100	120	14	1
HP7	2100	180	14	1
HP8	2100	60	2	1
HP9	2100	60	6	1
HP10	2100	60	10	1
HP11	1950	60	14	$\sim 10^{-4}$
HP12	1950	60	14	5
HP13	1950	60	14	10

* 1 MPa = 10.197 kgf·cm^{-2} ** 1 atm = 101325 Pa

3. Results

3.1. Structural Observations

It was found that strength of the sinter was greatly affected by ambient pressure. **Figure 2** shows the photographs, taken by a scanning electron microscope (SEM), of the specimens sintered at a varying ambient Ar gas pressure ((a): approximately 10^{-4}atm for HP11, (b): 1atm for HP2, and 10atm for HP13), with the other conditions set constant (sintering temperature: 1950°C, sintering time: 60min, and hot pressing pressure: 14MPa). The surface to be observed was polished by a diamond. The pores tended to grow faster as ambient pressure increased; growth of the grains was particularly noted with the specimen sintered at an ambient pressure of 10atm (c).

3.2. Effects of Sintering Temperature

The effects of sintering temperature in a range from 1800° to 2250°C (corresponding to HP1 through HP4, shown in Table 2) on density, lattice parameter and volumetric resistivity (**Fig.3**) and on Vickers hardness, flexural strength and Young's modulus (**Fig.4**) were investigated, while keeping the other conditions set constant (sintering time: 60min., hot-pressing pressure: 14MPa, and Ar gas ambient pressure: 1atm). Bulk density increased as sintering temperature increased, from approximately 4570 to 5130kg/m^3, which corresponded to a relative density of 84.0 to 94.2%, respectively. A lattice parameter of 0.424nm, very close to that of the stoichiometric composition, was obtained. It increased slightly as temperature increased up to 2100°C, but decreased thereafter. Volumetric resistivity and hardness increased from 0.280μΩm to 0.360μΩm and from 6.67 to 11.5GPa, respectively, as temperature increased. A similar trend was observed with 4-point bending (flexural) strength, which increased from 76.0 to 265MPa. Young's modulus increased from 248 to 387GPa for the static modulus determined by a strain gauge (marked with "static" in the figure) and from 298 to 493GPa for the dynamic modulus determined by the ultrasonic method

(marked with "dynamic" in the figure). Thus their trends were similar to each other, though the dynamic level was higher.

3.3. Effects of Sintering Time

The effects of sintering time in a range from 30 to 180min. (corresponding to HP3 and HP5 through HP7, shown in Table 2) were investigated, while keeping the other conditions set constant (sintering temperature: 2100°C, hot-pressing pressure: 14MPa, and Ar gas ambient pressure: 1atm). The results are shown in **Figs.5** and **6**. Bulk density and apparent density increased as sintering temperature increased, from 4790 to 5300kg/m^3 and from 4820 to 5290kg/m^3, respectively. The highest bulk density obtained in this study was 5300kg/m^3, corresponding to a relative density of 97.4%; the sample was hot-pressed at 2100°C for 180min. It was fairly higher than density of the sample hot-pressed at 2250°C for 60min. (5130kg/m^3), indicating that increasing sintering time densified the sinter more effectively than increasing sintering temperature. Lattice parameter increased slightly as sintering time increased. Resistivity was fairly constant at 0.360 to 0.534μΩm as a whole, though it decreased as sintering time increased up to 60min. and then increased thereafter. Hardness, flexural strength and Young's modulus increased as sintering time increased, from 8.36 to 11.0GPa, from 192 to 265MPa and from 374 to 560GPa, respectively.

3.4. Effects of Hot-Pressing Pressure

The effects of hot-pressing pressure in a range from 2 to 14MPa (corresponding to HP3 and HP8 through HP10, shown in Table 2) were investigated, while keeping the other

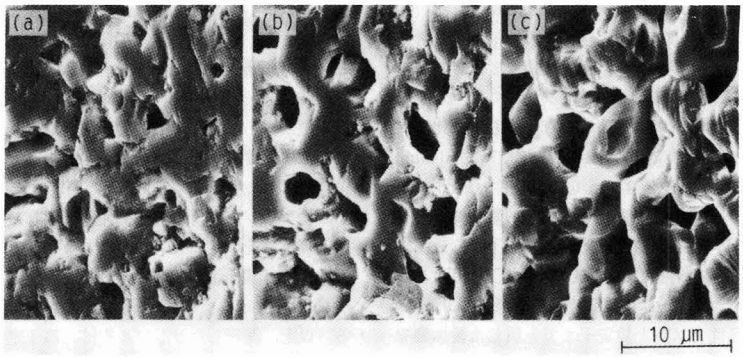

Fig. 2. SEM photographs for HP-TiN ceramics fabricated under the following ambient gas pressure of Ar.
(a): ~ 10^{-4}atm (HP11), (b): 1atm (HP2), (c): 10atm (HP13). (Sintering temperature: 1950°C, Sintering time: 60min, HP pressure: 14MPa)

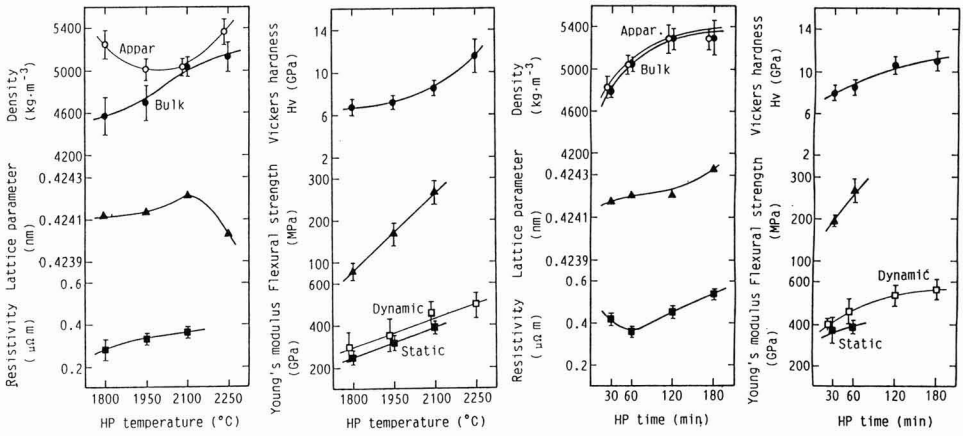

Fig. 3 Fig. 4 Fig. 5 Fig. 6

Fig. 3. The effect of sintering temperature on the density, the lattice parameter and the resistivity of HP-TiN ceramics. (Sintering time: 60min, HP pressure: 14MPa, Ambient gas pressure: 1atm).

Fig. 4. The effect of sintering temperature on the Vickers microhardness, the flexural strength and the Young's modulus of HP-TiN ceramics. (Sintering time: 60min, HP pressure: 14MPa, Ambient gas pressure: 1atm).

Fig. 5. The effect of sintering time on the density, the lattice parameter and the resistivity of HP-TiN ceramics. (Sintering temperature: 2100°C, HP pressure: 14MPa, Ambient gas pressure: 1atm).

Fig. 6. The effect of sintering time on the Vickers microhardness, the flexural strength and the Young's modulus of HP-TiN ceramics. (Sintering temperature: 2100°C, HP pressure: 14MPa, Ambient gas pressure: 1atm).

conditions set constant (sintering temperature: 2100°C, sintering time: 60min., and Ar gas ambient pressure: 1atm). The results are shown in **Figs.7** and **8**. Bulk density was greatly affected by hot-pressing pressure, increasing from approximately 3630 to 5050kg/m^3 (corresponding to 66.6 to 92.8% as relative density). Apparent density, on the other hand, increased only slightly with hot-pressing pressure. The lattice parameter also increased slightly with pressure. Resistivity decreased as well, from 0.557 to 0.360μΩm, as pressure increased because of increased density of the sintered sample. Hardness, flexural strength and Young's modulus increased with pressure, from 3.04 to 8.52GPa, from 67.0 to 265MPa and from 235 to 459GPa, respectively.

3.5. Effects of Ambient Pressure

The effects of pressure of the ambient gas (high-purity Ar as the inert gas) in a range from a vacuum (approximately 10^{-4}atm or 10.1Pa) to a positive pressure of 10atm absolute (corresponding to HP2 and HP11 through HP13, shown in Table 2) were investigated, while keeping the other conditions set constant (sintering temperature: 1950°C, sintering time: 60min., and hot-pressing pressure: 14MPa). The results are shown in **Figs.9** and **10**. Bulk density was in a range from 4320 to 4700kg/m^3, tending to be higher when the sample was sintered under a vacuum or atmospheric pressure than when under an elevated pressure. Apparent density was fairly insensitive to ambient pressure. Resistivity was higher when the sample was sintered under a vacuum, 0.457μΩm than under either atmospheric or elevated pressure, 0.334 to 0.312μΩm. Hardness was also higher when the sample was sintered under a vacuum at approximately 10.3GPa than under atmospheric and an elevated pressure, 7.06 to 7.52GPa. Similar trends were observed with flexural strength and Young's modulus; flexural strength, static and dynamic moduli of elasticity, obtained under a vacuum were 249 MPa, 429GPa and 518GPa, respectively. These were roughly 30 to 40% higher than those obtained under atmospheric and elevated pressure.

4. Discussion

4.1. Density

Bulk density increased generally by increasing sintering temperature, hot-pressing pressure and sintering time, and by decreasing ambient pressure, as shown in Figs.3, 5, 7 and 9. Assuming that intrinsic density is equal to theoretical density, the difference between intrinsic and apparent density is attributable to the presence of open pores.[10] It is considered, based on quantity of the open pores present in the sinter, that density at which most of the open pores turn into closed (independent) pores by sintering is approximately 4800kg/m^3 (corresponding to a relative density of 88%). A proposed set of standard conditions to give closed pores is; sintering temperature: 2100°C or higher, sintering time: 30min or more, hot-pressing pressure: 14MPa or more, ambient pressure: 1atm or less. It was noted, however that the sample sintered at 2250°C had a larger quantity of open pores than that sintered at 2100°C, as shown in Fig.3. This was conceivably attributable to a number of fine cracks in the former sample, which increased apparent density to result in an observed increase in the quantity of open pores.

The sample was more densified under a reduced ambient pressure than under a positive pressure, as shown in Fig.9. Uematsu et al. investigated the effects of N/Ti ratio (=x) on sinterability of TiN_x ceramic materials, to discuss that sintering is accelerated as the ratio decreases, because of in-

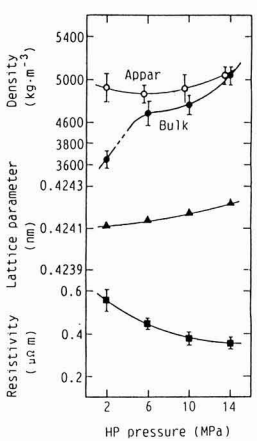

Fig. 7

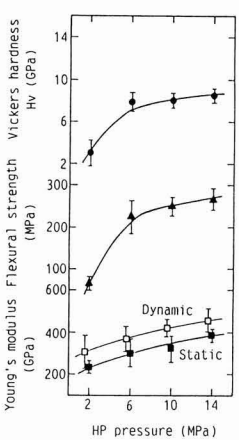

Fig. 8

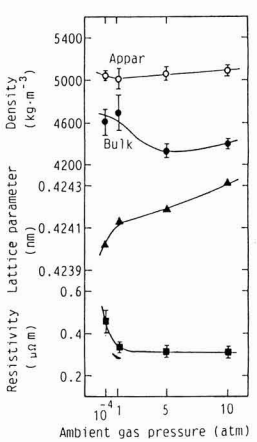

Fig. 9

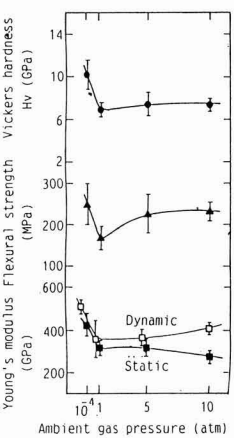

Fig. 10

Fig. 7. The effect of hot-pressing pressure on the density, the lattice parameter and the resistivity of HP-TiN ceramics. (Sintering temperature: 2100°C, Sintering time: 60min., Ambient gas pressure: 1atm).

Fig. 8. The effect of hot-pressing pressure on the Vickers microhardness, the flexural strength and the Young's modulus of HP-TiN ceramics. (Sintering temperature: 2100°C, Sintering time: 60min., Ambient gas pressure: 1atm).

Fig. 9. The effect of ambient gas pressure on the density, the lattice parameter and the resistivity of HP-TiN ceramics. (Sintering temperature: 1950°C, Sintering time: 60min., HP pressure: 14MPa).

Fig. 10. The effect of ambient gas pressure on the Vickers microhardness, the flexural strength and the Young's modulus of HP-TiN ceramics. (Sintering temperature: 1950°C, Sintering time: 60min., HP pressure: 14MPa).

creased diffusion coefficient of N atoms.[11] Mitani et al. sintered pure TiN powder under a vacuum (0.05Pa), to find that 0.23% of nitrogen is evaporated.[6] In this study, it was observed that the lattice parameter was fairly lower when the sample was sintered under a reduced ambient pressure than under a positive pressure, suggesting that nitrogen atoms were evaporated to increase the N/Ti ratio, with the result that sintering was accelerated, because of the increased diffusion coefficient of nitrogen, to increase sinter density.

4.2. Lattice Parameter

The lattice parameters of the TiN ceramics prepared in this study were, as a whole, slightly higher than the literature values,[1] and increased as sintering temperature, hot-pressing pressure, ambient pressure or sintering time increased. These conclusions were considered to result from the fact that the carbon in the graphite mold was diffused in the TiN sinter and dissolved therein to form a solid solution to increase the parameter, based on these observations; (1) small quantities of carbon and oxygen were found, but boron from the BN powder as the mold release was not in the sintered samples by the qualitative analysis with fluorescence X-ray, (2) carbon will increase the lattice parameter of TiN, when dissolved in the ceramic material,[12] and (3) TiN will lose lattice parameter when oxidized, and forms a solid solution with oxygen.[12] Diffusion of carbon is accelerated as sintering temperature or time increases, and this is in agreement with the observed changes of lattice parameter. Lattice parameter of the sample sintered at 2250°C was notably lower than the others, as shown in Fig.3, conceivably resulting from the rapidly increased dissociation pressure of TiN at approx. 2200°C or more.[13] This decreased N content and, hence, the level of the lattice parameter.

4.3. Electrical Resistivity

Volumetric resistivity increased under the conditions adopted in the study, as sintering temperature or time increased (refer to Figs.3 and 5). Generally speaking, the conditions that accelerate densification decrease resistivity because of a decreased quantity of pores. The contradicted results observed in this study may be attributable to the dissolution of carbon from the graphite mold in the TiN sinter, as discussed earlier, because (1) resistivity of TiC (0.70 to 1.73μΩm) is generally higher than that of TiN (0.22 to 1.30μΩm),[3] and (2) resistivity was found to change in a similar manner as did lattice parameter. Resistivity decreased as hot-pressing pressure increased, as shown in Fig.7, conceivably resulting from larger effects of densification than those of dissolution of carbon. The samples sintered under a positive ambient pressure had a fairly constant resistivity, in spite of reduced bulk density, as shown in Fig.9. This was considered to result from accelerated growth of TiN grains under a positive ambient pressure to decrease the lattice defects and to decrease resistivity created by the lattice defects and grain boundaries, judging from the SEM photographs (Fig.2) which showed the growth of the grains and increased quantity of the open pores under a positive ambient pressure. Notably increased resistivity of the samples sintered under a reduced ambient pressure in spite of the increased density was probably due to (1) the increased quantity of lattice defects (in particular, those associated with nitrogen atoms) accompanying the increased deviation of N/Ti ratio from stoichiometric ratio, as evidenced by sharply decreased lattice parameter, and (2) accelerated diffusion of carbon from the graphite mold, resulting from increased quantity of the lattice defects.

4.4. Hardness, Flexural Strength and Young's Modulus

Strength-related properties, such as hardness, flexural strength and Young's modulus, increased as sintering temperature, hot-pressing pressure and sintering time increased, and as ambient pressure decreased. In other words, they increased under the conditions that accelerated densification of the sinters, indicating that it is necessary to densify them in order to improve their strength-related properties. It is particularly noted that sintering under a vacuum is an effective means of accelerating densification under the same conditions of sintering temperature, time and hot-pressing pressure. The dynamic modulus of elasticity determined by the ultrasonic method was higher than the static modulus determined by a strain gauge. The difference came from the different analytical methods, i.e., the results varied, depending on whether the specimen was kept under thermal equilibrium , or thermally adiabatic conditions.

4.5. Density-Related Properties

The mechanical and electrical properties have been discussed in the previous sections. In this section, the density-related properties are discussed. **Figure 11** shows the results of bulk density, indicating that the strength-related properties, such as hardness, flexural strength and Young's modulus are basically related to bulk density. Hardness and Young's modulus of the HP11 specimen (bulk density: 4600kg/m^3), sintered at 1950°C for 60min. under a reduced ambient pressure, were higher than the respective averages represented by the linear relationship. However, it was not higher in bulk density than the HP2 specimen (bulk density: 4700kg/m^3) sintered under the same temperature and time conditions but under atmospheric ambient pressure. This means that the increased mechanical properties were attributable to other reasons, such as dissolution of carbon from

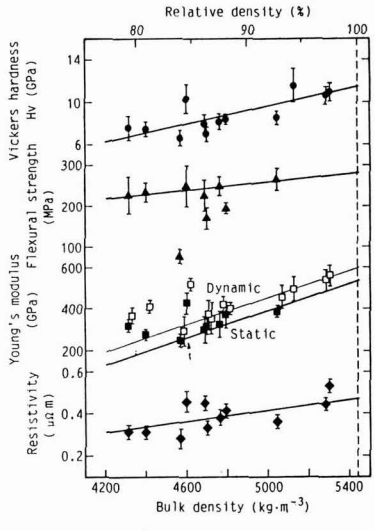

Fig. 11. The effect of volume density on the Vickers microhardness, the flexural strength, the Young's modulus and the electrical resistivity of *HP*-TiN ceramics.

the graphite mold and decreased N/Ti ratio. In an attempt to clarify the effects of dissolved carbon on strength-related properties, fluorescent X-ray analysis was conducted on the HP2, HP11 and HP3 specimens (bulk density: 5050kg/m^3), to determine their carbon contents. The HP11 specimen had roughly 1.5 times more quantity of dissolved carbon than the HP2 specimen and almost the same quantity of carbon as the HP3 specimen. The HP11 specimen was higher than the HP2 specimen in hardness and Young's modulus, in spite of a nearly identical dissolved carbon content and the former's fairly lower density. These results indicated that dissolution of carbon was not an essential condition of increasing strength. The results of TiN coating by the ion plating method, normally implemented under a vacuum, indicate that the highest hardness is realized at a composition, TiN_{1-x}, slightly lower in N content than the stoichiometric composition.[14,15] Therefore, the major reason for the increased strength of the HP11 specimen, prepared under a vacuum as is the case with ion plating, is not dissolution of carbon but decreased N/Ti ratio. Its slightly increased resistivity, in spite of its high density, is considered to result from dissolution of carbon from the graphite mold, as discussed earlier.

Extrapolating the data of each property to the point at the theoretical density (5440kg/m^3, broken line in Fig.11) will give the estimated property at the theoretical density; hardness: 11.4GPa, 4-point flexural strength: 280MPa, static modulus of elasticity: 530GPa, dynamic modulus of elasticity: 590GPa, and electrical resistivity: 0.47μΩm. The literature values of highly densified TiN ceramics are; hardness: 17.6 to 20.6GPa, Young's modulus: 250GPa, and volumetric resistivity: 0.22 to 1.3μΩm.[1,3] The samples prepared in this study are lower in hardness, roughly 2 times higher in Young's modulus than, and same level in resistivity with, the literature samples. The difference observed in hardness and Young's modulus will be discussed in the future, based on the further investigations by adequate methods, including composition analysis.

4.6. Comparison

The results of this study are compared with the literature results. Yamada et al. produce the single-phase hot-pressed TiN sinters from two different types of starting powders; fine and coarse ones, the former having an average particle size of 0.05μm and the latter having particles of 6 to 12μm, sintered under conditions of 800° to 1800°C, 60min. and a very high pressing pressure of 1.0 to 5.0GPa in the ambient N_2 gas, into 5mm diameter, 3mm high shapes.[7] A relative density of 95% or more is obtained from both starting materials when they are treated under conditions of 1600°C, 60min and hot-pressing pressure of 3GPa or higher. In particular, a relative density of 98% or more is obtained from the coarser powder treated at 1500°C or higher. The highly densified sinter has a Vickers hardness of approx. 18GPa, determined at room temperature. No mechanical or electrical property, other than hardness, is reported for the high-density TiN sinters. The HP6 and HP7 specimens having a relative density of about 97% (sintered under the conditions of 2100°C, 120 to 180min, and 14MPa hot-pressing pressure) are considered, based on the hardness and density results, to be comparable with the samples, hot pressed at 1600°C and a very high pressure of 1.0 to 5.0GPa.

5. Conclusions

Pure TiN powder was hot-pressed under conditions of 1800° to 2250°C sintering temperature, 30 to 180min. sintering time, 2 to 14MPa pressing pressure and 10^{-4} to 10atm (absolute) ambient pressure in order to investigate mechanical and electrical properties of the sinters. No sintering aid was used.

1) Increasing temperature accelerated densification of the sinter to 4570 to 5130kg/m^3 (corresponding to a relative densities of 84.0 to 94.2%). Vickers hardness of the sinters was in a range of from 6.67 to 11.5GPa, 4-point flexural strength from 76 to 265MPa, Young's modulus from 248 to 493GPa, and volumetric resistivity from 0.280 to 0.360μΩm.
2) Increasing sintering time accelerated densification, mainly as a result of reduced quantity of closed pores. Densification accelerated to a relative density of 88.1 to 97.4%. Hardness of the sinters was in a range from 8.36 to 11.0GPa, and Young's modulus from 374 to 560GPa.
3) Increasing hot-pressing pressure accelerated densification, mainly as a result of reduced quantity of the open pores. Pressure of 14MPa gave a relative density of 92.8%, under conditions of 2100°C and 60min.
4) Decreasing ambient pressure accelerated densification, mainly as a result of reduced quantity of the open pores. The sinter prepared under a vacuum had more favorable properties than any other sample prepared in this study; 10.3GPa as Vickers hardness, 249MPa as flexural strength, 429GPa as static modulus of elasticity, 518GPa as dynamic modulus of elasticity, and 0.457μΩm as volumetric resistivity. These levels were 30 to 40% higher on the average than those of the sinters prepared under atmospheric or elevated pressure. Sintering under a reduced ambient pressure, therefore, is an effective means of densification.
5) The properties of the TiN sinter, estimated by extrapolating each datum to the level at the theoretical density, are; Vickers hardness: 11.4GPa, flexural strength: 280MPa, static modulus of elasticity: 530GPa, dynamic modulus of elasticity: 590GPa, and resistivity: 0.47μΩm.

References:

1) L.E. Toth, "Transition metal Carbides and Nitrides," Academic press (1971), pp.1-262.
2) P. Schwarzkopf and R. Kieffer, "Refractory hard Metals," the Macmillan Company (1953), pp.223-35.
3) "Handbook of Fine Ceramics," edited by the committee for editing handbook of fine ceramics, Giho-do (1987), pp.631-44.
4) Y. Shiraki, "Fine Ceramics," Giho-do, (1976), pp.630-35.
5) A. Tsuge, H. Inoue and K. Komeya, Yogyo-Kyokai-Shi, 82, 587-96 (1974).
6) H. Mitani, H. Nagai and M. Fukuhara, J. of the Japan Institute for Metals, 42, 582-88 (1978).
7) T. Yamada, M. Shimada and M. Koizumi, Am. Ceram. Soc. Bull., 59, 611-16 (1980).
8) P. Chiotti, J. Am. Ceram. Soc., 35, 123-30 (1952).
9) T. Abe and M. Murayama, "Electrical and electronic measurement," Morikita Shuppan (1988), pp.73-74.
10) "Techniques for Characterizing Ceramic Materials," edited by Ceramic Society of Japan, (1987), pp.2-5.
11) K. Uematsu, N. Kieda, O. Sakurai, N. Mizutani and M. Kato, Yogyo-Kyokai-Shi, 90, 597-603 (1982).
12) F.S. Galasso, "Structure and Properties of Inorganic Solids," Per-

gamon Press (1970), pp.63-34.
13) "High-Temperature Technology," edited by I.E. Campbell (Translated by C. kawashima et. al., Corona-sha, (1963), pp.186.
14) A. Matthews and D.G. Teer, Thin Solid Films, 72, 541-49 (1980).
15) W.D. Sproul, Thin Solid Films, 107, 141-47 (1983).

This article is a full translation of the article which appeared in Nippon Seramikkusu Kyokai Gakujutsu Ronbunshi (Japanese version), Vol.99, No.4, 1991.

Effects of Grain Size on Creep of Mullite Ceramics

Masahiro Ashizuka, Takeshi Honda* and Yoshitaka Kubota**

Department of Materials Science and Engineering, Kyushu Institute of Technology
1-1, Sensui-cho, Tobata-ku, Kitakyushu-shi 804, Japan
*Graduate Student, Department of Materials Science and Engineering, Kyushu Institute of Technology
1-1, Sensui-cho, Tobata-ku, Kitakyushu-shi 804, Japan
**Advanced Materials Laboratory, Tosoh Corporation
2743, Hayakawa, Ayase-shi 252, Japan

The effect of grain size on creep in mullite ceramics containing 71, 72 and 74 wt% Al_2O_3 (71A, 72A, and 74A, respectively) has been studied. It is shown that a glass phase existed around grain boundary triple points for 72A, whereas it did not exist for 74A from the observation by transmission electron microscope. Stress exponents (n) for creep deformation were 1.1-1.2, 1.2-1.3 and 1.3-1.5, and grain size exponents (m) were 2.4, 2.0 and 1.2 for 71A, 72A and 74A respectively. It was assumed that the creep deformation was controlled by grain boundary sliding accommodated by cavitation for 74A, diffusion in glass phase at grain boundaries for 71A and their combined mechanism for 72A.
[Received August 9, 1990; Accepted December 14, 1990]

Key-words: Mullite, SiO_2-Al_2O_3 ceramics, Creep, Microstructure, Grain boundary sliding, Diffusion, Glass phase, Stress exponent, Grain size exponent

1. Introduction

Mullite ($3Al_2O_3 \cdot SiO_2$) has been widely used for furnal tubes and various products for scientific research, because of its high melting point, low coefficient of thermal expansion and stability at high temperature. Conventional mullite ceramics, however, are rarely used as structural materials, because they contain sufficiently high concentrations of impuritie, such as CaO and Na_2O, which cause softening at temperature above 1100°C. More recently, they have been sufficiently densified and purified to attract attention as high-temperature structural materials.[1-6] The authors have prepared the mullite ceramics by pressurelessly sintering the coprecipitation-synthesized powder to find that 74wt% Al_2O_3 mullite is highly resistant to creep at 1350° to 1500°C.[7] In this study the creep rate was measured for various mullite compositions of different grain sizes; Three types of the 71wt%Al_2O_3(71A) composition at 1400°C, three types of the 72wt%Al_2O_3(72A) composition at 1400°C, and two types of the 74wt%Al_2O_3(74A) composition at 1450°C. Based on these results coupled with previous results, the authors investigated the effects of grain size on the creep deformation rate of the mullite ceramics, to discuss the creep deformation mechanisms.

2. Experimental Procedure

Mullite powders of 71, 72 and 74wt% Al_2O_3 compositions, prepared by the coprecipitation method,[8,9] were preformed in a metal mold, compacted by cold isostatic pressing and then sintered at 1650°C, to prepare test pieces, which were cut into the specimens of 3×4×45mm. Grain size was controlled by changing the sintering time. The tensile surface of each specimen was mirror-polished by 1μm diamond paste.

The 4-point bending jig (inner span: 10mm, outer span: 30mm) made of high-purity mullite was used for the measurement of creep behavior. Stress was applied by a balance-type system, and displacement was measured by a differential transformer.[7] A scanning electron microscope was used for the observation of the microstructures of the specimen, mirror-polished, thermally etched at 1550°C for 30min, and then placed in 1% HF solution which was kept at 0°C for 24h for chemical etching. A transmission electron microscope was used to observe the area around the triple points in the grain boundaries of the 72A and 74A compositions, and to investigate the presence of the glass phase. Grain size of each sintered specimen was determined by the intercept segment method.[10]

3. Results and Discussion

3.1. Microstructures

Figure 1 presents the microstructure of the 71A, 72A and 74A compositions, observed by a scanning electron microscope. The 71A compositions contained a larger quantity of the highly anisotropic rod-like crystals than the others. The 74A composition, on the other hand, consisted essentially of isotropic crystals, and the 72A composition was in-between. **Figure 2** presents the microstructures of the 74A composition; Figure 2(a) a shows the photograph of the triple point, taken by a transmission electron microscope (TEM) (Point T: triple point), proving that the boundaries meet at a dihedral angle of 120°, and Figure 2(b) exhibits the photograph in the vincity of the triple point and grain boundary, taken by a high-resolution electron microscope, showing that lattice fringes in each grain extend to the boundary without any confusion. These photographs indicated that there was no amorphous phase (hereinafter referred to as the glass phase) around the triple point and grain boundary. **Figure 3** shows the photograph of a triple point in the grain boundary of the 72A composition, taken by a high-resolution electron microscope, indicating that

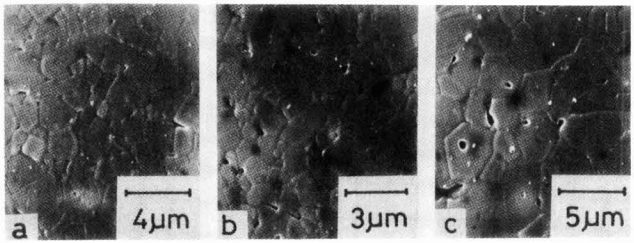

Fig. 1. Microstructures of mullite ceramics (chemically etched by 1%HF aqueous solution at 0°C) (a)71wt%Al_2O_3.

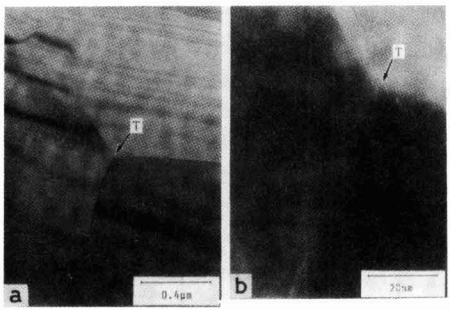

Fig. 2. (a)Transmission electron micrograph and (b)High-resolution electron micrograph of 74wt%Al_2O_3-mullite ceramics. "T" indicates the grain boundary triple point.

there was a glass phase (Region A in the figure) around the triple point. It was considered that the 71A composition contained a still larger quantity of the glass phase. The average grain size of the specimens used in this study was 1.3,1.5 and 2.0μm for the 71A, 1.3, 2.1 and 3.0μm for the 72A, and 2.4 and 3.8μm for the 74A.

3.2. Measurement of Creep

The deflection-time curves obtained in this study for a variety of loads were similar to those already discussed, showing the presence of steady-state creep region following the transition region.[7] It is generally accepted that the strain rate $\dot{\varepsilon}$ in the steady-state creep region is correlated withapplied stress σ by the following formula:[11]

$$\dot{\varepsilon} = \frac{ADGb}{kT}\left(\frac{b}{d}\right)^m\left(\frac{\sigma}{G}\right)^n \quad \cdots\cdots\cdots\cdots\cdots (1)$$

where

A : constant
D : diffusion coefficient
G : shear modulus
b : Berger's vector
d : grain size
m : grain size exponent
n : stress exponent
k : Boltzmann constant
T : absolute temperature

The grain size exponent m and stress exponent n are related to the creep deformation mechanisms.[11] In the case of diffusional creep, n=1 and m=2 for the Nabarro-Herring creep where the paths for the diffusion rate-determining species are within the grains, and n=1 and m=3 for the Coble creep where these paths are in the grain boundaries. In the case involving the mechanism of grain boundary sliding, it is necessary to consider two cases, depending on whether a liquid phase is present in the grain boundaries or not. When a liquid phase is present in the grain boundary, the stress exponent n is 1 and the grain size exponent m is 1. On the other hand, when a liquid phase is absent in the grain boundary, Langdon discusses that the grain boundary sliding is accomodated by the formation of cavities in the grain boundary. In such a case, n value becomes 2, m value becomes 1 and the activation energy agrees with that of lattice difusion.[11] Evans and Rana developed a statistical model to the phenomena related to creep deformation in the case that cavities are formed, and showed that the n value is 2.[12]

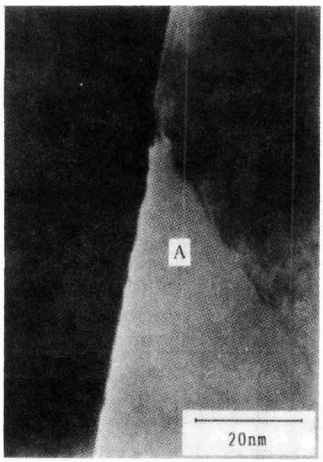

Fig. 3. High-resolution electron micrograph of 72wt%Al_2O_3-mullite. "A" indicates the amorphous phase at the grain boundary triple point.

When the glass phase is present in the grain boundaries, such as 71A and 72A in this study, there may be creep mechanism related to dissolution and precipitation occurring between the grains and the glass phase

In the above case, the overall reaction rate is determined either by reactions in the interfaces or by diffusion through the glass phase. The stress and grain size exponents will be n=1 and m=1 for the interface reaction-controlling process, and n=1 and m=3 for the diffusion-controlling process.[13] The n and m values for the case that the diffusion through the glass phase in grain boundary is the rate-controlling step are the same as those for the Coble creep that diffusion through the grain boundaries is the rate-controlling step. **Figures 4** through **6** present the results observed in this

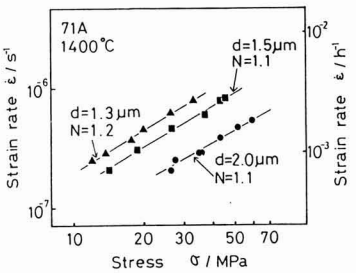

Fig. 4. Relation between creep rate $\dot{\varepsilon}$ and applied stress σ for 71wt%Al_2O_3-mullite with grain sizes of 1.3, 1.5 and 2.0mm.

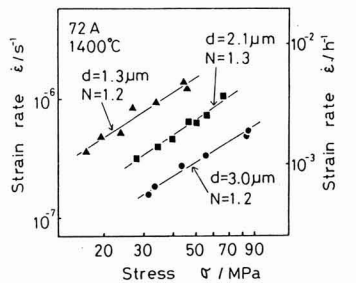

Fig. 5. Relation between creep rate $\dot{\varepsilon}$ and applied stress σ for 72wt%Al_2O_3-mullite with grain sizes of 1.3, 2.1 and 3.0m.

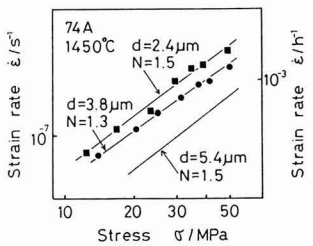

Fig. 6. Relation between creep rate $\dot{\varepsilon}$ and applied stress s for 74wt%Al_2P_3-mullite with grain sizes of 2.4 and 3.8m. The line for 5.6m is from reference 7.

study.

Figure 7 shows the effects of average grain size d on strain rate $\dot{\varepsilon}$ under an applied stress of 40MPa, combined the results obtained in this study with those reported previously. The slope of each curve gives grain size exponent m in Equation (1); 2.4, 2.0 and 1.2 for the 71A, 72A and 74A, respectively. The m value of the 74A is lower than those proposed by other researchers for mullite ceramics.[14,15]

Table 1 summarizes the stress exponent n, grain size exponent m and activation energy Q proposed by several researchers, including the authors.[1,14,15,16] The stress exponent n observed in this study increased slightly as Al_2O_3 content increased: 1.1 to 1.2, 1.2 to 1.3 and 1.3 to 1.5 for the 71A, 72A and 74A, respectively. The opposite trends were observed for the grain size exponent m: 2.4,2.0 and 1.2 for these compositions.

The authors have proposed grain boundary sliding as the basic mechanism for creep deformation of mullite ceramics, based on SEM observations of the tensile specimen surface after creep test..[7] In the case of the 74A which contained not only glass phase but also other material phase in the grain boundaries (as revealed by the TEM analysis), it is difficult to consider diffusion through the grain boundaries as the mechanism to relax the stress concentration occurring at the triple point as a result of grain boundary sliding. Furthermore, because lattice diffusion in mullite was slow, it is estimated that creep deformation rate was reduced.

In the case of grain boundary sliding, the stress exponent n and grain size exponent m will be 1 and 2, respectively, as discussed earlier. The observed grain size exponent m of 1.2, as shown in Fig. 7 and Table 1, suggests that the grain boundary sliding is basic mechanism in the creep deformation in the 74A. The stress exponent n of the 74A (1.3 to 1.5) was slightly higher than those of the 71A and 72A compositions (71A: 1.1 to 1.2, 72A: 1.2 to 1.3), conceivably resulting from a greater contribution in the grain boundary sliding mechanism, and formation and growth of the cavities in the grain boundaries accelerated as applied stress became larger or loading time increased. The observed activation energy (168 to 169kcal/mol) of the 74A was very close to that of the lattice diffusion (168kcal/mol), reported by Aksay.[15]

As discussed earlier for the microstructure, the 71A and 72A had the glass phase in the grain boundaries, the former containing a larger quantity.[9] Increased quantity of the glassy phase will accelerate the grain boundary sliding. In addition, the presence of the glass phase allows the mullite matrix with highly anisotropic rod-like crystals. Itis estimated that the resistance to grain boundary sliding increases with increasing the proportion of rod-like crystals in mullite

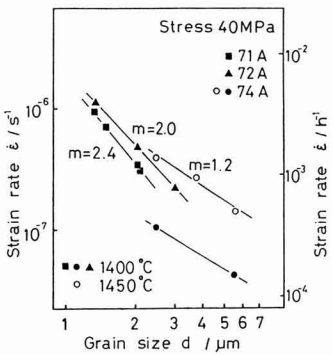

Fig. 7. Creep rate $\dot{\varepsilon}$ as a function of grain size d.

Table 1. Stress exponent n; grain size exponent m, and activation energy on creep in mullite ceramics

Researcher	Stress exponent n	Grain size exponent m	Activation energy kcal/mol	Ref.
71wt%Al_2O_3				
Present work	1.1~1.2	2.4	138	7
71.8wt%Al_2O_3				
P.A.Lessing, R.S.Gordon	0.95	-	164	14
P.C.Dokko, J.A.Pask K.S.Mazdiyasni	1.0	2.0	170	15
Okamoto, Fukutome, Hayasi Nishikawa, Yano	1.0	2.5	194	17
72wt%Al_2O_3				
Present work	1.2~1.3	2.0	171	16
74wt%Al_2O_3				
Present work	1.3~1.5	1.2	168, 169	7

matrix. In other words, the presence of the glass phase creates two results contradictory to each other: acceleration of and resistance to grain boundary sliding.

It is possible to suppose, when the glass phase is present in the grain boundaries, a creep deformation mechanism in which diffusion through the glass phase is involved. In this case, the predicted grain size and stress exponents are m=3 and n=1, m value of 2.4 and n value of 1.1 to 1.2 for the 71A shown in **Figure 4** and Table 1 may suggest a greater role of diffusion through the glass phase in the grain boundaries. In other words, a higher creep deformation rate of the 71A than that of the 74A may be due to diffusion through the glass phase to relax the stress concentration at the triple point, generated as a result of the grain boundary sliding.

Lessing et al. and Dokko et al. investigated the stoichiometric mullite composition (71.8wt% of Al_2O_3) very close to the 72A prepared in this study. They proposed the n value of 0.95 (Lessing et al.), and n of 1.0 and m value of 2 (Dokko), which are also very close to those observed in this study, and concluded that lattice diffusion is responsible for the creep deformation of the mullite ceramics, because these values are close to those predicted based on Nabarro-Herring's lattice diffusion mechanism and the activation energy observed is close to that associated with the lattice diffusion (168kcal/mol) proposed by Aksay.[14,15] Although the n and m values observed in this study and the activation energies observed previously for the 72A are close to those proposed by Dokko et al., the authors estimayed that creep deformation rate of 72A are not controlled by the lattice diffusion but rather by acombination of diffusion inthe glass phase and the grain boundary sliding, i.e., the intermediate between those for the 74A and 71A.

For the creep deformation rate at the same grain size, that of the 72A was higher than the 71A, as shown in **Fig.7**. It is considered, in general, that grain boundary sliding occurs to a greater extent in the 71A than in the 72A because of the former's higher concentration of the glass phase, and hence the former has a higher creep deformation rate. On the other hand, the 71A has a higher proportion of rod-like crystals than the 72A, which makes the former more resistant to the grain boundary sliding and gives it a lower creep deformation rate. The observed higher creep deformation rate of the 72A indicates that the latter effects predominate.

4. Conclusions

The effects of grain size on creep deformation of mullite ceramics of 71wt% Al_2O_3 composition (71A), 72wt% Al_2O_3 (72A) and 74wt% Al_2O_3 (74A) were investigated. The results obtained are as follows:

1) The glass phase was found around the triple point in the grain boundaries of the 72A, but not around the triple point or in the grain boundaries of the 74A.
2) The 71A, 72A and 74A had stress exponents of 1.1 to 1.2, 1.2 to 1.3 and 1.3 to 1.5, respectively.
3) The 71A, 72A and 74A had grain size exponent of 2.4, 2.0 and 1.2, respectively.
4) The creep deformation mechanism of the 74A are grain boundary sliding accomodated by the formation of cavities.
5) It is considered that diffusion through the glass phase in the grain boundaries plays a greater role in the creep deformation of the 71A than in the others.
6) The creep deformation of the 72A is represented by the combination of the grain boundary sliding and diffusion through the glass phase in the grain boundaries.

Acknowledgements

The authors thank Messrs. K. Tsutsumi, H. Ito and M. Oshita, students Kyushu Institute of Technology's Faculty of Engineering, for their cooperation. The TEM photographs were taken with the cooperation of Tosoh Corp.

Reference:

1) S. Somiya, "New Materials Series, Mullite," edited by S. Somiya, Uchida Rokaku-ho, (1985), p.1-11
2) T. Kawanami, ibid., Uchida Rokaku-ho, (1985), p.123-135
3) P.C. Dokko, J.A. Pask and K.S. Mazdiyasni, J. Amer. Ceram. Soc., 60, 150-155 (1977).
4) K. Hamano, Z. Nakagawa, K. Sunsai and T. Sato, "New Materials Series, Mullite," edited by S. Somiya, Uchida Rokaku-ho, (1985), p.37-49
5) K. Sunsai, K. Hamano and Z. Nakagawa, Yogyo Kyokai-shi, 94, 583-589 (1986)
6) K. Hamano, T. Sato and Z. Nakagawa, ibid., 94, 818-822 (1986)
7) M. Ashizuka, T. Okuno and Y. Kubota, J. of Ceramic Society of Japan, 97, 622-668(1989)
8) Y. Kubota and H. Takagi, Proc. Brit. Ceram. Soc., 37, 179-188(1986).
9) Y. Kubota and H. Takagi, "New Materials Series, Mullite," edited by S.Somiya, Uchida Rokaku-ho, (1985), p.1-11
10) R.L. Fullman, Trans, AIME, 197, 447-452(1953).
11) W.R. Cannon and T.G. Langdon, J. Mater. Sci., 18, 1-50 (1983).
12) A.G. Evans and A. Rana, Acta Metall., 28, 129-141(1980)
13) R. Raj and C.K. Chyung, Act Met., 29, 159-166(1981).
14) P.A. Lessing, R.S. Gordon and K.S. Mazdiyasni, J. Amer. Ceram. Soc., 58, 149(1975).
15) P.C. Dokko, J.A. Pask and K.S. Mazdiyasni, J. Amer. Ceram. Soc., 60, 150-155 (1977).
16) M. Ashizuka, T. Honda and Y. Kubota, J. of Ceramic Society of Japan, 99, 357-360 (1991)
17) Y.Okamoto, H.Fukutome, K.Hayashi, T.Nishikawa and J.Yano, The Ceramic Society of Japan Annual Meeting Proceedings (May 15-19, 1989) p.240

This article is a full translation of the article which appeared in Nippon Seramikkusu Kyokai Gakujutsu Ronbunshi (Japanese version), Vol.99, No.4, 1991.

Effects of Crack Size on Fatigue Behavior in Silicon Nitride

Tomonori Niwa, Kazuhiro Urashima, Yo Tajima and Masakazu Watanabe

NGK Spark Plug Co., Ltd.
2808 Iwasaki, Komaki, Aichi, 485, Japan

The fatigue behavior of gas pressure sintered silicon nitride ceramics at room temperature in air was investigated. Cyclic and static fatigue tests were carried out for smooth and precracked specimens. Precracks were introduced by indentation at the center of the tension side surfaces. All the testing was conducted by the 3-point bending method.

Smooth specimens showed no significant enhancement of the subcritical crack growth by cycling. On the other hand, enhanced fatigue was observed for precracked specimens. In addition, it is suggested that the fatigue behavior depends on the size of the precracks. Cyclic fatigue behavior was not influenced by residual stress introduced by Vickers indentation.

[Received August 30, 1990; Accepted January 24, 1991]

Key-words: Silicon nitride, Cyclic fatigue, Static fatigue, Precracked specimen, Smooth specimen, Residual stress

1. Introduction

Recently, silicon nitride is being applied to engine and industrial parts.[1] However, it is necessary to understand the fatigue behavior of silicon nitride before it can be used as structural material. A number of researchers are discussing fatigue of silicon nitride with specimens of various shapes being tested under diverse conditions. The test results presented so far fall into two general categories; those which are not precracked and those with precracked specimens. Some of the results falling into the former category show a time-dependent fatigue behavior,[2,3] and an accelerated fatigue is observed in specimens under tension-compression stress than under tension-tension stress[4-6]. The results falling into the latter category include the effects of cyclic loading and precrack length on fatigue.[11,12]

Thus, extensive efforts have been devoted to fatigue characteristics of various types of silicon nitride, different from each other in sintering method, kinds and amounts of sintering aids, porosity, and so on. However, the effects of cyclic loading and initial defect size are not yet well understood. In this study, the authors investigated fatigue behavior of the smooth and precracked specimens of silicon nitride at room temperature, prepared by the gas pressure sintering method,[2] to clarify the effects of precrack length, load frequency and stress ratio. The effects of residual stress were also investigated on the samples precracked by a Vickers indenter.

2. Experimental Procedure

2.1. Specimen Preparation

The specimens used in this study were of gas pressure sintered silicon nitride, doped with Al_2O_3 and Y_2O_3.

Table 1 summarizes the properties of the material.

Each specimen shaped (3mm thick, 4mm wide and 40mm long) as specified by JIS R1601, was ground by a #140 diamond wheel with downfeed of 5μm to remove 200μm before finishing to final dimensions.

Two types of specimens were used; one was smooth and the other precracked. For the latter a Vickers indenter was pressed on a smooth specimen at its center to introduce a crack. Three types of specimens of different precrack length 2C (20, 40 and 180μm) were prepared by changing Vickers load P (200g, 500g and 5kg for the above lengths, respectively) to investigate the effects of precrack length. The above crack lengths were measured after applying a Vickers indenter to the mirror-polished surface. Furthermore, some precracked specimens were ground to remove residual stress to determine whether residual stress, generated by pressing a Vickers indenter on the surface, affected the fatigue behavior. These specimens, after having been indented, were ground to remove a thickness of 50, 70, 90, 100 or 120μm; to determine how far the specimen should be ground to completely remove residual stress. Each specimen was ground with downfeed of 5μm by a #140 diamond wheel. Each ground specimen was tested by the 3-point bending method, to determine its fracture toughness using the Raju-Newman equation[13] and establish the relationship between fracture toughness and ground depth. The ground depth at which fracture toughness of the specimen increased back to the original K_{IC} level was regarded as the depth at which residual stress was removed.

2.2. Fatigue Tests

Both static and cyclic fatigue tests were carried out at room temperature by the 3-point bending method with a span of 30mm. Sinusoidal cyclic loads were applied to the specimen by a hydraulic servo fatigue tester at a frequency of 10 or 1Hz and a stress ratio (R) of 0.1 or 0.5. Static loads were applied to the specimen by a counterweight type fatigue tester with a leverage of 1:5. The test was stopped after a period of 10^6sec in both static and cyclic testing.

Table 1. Properties of gas pressure sintered silicon nitrides (GPSSN).

Density (g/cm^3)	Young's Modulus (GPa)	Vickers Hardness (GPa)	Fracture Toughness by SEPB ($MPa \cdot m^{1/2}$)	Thermal Expansion Coefficient (/K)	Thermal Conductivity (W/m·K)
3.23	320	14.3	6.0	2.8×10^{-6} (r.t.-800°C)	27

3. Results and Discussion

3.1. Fatigue Behavior of Smooth Specimens

Figure 1 shows the relationship between maximum stress and effective time to failure of the smooth specimens. Effective time to failure was chosen in abscissa to compare the static test results with the cyclic test results. Effective time to failure and the fatigue parameter n were estimated from the cyclic test results by the procedure described elsewhere.[2] The data marked with arrows represent the specimens which were not broken in the test period.

Cyclic fatigue life is correlated with effective time to failure, irrespective of frequency and stress ratio under which each specimen was tested. Moreover, it was noted that the static and cyclic test results lay almost on a single line, when correlated with effective time to failure. These results indicate that the cyclic loading does not affect on the smooth specimens, and the fatigue behavior is of a time-dependent type which can be treated by effective time to failure. Ohtsuka et al. determined fatigue life in the rod-shape specimens of silicon nitride, prepared by gas pressure sintering similar to that used in this study, to discuss that fatigue life can be represented by a time-dependent type correlation.[3] The results observed on smooth specimens in this study are in agreement with Ohtsuka et al.'s.

3.2. Fatigue Behavior of Precracked Specimens

3.2.1. Fatigue Behavior of Specimens with Large Precrack

Figure 2 shows the static and cyclic test results of the precracked specimens with a crack length(2C) of 180μm. Fatigue life under the cyclic loading was obviously shorter than under the static loading, and the curve of the former fatigue life was characterized by a reversed S-shape. The fatigue parameter values determined by the least-square method were n=96 for the static test results and n=27 and for the cyclic test results under the condition of 10Hz, R=0.1. These results are in agreement with those reported by Kawakubo et al.[7]

The results with the precracked specimens were also affected by frequency and stress ratio. The fatigue life decreased as stress ratio decreased from R=0.5 to R=0.1, and as frequency increased from 1 to 10Hz. **Figure 3** shows the relationship between maximum stress and number of cycles, under the condition of 10Hz and 1Hz and a constant stress ratio of R=0.1. It is a copy of Fig.2 except that effective time to failure is replaced by number of cycles, indicating that the fatigue behavior of the precracked specimen is of a cycle-dependent type. However, the effects of stress ratio are noted; the fatigue life tended to decrease as stress ratio decreased (i.e. as load amplitude increased).

Thus, the smooth specimen is clearly different in fatigue behavior from the specimen with a large precrack.

3.2.2. Effects of Residual Stress

Pressing a Vickers indenter against the specimen would invariably generate residual stress in the specimen, and the effects of residual stress on fatigue behavior were investigated.

Prior to the fatigue tests, depth of a surface layer to be removed by grinding was determined. **Figure 4** shows the relationship between fracture toughness and removed depth, with the specimens indented at a load of P=20kg. Length of the crack used in calculating fracture toughness was determined from the initial length, where it was assumed that the initial precrack was a semicircle in shape and was not extended while it was processed. The fracture toughness value determined by the single edge precracked beam (SEPB) method is also shown in the figure, for comparison.

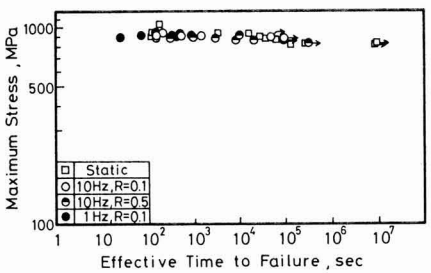

Fig. 1. Fatigue behavior of smooth specimens.

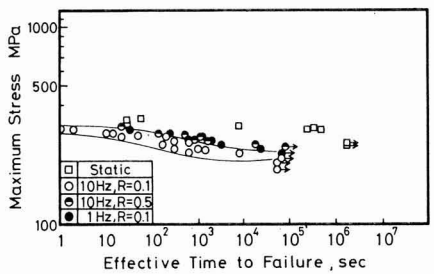

Fig. 2. Fatigue behavior of precracked specimens (crack length 2C=180μm).

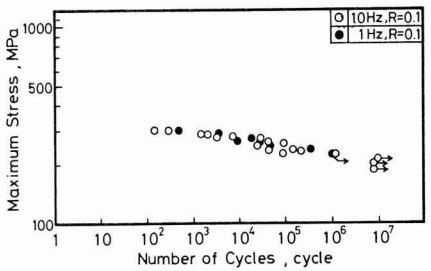

Fig. 3. Results of cyclic fatigue test for precracked specimens (crack length 2C=180μm).

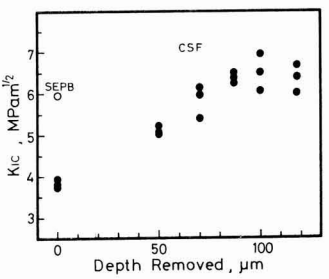

Fig. 4. Fracture toughness values as a function of depth removed for precracked specimens with P=20Kg.

Fracture toughness K_{IC} of the precracked specimen was approximately 3.8MPa·$m^{1/2}$ before it was ground, and K_{IC} =5.1, 6.0 and 6.3MPa·$m^{1/2}$ when it was ground to a depth of 50, 70 and 90μ or more, respectively, from which it was judged that residual stress could be removed if the precracked specimen was ground to a depth of 90μm or more. So as a result the specimen was ground to a depth of 100μm. Depth C of the precrack on the ground specimen was 100μm, estimated from the initial crack depth, which was almost the same as the crack depth C=90μm of the precracked specimen under a load of P=5kg, having a precrack length of 2C=180μm. Petrovic et al.[14] and Yamauchi et[15] al. report that residual stress can be removed when the specimen is ground to a depth 3 times that of a Knoop indentation, whereas Kishimoto et al.[8] report a depth of 7 times. The ground depth of 90μm found in this study was roughly 4 times that of the indentation depth of 23μm. The removed depth, therefore, is considered adequate, though a Vickers indenter is different from a Knoop indenter.

Figure 5 shows the cyclic fatigue behavior of as-indented specimens (2C: 180μm) and the ground specimens tested under the cyclic loading (10Hz, R=0.1). The fatigue characteristic curves of both sample types are represented by a reverse S-shape, with a fatigue parameter of n=27 for the as-indented specimens and n=32 for the ground specimens. These specimen types are similar to each other in fatigue behavior, though different in fracture stress level. Therefore, it may be concluded that fatigue behavior of precracked specimens is unaffected by residual stress generated by a Vickers indenter.

3.2.3. Effects of Precrack Length

It was discussed in Section 3.2.1 that the smooth specimen was clearly different from the specimen with 180μm long precrack in fatigue behavior. Then, fatigue behavior of specimens with smaller precracks was investigated. It was confirmed, as discussed in Section 3.2.2, that fatigue behavior was unaffected by residual stress, and hence Vickers load applied to each specimen was changed to decrease the precrack size from 180 to 40 and 20μm. The SEM analysis of the fracture surfaces indicated that all of these precracks were median cracks.

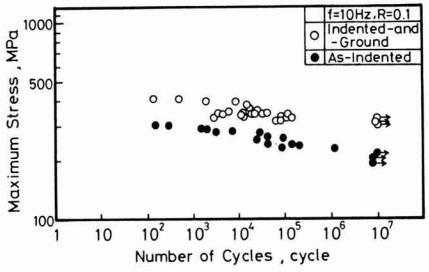

Fig. 5. Comparison of cyclic fatigue behavior between indented-and-ground and as-indented specimens.

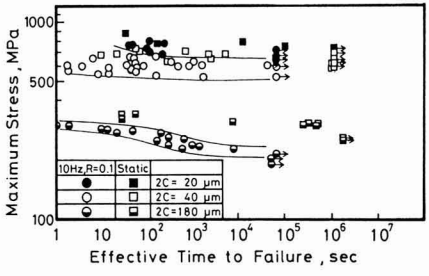

Fig. 6. Fatigue behavior of precracked specimens with different precrack sizes.

Figure 6 presents the static and cyclic test (10Hz, R=0.1) results, showing the effective time to failure as a function of maximum stress for the precracked specimens of varying precrack length. Difference between static and cyclic behaviors of the specimens with a precrack length of 40μm was smaller than that of the specimen with a precrack length of 180μm, and the difference of the specimens with a precrack length of 20μm was even smaller. Thus, decreasing precrack length decreased the effects of cyclic loading on fatigue behavior, and hence the difference between the static and cyclic behaviors. The precrack was found to serve as the fracture origin in all the specimens except a few specimens with a precrack length of 2C=20μm. The fatigue life data of the specimens with precrack length of 2C=20μm and 40μm were more widely scattered than those of the other specimens. The microstructures of the specimens prepared in this study consisted of small grains around 1μm and the columnar grains of about 10μm at the longest. **Figure 7** presents the back-scattered electron image of the precracked specimen pressed by a Vickers indenter under a load of P=500g (precrack length: 40μm). The precracks extending in all directions had varying lengths, on account of the columnar grains dispersed in the specimen, which conceivably caused the wider scatter in its effective time to failure. Kishimoto et al. report that a short crack propagates so slowly that its propagation behavior can not be estimated from the propagation data for long cracks. They consider a long precrack to be 20mm or more in length, and a short one 350μm or so. According to their classification, the precracks on the specimens prepared in this study are still shorter than the short precracks. The present study indicated that the specimens with long cracks and short ones and the smooth specimen are different from each other in fatigue behavior.

The detailed SEM analysis of the fracture surfaces of the fatigue-tested specimens showed no fragments sticking to

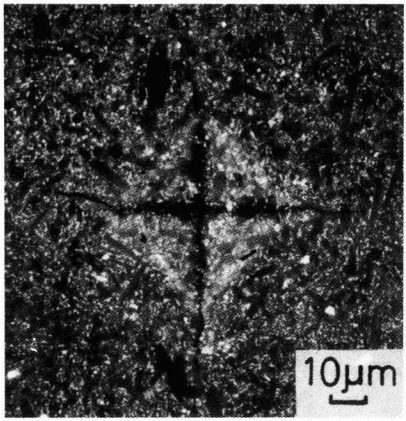

Fig. 7. SEM micrograph (backscattered electron image) of precracks due to Vickers indentation at P=20Kg.

the surfaces, unlike the observations by Kishimoto et. al.[18] and Tanaka et. al.,[16] nor evidence to suggest a difference between the fracture surfaces of static and cyclic tested specimens.

Many researchers have proposed various mechanisms to explain the accelerated fatigue phenomena under cyclic loading, such as the effects of residual stress present in the specimen,[17] sticking of the fragments to the surfaces,[10] non-conformation of the fractured surfaces (indentation-induced damages),[17] and the effects of non-linear process zones at the crack tips,[18] and so on. No evidence, however, was found in this study to support these hypotheses.

The results of this study show a dependence of fatigue behavior on precrack length and have suggested still another mechanism related to the R-curve behavior. Maniette et al. observe the R-curve behavior with material similar to those used in this study, proposing the grains bridging at the crack wake.[19] Difference between the specimens tested under the cyclic and static conditions may be explained by assuming that the grain bridging effects are reduced under cyclic loading. The authors plan to further investigate the crack propagation behavior in order to confirm the validity of this hypothesis.

4. Conclusions

Fatigue behavior at room temperature in gas pressure sintered silicon nitride was investigated.

1) The smooth specimen was significant by different from the specimen with a large precrack in fatigue behavior; the former specimen showed time-dependent type behavior, whereas the precracked one with a precrack of 2C=180μm showed behavior dependent on the number of load cycles, in which the effects of stress ratio was noted.
2) Residual stress in the precracked specimen, generated by pressing a Vickers indenter under a load of 30kg, could be removed by grinding the specimen to a depth of 90μm.
3) Residual stress, generated by pressing a Vickers indenter, had no effect on the fatigue behavior of precracked specimens.
4) The effects of the cyclic loading decreased as precrack length decreased. (The results were presented to the second Ceramic Society of Japan fall symposium, October, 1989)

References:

1) Y. Hattori, Kino Zairyo, 9, 32-42 (1989).
2) Y. Tajima, K. Urashima, M. Watanabe and Y. Matsuo, Ceramic Materials and Components for Engines, (1988) pp.719-728.
3) A. Ohtsuka, Y. Ishihara and K. Togo, The Materials Society of Japan's Fatigue Symposium Proceedings, 1988.
4) M. Masuda, T. Soma, M. Matsui and I. Oda, Seramikkusu Ronbunshi, 96, 277-283 (1988).
5) M. Masuda, N. Yamada, T. Soma, M. Matsui and I. Oda, Seramikkusu Ronbun-shi, 97, 520-524 (1989).
6) Y. Yamauchi, K. Sakai, M. Ito, T. Ohtsukasa, W. Kanematsu and M. Ito, Report of Government Industrial Research Institute, Nagoya, 35, 179-184 (1986).
7) T. Kawakubo, K. Komeya, J. Am. Ceram. Soc., 70, 400-405 (1987).
8) Y. Yamauchi, K. Sakai, M. Ito, T. Ohji, W. Kanematsu and M. Ito, Report of Government Industrial Research Institute, Nagoya, 35, 325-330 (1986).
9) H. Kishimoto, A. Ueno and H. Kawamoto, Zairyo, 36, 1122-1127 (1987).
10) H. Kishimoto, A. Ueno, H. Kawamoto and Y. Fujii, Zairyo, 38, 1212-1217 (1989).
11) A. Ueno, H. Kishimoto, H. Kawamoto and H. Mori, 5th Fracture Mechanics Symposium Proceedings, 6-10 (1989).
12) H. Kishimoto, A. Ueno, H. Kawamoto, Y. Fujii and M. Asakura, 5th Fracture Mechanics Symposium Proceedings, 16-20 (1989).
13) J.C. Newman, Jr. and I.S. Raju, "Analyses of Surface Cracks in Finite Plates under Tension or Bending Loads" in NASA Technical Paper 1578 (1979).
14) J.J. Petrovic, R.A. Dirks, L.A. Jacobson, and M.G. Mendiratta, J. Am. Ceram. Soc., 59, 177-178 (1976).
15) Y. Yamauchi, K. Sakai, M. Ito, M. Ito, T. Ohji and W. Kanematsu, Government Industrial Research Institute Nagoya Symposium, 38, 84-85 (1985).
16) T. Tanaka, N. Okabe and Y. Ishimaru, Zairyo 38, 137-143 (1989).
17) S. Horibe Iron and Steel, 75th, Vol.4, 578-586 (1989).
18) H. Kobayashi and T. Kawakubo, Bull of Japan Inst. of Metals, 27, 757-765 (1988).
19) Yves Maniette, M. Sakai and M. Inagaki, Ceramic Society of Japan Annual Meeting Proceedings, 458 (1990).

This article is a full translation of the article which appeared in Nippon Seramikkusu Kyokai Gakujutsu Ronbunshi (Japanese version), Vol.99, No.4, 1991.

Influence of Alcoholic Solvent on Formation of Monodispersed Particles by Hydrolysis of Zirconia Tetra-n-butoxide

Lee Seok-Keun, Masaki Ikeda* and Nobuyasu Mizutani

Department of Inorganic Materials, Faculty of Engineering, Tokyo Institute of Technology
2-12-1, O-okayama, Meguro-ku, Tokyo 152, Japan
*Nippon Light Metal Co., Ltd.
4025-1, Miho, Simizu-shi, Sizuoka 424, Japan

The influence of chain length and molecular structure of alcoholic solvent on the hydrolysis behavior of zirconium tetra butoxide (ZBu) and morphology of product particles was investigated.
ZBu dissolved in alcoholic solvents except methanol. Monodispersed zirconia particles with submicron size were obtained in the range of water to ZBu molar ratio of 1.6-2.5 in ethanol and 2.1-2.2 in propanol. In contrast, in alcohols with longer chain lengths than butanol, a mixture of agglomerates and large spherical particles was obtained. The formation of the mixture was related to induction time and hydrolysis rate of ZBu.
On the other hand, an increase in the number of carbon branches in butanol increases the amount of agglomerates.
[Received September 21, 1990; Accepted December 14, 1990]

Key-words: Synthesis, Hydrolysis, Alkoxide, Solvent, Monodispersed particle, Zirconia

1. Introduction

The sintering rate for submicron particles is accelerated due to an increase in the driving force of the sinter caused by the surface effects, enabling the preparation of ceramics at a lower temperature and in a shorter time. Barringer et al. obtained a highly dense sintered body at several hundred degrees below the conventional temperature of 1300 to 1400°C, using TiO_2 particles of 0.35μm in diameter.[1] Such fine particles, on the other hand, tend to agglomerate with each other due to the increasing adhesive force. It is therefore necessary to liberate the particles from agglomeration so as for each particle to sinter independently. Rhodes produced a body formed in a close agreement with the theoretical value of the closest packing, using starting powders of agglomeration-free, monodispersed YSZ particles.[2]

The synthesis of monodispersed particles from metal alkoxides, which has recently been drawing attention from the above viewpoint, has been carried out successfully with not only SiO_2,[3] but also TiO_2,[4] ZrO_2,[5,6] Y-doped ZrO_2,[7] B-doped SiO_2,[8] Ta_2O_5.[9,10] $SrTiO_3$.[11], and PZT.[12,13] A variety of parameters, such as the type and concentration of metal alkoxide, the type of solvent, water concentration, the aging temperature and time duration, are involved in the synthesis of those monodispersed particles, of which the solvent type is considered to be one of the most influential factors. A solvent must dissolve both alkoxide and water. A number of solvents satisfy this condition, but ethanol is most frequently used.

Stöber et al. have synthesized monodispersed, amorphous, spherical silica particles from combinations of different silicon alkoxides and alcohols.[3] It was found that the hydrolytic rate became slower in the order of methanol, ethanol, n-propanol, and n-butanol. Moreover, it was discovered that the size of particles obtained under nearly the same conditions was the smallest in the case of methanol and the largest for n-butanol. Nevertheless, the particle distribution had a tendency to become wider as the higher alcohol was used. A solvent consisting of methanol and butanol in a ratio of 1:1 produced uniform and also large particles. Bowen et al. synthesized $SrTiO_3$, from a composite alkoxide of Sr and Ti, using a mixed solvent of n-butanol and acetonitrile[11]. This was not possible with the use of ethanol.

It is therefore suspected that the solvent type greatly affects the hydrolytic rate and the size of the particles formed and, moreover, largely influences whether the formation of monodispersed particles is possible or not.

Accordingly, the present study is intended to investigate the effects of the carbon chain length and branching of solvent alcohols on the hydrolytic and condensation polymerizing reactions of alkoxide and also on the morphology of the particles formed, taking the synthesis of zirconia particles as an example.

2. Experimental Procedure

2.1. Sample preparation

Zirconium tetra butoxide (hereinafter referred to as ZBu), manufactured by Soegawa Rikagaku, was dissolved in seven different alcohol solvents: methanol, ethanol, n-propanol, n-butanol, n-pentanol, n-hexanol, and n-heptanol to produce seven solutions (0.1mol/l), while redistilled water was added to each of these solvents (0.1 to 0.6mol/l). The two solutions having the same solvent were then mixed at room temperature and hydrolyzed. Furthermore, in order to investigate the effects of the branching of alcohols, hydrolysis was conducted in each of the four isomers (n-, i-, sec-, and tirt-) of butanol. Because water is insoluble in n-hexanol and n-heptanol, a small amount of ethanol (approximately 2vol%) was added to these alcohols, in which water was then dissolved. **Table 1** gives the solubilities of water

and alkoxide in each alcohol. Each alcohol had been pretreated by passage through a molecular sieve (3Å, Wako Junyaku) to reduce moisture to 50ppm or less. The precipitates thus obtained were aged in water at 50°C for 5h. Solid part was then separated by a centrifuge and dried at 60°C for 12h to obtain products.

2.2. Measurement of Induction Time

When water is added to an alkoxide diluted with a solvent, hydrolysis occurs and the mixed solution begins to become turbid. This is a visual condition in which the solution assumes a milky color, and such a period will be referred to as induction time A. According to Shimohira et al.,[14] induction time A represents the phenomenon up to the time when nuclei several hundred Å in size, formed by the hydrolysis of an alkoxide, combine or agglomerate. In other words, it represents the point in time at which the first visual recognition is made of the fact that the particles formed by the hydrolysis scatter light and hence reduce the intensity of the light transmitting through the solution (Tyndall phenomenon). With passage of time, the solution gradually changes its color to deep milk-white and, some time later, no longer allows the transmission of light. In order to examine the behavior of hydrolysis, therefore, measurements were made of the induction time A and the time duration till the milk-white color of the solution becomes deep enough to prevent light to transmit through the solution and a mark on the bottom of the 30mm thick solution layer becomes invisible (this will be referred to as induction time B). Although induction time A and B were affected considerably by subjective fractors, the repeatability was checked to find that the disparity was within a range of 10%.

Table 1. The solubility of zirconium tetra-*n*-butoxide (ZBu) and water (H_2O) in alcohols used as solvents.

solvent	ZBu	H_2O	b. p. (°C)
methanol	×	○	64.7
ethanol	○	○	78.3
propanol	○	○	97.2
butanol	○	○	117.3
pentanol	○	△	138.0
hexanol	○	×	157.1
heptanol	○	×	176.2

○ soluble, △ little soluble, × insoluble

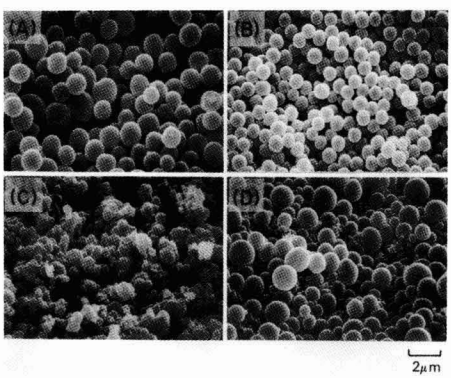

Fig. 1. SEM photographs of ZrO_2 particles prepared by hydrolyzing zirconium tetra-*n*-butoxide (ZBu); (A) H_2O/ZBu=1.3 in ethanol, (B) H_2O/ZBu=1.8 in ethanol, (C) H_2O/ZBu=3.5 in ethanol, (D) H_2O/ZBu=4.4 in butanol.

2.3. Evaluation of the Samples

The shapes of particles and their agglomerated states were observed by a scanning electron microscope (SEM, JEOL, Model JSM-T200). For the determination of the average size of the monodispersed particles, 400 particles were randomly selected from the SEM photograph and their diameters were measured by a digitizer to obtain the average value. The product yield was found by dividing the weight of the synthesized powder after calcination at 1000°C for 1h by the theoretical yield computed from the alkoxide concentration, with the purity of the alkoxide being assumed to be 100%.

3. Results and Discussions

3.1. Effects of Solvents on Product Morphology

3.1.1. Ethanol and Propanol

ZBu did not dissolve in methanol even when it was heated to near its melting point (64.7°C). **Figure 1** presents the typical SEM photographs of products obtained from ZBu hydrolyzed and condensation-polymerized in alcohols having the straight-chain alkyl group. The product morphology falls into three general categories: spherical particles (Fig.1 (A) and (B)), agglomerated particles (Fig.1 (C)) and a mixture of superfine particles agglomerated into complex shapes and relatively large spherical particles (Fig.1

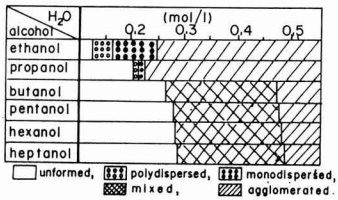

Fig. 2. Effect of the amount of water on the morphology of particles prepared in various alcohols.

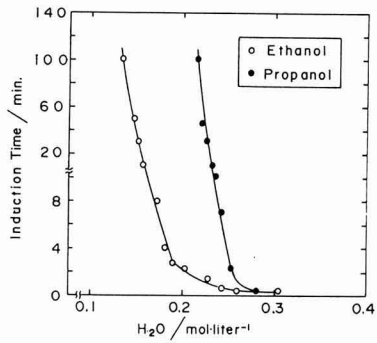

Fig. 3. The relation of induction time A and water concentration in ehanol and propanol.

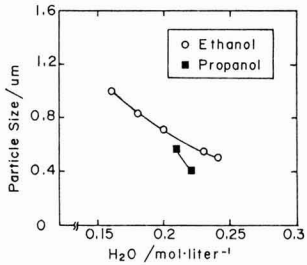

Fig. 4. The relation of particle size and water concentration of ethanol and propanol.

(D)). The spherical particles are further subdivided into two groups: spherical polydispersed particles of different sizes (Fig.1 (A)) and monodispersed particles of a uniform size (Fig.1 (B)). **Figure 2** shows the ranges for the formation of each type of particles associated with changes in the water concentration in each solvent. It is seen that ethanol and propanol are very different from other alcohols in the formation pattern of products associated with an increase in the water concentration. Ethanol and propanol did not produce any precipitate as the water concentration levels were below 0.12mol/l and 0.21mol/l, respectively; above these levels, products were formed but shifted from polydispersed to monodispersed, and then to agglomerated paticles as the water concentration increased. As shown in Fig.2, ethanol provides a fairly wide range in which spherical particles are formed and also a relatively wide range where monodispersed particles are formed. In contrast, propanol only provides very narrow ranges near 0.22mol/l where spherical and monodispersed particles are obtained.

Figure 3 shows the relationship between water concentration and induction time A for each solvent. It is seen from Fig.3 that the induction time A of propanol is more dependent on water concentration than that of ethanol, at a constant ZBu concentration of 0.1mol/l. In the case of ethanol, induction time A up to the time of the formation of monodispersed particles falls in a range of 90 to 900 sec. When induction time A is shorter than this optimal range, hydrolysis occurs more quickly and an excessive number of nuclei are formed. These nuclei then combine with each other to form agglomerates, as shown in Fig.1 (C). If it is longer, on the other hand, the period for the nucleus formation has a certain time width, so that the nucleus formation and particle growth can proceed simultaneously to form polydispersed particles as shown in Fig.1 (A).[15]

Figure 4 shows the relationship between water concentration and the average particle size which was obtained from SEM photographs of monodispersed particles produced by ethanol and propanol. The size of all the monodispersed particles is smaller than a micron, and tends to decrease as the water concentration increases in both cases. This is presumably because an increase in water concentration increases the relative number of nuclei formed by the hydrolysis and also the yield, thereby limiting the size of the particles finally obtained.

3.1.2. Butanol and Higher Alcohols

The addition of water to ZBu dissolved in any solvent, other than ethanol and propanol, makes the solution turbid instantaneously so as to make the measurement of induction time A impossible. Taking butanol as an example, no turbidity occurs at a water concentration below 0.27mol/l; above this level, turbidity always takes place as soon as water is added. The suspension thus formed is unstable and tends to sedimentate in several minutes. In other words, induction time A is always zero at a water concentration above 0.27mol/l. When the hydrolytic rate is very high, agglomerates are generally obtained. However, in the case of solvent alcohols having 4 carbon atoms (butanol) or more, mixed particles or agglomerates are obtained. Although the formative ranges of products are affected by the type of solvent alcohol, all the formation patterns are the same: from no products to a mixture and to agglomerates, in succession. Of particular interest among these formations is the mixture of large spherical particles and agglomerates of ultrafine particles. In order to investigate the process for the formation of such a mixture in more detail, the sedimentation part and the suspension part of a solution with butanol as a solvent were separated and observed. The results are shown in **Fig.5**. Figure 5 (A), (B), and (C) represent SEM photographs of products obtained by first adding water to alkoxides, aging the solutions for 10 min, 1h, and 5h, respectively, separating the sedimentation parts and the suspension parts of the solutions, centrifuging each part and finally drying them at 60°C. The tiny particles seen in the photographs of the products in the suspension parts (left side of Fig.5) are the same in shape as those found in the sedimentation parts (right side of Fig.5), so that they are considered to be particles strayed in from the sedimentation parts at the time of the separation process. It is seen from Fig.5 that the particles in the sedimentation parts are totally different in shape from those in the suspension parts. Those particles in the suspension parts grow quickly, measuring 0.5 to 0.8μm in 10 min, 1 to 1.2μm 1h later, and 1.5μm after 5h. Moreover, the size of the particles at each time stage is uniform to a certain extent, although there are a few fine particles of around 0.2μm mixed in. In contrast, the size of the particles agglomerated in the sedimentation parts tends

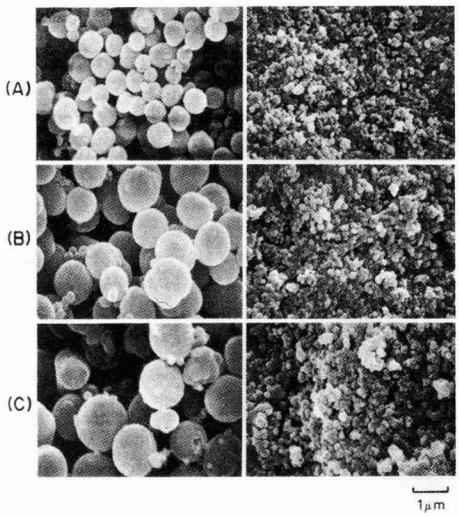

Fig. 5. SEM photographs of particles prepared by hydrolyzing zirconium tetra-*n*-butoxide at H_2O/ZBu=4.0 in butanol having various aging time; (A) 10 min, (B) 1 h and (C) 5 h.
Left: suspension part, right: sedimentation part

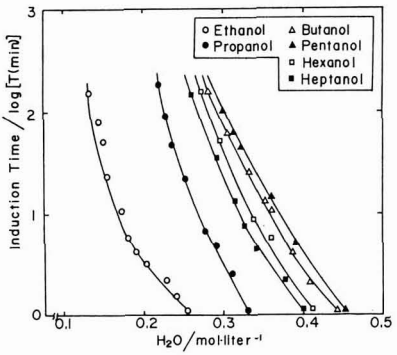

Fig. 6. The relation of induction time B and water concentration in various alcohols.

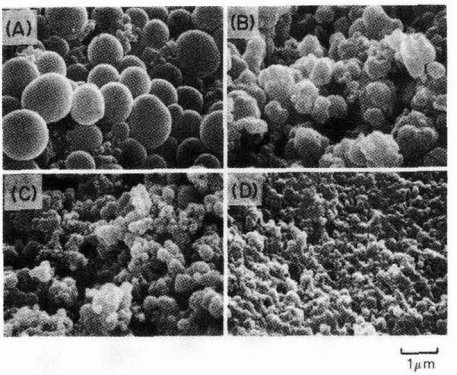

Fig. 7. SEM photographs of particles prepared by hydrolyzing zirconium tetra-n-butoxide at $H_2O/ZBu=4.4$ in (A) n-butanol, (B) sec-butanol, (C) iso-butanol and (D) tert-butanol.

to increase as time elapss, but remains less than 0.2μm after 5h. In other words, the particles in a suspension part grow quickly and continue to grow thereafter, whereas those in a sedimentation part are small and agglomerate with each other, so that the growth of the particles hardly occurs. An attempt has been made to explain this phenomenon, based on limited data. The addition of water causes abrupt hydrolytic reactions to take place to form a large number of nuclei. For this reason, these collide with each other to form clusters. These clusters then grow to a size of 0.1 to 0.2μm, and precipitate by agglomeration. In the suspension part of the solution thus precipitated, there exist nuclei which did not participate in any cluster or particles whose clusters did not grow sufficiently large, with the density of nuclei and particles being probably low. In this portion, the growth of the particles occurs while the solute is eing ingested, and the particles continue to grow without agglomeration. It is not clearly understood why such phenomenon occurs with butanol or higher alcohols; however, there are some experimental results concerning water concentration, as described below. **Figure 6** shows the relationship between water concentration and induction time B for each solvent. The tendency of induction time B to decrease as water concentration increases is the same, irrespective of the type of solvent used; moreover, the slop of all the curves are not very different. It is also noted that alcohols having more carbon atoms than ethanol need a larger amount of water to make the solutions turbid. From the viewpoint of yield, a water amount of 0.23mol/l gave a product yield of 70% for ethanol, which compares with 0.37 to 0.40mol/l at a yield level of also 70% for butanol and higher alcohols. In other words, butanol and higher alcohols require considerably more water than ethanol to obtain the same yield.

3.2. Effects of Branching on Product Morphologies

Solvents such as n-, sec-, iso-, and tert-butanol were used to investigate the effects of branching on hydrolytic behavior and product morphologies. **Figure 7** presents SEM photographs of the products. In the case of n-butanol, a mixture consisting of particles and minute agglomerates were formed as shown in Fig.7 (A), but the other branching isomers produced only agglomerates in the entire ranges. Moreover, these agglomerates assume a composition consisting of fine particles and the agglomeration tends to accelerate, as the number of alkyl group branches increases. These results have suggested that alcohols having no branches are appropriate for synthesizing fine particles.

4. Conclusions

The authors have investigated the effects of carbon chain length and branching of solvent alcohols on hydrolytic and condensation-polymerizing reactions of zirconium tetra butoxide, and examined the morphologies of the products, with the following results:

1) Ethanol and propanol gave no products, polydispersed, monodispersed, and agglomerated particles in that order as water concentration increased. The size of all the monodispersed particles was below a micron, and tended to decrease, as water concentration increased.
2) Butanol and higher alcohols hydrolyzed zirconium tetra butoxide much faster than ethanol. All the product patterns had no products, a mixture, and agglomerates in that sequence as water concentration increased. Moreover, this mixture consisted of relatively uniform and large spherical particles and agglomerates of fine particles measuring less than 0.2μm; the former coming from the suspension part of the hydrolyzed solution and the latter from the sedimentation part.
3) As the number of alkyl group branches of an alcohol increases, the agglomeration accelerates and becomes more minute. Accordingly, alcohols having no branches are considered appropriate for the synthesis of particles.

References:

1) E.A. Barringer and H.K;. Bowen, J. Am. Ceram. Soc., 65, C199-201 (1982).
2) W.W. Rhodes, ibid., 64, 19-22 (1981).
3) W. Stöber, A. Fink and E. Bohn, J. Colloid Interface Sci., 26, 62-69 (1968).
4) B. Fegley Jr. and E.A. Barringer, "Better Ceramics Through Chemistry," Elsevier New York, (1984) pp.187-97.
5) E.A. Barringer, N. Jubb, B. Fegley Jr., P.L. Pober and H.K. Bowen, "Ultrastructure Processing of Ceramics, Glasses and Composites," John Wiley & Sons, New York, (1984) pp.315-33.
6) T. Ogihara, N. Mizutani and M. Kato, Ceramics International, 13, 35-40 (1987).
7) K. Uchiyama, T. Ogihara, T. Ikemoto, N. Mizutani and M. Kato, J.

Mater. Sci., 22, 4343-47 (1987).
8) N. Jubb and H.K. Bowen, J. Mater. Sci., 22, 1963-70 (1987).
9) K. Nakanishi, Y. Takamiya and K. Shimohira, Yokyo, 94, 1023-28 (1986).
10) T. Ogihara, T. Ikemoto, N. Mizutani and M. Kato, J. Mater. Sci., 21, 2771-74 (1986).
11) A.B. Hardy, G. Gowda, T.J. Mcmahon, R.E. Riman, w.E. Rhine and H.K. Bowen, "Ultrastructure Processing of Advanced Ceramics," John Wiley & Sons, New York, (1987) pp.407-28.
12) I. Kakegawa, J. Mouri, K. Imai, S. Shirasaki and K. Takahashi, Journal of the Chemical Society of Japan 692-97 (1985).
13) T. Ogihara, H. Kaneko, N. Mizutani and M. Kato, J. Mater. Sci. Lettter, 7, 867-72 (1988).
14) K. Shimohira, H. Ishijima, Journal of the Chemical Society of Japan, 1503-5 (1981).
15) T. Ikemoto, K. Uematsu, T. Mizutani, S. Kato, Yokyo, 93, 261-66 (1985).

This article is a full translation of the article which appeared in Nippon Seramikkusu Kyokai Gakujutsu Ronbunshi (Japanese version), Vol.99, No.4, 1991.

Preparation of $Y_{1-x}Ca_xBa_2Cu_{4DO8}$ ($0 \leq x \leq 0.1$) Superconductor Films by the Dipping-Pyrolysis Process

Takaaki Manabe, Wakichi Kondo, Susumu Mizuta and Toshiya Kumagai

National Chemical Laboratory for Industry
1-1, Higashi, Tsukuba-shi, 305, Japan

Superconducting $YBa_2Cu_4O_8$ (1-2-4) films were prepared by the dipping-pyrolysis process, and the effects of heat-treatment conditions and partial-substitution of Y for Ca on the product films were investigated by XRD,SEM and resistance measurement. Films of the 1-2-4 phase with $T_{c,zero}$=70 and 55K were prepared by direct heat-treatment of (Y_2O_3-$BaCO_3$-CuO) precursor films (Y:Ba:Cu=1:2:4 in molar ratio) in O_2 at 780°C for 24-72h followed by slow-cooling and quenching, respectively. Both films showed metallic behavior above the transition temperatures, indicating the formation of the 1-2-4 phase. However, once a mixture of $YBa_2Cu_3O_7$ (1-2-3) and CuO was formed by heat-treatment at 820°C ($p(O_2)$=10^{-3} atm) or at 700°C ($p(O_2)$=10^{-2} ~ 10M^-4 atm), conversion into the 1-2-4 phase was very difficult after the subsequent heat treatment within the stability region (780°C, $p(O_2)$=1 atm) of the 1-2-4 phase. The Y_{1-x}Ca-MIx$Ba_2Cu_4O_8$ (x=0.05 and 0.1) films exhibited higher $T_{c,onset}$ values, however, the film of x=0.1 was found to contain only a small fraction of the 1-2-4 phase. Moreover, when the precursor films containing Ca were fired in an atmosphere with $p(O_2)$ of 10^{-3}~10^{-4} atm at 700°C, the product films gave an XRD pattern of (1-2-3) + (1-2-4) mixture.

[Received October 1, 1990; Accepted December 14, 1990]

Key-words: Dipping-pyrolysis process, $YBa_2Cu_4O_8$, $YBa_2Cu_3O_7$, Superconductor, Film, Ca-addition.

1. Introduction

$Y_1Ba_2Cu_3O_7$ (hereinafter referred to as 1-2-3), $Y_1Ba_2Cu_{3.5}O_{7.5}$ and $Y_1Ba_2Cu_4O_8$ (hereinafter referred to as 1-2-4) are the known three kinds of superconductors of the Y-Ba-Cu-O system. Although 1-2-3 is a superconductor of 90K class, it releases or absorbs oxygen when heated or cooled because of its nonstoichiometry, causing at the same time the orthorhombic-tetragonal transition changing its superconductive properties. For this reason attention has gradually focused on the stable superconductivity of 1-2-4, a superconductor of the 80K class, since almost no oxygen is released even when heated to 800°C.[1)]

The 1-2-4 was originally found as a structural defect in the 1-2-3 phase, whose bulk was successfully synthesized thereafter[1)] under high pressure, while same reports have been published recently on the product synthesis at ambient pressure.[3,4)] The *P-T* (pressure-temperature) diagram of the 1-2-4-(1-2-3+CuO) system has gradually been made clear.[5-8)] Furthermore, it was found recently that superconducting transition temperature T_c can be improved up to 90K when the carrier concentration is changed by partially substituting Y for Ca in the 1-2-4.[9)]

This paper deals with the results of our study in which an attempt was made to prepare, the 1-2-4 films by the dipping-pyrolysis process; using metal acetylacetonates as the starting materials, to investigate the effects of various heat-treatment conditions and Ca- addition on the films thus synthesized. As can be expected from the *P-T* diagram of 1-2-4, the problems in synthesizing the 1-2-4 at ambient pressure are its decomposition at high temperature, while its formation reaction hardly progresses due to slow decomposition of $BaCO_3$ at lower temperatures. Thus, we have used the following 3 methods for preparing the 1-2-4 films by heat treatment of the mixed films of (Y_2O_3-$BaCO_3$-CuO) obtained by prefiring up to 500°C.

1) Method of synthesizing the 1-2-4 films directly from the prefired films.
2) Method of synthesizing (*c*- axis-oriented 1-2-3 + CuO) films at 820°C before converting them to 1-2-4 films.
3) Method of synthesizing (micro 1-2-3 + CuO) films before converting them to 1-2-4 films.

The above methods (2) and (3) are the 2-stage heat-treatment method utilizing the results of our recent study on the preparation of 1-2-3 films, in which with the dipping-pyrolysis process under low oxygen partial pressure (10^{-2}~10^{-4}atm) (a) *c*-axis-oriented 1-2-3 films at 820~880°C and (b) 1-2-3 films consisting of fine particles at 700~750°C are obtained. The samples were also prepared by quenching of the films prepared by method (1) to ascertain whether the superconductive properties are attributable to the formation of the 1-2-4 phase.

2. Experimental Method

Metal acetylacetonates were used as the starting materials for the preparation of coating solutions by approximately the same way referred to in the previous paper.[10)] After acetylacetonates of Y, Ba, and Cu (Y:Ba:Cu=1:2:4 in a molar ratio) were dissolved in a mixture of pyridine and propionic acid, most of the solvent was removed by a rotary evaporator, and the residue was dissolved in methanol to obtain a green-colored homogeneous solution. Ca-containing solutions were prepared by partially substituting Y acetylacetonate, the starting material, for Ca acetylacetonate, and a solution of Y:Ca:Ba:Cu=1-*x*:*x*:2:4 (x=0.05, 0.1) in a molar ratio was prepared by the similar method.

These solutions were spin-coated on yttria-stabilized-zirconia (YSZ) substrates (Y_2O_3: 3mol%, 25x25x0.7mm^3) at 2000rpm for 5s and heated up to 500°C in air at a rate of 20°C/min. This procedure was repeated several times to

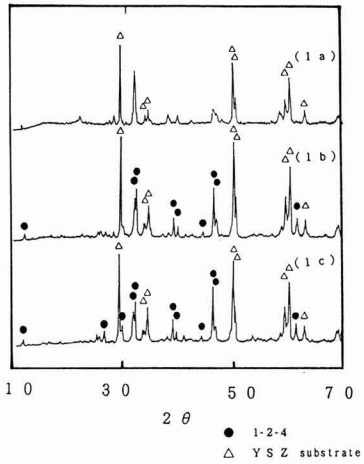

Fig. 1. X-ray diffraction patterns of 1-2-4 films heat-treated in O_2 at 780°C for (1a) 3h, (1b) 24h and (1c) 48h.

prepare prefired films of 2~3128um in thickness. The prefired films are a mixture of (Y_2O_3-($CaCO_3$)-$BaCO_3$D-CuO) with lower crystallinity. After these films were cut into pieces about 6×10mm^2 in size, they were placed on a platinum boat fastened to a thermocouple and heat-treated in a tube furnace under the following conditions to obtain product films.

1) Method of synthesizing the 1-2-4 films directly from the prefired films.

The precalcined films were heat-treated in oxygen at 780°C for 3h, 24h or 48h before furnace cooling.

2) Method of synthesizing the (*c*-axis-oriented 1-2-3 + CuO) films before converting them to 1-2-4.

After the precalcined films were heat-treated at 820°C, $p(O_2)=10^{-3}$ atm, for 1h, the atmosphere switched to oxygen was retained for 0.5h before furnace cooling. These films were further heat-treated in oxygen at 780°C for 24h, 48h or 72h before furnace cooling.

3) Method of synthesizing the (micro 1-2-3 + CuO) films before converting them to 1-2-4.

After the precalcined films were heat-treated at 700°C, $p(O_2)=10^{-2}$, 10^{-3}, or 10^{-4} atm, they were cooled in a furnace, and these films were again heat-treated in oxygen at 780°C for 24h before furnace cooling.

Oxygen partial pressure, $p(O_2)$, for the above heat-treatment methods (2) and (3) was adjusted by allowing the mixed gas of Ar + O_2 in an appropriate concentration to flow through the furnace tube and the $p(O_2)$ was monitored at the exit of the furnace tube using a zirconia-type oxygen analyzer.

Finally, in an attempt to confirm that superconductive properties of the films prepared by the above method are attributable to the formation of the 1-2-4 phase, quenched samples were prepared by the following method and compared with those furnace-cooled.

4) Method of quenching the 1-2-4 films prepared by method (1) after re-heat-treatment.

As mentioned later, the above method (1) was found to be most suitable to the formation of 1-2-4 films. After the 1-2-4 films prepared by this method (heat-treated for 48h) were re-heat-treated in oxygen at 780°C for 24h, the product film together with the platinum boat was taken out of the furnace for quenching.

On the films prepared by the above methods the product phases were identified by X-ray diffraction (XRD), the resistance was measured by the DC 4-terminal method, and the film texture was observed by scanning electron microscopy (SEM).

3. Results and Discussion

3.1. Method of Synthesizing the 1-2-4 Films Directly in Oxygen at 780°C From the Prefired Film

Figure 1 shows the XRD patterns of films after heat-treatment. In film (1a) the starting materials such as $BaCO_3$ were found to have disappeared due to decomposition after 3h of heat treatment. The peaks of the superconductive phase were observed at 2θ=32.8° etc. These peaks were rather broad, and whether it was 1-2-4 or 1-2-3 was not determined. Since the characteristics of 1-2-4 (for instance, the existence of peaks at 13.0° (004) and 39.5° (0012)) could not be recognized, it was more or less similar to the pattern of 1-2-3. On the other hand, the single-phase XRD pattern of 1-2-4 was obtained in films (1b) and (1c) fired for 24h and 48h, respectively.

When the resistance of these films was measured, film (1a) showed semiconductive behavior in the normal state and no zero resistance was obtained at a temperature above 50K, while the films of both (1b) and (1c) showed metallic behavior, for which $T_{c,onset}$=80K and $T_{c,zero}$=70K were obtained. The results on film (1c) are shown in **Fig.2.**

Next, the Ca-containing films ($Y_{1-x}CaxBa_2Cu_4O_8$(x=0.05 and 0.1)) were also heat-treated in oxygen at 780°C. As for the films of x=0.05 (1d), the results of X-ray diffraction showed the formation of 1-2-4 when calcined for 24h in the same way as in the case where Ca was not added, while the crystallinity of the film (1e) of x=0.1 was poor even after calcination for 48h, and only the 1-2-4 films with weaker diffraction peaks than films of x=0 and 0.05 were obtained.

Figure 2 shows the results of resistance measurement of the films that were calcined for 48h. Although $T_{c,onset}$ of the films, (1d) of x=0.05 and (1e) of x=0.1, were improved, their superconductive transition was broad and had a tailing; values of $T_{c,zero}$ were found to be 69K and 55K, respectively. These results show that when 10% of Ca was added and heat-treated in oxygen at 780°C for 48h the formation of 1-2-4 was minor as indicated by XRD analysis, and that

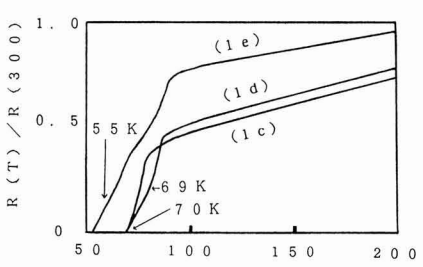

Fig. 2. Resistance vs. temperature relationship for Ca-substituted 1-2-4 films heat-treated in O_2 at 780°C for 48h before being furnace-cooled: (1c) x=0, (1d) x=0.05 and (1e) x=0.1, where Y:Ca:Ba:Cu=1-x:x:2:4 in molar ratio.

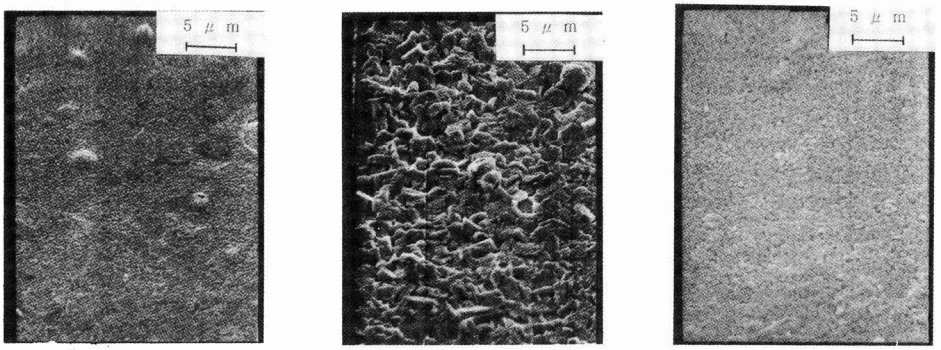

Fig. 3. Typical scanning electron micrographs of free surfaces of 1-2-4 films; A:(1c), B:(2c) and C:(3c').

$T_{c,zero}$ had also notably declined. The reason why $T_{c,onest}$ was improved in the films containing Ca will be discussed later together with the results of heat treatment (4), because it is difficult to determine from the results shown in Fig.2, whether it was caused by incorporation of Ca in 1-2-4 phase forming a solid solution, or by additional formation of 1-2-3 phase.

When these films were observed by SEM, they were composed of extremely fine particles with a smooth surface and contained some micro cracks as shown in **Fig.3(A)** of the film (1c). Since similar cracks were recognized in the SEM pictures of the precalcined 1-2-4 films, they were considered to have developed when the coated films were pyrolyzed up to 500°C. No grain growth was found to have occurred in the prepared film and resulted in an agglomerate of extremely fine particles, since the calcining temperature for synthesizing 1-2-4 must be lower than that for 1-2-3 (as shown in the *P-T* diagram of the 1-2-4-(1-2-3 + CuO) system) as was mentioned in the introduction. It is therefore conceivable that the microstructure (crack) formed at pyrolysis was not sintered, but retained as it was at this low temperature (=780°C) of heat treatment. Thus, it is particularly important to prepare smooth and uniform films at the stage of pyrolysis when the 1-2-4 films are prepared. For the above reason, the selection of starting materials together with the pyrolytic conditions, need to be further studied in the future.

However, the fact that the 1-2-4 films were synthesized at ambient pressure for 24h without using fluxes such as alkaline metal salts[3] indicates an advantage of the dipping-pyrolysis process because $BaCO_3$, Y_2O_3, and CuO were thoroughly mixed in a micro scale in the prefired films.

3.2. Method of Synthesizing (*c*-axis-oriented 1-2-3 + CuO) Films Before Converting Them to 1-2-4

After the precalcined films were heat-treated at 820°C, $p(O_2)=10^{-3}$ atm, for 1h, the atmosphere was switched to oxygen and the films were annealed at the same temperature for 0.5h before furnace cooling in the oxygen atmosphere. **Figure 4(2a)** shows their X-ray patterns. It is clearly seen from the figure, that the film (2a) is an almost single phase of 1-2-3, and that CuO was observed only in the strongest peak at $2\theta=35.6°$. In the X-ray pattern (00*l*) peaks of 1-2-3 being relatively stronger than the other peaks, *c*-axis orientation is indicated. However, the preferred orientation in this case is not as strong as that of films prepared from the precursor of the 1-2-3 composition not including excess CuO.

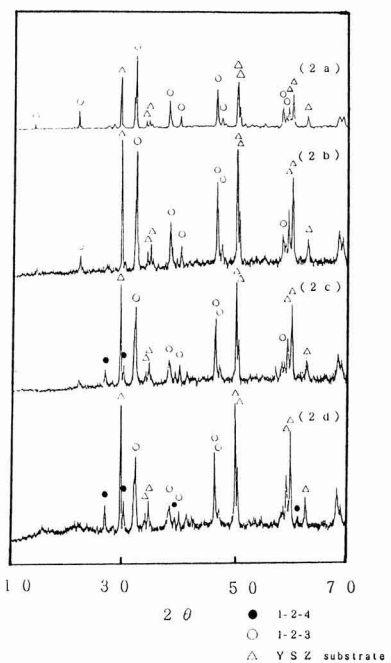

Fig. 4. X-ray diffraction patterns of 1-2-4 films: (2a) heat-treated under $p(O2)=10\text{-}3$ atm at 820°C for 1h followed by O2 treatment at 820°C for 0.5h; and subsequently heat-treated in O_2 at 780°C for (2b) 24h, (2c) 48h and (2d) 72h.

Subsequently, these films were further heat-treated at 780°C in oxygen for 24, 48 or 72h, resulting in the X-ray patterns included in Fig.4(2b), (2c) and (2d). Though it is difficult to discriminate 1-2-4 peaks from 1-2-3 peaks because of their low crystallinity, only 1-2-3 peaks were detected for the film heat-treated for 24h (2d).

As for the films (2c) and (2d) heat-treated for longer periods of 48h and 72h, the 1-2-3 peak intensities tended to be weaker with reference to these of the substrate, while the 1-2-4 peaks appeared at $2\theta=26.5°$ (104), 30.5° (106) and so on; thus, the conversion, though slightly, from (1-2-3 + CuO) to (1-2-4) appeared to be progressing.

Next, when the resistance of the films (2b) and (2c) was measured, $T_{c,onset}$=90K and $T_{c,onset}$=78K were obtained for both of these films. However, when the results were referred to those of XRD, the superconductivity of these films was more reasonably considered to be attributed to the 1-2-3 phase. When the film (2c) was observed by SEM, it was consisted of particles developed to μm–order seak as shown in Fig.3(B). Thus, the difficulty in the conversion from 1-2-3 to 1-2-4 may be explained by the synthetic reaction of 1-2-4 from 1-2-3 and CuO that occurs only in the grain boundary of 1-2-3 particles; once they are allowed to develope to the order of μm, the surface area at the beginning of synthetic reaction of 1-2-4 is conceivably limited. Furthermore, when the Ca-containing films were also heat-treated under similar firing conditions, 1-2-3 films were formed, without appreciable conversion from 1-2-3 to 1-2-4 in oxygen at 780°C for 72h.

3.3. Method of Synthesizing (micro 1-2-3 + CuO) Films Before Converting Them to 1-2-4

When the prefired films of the 1-2-4 composition were heat-treated at 700°C under respective low oxygen partial pressures, ($p(O_2)=10^{-2}$~10^{-4} atm), for 24h and examined by X-ray diffraction, the peaks of the starting materials such as $BaCO_3$, had already disappeared at this stage and broader 1-2-3 peaks were observed, but no CuO peaks were recognized. Since the differences in intensitives of the 1-2-3 (002) peak and the 1-2-4 (004) peak were most significant when the results of XRD of the films calcined under various conditions were compared, these peaks were selected as a measure of the amounts of the respective products and their crystallinity; the regions of 2θ 10° - 25° are shown in **Figs.5, 6** and **7.**

For non-Ca-containing films (Fig.5), 1-2-3 (002) peak at 2θ=15.1° is scarcely detected for $p(O_2)=10^{-2}$atm, but clearly observed for $p(O_2)=10^{-4}$atm ((3a), (3b), (3c)). These results are consistent with the results[10),11)] that the 1-2-3 films are synthesized at a lower temperature as the oxygen partial pressure decreases.

The results obtained from the Ca-containing films of x=0.05, and 0.1 are shown in Figs.6 and 7; the 1-2-4 (004) peak at 2θ=13.0° was observed in addition to 1-2-3 peaks for the films calcined at 700°C for 24h, $p(O_2)=10^{-3}$ and 10^{-4} atm ((3e), (3f), (3g), (3h), (3i)). However, the rest of 1-2-4 peaks could not be confirmed.

Next, the films heat-treated under each oxygen partial pressure were further heat-treated in oxygen at 780°C for 24h. The results obtained by X-ray diffraction are also shown in Fig.5(3a'), (3b'), (3c'), Fig.6(3d'), (3e'), (3f') and Fig.7(3g'), (3h'), (3i'). When no Ca is contained in the film (Fig.5), the 1-2-4 peaks including the (004) were definitely observed ((3a'), (3b')) in the films initially heat-treated at $p(O_2)=10^{-2}$ and 10^{-3} atm, and the 1-2-4 films of an almost single phase were obtained. On the other hand, this peak (004) was not observed in the film (3c') initially calcined at $p(O_2)=10^{-4}$ atm, this film exhibited an XRD pattern similar to that of the film (1a) with lower crystallinity.

As for the films containing Ca, x=0.05 and 0.1 (Figs.6 and 7), the 1-2-4 (004) peak was observed in the films of x=0.05 which were initially calcined at $p(O_2)=10^{-2}$atm (3d'), whereas this peak was not observed in the films calcined at $p(O_2)=10^{-3}$, and 10^{-4} atm ((3e'), (3f'), (3g'), (3h'), (3i')).

Summarizing the results of XRD on the films before and after oxygen treatment shown in Figs.5, 6 and 7, the 1-2-3 film, initialy heat-treated at 700°C under low oxygen partial pressure, of good crystallinity with definte 1-2-3 (002) peak, became lower in crystallinity with no 1-2-3 (002) peak nor 1-2-4 (004) peak after further heat treatment at 780°C in oxygen. On the other hand, for the films of rather poor crystallinity with no 1-2-3 (002) peak after initial heat treatment under the same conditions, further oxygen treatment made the (004) and other 1-2-4 peaks observed clearly, thus proving that films of 1-2-4 single phase were obtained.

It was not clear why 1-2-4 once formed coexisting with 1-2-3 disappeared together with 1-2-3 when heat-treated in a stable region of 1-2-4, in the films (3e'), (3f') and (3i'). One possible explanation is that 1-2-3 and 1-2-4 are not different primary particles separately existing in the films, but that 1-2-4 exists in the 1-2-3 particles as a structural defect.

The surface of these oxygen-treated films observed by SEM Fig.3(c), was found to be very smooth, consisted of fine particles similar to that of Fig.3(A). The results obtained from the resistance measurement of the films after oxygen-treatment are shown in **Table 1.**

As shown in Table 1, $T_{c,zero}$=70K was obtained for the films (3a') and (3d') of Ca amount, x=0 and 0.05,initially calcined at $p(O_2)=10^{-2}$ atm and the film (3b') of x=0 initially

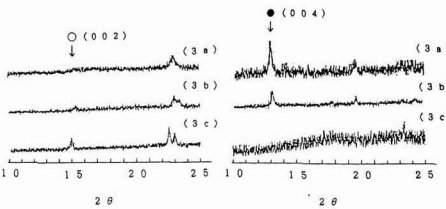

Fig. 5. X-ray diffraction patterns of 1-2-4 films heat-treated at 700°C for 24h under $p(O_2)$ of (3a) 10^{-2}, (3b) 10^{-3} and (3c) 10^{-4} atm. Primes are for those with subsequent O_2 treatment at 780°C for 24h.

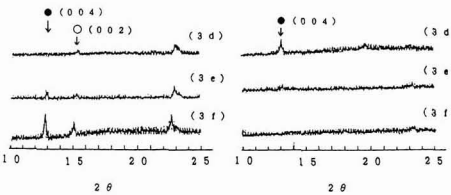

Fig. 6. X-ray diffraction patterns of $Y_{0.95}Ca_{0.05}Ba_2Cu_4O_8$ films heat-treated at 700°C for 24h under $p(O_2)$ for (3d) 10^{-2}, (3e) 10^{-3} and (3f) 10^{-4} atm. Primes are for those with subsequent O_2 treatment at 780°C for 24h.

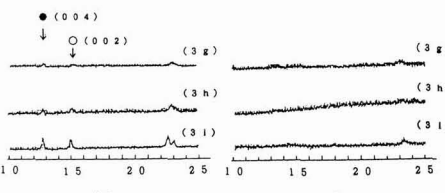

Fig. 7. X-ray diffraction patterns of $Y_{0.9}Ca_{0.1}Ba_2Cu_4O_8$ films heat-treated at 700°C for 24h under $p(O_2)$ of (3g) 10^{-2}, (3h) 10^{-3} and (3i) 10^{-4} atm. Primes are for those with subsequent O_2 treatment at 780°C for 24h.

calcined at $p(O_2)=10^{-3}$ atm, while the $T_{c,zero}$ for the rest of films was lower than 70K. The value of T_c decreased as an amount of Ca addition, x, was increased, and this tendency is in accord with the results obtained from direct synthesis of 1-2-4, the method (1). As it is clear from the comparison of Table 1 with Figs.5, 6 and 7, what attracts attention about the relation between T_c and the structure is that T_c is about 70K for the 1-2-4 films with favorable crystallinity and well developed 1-2-4 peak (004), but that the T_c level was lower for the film whose (004) peak was not recognized. In any case, the zero resistance temperature, 70K, was comparable with T_c of the films prepared by method (1) for 48h, and thus no advantage was recognized in the preliminary preparation of films consisting of micro-sized 1-2-3 +CuO.

3.4. Method of Quenching 1-2-4 Films Prepared by the Method (1) After Second Heat-treatment

The results of XRD and the resistance measurement on the above methods (1)~(3) suggested that the method (1) is most suitable to the preparation of 1-2-4 films. The films prepared by the method (1) (in oxygen 780°C, 48h, furnace cooled) were again heat-treated and quenched by method (4) for the resistance measurement in an attempt to clarify whether the superconductivity of these films, particularly Ca-containing films, is attributable to the 1-2-4 or the coexisting 1-2-3. The 1-2-3 films ($T_{c,zreo}$=88K) prepared by the method[10] of the previous report were also treated by re-heating and quenching under the same conditions for further reference. Since the 1-2-4 phase after quenching did not absorb or release oxygen without changes in the superconductivity, while the superconductivity of the 1-2-3 phase declined because of the loss of oxygen, it is conceivably possible to eliminate the effects of superconductivity due to the presence of 1-2-3. In fact, the 1-2-3 films prepared by the method of the previous report showed not only a semiconductive behavior with high resistance at ambient temperature after the re-heat-treatment, but both the values of $T_{c,onset}$ and $T_{c,zero}$ declined (broken lines in **Fig.8**). On the other hand, the 1-2-4 films prepared by method (4), namely non-Ca-containing film (1c') and Ca-containing x=0.05 film (1d') (corresponding to the films (1c) and (1d) in Fig.2, respectively) showed a metallic behavior despite the quenching from 780°C, where $T_{c,onset}$ showed 80K and 87K, and $T_{c,zero}$, 55K, 58K, respectively. This proved that the major phase in these films was 1-2-4.

Since $T_{c,onset}$ of the film (1d') of x=0.05 was higher than that of film (1c') of x=0, it is conceivable that T_c is improved by the Ca solid solution formed in the 1-2-4 film. However, because resistance curves of these quenched films showed a tailing, and $T_{c,zero}$ declines more than that of the furnace cooled films, the 1-2-3 phase existing in the grain boundary, etc. may form a weak link owing to the loss of superconductivity after quenching. Although the film of Ca content x=0.1 (1e') showed somewhat semiconductive behavier and $T_{c,zero}$ below 50K, $T_{c,onset}$ was 87K. Thus, it was found that 1-2-4 was also formed in the film of x=0.1.

In view of the results obtained from the methods (1)~(4) and the summarized discussion thereof, the formation of 1-2-4 is apparently in competition with that of 1-2-3; their behavior is quite complicated as the final product depends on the routes of reaction. Moreover, the results obtainable by the 2-stage heat-treatment method (2) and (3) are common in that the conversion from 1-2-3 to 1-2-4 is extremely difficult at ambient pressure once the former is produced. On the other hand, an interesting fact is unveiled by the results obtained by the method (3): a mixture of 1-2-3 and 1-2-4 is obtained in the Ca containing films (700°C, 10^{-3} ~ 10^{-4} atm). Thus, further detailed investigation including the formation process of 1-2-4 is needed.

Table 1. Values of $T_{c,zero}$ for Ca-substituted 1-2-4 films heat-treated under various $p(O_2)$'s at 700°C for 24h followed by O_2 treatment at 780°C for 24h. Y:Ca:Ba:Cu=1-x:x:2:4 in molar ratio.

x \ $p(O_2)$ /atm	10^{-2}	10^{-3}	10^{-4}
0	70	71	60
0.05	71	<60	<60
0.1	63	<60	<60

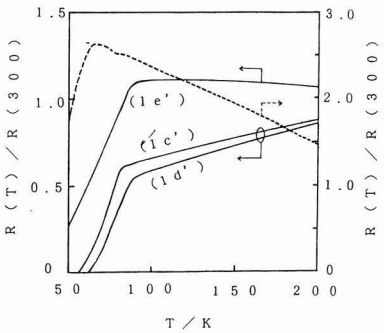

Fig. 8. Resistance vs. temperature relationship for quenched 1-2-4 films; films in Fig.2 were re-heat-treated in O_2 at 780°C for 24h before being quenched from 780°C and are denoted with primes. The dashed line represents that for the 1-2-3 film, which originally had $T_{c,zero}$=88K, quenched under the same condition.

4. Conclusion

1) In an attempt to prepare the 1-2-4 film by the dipping pyrolysis process, a film with an almost single phase of 1-2-4 as proved by X-ray and $T_{c,zero}$=70K was obtained when the prefined film was calcined in oxygen at 780°C for 24h. It was suggested that the film had the major phase 1-2-4 coexisting with some of the 1-2-3 phase from the resistance measurement of the films furnace-cooled and quenched after heat-treatment. It was also suggested that $BaCO_3$, Y_2O_3 and CuO were possibly mixed and dispersed in an extremely minute scale in the prefired films by the dipping-pyrolysis process, when the 1-2-4 film could be synthesized at ambient pressure in a relatively short time of 24h, and this indicated an advantage of this method.
2) In the preparation 1-2-4 films it is recommendable to directly heat-treat the prefired films in a stable region of 1-2-4 in the *P-T* diagram of the 1-2-4-(1-2-3 + CuO) system, while it was found difficult to convert the 1-2-3 + CuO film to 1-2-4 once the former has been prepared.
3) The value of $T_{c,onset}$ was improved in the film when Y was partially (5% and 10%) substituted for Ca. However,

the 1-2-4 formation tended to be inhibited when a substituted amount was increased up to 10%, and the value of $T_{c,zero}$ level tended to be lower.

4) When Y was partially substituted for Ca and the film was heat-treated at 700°C, $p(O_2)=10^{-3}\sim10^{-4}$ atm, a film composed of a mixture of 1-2-3 and 1-2-4 was obtained.

References:

1) J. Karpinski, E. Kaldis, E. Jilek, S. Rusiecki, and B. Bucher, Nature, 336, 660-62 (1988).
2) H.W. Zandbergen, R. Gronsky, K. Wang, and G. Thomas, Nature, 331, 596-99 (1988).
3) R.J. Cava, J.J. Karajewski, W.F. Peck, Jr., B.Batlogg, L.W. Rupp, Jr., R.M. Fleming, A. C. W. P. James and P. Marsh, Nature, 338, 328-30 (1989).
4) H. Murakami, S. Yaegashi, J. Nishio, Y. Shiobara and S. Tanaka, Jpn. J. Appl. Phys., 29, L445-46 (1990).
5) J. Karpinski, S. Rusiecki, E. Kaldis, B.Bucher and E. Jilek, Physica C, 160, 449-57 (1989).
6) D.E. Morris, A.G. Markelz, B.Fayn and J.H. Nickel, Physica C, 168, 153-60 (1990).
7) T. Wada, N. Suzuki, A. Ichinose, Y. Yaegashi, H. Yamauchi and S. Tanaka, Appl. Phys. Lett., 57, 81-83, (1990).
8) T. Wada, N. Suzuki, A. Ichinose, Y. Yaegashi, H. Yamauchi and S. Tanaka, Jpn. J. Appl. Phys., 29, L915-18 (1990).
9) T. Miyatake, S. Gotoh, N. Koshizuka, and S.Tanaka, Nature, 341, 41-42 (1989).
10) T. Kumagai, T. Manabe, W. Kondo, H. Minamiue and S. Mizuta, Jpn. J. Appl. Phys, 29, L940-942 (1990).
11) T. Kumagai, T. Manabe, W. Kondo and S. Mizuta, Jpn. J. Appl. Phys., 30, L28-31 (1991).
12) H. Sawada, T. Iwazumi, Y. Saito, Y. Abe, H. Ikeda and R. Yoshizaki, Jpn. J. Appl. Phys., 26, L1054-1056 (1987).

This article is a full translation of the article which appeared in Nippon Seramikkusu Kyokai Gakujutsu Ronbunshi (Japanese version), Vol.99, No.4, 1991.

An Effort on Preparing Sintered Bodies of Fe_4N

Kensuke Nakajima, Kensuke Taki*, Masasuke Takata and Shoichi Okamoto**

Faculty of Engineering, Nagaoka University of Technology
1603-1, Kamitomioka-machi, Nagaoka-shi, 940-21, Japan
*Gunze Co., Shiga Laboratory
163 Morikawara-machi, Moriyama-shi, 524, Japan
**Nagaoka College of Technology
888 Nishikatakai-machi, Nagaoka-shi, 940, Japan

Sintered bodies of Fe_4N were prepare by way of a hot-press, followed by firing in an atmosphere containing NH_3 and H_2 gases. After the hot-press, Fe_4N was not sintered and impurities of an iron oxide and a paramagnetic compound coexisted. The sintered bodies were obtained by firing the hot-pressed bodies in the atmosphere. It was found that, Fe_4N was reduced in firing and sintered above the decomposition temperature (approx. 670 °C); the sintered bodies were then rapidly renitrified in the atmosphere to Fe_4N through open pores in cooling. X-ray diffraction and Mössbauer spectra showed that the sintered bodies were Fe_4N single phase.
[Received October 1, 1990; Accepted December 14, 1990]

Key-words: Iron nitride, Fe_4N, Sintering, Nitriding atmosphere

1. Introduction

Fe_4N whose saturation magnetization is as large as 191emu/g is characterized by high chemical stability and mechanical strength. Magnetic powders of Fe_4N can easily be obtained by nitriding α-Fe powders in an ammoniac atmosphere. Thus, the magnetic properties of Fe_4N powders have been reported by many researchers,[1,2] and an application of Fe_4N powders to be substituted for magnetic powders of iron oxide as an particulate magnetic recording materials have also been studied.[3,4]

As shown in **Fig.1**, the crystal structure of Fe_4N is composed of iron atoms making a face-centered cubic lattice, and a nitrogen atom occupying its body-centered site. Because of this cubic symmetry, magnetic anisotropy is conceivably not notable, and the sintered bodies are expected to show soft magnetic properties.

When the sintered bodies of Fe_4N are considered as magnetic core materials, they can be used not only in place of the magnetic ferrite core or iron dust core because of their higher saturation magnetization, but also of magnetic circuit parts requiring high anticorrosion and wear resistance properties.

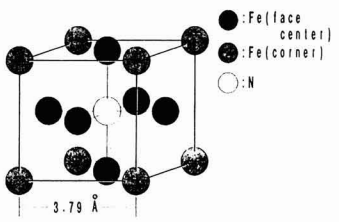

Fig. 1. Crystal structure of Fe_4N.

However, since Fe_4N is decomposed at about 670°C,[5] it is difficult to prepare dense sintered bodies. Thus, we have tried to prepare dense sintered bodies of Fe_4N using the hot-press method at a relatively lower temperature. We present here results on microstructure and magnetic properties of sintered Fe_4N, and on sintering process investigation by thermogravimetric analysis. For samples, Fe_4N powders were pre-sintered by hot-pressing in air, and then fired in flow of mixed gas of hydrogen with ammonia.

2. Experiment

2.1. Preparation of Samples

Fe_4N powders were prepared from commercially available carbonyl iron (99.5% Fe with mean particle diameter of 3μm manufactured by Rare Metallic Co., Ltd.) by ammonia-nitriding. Nitriding was performed heating at 500°C for 4h in flow of mixed gas of 40ml/min of hydrogen with 60ml/min of ammonia, and cooling in the furnace. The nitrided iron power thus obtained was identified as a single phase of Fe_4N by X-ray diffraction and by Mössbauer spectroscopy. When observed by SEM, no interparticle sintering was found in the fine spherical particle of Fe_4N whose diameter was almost identical to that of carbonyl iron particles (**Fig.2(a)**).

The above Fe_4N powders amounting to 2g were filled in a troid-type die 13mm in inner diameter and 20mm in outer diameter, heated at 500°C in air and hot-pressed at 3t/cm^2 for 5min, to obtain the troid type sintered bodies. Since these samples prepared by hot-press alone show poor sintering properties, they were improved through firing at 600 ~ 1200°C for 2h in flow of mixed gas of hydrogen with ammonia.

2.2. Measurement

The samples were identified by X-ray diffraction using CuKα radiation and 57 Fe Mössbauer spectroscopy after the sintered bodies were ground. The density of sintered bodies was measured by the Archimedean method and divided by the theoretical density (7.25g/cm^3) of Fe_4N to determine the relative density. The microstructure of sintered bodies was observed by SEM, while the magnetic properties were measured using a vibrating sample magnetometer (VSM). Saturation magnetization was determined by extrapolating the magnetization curves obtained

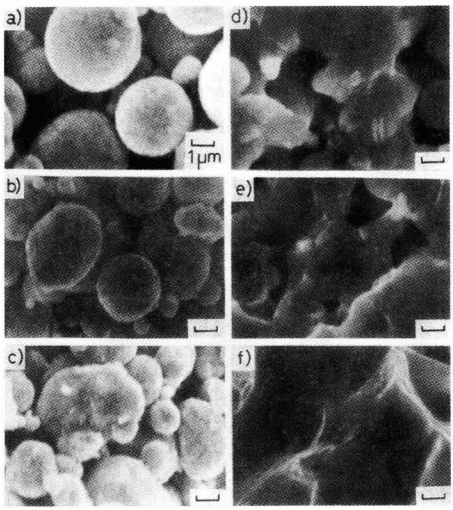

Fig. 2. SEM photographs of (a) Fe_4N powder, (b) hot-pressed Fe_4N, (c) Fe_4N fired at 600°C, (d) at 800°C, (e) at 1000°C and (f) at 1200°C. firing atmosphere was a mixture of NH_3, 50% and H_2, 50%.

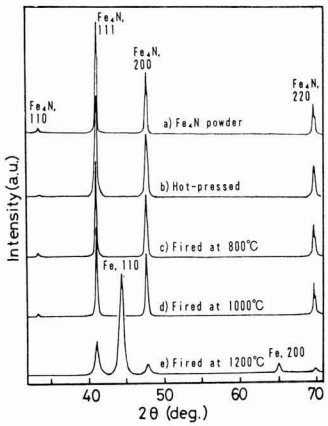

Fig. 3. X-ray diffraction patterns of (a) Fe_4N powder, (b) hot-pressed Fe_4N, (c) Fe_4N fired at 800°C, (d) at 1000°C and (e) at 1200°C. Firing atmosphere was a mixture of NH_3, 50% and H_2, 50%.

at room temperature, to the infinite magnetic field.

3. Results and Discussion

3.1. Hot-press

The relative density of samples prepared by hot-press alone is 71.9%. As shown in the SEM picture of a fractured surface (Fig.2(b)), almost no progress is made in the sintering at this stage. In view of an X-ray diffraction pattern in **Fig.3(b)**, the hot-pressed sample is determined as a single phase of Fe_4N. However, its saturation magnetization is 161emu/g, which is considerably less than the value in the literature (σ_s=191emu/g at 17°C[6]).

Mössbauer spectra of the samples are shown in **Fig.4**. The proper spectra of Fe_4N are composed of 3 kinds of iron spectra due to Zeeman splitting, namely FeI, FeIIa and FeIIb like the spectra of Fe_4N powder prior to hot-press shown in Fig.4(a). Of these spectra, FeI corresponds to iron atoms at a corner position of the face-centered cubic lattice of Fe_4N shown in Fig.1. On the other hand, iron atoms at the face-centered position, although crystallographicaly equivalent, provide 2 kinds of spectra of slightly different FeIIa and FeIIb[7]. The ratio of spectral areas of FeI, to the total of FeIIa and FeIIb is in good agreement with 1:3, the ratio of the number of atoms per unit cell.

In Mössbauer spectra of the hot-pressed samples (Fig.4(b)), two spectra with larger Zeeman splitting and a paramagnetic spectrum with no splitting were observed overlapping to the Fe_4N spectra. The former was identified as the Fe_2O_3 spectra from the size of hyperfine fields, while the latter is conceivably attributable to paramagnetic phases such as Fe_2N or austenite phase. Thus, the saturation magnetization levels of hot-pressed samples lower than that of Fe_4N in the literature are attributable to the formation of Fe_3O_4 with lower saturation magnetization ($\sigma_s \approx$ 80emμ/g) and the paramagnetic phase detected by Mössbauer spectroscopy.

3.2. Firing

With the intention of obtaining highly densified sintered bodies of single phase Fe_4N through re-nitriding, the hot-pressed samples were fired in flow of the mixed gas of hydrogen with ammonia at the fixed total flow rate of 100ml/min.

Figure 5 shows the crystal phases and its ratio that appear in X-ray diffraction patterns of samples fired at 600°C,

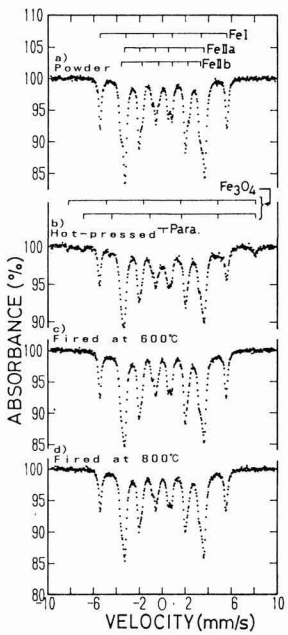

Fig. 4. Mössbauer spectra of (a) Fe_4N powder, (b) hot-pressed Fe_4N, (c) Fe_4N fired at 600°C and (d) at 800°C. Firing atmosphere was a mixture of NH_3, 50% and H_2, 50%.

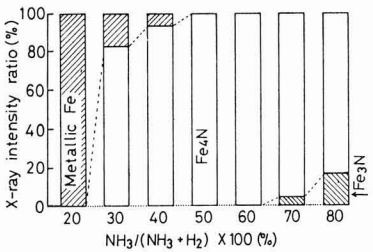

Fig. 5. Changes in crystalline phases of samples fired in the nitriding atmosphere with various ratios of NH_3 and H_2.

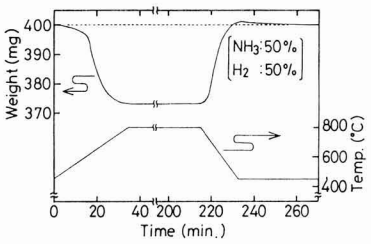

Fig. 6. Changes in sample weight during firing in a mixture of NH_3 and H_2.

a temperature lower than the decomposition temperature of Fe_4N ($\approx$ 670°C) for 2hr varying the flow rate of component gases. The ratio of respective phases is represented by intensity ratio of the strongest line of each phase observed, namely 110 of α-Fe, 111 of Fe_4N, and 101 of Fe_3N. It is clear from this figure that a single phase of Fe_4N can be obtained when the flow ratio of ammonia is within a range from 50% to 60%. In addition, iron oxide and paramagnetic phases are not observed in Mössbauer spectra in this range (Fig.4(c)). In other words, the purity of Fe_4N is improved as the reduction and renitriding of Fe_3O_4 as well as the phase transition from paramagnetic iron nitriding phase to Fe_4N can be achieved under these firing conditions.

Although the saturation magnetization of the samples thus obtained rose to 181emu/g, the relative density remained almost unchanged at 71.5%. It is also clear that almost no progress is made in the sintering as globular Fe_4N particles similar to those before firing are recognized in the SEM picture of a fracture surface of this sample (Fig.2(c)).

Next, keeping the flow ratio of ammonia at 50%, firing temperature was raised to 800°C, which was higher than the decomposition temperature of Fe_4N, and the change in sintering behavior and nitride phases were investigated on the samples fired for 2h. The SEM picture of the fractured surface (Fig.2(d)) showed apparent improvement of sintering compared with that of samples shown in the same picture, (b) and (c), while the relative density was also improved to 79.9%, nearly 10% higher than that of other samples.

It was found from the X-ray diffraction pattern in Fig.3(c) that the sample was a single phase of Fe_4N despite of the firing temperature higher than the decomposition temperature (670°C) of Fe_4N. Mössbauer spectra of this sample shown in Fig.4(d) indicate that this sample is pure Fe_4N without any other phase. The saturation magnetization was 181emu/g, which was the same as that of samples fired at 600°C.

The weight variation of samples during firing was measured using a thermobalance in an attempt to clarify the sintering process of this sample. **Figure 6** shows a temperature diagram of the thermobalance (lower line) and corresponding weight variation of samples (upper line). This diagram indicates that the weight of samples (hot-pressed Fe_4N) rapidly decreases when exceeding 600°C, but reaches a stable level about 780°C. Since the weight loss at this stage almost agrees with the total weight of nitrogen contained in 400mg Fe_4N, denitrification is completely achieved at 780°C. Furthermore, the weight is rapidly increased, on the contrary, during the process of temperature decline, and recovered about 400°C to a level before the rise of temperature. Thus, it is conceivable that Fe_4N was once completely denitrided and decomposed to metallic iron in the process of temperature rising, and after it was sintered, changed to Fe_4N when renitriding had rapidly advanced in the process of temperature falling.

It was, therefore, found that highly dense sintered bodies of Fe_4N could be obtained when renitriding was performed in the process of temperature falling, by controlling the firing atmosphere even when Fe_4N is fired at a temperature higher than its decomposition temperature.

However, with regard to the re-nitrification in the process of firing in the nitriding atmosphere, it is easily presumable that the higher the density of the sintered body, the more difficult the re-nitrification because of less surfaces area to be exposed to the atmosphere.

In fact, sintered bodies in which a number of open pores were observed in SEM picture of fractured surface (Fig.2(e)) gave the X-ray diffraction pattern of single phase Fe_4N (Fig.3(d)). This was the case up to 1000°C of firing temperature, while the sample fired at 1200°C in which no open pores was recognized (Fig.2(f)) revealed strong lines of α-Fe in its X-ray diffraction pattern (Fig.3(e)), proving insufficient re-nitrification.

To obtain Fe_4N sintered body of high density, it is important to promote renitrification at the stage of temperature falling, and further optimization in the firing process including control of atmosphere.

4. Summary

In an attempt to prepare high-density Fe_4N sintered bodies, samples presintered by hot-pressing below the decomposition temperature of Fe_4N were fired in flow of mixed gas of hydrogen with ammonia.

It was found that by firing at temperature higher than the decomposition level, Fe_4N was reduced to metallic iron and sintered, then in the stage of temperature falling in the nitriding atmosphere it is rapidly renitrified through the open pores. This process resulted in a sintered body of single phase Fe_4N.

In order to prepare sintered bodies of even higher density, it is important to control atmosphere and pores.

Acknowledgements
We thank the staff of the Ceramics Division of the New Material Development Department of Nihon Kokan K.K., where we were allowed to perform thermogravimetric analysis.

References:

1) K. Tagawa, E. Kita and A. Tasaki, Jpn. J. Appl. Phys., 21, 1596-1598

(1982).

2) K. Nakajima, T. Sato, S. Okamoto, The Magnetics Society of Japan 14, 77-80 (1990).
3) S. Suzuki, H. Sakumoto, Y. Omoto and J. Minegishi, IEEE Trans on Magn, MAG-20, 48-50 (1984).
4) S.F. Matar, G. Demazeau and B. Siberchicot, IEEE Trans on Magn., MAG-26, 60-62 (1990).
5) K.H. Jack, Proc. Roy. Soc. London, A208, 200-215 (1984).
6) C. Guillaud and H. Creveaux, Compt. Rend. Acad. Sci., 222, 1170-1173 (1946).
7) A.J. Nozik, J.C. Wood, and G. Haacke, Solid State Commun., 7, 1677-1679 (1969).

This article is a full translation of the article which appeared in Nippon Seramikkusu Kyokai Gakujutsu Ronbunshi (Japanese version), Vol.99, No.4, 1991.

Preparation of $SiCl_4$ from Rice Hull Ashes (Part 2)†
– Effect of Alkaline and Alkaline Earth Metal Salt Additives on Chlorination of Rice Hull Ashes –

Takeshi Okutani, Yoshinori Nakata, Kazuhiro Ishikawa* and Kenji Takeda*

Government Industrial Development Laboratory,
Hokkaido 2-17, Tsukisamu-Higashi, Toyohira-ku, Sapporo-shi, 062, Japan
*Hokkaido Soda Co., Ltd.
134-122, Aza-Numanohata, Tomakomai-shi, 059-13, Japan

In order to produce $SiCl_4$ efficiently from active SiO_2 in rice hulls, rice hull ash (combustion waste of rice hull) was chlorinated under the coexistence of alkaline and alkaline earth additives such as potassium compounds in the temperature range of 600 to 1000°C. These additives changed to chlorides under the condition of chlorination. Potassium compounds accelerated the chlorination of the rice hull ash. Other alkaline and alkaline earth compounds such as sodium, magnesium and calcium inhibited the chlorination. The acceleration effect of potassium in the chlorination of SiO_2 was explained by assuming that the diffusion of K^+ ion in SiO_2 lattice caused the distortion of SiO_2 lattice and the chlorinating species such as chlorinated carbon were easy to diffuse in SiO_2 lattice. The inhibitory effect of other elements was interpreted in terms of the absence of SiO_2 lattice distortion, since the ionic radii of these elements are smaller than that of K^+. It is also inferred that the melts of these chlorides covered the contact points of SiO_2 and C.

[Received October 4, 1990; Accepted December 14, 1990]

Key-words: Rice hull ash, Active SiO_2, chlorination, $SiCl_4$, Potassium accelerator, Alkaline and alkaline earth salt additives

1. Introduction

Silicon tetrachloride ($SiCl_4$) has a boiling point of 56.7°C and is easily purified by evaporation. High-purity $SiCl_4$ has been converted into high-purity SiO_2 and utilized as a source material for artificial quartz or fine silica. In addition to these applications, it has recently been adopted as a material gas in the CVD process of fine ceramics such as SiC and Si_3N_4.[1-4]

Previously, $SiCl_4$ was produced by reacting chlorine (Cl_2) at about 600°C with SiC prepared from a mixture of SiO_2 and C,[5] but now it is obtained as a byproduct during the production of $SiHCl_3$ by chlorinating metallic silicon (produced by reduction of SiO_2) with HCl, and this process is being used for industrial applications. Other methods include an energy saving process uses a SiO_2/C mixture which is directly exposed to Cl_2 over 1000°C to obtain $SiCl_4$. The Cl_2 gas is corrosive and it requires extreme caution in industrial handling at high temperatures, as is the case with present titanium refining at 1000°C.[6]

Rice hulls, an agricultural waste, consist of inorganic (13–29wt%) and organic substances such as cellulose (71-87wt%), the proportion depending on rice varieties, climate, and other geographical conditions. The inorganic components consist of silica (87-97wt%) (SiO_2), alkali metal compounds and other trace elements. This silica is more active than mineral silica. The authors[7] noticed this property and have been studying to produce $SiCl_4$ from SiO_2 in rice hulls by chlorination under 1000°C.

In the previous report,[8] the authors showed that a rice hull charcoal (a mixture of SiO_2 and C prepared by the thermal decomposition of cellulose in an inert gas) is chlorinated to convert about 80% of SiO_2 into $SiCl_4$ at 900°C. Collection of rice hulls may be a problem in the utilization of SiO_2 of rice hulls. At present, 71-87wt% of organic matter such as cellulose contained in rice hulls is used as a fuel in Southeast Asia.[9] The utilization of rice hull ashes, the byproduct of conbustion of rice hulls, facilitates availability of rice hulls because rice hull ashes are easier to collect than rice hulls.

This study was intended to produce $SiCl_4$ by the efficient chlorination of rice hull ashes. The chlorination of rice hull ashes added alkali and alkaline earth salts that easily break Si-O bonding and easily react with SiO_2 in rice hull ashes was reported in this paper.

2. Method of Experiment

2.1. Sample

Table 1 shows the composition of SiO_2, K_2O, etc. in three rice hull ashes used in this report, Ash-1,-2 and -3. Among them Ash-1 and -2 were prepared with a circulating fluidized bed furnace (made by Hokuto Engineering Co., Ltd.) now under operation at a rice center in Hokkaido as a hot-air generator to dry cereals. The conditions for Ash-1 used a furnace (type WHB-80-D), 80kg/h was the feed rate of the rice hulls, 800±80°C for the combustion temperature, and 4hrs for residence time. Those for Ash-2 were WHB-450-M for furnace type, 450kg/h for the feed rate, 900°C±100°C for combustion temperature, and 4hrs for residence time. On the other hand, Ash-3 was obtained by charging 20g of dried rice hulls in a quartz reactor tube 55mm in the inside diameter (layer height: 10cm) and then

† (Part 1); T.Okutani and Y. Nakada, "Preparation of $SiCl_4$ from Rice Hulls" in High Tech. Ceramics, Edited by P. Vincenzini, Elsevier Publishing Co., Amsterdam (1987) p.511.

heating it at 800°C under air flow rate of 2l/min.

In SiO_2 analysis of ashes and reaction residues, samples were treated with nitric acid and perchloric acid to make SiO_2 insoluble, and then filtered, ignited and weighed the SiO_2. Li, Na, K, Mg, and Ca were determined by atomic absorption analysis with filtrate obtained in SiO_2 analysis. The carbon content of the samples was determined by ignition loss in air.

The chlorination of SiO_2 ($SiO_2+2Cl_2+2C \rightarrow SiCl_4+2CO$) requires carbon. In this study, commercial active carbon (specific surface area: 900m^2/g) was added when necessary to rice hull ash to ensure a C/SiO_2 molar ratio of 2.5.

In order to investigate the effect of adding alkali and alkaline earth metal salts on the chlorination of SiO_2, twelve kinds of reagents such as K_2CO_3, KCl, $KHSO_4$, NaCl, $MgCl_2$, and $CaCl_2$ were mixed into chlorination samples of rice hull ash – carbon mixtures. The samples were ground with an Ishikawa-type agitator for 1hr followed by vacuum drying at 100°C for 1hr. Silica sand (α-quartz; SiO_2 content: 97.7%) and a silicic anhydride reagent (Furuuchi Chemicals; SiO_2 content: 99.999%) were tested for comparison with rice hull ashes.

2.2. Chlorination

In the chlorination experiment, a quartz tube 30mm in inside diameter was installed in a horizontal electric furnace, and an alumina combustion boat with about one gram of sample was placed in its center. Subsequently, the quatz tube was evacuated to 10^{-1}mmHg and then filled with Ar, and the sample was heated to the prescribed temperature at a rate of 26°C/min where it was held for 30 minutes and then a Cl_2 gas was introduced. The point was set as zero for the reaction time. The reaction temperature was controlled within ±9°C at 600–900°C. The flow rate of Cl_2 was 100ml/min. After the prescribed reaction time, the gas was shifted to Ar and the sample was cooled to room temperature; the sample was weighed accurately to obtain weight loss. The conversion from SiO_2 to $SiCl_4$ was determined by the content of SiO_2 in samples taken before and after the reaction. As for the amount of formed $SiCl_4$, a gas from the reactor outlet was introduced into a methanol-dry ice trap at −30°C to liquefy gaseous $SiCl_4$ for weight measurement. From the data of $SiCl_4$ formation as well as SiO_2 analysis in samples before and after the reaction, the weight loss of SiO_2 was found to be equal to the amount of formed $SiCl_4$, thus confirming that SiO_2 was entirely converted into $SiCl_4$.

Table 1. Contents of SiO_2, Na_2O, MgO, CaO and C in ash, silica sand and commercial SiO_2, crystalline structure and specific surface areas of samples.

Sample	Content (wt%) SiO_2	Na_2O	K_2O	MgO	CaO	C	Crystalline structure	Specific surface area (m^2/g)
Ash-1	74.1	0.34	0.89	0.19	0.91	21.3	Cristobalite	76
Ash-2	96.5	0.07	0.75	0.06	0.10	2.1	〃	4
Ash-3	97.2	0.16	0.43	0.16	0.20	0	Amorphous	44
Silica sand	97.7	0.16	0.21	0.01	0.07	0	α-Quartz	2
Commercial SiO_2	99.999	0	0	0	0	0	Amorphous	13

3. Results and Discussion

3.1. Changes in Composition and Chlorination Reactivity of Rice Hull Ashes Produced at Various Combustion Temperatures

The composition of rice hull ashes somewhat varies with production areas, and probably with combustion temperature. As in **Table 2**, higher combustion temperature results in higher content of SiO_2 and lower content of Na, K, Mg, and Ca.[10] **Figure 1** shows the effect of combustion temperature of rice hulls on the conversion of SiO_2 in rice hull ashes to $SiCl_4$. At combustion temperatures of 600°C and 700°C, the conversion was almost at the same level, while over 800°C it decreased with temperature. The specific surface area of rice hull ashes was mostly constant (44m^2/g) throughout the whole range of combustion temperature, and SiO_2 in ashes was amorphous. As described in the earlier report,[10] rice hulls release low molecular substance (volatile) over 200°C by thermal decomposition in the heating process from room temperature to a prescribed temperature (600~ 900°C), and the combustion of these volatile components sharply increases the temperature from about 400°C to 1000°C. Consequently, the combustion of rice hulls over 600°C seems to provide the same specific surface area. As stated above, no change is encountered in the specific surface area nor crystal structure of ashes prepared at 600 ~ 900°C, while the chlorination reactivity of ashes prepared by combustion over 800°C shows a decrease. As in Table 2, no change is detected in the content of each component at 600°C and 700°C, whereas those, except for SiO_2, decrease over 800°C. It is inferred that there is a relationship between this trend and chlorination reactivity.

In the next step, a relationship between the content of Na_2O, K_2O, MgO, and CaO in ashes prepared at 600 ~

Table 2. Contents of SiO_2, Na_2O, K_2O, MgO and CaO in ash prepared at various combustion temperatures.

Combustion temp.	Content (wt%) SiO_2	Na_2O	K_2O	MgO	CaO
600	94.7	0.14	0.67	0.39	0.41
700	95.9	0.17	0.71	0.36	0.57
800	97.2	0.16	0.43	0.16	0.20
900	98.1	0.07	0.16	0.16	0.10

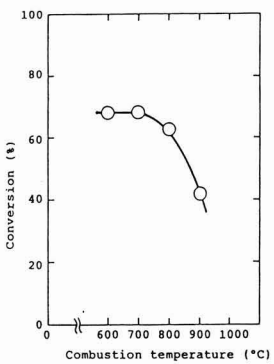

Fig. 1. Effect of combustion temperature on chlorination of ash+C (50wt% for SiO_2) at 900°C for 1hr.

900°C and the conversion of SiO_2 in ashes to $SiCl_4$ at 900°C for 1 hr was examined. As a result, only the K_2O content (**Fig.2**) showed linearity. Thus, it was found that potassium content affects the chlorination.

3.2. Relationship Between Composition of Rice Hull Ashes and Chlorination Reactivity

Table 1 lists chemical components such as SiO_2 and K_2O, crystal structures, and specific surface area of Ash-1, -2, and -3, as well as silica sand and a silicic acid anhydride reagent. In Ash-1, 21.3% of the carbon remains unburned. The effects of each factor on chlorination was studied. It is generally believed that higher specific surface area leads to higher reactivity, and that amorphous SiO_2 is more reactive than crystalline SiO_2 such as cristobalite; in this study however, no relationship was detected between the specific surface area or crystallinity of SiO_2 and chlorination reactivity. As stated in the previous chapter, chlorination reactivity was correlated with potassium content.

In order to examine the effects of alkali and alkaline earth metals on the chlorination of rice hull ashes, the compounds of these metals were added to the rice hull ashes before chlorination. The results are given in **Table 3**. The conversion of chlorination was 60.4% for Ash-1 with 21.3% of unburned carbon, while potassium salts added to Ash-1 by 10wt% for SiO_2 accelerated the reaction of chlorination (Exp. No. 1 ~ 7). On the other hand, the addition of sodium salts (Exp. No. 8 ~ 9), a magnesium salt (Exp. No.10) and a calcium salt (Exp. No.11) inhibited the reaction. This trend was observed also in the case of Ash-2+C, and Ash-3+C.

X-ray diffraction with samples after chlorination at 600~1000°C indicated that those containing alkali and alkaline earth metal salts were entirely changed into chlorides. That is, after chlorination, all of each additive is present in the sample as a chloride.

3.3. Mechanisms of Chlorination Acceleration by K and Chlorination Inhibition by Na, Ca, and Mg

The mechanism of chlorination acceleration by K as well as that of chlorination inhibition by Na, Ca, and Mg was discussed as follows. It is familiar that such ions as K^+ and Na^+ in SiO_2 glass are ion-conductive at high temperatures. The melting points of KCl, LiCl, NaCl, $CaCl_2$ and $MgCl_2$ are 776, 614, 800.4, 774, and 714°C respectively, thus being brought into contact with SiO_2 in the molten state over 800°C.

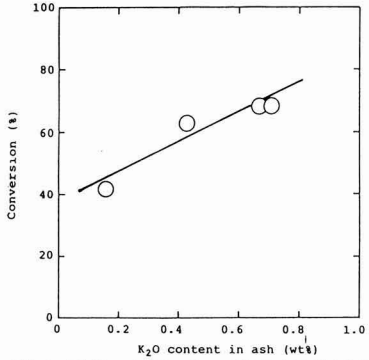

Fig. 2. Effect of K_2O content in ash on chlorination of Ash+C (C=50wt% for SiO_2) at 900°C for 1hr.

Table 3. Effect of alkaline and alkaline earth metal salt additives on chlorination of rice hull ashes at 900°C for 1h.

Exp. No.	Sample	Additive (10wt% for SiO_2)	Conversion (wt% for SiO_2)
1	Ash-1	-	60.4
2	〃	K_2CO_3	66.3
3	〃	KCl	71.7(72.2)
4	〃	$KHSO_4$	70.4
5	〃	KOH	69.2
6	〃	KNO_3	67.8
7	〃	K_2SO_4	69.1
8	〃	Na_2CO_3	44.0
9	〃	NaCl	56.7
10	〃	$MgCl_2$	55.3
11	〃	$CaCl_2$	45.8
12	Ash-1+C	-	81.0
13	〃	$KHSO_4$	87.9(84.5)
14	Ash-2	K_2CO_3	1.3
15	Ash-2+C	-	47.9
16	〃	K_2CO_3	79.5
17	〃	KCl	79.9
18	〃	$KHSO_4$	82.1(81.9)
19	〃	KOH	76 9
20	〃	KNO_3	80.4
21	Ash-3+C	-	49.2
22	〃	$KHSO_4$	70.2
23	〃	Li_2CO_3	22.9
24	〃	Na_2CO_3	32.5
25	〃	$MgCO_3$	18.9
26	〃	$CaCO_3$	18.2
27	Silica sand+C	-	8.7
28	〃	$KHSO_4$	26.2
29	Commercial SiO_2+C	-	7.4
30	〃	$KHSO_4$	53.8

A part of the molten salt is expected to diffuse in SiO_2 as K^+, Na^+ etc. In this case, a reaction with chlorine may be accelerated by breaking Si-O bond and distorting a Si-O lattice. The interatomic distance of Si-O in SiO_2 (solid) is 1.609A. As stated in the earlier report,[8] Cl_2 is considered to react with C to form gaseous carbon chloride which reacts with SiO_2. At present, the details of carbon chloride structure are not known, while the interatomic distance between C and Cl is in the range of 1.67 ~ 1.77A with various bonding states including Cl-C-, Cl-C=, Cl-C (aromatic compounds), and Cl-C.[11] Carbon chloride having an interatomic distance of 1.67-1.77A, cannot diffuse into Si-O lattice. The progress of the reaction requires contact between Si-O and carbon chloride as well as the formation of bonding; yet the Si-O distance is short and the diffusion of carbon chloride is insufficient. The ionic radii of 6-coordinated K^+, Li^+, Na^+, Mg^{2+} and Ca^{2+} are 1.52, 0.90, 1.16, 0.86, and 1.14A, respectively.[11] These ions are supposed to diffuse in the SiO_2 lattice, and the ionic radius of K^+ is the greatest so that it probably distorts the Si-O lattice most. As the degree will be so great as to allow carbon chloride to diffuse in the Si-O lattice, it is considered to accelerate chlorination. The ionic radii of Li^+, Na^+, Mg^{2+} and Ca^{2+} are small, the lattice distortion is insufficient, and thus the reaction seems not to be accelerated. In other words, the effect of their diffusion in the SiO_2 lattice is less than that of a molten salt to cover SiO_2 and C preventing contact with Cl_2, so that the inhibition of chlorination is probably observed. One support for the above consideration is that the addition of K, Na, Ca, and Mg salts did not affect chlorination below the melting point of each chloride, and conversion of SiO_2 to $SiCl_4$ were

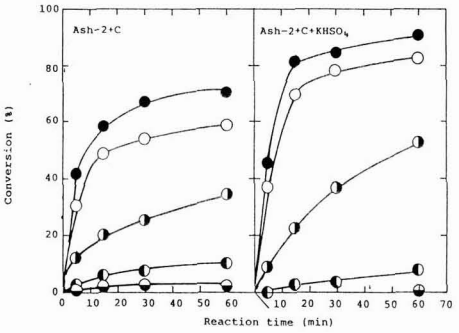

Fig. 3. Reaction rate curves of chlorination of Ash-2+C and Ash-2+C+$KHSO_4$ at various reaction temperatures.
●: 1000°C, ○: 900°C, ◑: 800°C, ◐: 700°C, ◒: 600°C.

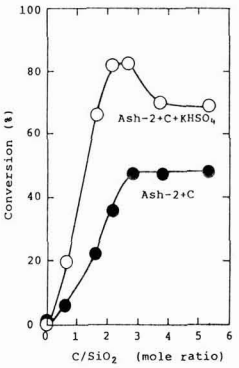

Fig. 4. Effect of C/SiO_2 mole ratio on chlorination of Ash-2+C and Ash-2+C+$KHSO_4$ (10wt% for SiO_2) at 900°C for 1hr.

almost the same as those without the addition. **Figure 3** shows reaction rate curves of Ash-2+C and Ash-2+C+$KHSO_4$ during chlorination at 600 ~ 1000°C. The melting point of KCl is 776°C and the addition effect is positive at chlorination temperatures over 800°C but is not at 600 and 700°C.

3.4. Chlorination Behavior of Rice Hull Ash – C – K Mixtures

The chlorination behavior of each ash containing C and K is as follows. The molar ratio of C and SiO_2 in Ash–1 is C/SiO_2=1.544 (mole/mole) are calculated from the values in Table 2. The chlorination of SiO_2 is expressed by the following equation:

$$SiO_2 + 2C + 2Cl_2 \rightarrow SiCl_4 + 2CO;$$

and the stoichiometric ratio of C/SiO_2 is 2.0. Active carbon was added to Ash–1 so as to be C/SiO_2=2.5 (mole/mole) before mixing. The results of chlorination with this mixture are shown as Exp. No.12 in Table 3. When $KHSO_4$ is added to the Ash–1+C mixture its conversion increases from 81.0 to 87.9% (Exp. No.13). In the chlorination of single Ash–2 with 2.1wt% of C the conversion is 1.3% (Exp. No.14). When carbon is added to it the conversion becomes 47.9% (Exp. No.15), and further with $KHSO_4$ it reaches 82.1% (Exp. No.18) proving the greater addition effect. In the case of adding $KHSO_4$ (Exp. No.22) to the Ash–3+C mixture (Exp. No.21), the addition effect is recognized but not greater than that for the Ash–2+C mixture.

The crystal structure of SiO_2 in Ash–3 is amorphous and its specific surface area is 44m^2/g, while it is less active than Ash–2 with a cristobalite structure and specific surface area of 4m^2/g. The reason may be differences in the preparation of rice hull ashes and production areas of rice hulls, but the details are not known. The addition effect of potassium salts is noticed also in silica sand and SiO_2 reagent, mixed with C.

Figure 4 plots the results of the Ash-2+C+$KHSO_4$ mixture with different carbon contents chlorinated at 900°C for 1hr. For comparison, those of the Ash–2+C mixture are given as well. The figure indicates that the addition of $KHSO_4$ leads to a higher conversion than cases without addition, and that its peak is at a C/SiO_2 molar ratio of 2 ~ 2.5.

10wt% for SiO_2 of pottasium salts, added to samples of Exp. 2~7 in Table 3, corresponds to percentages of pottasium metal of 3.6% for K(KCl), 2.0% for K($KHSO_4$), 4.8% for K(KOH), 2.7% for K(KNO_3), and 3.1% for K(K_2SO_4). The potassium salts are all present as KCl in the chlorine atmosphere over 600°C. The chlorination conversion of samples containing various potassium salts by 10wt% for SiO_2 is 66.3 ~ 72.2%, and no correlation is detected between the conversion and the amount of potassium metal in potassium salts.

Figure 5 presents reaction rate curves at 900°C of the

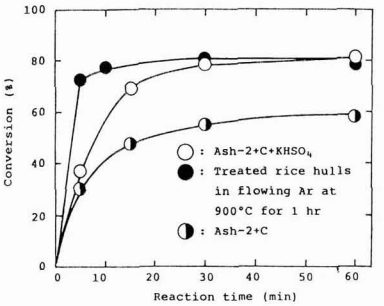

Fig. 5. Reaction rate curves of chlorination of Ash-2+C (50wt% for SiO_2)+$KHSO_4$ (10wt% for SiO_2), treated rice hulls in flowing Ar at 900°C for 1hr and Ash-2+C (50wt% for SiO_2).

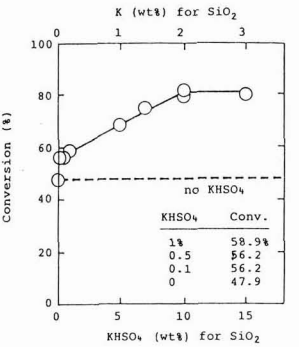

Fig. 6. Effect of amount of $KHSO_4$ added to ash on chlorination of Ash-2+C+$KHSO_4$ at 900°C for 1hr.

Ash-2+C mixture containing $KHSO_4$. For comparison, Ash-2+C is also given as well as rice hull charcoal obtained by decomposing rice hulls at 900°C for 1hr in an argon flow. The latter is a SiO_2+C mixture (SiO_2; 40wt%; C: 60wt%) prepared by the thermal decomposition of organic matter such as cellulose contained in rice hulls by about 80%. The Ash-2+C mixture with $KHSO_4$ is more reactive than the Ash-2+C mixture. Moreover, it is less reactive than rice hull charcoal at a reaction time of within 30 minutes, but is almost the same over that period.

Figure 6 shows the conversion of the Ash–2+C mixture containing $KHSO_4$ by 0.1 ~ 15wt% for SiO_2 (potassium metal equivalence: 0.02 ~ 3wt%) and after chlorination at 900°C for 1hr. The effect to accelerate chlorination is constant over 10% of $KHSO_4$. It is encountered also in the case of adding 0.1wt% of $KHSO_4$.

4. Conclusion

When SiO_2 in rice hull ashes, which is a remainder obtained by the combustion of rice hulls, was chlorinated to produce $SiCl_4$, it was found that alkali and alkaline earth metal salts affect the reaction of chlorination (either acceleration or inhibition). These effects were studied to obtain the following results.

1) Potassium metal salts accelerated chlorination while lithium, sodium, calcium, and magnesium metal salts inhibited the reaction.
2) No correlation was detected between the crystal structure and specific surface area of SiO_2 in rice hull ashes and the conversion to $SiCl_4$.
3) Alkali and Alkaline earth metal salts were entirely converted into chlorides at a chlorination temperature of over 600°C, and their acceleration or inhibition occurred at temperatures exceeding the melting point of each chloride.
4) The mechanism is considered to be that K^+ with the greatest ionic radius in alkali and alkaline earth metal ions enter SiO_2 to distort the SiO_2 lattice, thereby facilitating the diffusion of a chlorinating species (carbon chloride) in the SiO_2 lattice and causing the acceleration effect.
5) By contrast, the ionic radii of Li, Na, Mg, and Ca metal salts are smaller than that of $K,^+$ and cannot distort the Si-O lattice enough to allow satisfactory diffusion. Additionally, they become chlorides during chlorination which are molten over 800°C, and cover the reaction points of SiO_2 and C to prevent contact with Cl_2: a probable reason for the inhibitory effect.

References:

1) A. Kato, Hyomen, 21, 65-76 (1983).
2) A. Kato, T. Ono, S. Kawazoe, and I. Mochida, Yogyo-Kyokai-Shi, 80, 114-20 (1972).
3) T. Tani, T. Yoshida and K. Akashi, Yogyo-Kyokai-Shi, 94, 1-6 (1986).
4) T. Yoshida, Y. Tanau, K. Eguchi and K. Akashi, "The Preparation of Ultrafine Si_3N_4 and SiC Powders in a Hybrid Plasma," Proc. 8th Int. Conf. on Vacuum Meta. 8th-ICVM, Linz, Austria, 473-51 (1985).
5) "Encyclopedia of Chemical Technology, Vol.12" ed. by R.E. Kirk and D.F. Othmer, Japanese Reprint Edition, The International Encyclopedia. Inc., New York, Maruzen Co., Ltd., Tokyo, 369 (1961).
6) Nihon Kagakukai, Kagaku Binran Oyohen 3rd Edition, Maruzen, 289 (1980).
7) P.K. Basu, C.J. King and S. Lynn, AIChE Journal, 19, 439-45 (1973).
8) T. Okutani and Y. Nakata. "Preparation of $SiCl_4$ from Rice Hulls" in High Tech Ceramics, Edited by P. Vincenzini, Elsevier Publishing Co., Amsterdam, 511-16 (1987).
9) N. Hara, "Potential Usability of Rice Husk and Rice Husk Ash for Industry" proc. Workshop on Co-operation among Developing Countries in the Field of Cement, Lime and Related Industries, Bangkok, 1-14 (1987).
10) Y. Nakata, M. Suzuki, T. Okutani, M. Kikuchi and T. Akiyama, Seramikkusu Ronbunshi, 97, 842-49 (1989).
11) Nihon Kagakukai, Kagaku Binran, Kisohen II, Maruzen, II-714-17 (1988).

This article is a full translation of the article which appeared in Nippon Seramikkusu Kyokai Gakujutsu Ronbunshi (Japanese version), Vol.99, No.4, 1991.

Grain Size Dependence of the Fracture Toughness of Silicon Nitride Ceramics

Takeshi Kawashima, Hiromi Okamoto, Hideharu Yamamoto and Akira Kitamura

Advanced Technology Research Center, NKK Corporation
1-1 Minamiwataridacho, Kawasaki-ku, Kawasaki-shi 210, Japan

Improved K_{IC} values of monolithic Si_3N_4 ceramics will be expected by growing - in a matrix of microcrystals of β-phase Si_3N_4 - an appreciable amount of extensively large, rod-shape crystals of the same phase. It is anticipated that the large grains should play as crack impediments like whiskers mixed in composite ceramics. The test materials prepared by changing firing conditions had such well-grown crystals of different size, ranging from 2 to 10 microns in diameter. The fracture toughness (measured by the SEPB method) increases up to 11.3MPa·m$^{1/2}$ with the increase in the grain size. Prominent crack bridging along the fracture surface behind the propagating crack tip is found to be the possible toughening mechanism.

[Received October 15, 1990; Accepted December 14, 1990]

Key-words: Silicon nitride, Fracture toughness, Microstructure, Grain size, High toughness, Crack bridging, Crack deflection, Grain growth.

1. Introduction

Covalent bonds of silicon nitride make it stabler than oxide ceramic materials at high temperature, permitting application to various engine parts such as turbocharger rotors.[1] The common disadvantages of ceramic materials are their fragility and lower reliability than metals, which tend to limit wide industrial applications. It is essential for silicon nitride ceramics to have improved fracture toughness in order to be used on a wide scale as structural materials. One possible method to improve fracture toughness is to form microscopic mechanisms within the sinter structures to augument fracture energy. Reinforcement with whiskers, long carbon fibers and dispersed particles are being attempted to improve the fracture toughness of silicon nitride.[2,3]

Structure of sintered silicon nitride is characterized by acicular β-Si_3N_4 grains entwined three-dimensionally with each other, the grains being formed by the α→ β transformation via the liquid phase and giving microscopic structure similar to those of composite materials reinforced with whiskers. Sintered silicon nitride, therefore, is sometimes called "in-situ composite." Meanwhile, some researchers are improving fracture toughness by growing whisker-like acicular grains.[4,5]

In this study, several types of silicon nitride sinters were prepared in which the size of acicular grains was changed by controlling the operating conditions to investigate the effects of grain size on fracture toughness of the sinter. As a result, it has been found that fracture toughness increases in proportion to the square root of the size of the acicular β-Si_3N_4 grains, to a maximum 11.3MPa·m$^{1/2}$. Moreover, crack propagation was observed for discussion on its effects on the mechanisms for improving fracture toughness.

2. Experiments

2.1. Experimental Procedure

Figure 1 illustrates the flow diagram for the preparation of sintered silicon nitride. The starting material was silicon nitride powder prepared by the imide process and containing 5wt% of Y_2O_3 and 2wt% of Al_2O_3 as the sintering aids (SN-COC, Ube Industries). After adding a dispersant and binder, the starting powder was mixed in the presence of a solvent and then crushed/mixed by an attrition mill (also in the presence of a solvent). The mixture was treated ultrasonically, and then granulated/dried by a spray drier into 150-μm granules which were pressed uniaxially under a pressure of 30MPa into 15x25x80mm blocks. Each block was treated by cold isostatic pressing under a pressure of 300MPa, degreased and sintered. In this study, a total of more than 10 types of sintered silicon nitride, consisting of acicular grains of different size, were prepared by changing the sintering conditions only.

The sintered bodies were analyzed by several methods: scanning electron microscopic (SEM) analysis to observe the fractured and ground surfaces, and the SEPB method (in acccordance with JIS R1607) to determine fracture toughness K_{IC}. Furthermore, acicular grain size was determined on photographs by the method described later to investigate the effects of grain size on fracture toughness.

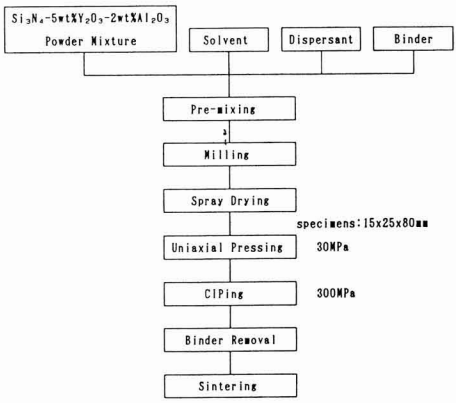

Fig. 1. Processing of the silicon nitride ceramics

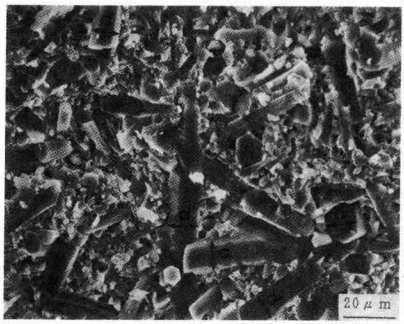

Fig. 2. SEM fractograph of a sintered Si_3N_4: Arrows define the diameter of large grains.

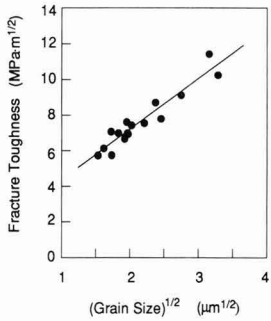

Fig. 3. Dependence of the fracture toughness on the grain size of the Si_3N_4 ceramics

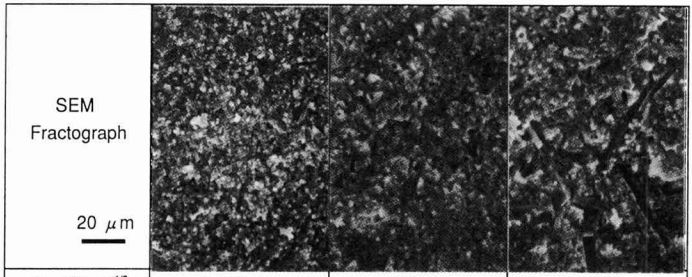

K_{IC} (MPa·m$^{1/2}$)	5.7	6.9	7.7
Grain-Size: d (μm)	2.4	3.9	6.0
$d^{1/2}$ (μm)$^{1/2}$	1.55	1.97	2.45

Fig. 4. SEM fractographs and the fracture toughness

2.2. Observation of Structure

After K_{IC} was measured by SEPB method, the fractured surface of the specimen was observed by SEM. Polished surfaces with Vickers indentation, and those after etched with 50%HF + 50%HNO_3 were also observed by SEM to examine propagation of cracks.

2.3. Measurement of Acicular Grain Size

On each of 5 fields of SEM photograph of fractured surface of a specimen, 10 "coarse" acicular crystals were selected and minor axes were measured. The average value of the largest 20 out of 50 measurements was defined as the grain size of each specimen. The black arrows shown in **Figure2** indicate the measured grains.

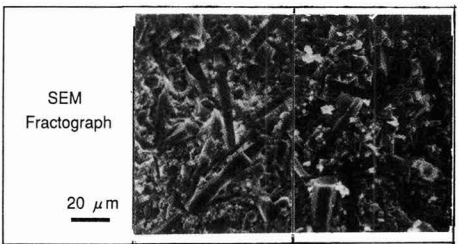

K_{IC} (MPa·m$^{1/2}$)	9.2	11.3
Grain-Size: d (μm)	7.7	10.0
$d^{1/2}$ (μm)$^{1/2}$	2.77	3.16

Fig. 5. SEM fractographs and the fracture toughness

3. Results and Discussion

3.1. Effects of Size of Acicular β-Si_3N_4 Grains on Fracture Toughness

Figure 3 shows the effects of the size of acicular β-Si_3N_4 grains on fracture toughness of the sinter, and **Figs.4** and **5** show the SEM photographs of the fracture faces of the typical silicon nitride sinters, together with their K_{IC}, acicular grain size values and square root of the size. Fracture toughness is proportional to square root of the grain size, as shown in Fig.3. This relationship is in agreement with that for alumina reinforced with SiC whiskers obtained by P.F. Becher et al., assuming that improved fracture toughness results from crack bridging.[6] It also coinsides with results presented by Maeda et al., who investigated the effects of the size of thick whiskers (up to 1.85μm or less in diameter) on fracture toughness.[7] The grain size of silicon nitride prepared in this study were fairly large (maximum 10μm) as shown in Fig.5, and the sinter had a K_{IC} value of 11.3MPa·m$^{1/2}$, which was roughly 2 times higher than that of the sinter having a grain size of 2.4μm. Thus, increasing size of the acicular grains has been found to increase fracture toughness of the monolithic silicon nitride ceramics, as

increasing size of SiC whiskers added increases fracture toughness of alumina composites. It is therefore considered that coarse acicular grains play a role similar to that of whiskers in improving fracture toughness.

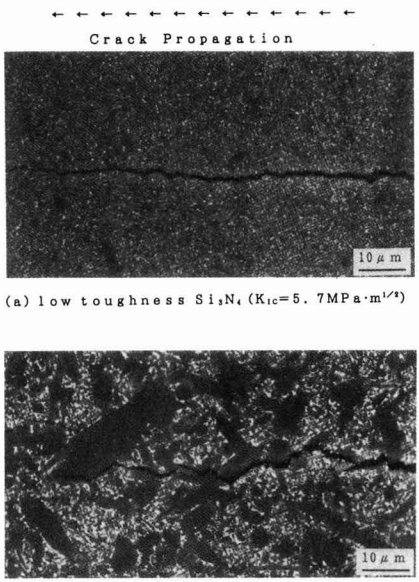

Fig. 6. Crack propagation morphology of two different types of Si_3N_4-ceramics: (a)low toughness Si_3N_4 (K_{IC}=5.7MPa·$m^{1/2}$), (b)high toughness Si_3N_4 (K_{IC}=11.3MPa·$m^{1/2}$). (Back scattered electron image)

3.2. Mechanisms for Improving Fracture Toughness of Silicon Nitride

Propagation of cracks through silicon nitride ceramics, with improved toughness by increasing size of the acicular grains, was observed to discuss the mechanisms for improving fracture toughness. **Figure 6** shows cracks originating from Vickers indents on the ground surfaces and running through the sintered silicon nitride specimens having a fracture toughness K_{IC} of 5.7 and 11.3MPa·$m^{1/2}$. The crack ran almost straight in the specimen of smaller grains (K_{IC}: 5.7MPa·$m^{1/2}$), whereas it zig-zagged along the grain boundaries around the coarse acicular grains in the specimen of larger grains (K_{IC}: 11.3MPa·$m^{1/2}$) showing so-called crack deflection.

Figures 7 and **8** show the cracks induced by the Vickers indents on the ground surfaces of the specimen having a K_{IC} of 9.2MPa·$m^{1/2}$. Around the coarse acicular crystals in Fig. 7, crack bridgings (marked with C) and branched cracks running in parallel (marked with B) are seen. In Fig.8, pull-out of the coarse acicular grains was observed (marked with P).

Figure 9 shows the indent-induced crack running on the ground surface etched with 50% HF + 50% HNO_3. The specimen had a K_{IC} of 9.2MPa·$m^{1/2}$. Crack bridging is shown in which the crack propagates in zig-zag fashion along the grain boundaries around the coarse acicular grains and breaks the coarse grains.

Thus, SEM analysis has shown the presence of crack deflection, branching and bridging as well as grain pull-out as a result of the introduction of coarse, acicular β-Si_3N_4 grains. The crack deflection theory[8] assumes that fracture toughness increases depending on the volumetric fraction and aspect ratio of the secondary phase (corresponding to the coarse acicular crystals in our specimens crystals), but not on the thickness of the whiskers or the acicular crystals.

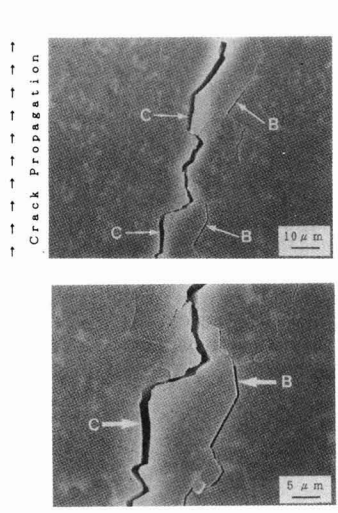

Fig. 7

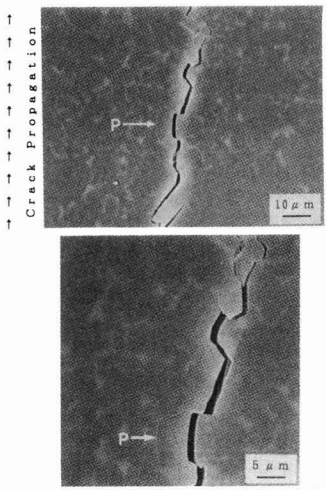

Fig. 8

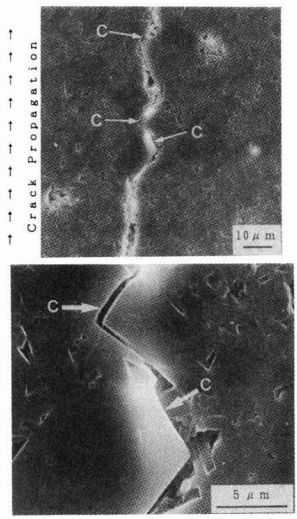

Fig. 9

Fig. 7. Crack bridging and branch-off phenomena in a high toughness Si_3N_4: B=branch-off, C=crack bridging (Back scattered electron image).

Fig. 8. Pull-out phenomena in a high toughness Si_3N_4: P=pull-out (Back scattered electron image).

Fig. 9. Crack deflection and crack bridging phenomena in a high toughness Si_3N_4: C=crack bridging (Back scattered electron image; etched with 50%HF + 50%HNO_3)

The pull-out theory considers increased fracture toughness as resulting from friction working in the interface between the whisker or grain and the matrix, which dissipates energy. The crack bridging theory, on the other hand, maintains that increased fracture toughness is due to crack bridging as a result of the separation of the whisker from the matrix, assuming that increased fracture toughness dK is given by the following formula:[6)]

$$dK = \sigma_f^w(V_f E^c G^m r/6(1-\nu^2)E^w G^i)M\text{^}1/2$$

where

E : modulus of elasticity
G : energy release rate
V_f : volumetric ratio of whiskers
r : whisker radius
σ_f^w : whisker strength
ν : Poisson ratio

subscripts c, w, m and i stand for composite, whisker, matrix and interface.

In other words, fracture toughness of a whisker-reinforced ceramic increases in proportion to the square root of whisker diameter. Fracture toughness of the sinters prepared in this study was found to increase in proportion to the square root of acicular β-Si_3N_4 grain size, indicating that above formula was valid for the results of this study when the coarse acicular grain was regarded as a whisker. It was also observed that there were some fractures considered to result from bridging of the coarse acicular grains. Thus, the increased fracture toughness observed in this study is explained much better by crack bridging by the coarse acicular grains than by crack deflection, crack branching or pull-out of the coarse acicular grains.

It has been demonstrated that formation of the coarse acicular β-Si_3N_4 grains within the sinter structure increased fracture toughness of the sinter to a maximum 11.3MPa·$m^{1/2}$. This method to improve fracture toughness will be particularly useful for the process to produce complex shapes, because it is free of the problems associated with the production of whisker-reinforced and other composite materials such as orientation of the reinforcing materials and sintering.

4. Conclusions

1) Fracture toughness of sintered silicon nitride was increased by introducing coarse acicular β-Si_3N_4 grains into the sinter structures in proportion to square root of the grain size (length of the minor axis).
2) Increasing the average size of acicular β-Si_3N_4 grains to 10μm increased fracture toughness K_{IC} of the sintered Si_3N_4 to 11.3MPa·$m^{1/2}$.
3) It is considered that the increased fracture toughness observed in this study is mainly due to crack bridging effects by the coarse acicular grains.

References:

1) T. Ito, J. of Gas Turbine Society of Japan, 17-67, 41-49 (1989).
2) P.D. Shales, J.J. Petrovic, G.F. Hurley and F.D. Gac, 65, 351-56 (1986).
3) M. Iwata and E. Hisada, Fine Ceramics, 10, 162-69 (1989).
4) E. Tani, S. Umebayashi, K. Kobayashi and M.Nishijima, Am. Ceram. Soc. Bull., 65, 1311-15 (1986).
5) K. Matsuhiro and T. Takahashi, Ceram. Eng. Sci. Proc., 10, 807-16 (1989).
6) P.F. Becher, C.H.Hsueh, P.Angelini and T.N. Tiegs, J. Am. Ceram. Soc., 71, 1050-61 (1988).
7) E. Maeda and T. Funahashi, Kagaku Kogyo, 40, 792-98 (1989).
8) K.T. Faber and A.G. Evans, Acta Metall., 31, 565-76 (1983).
9) F.F. Lange, Phill. Mag., 22, 983-992 (1970).

This article is a full translation of the article which appeared in Nippon Seramikkusu Kyokai Gakujutsu Ronbunshi (Japanese version), Vol.99, No.4, 1991.

Growth Behavior of Manganese-Metallized Layer on Silicon–Nitride Ceramics

Toshiyuki Takashima, Tsuyoshi Yamamoto and Toshio Narita*

Dept. of Mechanical Engineering, Hokkaido Institute of Technology
4-1, 15-chome, 7-jo, Maeda, Teine-ku, Sapporo-shi 006, Japan
*Dept. of Metallurgical Engineering, Faculty of Engineering, Hokkaido University
Nishi 8-chome, Kita 13-jo, Kita-ku, Sapporo-shi 060, Japan

The initial stage growth of a metallized layer of silicon-nitride ceramics was investigated by the vapor-diffusion method. The metallization was carried out using manganese powder as a vapor source under a dynamic vacuum condition from 1073 to 1273K up to 129.6ks.
The metallization process was found to be divided into two reaction stages. At the initial stage a two layer structure was found; the surface layer of Mn_6Si and alpha-Mn(Si), and the bottom layer of $MnSiN_2$ and oxide additives. The thickness of the bottom layer increased rapidly at the onset of the initial stage. This change in layer thickness is due to the reaction of Si_3N_4 ceramics with manganese gas molecules supplied directly through opening and pores in the growing surface layers.
After the initial transition period, the surface layer became compact, and a middle layer, a mixture of alpha-Mn(Si), Mn_6Si and oxide additives, was newly formed by decomposition of the bottom layer. Consequently, the thickness of the bottom layer decreased. Thereafter, it remained almost constant at 6.0μm at 1173K, 4.8μm at 1223K and 4.0μm at 1273K.
Under steady state condition, it was found that the growth of the surface layer and bottom plus middle layer obeyed the parabolic rate law, respectively.
[Received October 24, 1990; Accepted January 24, 1991]

Key-words: Metallization, Silicon-nitride, Manganese, Vapor-Diffusion, $MnSiN_2$, Mn_6Si, Surface modification

1. Introduction

The authors have been studying vapor-phase metallization of ceramic surfaces and metal-ceramic reactions, considering that ceramic materials are used, together with metals, as part of functional and structural materials.[1-3]

They have discussed structures and the formation mechanism of Mn-Metallized layers on silicon nitride.[4] The metallized layer consists of a bottom, middle and surface layer. The overall layer grew, following the parabolic law, with a rate constant kp in a range from $3.2\times10^{-14}m^2\cdot s^{-1}$ at 1173K to $8.9\times10^{-13}m^2s^{-1}$ at 1273. Energy of activation Qkp on the growth of the overall layer was $414kJ\cdot mol.^{-1}$

It was found, during the initial stage, that the layer grew in a manner different from the steady-state behavior observed previously.[4] In this study, the authors have investigated the behavior of the growth layer during the initial stage of the metallization process and the mechanisms involved in the steady-state growth of individual bottom, middle and surface layers.

2. Experimental Procedure

2.1. Sample Preparation

The silicon nitride ceramic (Si_3N_4) samples were 12.5mm square, 3.5mm thick blocks, sintered under atmospheric pressure, and containing Y_2O_3, Al_2O_3 and a Ti compound as the sintering aids. They were 90wt% pure. The detailed sample preparation procedure is described elsewhere.[4] Their major properties were flexural strength of 735MPa, Young's modulus of 284GPa, Poisson ratio of 0.24 (all of these were at room temperature), and thermal expansion coefficient of $3.2\times10^{-6}K^{-1}$ (room temperature to 1073K). Both sides of each sample block were lapped by a #600GC wheel to an average roughness of 0.53μm Ra, and then buffed by diamond paste (particle size: 1.0μm max.). Each ground sample was cut into a 6mmx12.5mm specimen, which was ultrasonically degreased.

2.2. Metallization with Mn Vapor

The commercial Mn powder (purity: 99.0wt% or more, particle size: 200mesh or less) was used as the Mn vapor source. The metallization was carried out in the same manner as described previously,[4] in which the specimens were placed together with approximately 15g of the Mn powder in a steel container (inner diameter: 16mm), and heated by a horizontal resistance oven under a constant pressure of 1.3×10^{-2}Pa to 1073 to 1273K for a given time (0 to 129.6ks, where time 0 meant that the specimen was immediately cooled as soon as it reached a given time). Both heating and cooling rates were $8.3\times10^{-2}K\cdot s^{-1}$.

The Mn-metallized specimen was embedded into resin so as to be cut at a right angle to the metallized surface; the cross-section was observed by an optical microscope, scanning electron microscope (SEM) and an electron probe microanalyzer (EPMA), after the surface was ground. In addition, thickness of the metallized layer was determined by SEM photographs. The metallized surfaces were analyzed by the X-ray diffraction analysis (XRD), in addition to those used for the cross-sections.

3. Results and Discussion

3.1. Growth of Metallized Layer

Figure 1 presents the cross-sectional microstructure of the metallized sample, prepared at 1223K for 14.4ks, and

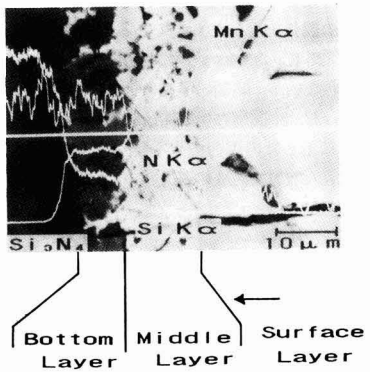

Fig. 1. Cross-sectional microstructure of a metallized layer at 1223K for 14.4 ks and EPMA line profiles of each element: Mn Kα, Si Kα and N Kα.

the EPMA-determined line profiles of Mn, Si and N. The metallized layer over Si_3N_4, prepared with the Mn vapor, consisted of the surface layer of the Mn_6Si phase and a Mn(Si) solid solution, the middle layer of the Mn_6Si phase and a Mn(Si) solid solution, as was the case with the surface layer, but containing a phase for the agglomerated sintering aids, and the bottom layer facing the Si_3N_4 surfaces of the ternary phase of $MnSiN_2$ containing the phase of the agglomerated sintering aids.

From the behavior of the sintering aids, position of original surface of the ceramics was estimated as the top most position of the region through which sintering aids dispersed. That is, the interface between middle and surface layers is the original surface of Si_3N_4, middle and bottom layers were decomposed layer of Si_3N_4 formed by metalization (combination of these layers is hereinafter referred to as the Si_3N_4 ceramic decomposition layer).

Figure 2 shows the effects of time on thickness of the decomposition(○), surface(Δ), and overall layers(❑) prepared at different temperature levels. Growth of each layer almost followed the parabolic law at each temperature level tested. **Table 1** presents rate constants *kp* of the growth of these layers.

The Arrhenius plots for the growth of the decomposition and surface layers yielded a group of straight lines, from which activation energy Q_{kp} was estimated as 434kJ·mol^{-1} and 401kJ·mol^{-1} for the decomposition and surface layers, respectively. Activation energy for the overall layer was 414kJ·mol^{-1}, which was lying between those for the decomposition and surface layers.

3.2. Structures of Layers Formed during Initial Stage of Metallization Process

Figure 3 presents the photographs showing changes in the cross-sectional structures of the metallized layers, prepared at 1223K for 3.6 to 57.6ks, where the left side of the figure represents the Si_3N_4 body. The dark portion on the right side of Fig.3 (a) represents the embedded resin to protect the surface. The metallized layer consisted of the surface layer and the bottom layers at 3.6ks (a). The middle layer between the surface and bottom layers appeared at 14.4ks (b), which grew with time. Only a portion of the surface layer is presented in Fig.3(b) and thereafter. As shown in these photographs, the bottom layer was relatively thick during the initial stages, but lost its thickness gradually with time. Similar trends were observed with the layers prepared at 1173 and 1273K. The EPMA and XRD analysis indicated that the surface layers consisted of the Mn_6Si phase containing the αMn phase, and the bottom layer mainly of the $MnSiN_2$ phase, as previously discussed.[4]

3.3. Behavior of Metallized Layer Growth

Figure 4 shows the effects of metallization time on thickness of the bottom layer, prepared at 1173, 1223 or 1273K. Thickness of the bottom layer was approximately 3μm, when it was prepared at 1173K for 3.6ks. It increased sharply with time to a maximum of approximately 10μm at 14.4ks, and then decreased thereafter with time to 6.0μm at 57.6ks. It attained a maximum of approximately 8.5μm at 3.6ks, when the layer was metallized at 1223K, and decreased thereafter with time until it reached a constant level of 4.8μm at 32.4ks. On the other hand, thickness of the bottom layer prepared at 1273K was the greatest (approximately 6.0μm) at a holding time (metallization time) of zero, and decreased thereafter until it reached a constant level of 4.0μm at 14.4ks. No peak of thickness was observed with the layer prepared at 1273K, unlike with the other ones. The layer started to grow at a relatively low temperature, as demonstrated by the results for 1173K, and hence it was considered that the bottom layer ceased to grow during the heating process before the temperature reached

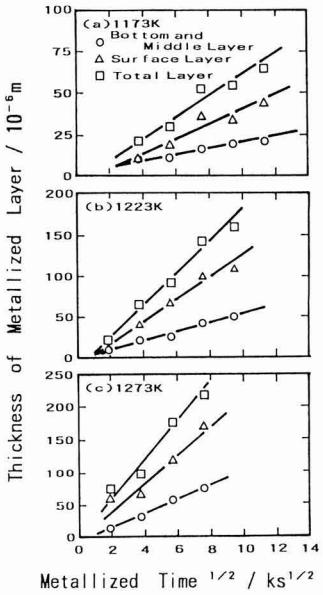

Fig. 2. Growth of bottom and middle layer (○), surface layer (Δ) and total layer (❑) with square root of metallized time at (a) 1173K, (b) 1223K and (c) 1273K.

Table 1. Rate constants (kp) for the growth of metallized layers

Layer	Surface	Bottom and Middle	Total
	kp / m²·s⁻¹	kp / m²·s⁻¹	kp / m²·s⁻¹
1173K	1.5×10⁻¹⁴	3.1×10⁻¹⁵	3.2×10⁻¹⁴
1223K	1.4×10⁻¹³	2.9×10⁻¹⁴	3.0×10⁻¹³
1273K	3.7×10⁻¹³	9.9×10⁻¹⁴	8.9×10⁻¹³

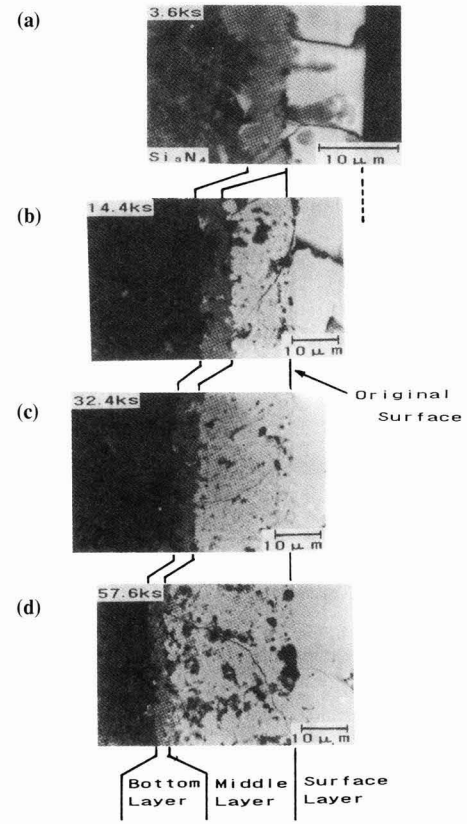

Fig. 3. Cross-sectional microstructure of the metallized layers at 1223K for 3.6ks to 57.6ks.

1273K.

The results indicated that the bottom layer became thicker during the initial stage of the metallization process, but decreased to a thickness characteristic of metallization temperature. The time periods in which the thickness changed and remained constant depended on the characteristic mechanisms of the growth layer.

Figure 5 shows the effects of metallization time on thickness of the middle layer, estimated from the distributions of the oxide-base sintering aids.[4] The middle layer was found to grow with time, though not detected by 14.4ks at 1223K, 3.6ks at 1223K and 0ks at 1273K. Time at which the middle layer started to grow almost corresponded to the region in which thickness of the bottom layer decreased, shown in Fig.4. Increased thickness of the middle layer was noted as metallization temperature increased.

3.4. Mechanisms of Layer Growth

Figure 6 presents the surface structure (SEI images) and X-ray images by EPMA (SiKα, MnKα, NKα, AlKα and YLα) taken to investigate growth of the layer during the initial stage, in which the sample was heated, in the same manner as in metallizing treatment, to 1073K and then immediately cooled. The surface structure was generally characterized by a mixture of relatively large (2 to 3μm in size) blocks and smaller (1μm or less) grains, though there were dark portions in places which were free of the above structure.

The EPMA analysis detected Mn (c) clearly in the blocks, and Si (b) and N (d) in the grains of 1μm or less in size. Al(e) and Y (f), in addition to Si and N, were detected in the dark portions where no blocks or grains were found. These results, coupled with those for Mn, Si and N shown in Fig.1, indicate that the block structure in which Mn was detected corresponded to the initial surface layer and the smaller grain structure, in which Mn, Si and N were detected, to the initial bottom layer. The dark portions represented the unreacted ceramic base.

The mechanisms involved in the growth of the metallized layer are discussed below: First, Si_3N_4 ceramic material (s) reacts directly with the Mn (g) vapor, to form

$$Si_3N_4(s) + 2Mn(g) \rightarrow 2MnSiN_2(s) + Si(s) \quad . . (1)$$

Si(s) formed by the reaction (1) reacts with the Mn(g) vapor on the surfaces, to form βMn(Si) (s.s.):

$$Si(s) + Mn(g) \rightarrow \beta Mn(Si)\ (s.s.) \quad . . . . . (2)$$

Assuming that Si_3N_4 is thermally decomposed at a high temperature and a high vacuum, the following reactions (3), (4) and (5) may possibly occur, to grow the metallized layer,

$$Si_3N_4(s) \rightarrow 3Si(s) + 2N_2(g) \quad . . . . . (3)$$

$$2Mn(g) + 3Si(s) + 2N_2(g) \rightarrow 2MnSiN_2(s) + .Si(s). \quad . . . . . (4)$$

$$Si(s) + Mn(g) \rightarrow \beta Mn(Si)\ (s.s.) \quad . . . . . (5)$$

though to only a limited extent, if they occur at all, because it has been confirmed that the metallized layer grew even

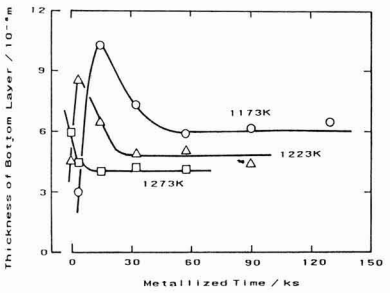

Fig. 4. Changes in thickness of bottom layer with metallized time at 1173K, 1223K and 1273K.

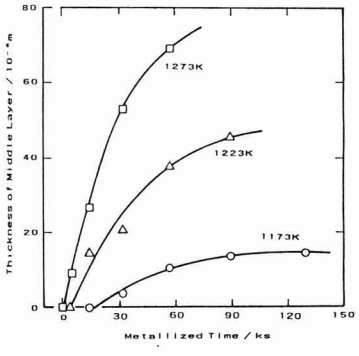

Fig. 5. Changes in thickness of middle layer with metallized time at 1173K, 1223K and 1273K.

at relatively mild conditions of 1073K and 10^{-2}Pa, as shown in Fig.6.

Figure 7 shows schematically the process of the metallized layer growth ((a) through (d)) and the layer structure model at room temperature (e). During the initial stage of the metallization process, it is apparent, as shown in Fig.6, that $MnSiN_2$ for the bottom layer and βMn (Si) for the surface layer are formed irregularly. It is therefore possible for the Mn vapor to go directly into the bottom layer and Si_3N_4 base through the unformed portions of the surface layer. There will be a number of pores in the surface layer, as shown in Fig.7(b), until the layer is fully densified, to provide passages for the Mn vapor. It is therefore considered that the directly supplied Mn vapor helps the bottom layer growth in a relatively short time.

The pores in the surface layer gradually diminished as the layer growth (Fig.7(c)). The supply of Mn depends on diffusion through the surface layer, instead of a direct supply, after these pores are disappeared.

As a result, decomposition of the bottom layer proceeds, in preference to its growth, and Mn and Si as the decomposition products will be consumed for the growth of the middle and surface layers, while nitrogen is driven off:

$$MnSiN_2(s) \rightarrow \beta Mn(Si)\ (s.s.) + N_2(g)\uparrow \quad \ldots . (6)$$

Thickness of the bottom layer under the steady-state metallization conditions (represented by Fig.7(d)) is constant, with a level characteristic of metallization temperature, as shown in Fig.4 (6μm at 1173K, 4.8μm at 1223K and 4μm at 1273K). This conceivably results from an equilibrium produced between decomposition and formation of $MnSiN_2$ in the bottom layer, the level of which is determined by temperature. Increasing metallization temperature reduces thickness of the bottom layer, which is a thermodynamically reasonable phenomenon, because the standard Gibbs free energies ΔG° of general nitrogen compounds approach a positive level, i.e., they become unstable, as temperature increases.

The cooled metalized layer consists of the bottom layer of the $MnSiN_2$ phase, as before, and the middle and surface layers of the mixed αMn (Si) and Mn_6Si phases, as shown in Fig.7(e). It is considered, based on the Mn-Si equilibrium phase diagram,[6] that Mn_6Si pecipitate first from the βMn(Si) during the cooling process, and then αMn and Mn_6Si precipitate by the eutectic transformation at 908K. The agglomerated phases of the sintering aids are dispersed in the bottom and middle layers.

4. Conclusions

The metal vapor diffusion method was used to metallize the silicon nitride ceramic surfaces with Mn vapor, to investigate the growth mechanisms and structure of the metallized layer during the initial stage of metallization.

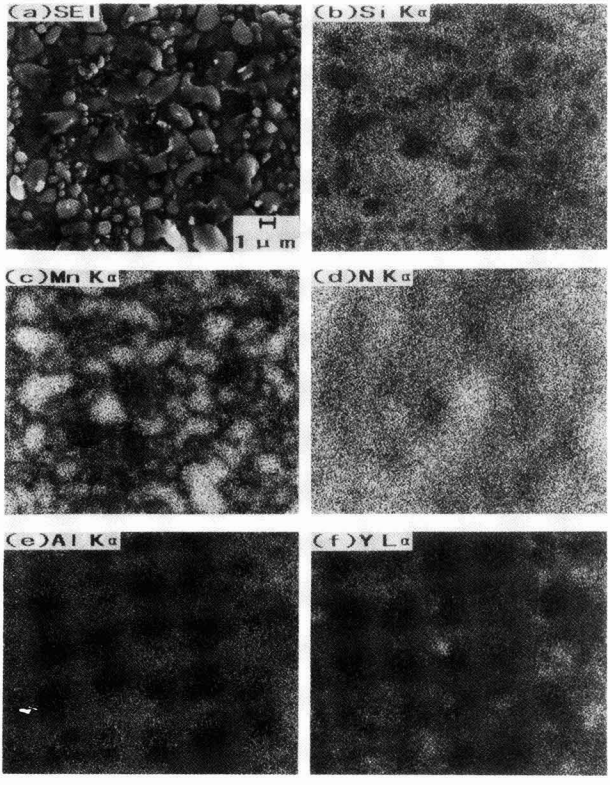

Fig. 6. Surface microstructure and X-ray image photographs of a metallized layer at 1073K for 0(zero)ks: (a) SEI, (b) Si Kα, (c) Mn Kα, (d) N Kα, (e) Al Kα and (f) Lα.

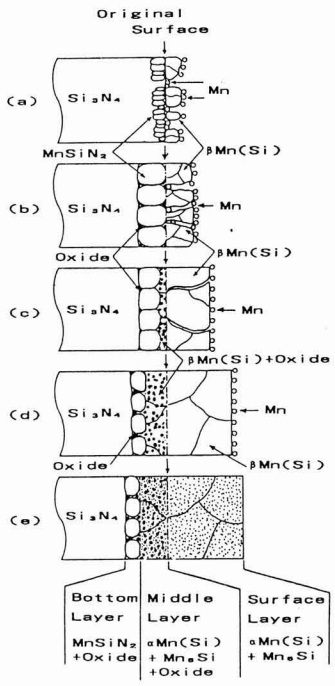

Fig. 7. Transition of metallized layer. (a) to (c) initial stage, (d) proceeding stage, and (e) room temperature.

1) The surface layer and the Si_3N_4 ceramic decomposition layer grew almost exactly following the parabolic law. The transition period was observed before the steady-state conditions were established, during the initial stage of the metallization process.
2) The metallized layer formed during the initial stage of metallization was of a two-layer structure, consisting of the surface layer (of the Mn_6Si phase containing the αMn) and bottom layer (of the $MnSiN_3$ phase containing the agglomerated oxide phase), and no middle layer was found.
3) Thickness of the bottom layer increased and decreased gradually during the initial stage of metallization, and attained thereafter a constant level determined by metallization temperature (6μm at 1173K, 4.8μm at 1223K and 4μm at 1273K).
4) Mn was supplied directly to the Si_3N_4 base through the pores in the irregular surface layer during the transition period in the initial stage of metallization. Supply of Mn was decreased after the surface layer densified, because it was dependant on diffusion through the solid phase of the surface layer.
5) The changed Mn supply mechanism caused decomposition to proceed preferentially in the bottom layer. Mn and Si formed by the decomposition were consumed for the growth of the layer, and N_2 was deflected from the system. As a result, thickness of the bottom layer decreased until it attained a constant level.

Reference:

1) T. Takashima, T. Yamamoto and T. Narita, Seramikkusu Ronbun-shi, 96, 1-5 (1988)
2) T. Takashima, T. Yamamoto and T. Narita, ibid., 97, 38-42 (1989)
3) T. Takashima, T. Yamamoto and T. Narita, ibid., 98, 36-42 (1990)
4) T. Takashima, T. Yamamoto and T. Narita, ibid., 98, 1034-38 (1990)
5) "Metals Data Book," edited by the Japan Institute of Metals, Maruzen, p.92
6) T.B. Massalski, J.L. Murray, L.H. Bennett, H.Baker, "Binary Alloy Phase Diagrams," A.S.M, Vol.2 (1986) p.1588.

This article is a full translation of the article which appeared in Nippon Seramikkusu Kyokai Gakujutsu Ronbunshi (Japanese version), Vol.99, No.4, 1991.

Fabrication and properties of (Y,Ce)-TZP/Al_2O_3 Substrates

Masanori Hirano and Hiroshi Inada

Noritake Co., Limited
Noritake, Nishi-ku, Nagoya-shi 451, Japan

The effect of alumina content on the electrical and thermal properties of substrates consisting of tetragonal zirconia polycrystals and various volume fractions of Al_2O_3 was studied. The substrates were fabricated by the doctorblade casting, using an Al_2O_3 powder and coprecipitated zirconia powders with compositions 4mol%$YO_{1.5}$-4mol%CeO_2-ZrO_2 and 3mol%Y_2O_3-ZrO_2, and their surface roughness and microstructure were investigated. The average surface roughness (Ra) of the substrates was smaller than 0.1μm. The dielectric constant(ε), dielectric loss tangent (tan δ) and thermal expansion coefficient of the substrates decreased with increasing alumina content. The volume resistivity of the substrates was not sensitive to the alumina content in the range of 33.9 to 69.8vol%. It depended on the volume resistivity of TZP.

[Received August 18, 1990; Accepted November 19, 1990]

Key-words: Tetragonal zirconia polycrystals, (Y,Ce)-TAP/Al_2O_3 substrate, Surface roughness, Volume resistivity, Dielectric constant, Dielectric loss tangent, Thermal expansion coefficient

1. Introduction

Partially stabilized zirconia (PSZ) which quasi stably contains tetragonal zirconia stable at high temperatures, and tetragonal zirconia polycrystals (TZP) show stress-induced martensitic phase transformation at the crack edges, which relaxes fracture stress.[1,2] This accounts for their high strength and toughness. It should be noted, however, that Y-TZP containing Y_2O_3 as stabilizing agent undergoes a phase transformation from the tetragonal into the monoclinic phase, when annealed at a low temperature of around 200°C, losing its strength.[3-5] Many researchers are examining this low-temperature degradation phenomenon and the improvement of thermal stability.[6-8] In particular, a composite material consisting of (Y, Ce)-TZP, containing Y_2O_3 and CeO_2 as stabilizing agents, and alumina have a sufficiently high thermal stability and mechanical strength.[9] Zirconia ceramics are being used as structural material for machines, because of their good mechanical properties at room temperatures. A number of researchers have been reporting mechanical properties of various types of zirconia ceramics as structural materials, but few have examined them as the materials for circuit substrates, for which alumina is now being extensively studied.[10] Zirconia ceramics have potential to be used as material for circuit substrates, because of their high strength above 1000MPa, which is more than twice that of alumina.

In this study, composite materials of (Y, Ce)-TZP in which Y_2O_3 and CeO_2 were dissolved and alumina fabricated to investigate properties such as dielectric constant, volume resistivity, thermal conductivity and thermal expansion coefficient, which are essential for substrate materials. The sheets of composite material were prepared by the "doctor blade" method and sintered to produce substrates of (Y,Ce)-TZP/Al_2O_3 composite, whose surface properties such as surface roughness and microstructures were analyzed.

2. Experimental Procedure

2.1. Sample Preparation

Figure 1 illustrates the sample preparation process. Three types of partially stabilized zirconia powders, synthesized by the wet process (**Table 1**), were mixed with α-alumina (AL160SG, 99.9% pure, Showa Denko) in a given ratio (also shown in Table 1) in the presence of a solvent. Each mixture was formed preliminarily under a pressure of 19.6MPa, and then formed by cold isostatic pressing under 196MPa; the resultant green compact was sintered at 1500° to 1550°C for 2h. Furthermore, the slurry prepared by the procedure shown in Fig.1 was formed into a sheet by the "doctor blade" method, and the green sheet was sintered at 1500° to 1550°C for 2h to form a 150 to 250μm thick substrate.

2.2. Analytical Procedure

Density was determined by the Archimedean method, firing shrinkage was compared by the longitudinal length of the die-cut green sheet against the sintered one, and surface roughness was measured by a probe-type surface roughness

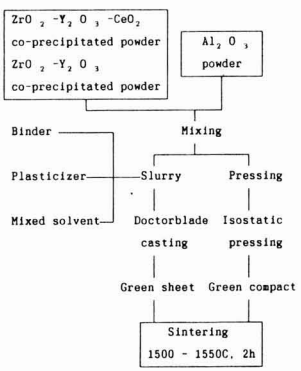

Fig.1. Flow diagram of the preparation of materials.

Table 1. Composition of specimens.

Material	Specimen	Composition				
		Zirconia powder			Al_2O_3	
		Composition (mol%)	(wt%)	(vol%)	(wt%)	(vol%)
	2.5Y	$2.5Y_2O_3$, $97.5ZrO_2$	100	(100)	0	(0)
Y-TZP	3Y	$3Y_2O_3$, $97ZrO_2$	100	(100)	0	(0)
(Y,Ce)-TZP	C	$4YO_{1.5}$, $4CeO_2$, $92ZrO_2$	100	(100)	0	(0)
	2.5Y25A	$2.5Y_2O_3$, $97.5ZrO_2$	75	(66.19)	25	(33.81)
	2.5Y40A	$2.5Y_2O_3$, $97.5ZrO_2$	60	(49.46)	40	(50.54)
	2.5Y60A	$2.5Y_2O_3$, $97.5ZrO_2$	40	(30.31)	60	(69.69)
Y-TZP/	3Y25A	$3Y_2O_3$, $97ZrO_2$	75	(66.22)	25	(33.78)
Al_2O_3	3Y40A	$3Y_2O_3$, $97ZrO_2$	60	(49.50)	40	(50.50)
	3Y50A	$3Y_2O_3$, $97ZrO_2$	50	(39.52)	50	(60.48)
	3Y60A	$3Y_2O_3$, $97ZrO_2$	40	(30.35)	60	(69.65)
	C12.5A	$4YO_{1.5}$, $4CeO_2$, $92ZrO_2$	87.5	(81.99)	12.5	(18.01)
(Y,Ce)-TZP/	C25A	$4YO_{1.5}$, $4CeO_2$, $92ZrO_2$	75	(66.11)	25	(33.89)
Al_2O_3	C40A	$4YO_{1.5}$, $4CeO_2$, $92ZrO_2$	60	(49.38)	40	(50.62)
	C50A	$4YO_{1.5}$, $4CeO_2$, $92ZrO_2$	50	(39.41)	50	(60.59)
	C60A	$4YO_{1.5}$, $4CeO_2$, $92ZrO_2$	40	(30.24)	60	(69.76)

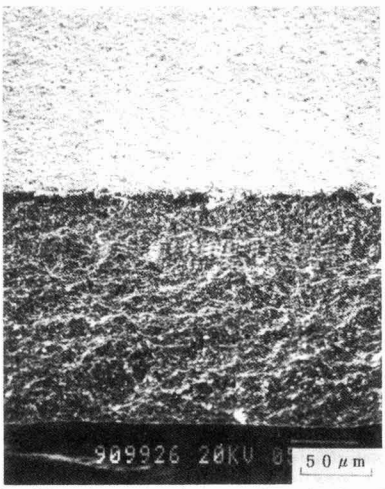

Fig.2. SEM photograph of the section of (4Y, 4Ce)-TZP/25wt%Al_2O_3 substrate.

Table 2. Thickness, density and firing shrinkage of substrates fired at 1500°C.

Material	Specimen	Density (g/cm^3)	Thickness (μm)	Firing shrinkage (%)
3Y-TZP	3Y	6.03	250	25.6
3Y-TZP/Al_2O_3	3Y25A	5.35	230	22.6
(Y,Ce)-TZP/Al_2O_3	C25A	5.37	210	22.0

meter (TAYLOR-HOBSON, Talysurf-10) for the center-line average roughness (Ra). The microstructures of the sintered samples were observed by a scanning electron microscope (SEM, Hitachi's S450). Identification and quantitative analysis of the surface phases were made by X-ray diffraction analysis, using the method proposed by Garvie et al.[11] Relative dielectric constant (ε), dielectric loss (tanδ) and volume resistivity were measured for the 52×52mm substrate specimen cut out of the 2.5mm thick sintered body. The specimen was screen-printed with electrode paste, and then baked. For volumetric resistivity, a voltage of 10 to 100V was applied to the specimen, to measure its resistance by a super insulation tester. Relative dielectric constant and dielectric loss were measured by an LCR meter (Yokogawa's 4275A) in a frequency range from 10kHz to 10MHz. Thermal conductivity was measured by the laser flash method (Shinku Riko Thermal constant analyzer, TC-3000), and thermal expansion coefficient was determined by a thermomechanical analyzer (Rigaku Denki TMA).

3. Results and Discussion

3.1. Surface Properties and Microstructures of the Substrate

Figure 2 presents the SEM photograph of the substrate prepared. **Table 2** gives density, thickness and firing shrinkage results of the three sheet specimens of 3Y-TZP, 3Y-TZP/25wt%Al_2O_3, and (4Y, 4Ce)-TZP/25wt%Al_2O_3, sintered at 1550°C. All of these specimens were prepared by the "doctor blade" method. They were sufficiently densified, to 99% or more of the theoretical density. All the specimens prepared in this study were 150 to 250μm thick. The alumina-containing sheets had a firing shrinkage 3% or more lower than the 3Y-TZP sheet, which is a result of improved conditions for packing density, such as alumina grains being larger than the zirconia grains and improved dispersion of the slurry in the presence of alumina. Kawamura et al. prepared 80 to 300μm thick zirconia/alumina composite sheets from partially stabilized zirconia with yttria and alumina hydrates as the starting materials, to investigate their microstructures and mechanical properties.[12] The composite sheet containing 90wt% of zirconia had a density of $4.9g/cm^3$ and a bending strength of 486MPa, and their report attributed insufficient strength to insufficient sinter density. The sheets prepared in this study attained a density of $5.37g/cm^3$, higher than 99% of the theoretical density, at a zirconia content of 75wt%.

Figure 3 and **Table 3** show the surface roughness results of the substrates prepared by the " doctor blade" method. The alumina-containing substrate surfaces, though rougher than those of the substrate of Y-TZP, were smoother than those of the conventional alumina substrate (alumina content: 96%, surface roughness: 0.3 to 0.4μm[13]), because the composite substrate prepared in this study from the micropowders, sintered at around 1500°C, consisted of

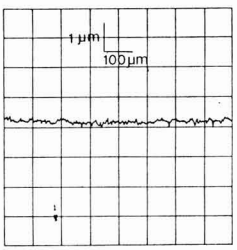

Fig.3. Surface roughness of (4Y, 4Ce)-TZP/25wt%Al_2O_3 substrate.

Table 3. Surface roughness of substrates fired at 1500°C.

Specimen	Ra(μm)
3Y	0.08
3Y25A	0.10
C25A	0.10

smaller particles than the conventional alumina substrate.

Figures 4 and **5** present the photographs of the surface and inside structures of the (4Y, 4Ce)-TZP/25wt%Al_2O_3 and 3Y-TZP/25wt%Al_2O_3 respectively sintered at 1500° and 1550°C, the black, angular particles representing alumina and the white particles zirconia. The structures of each sintered specimen are characterized by the alumina particles dispersed uniformly in the zirconia matrix. For the specimens sintered at 1500°C, the (4Y, 4Ce)-TZP/Al_2O_3 consisted of larger zirconia grains than the 3Y-TZP/Al_2O_3. For the specimens sintered at 1550°C, on the other hand, the 3Y-TZP/Al_2O_3 substrate consisted of the large and small zirconia grains, whereas the (4Y, 4Ce)-TZP/Al_2O_3 consisted of zirconia particles of relatively uniform size. It was also found that the TZP/Al_2O_3 substrate consisted of smaller zirconia particles than the alumina-free TZP substrate, conceivably because the alumina particles dispersed uniformly in the TZP matrix and worked to control growth of the zirconia grains.

3.2. Electrical Properties

Figure 6 shows the effects of Al_2O_3 content on dielectric constant of the TZP/Al_2O_3 sinters; dielectric constant decreased almost linearly as Al_2O_3 content increased. Dielectric constant of the (Y, Ce)-TZP was fairly high with a dielectric constant of 36.5, and that of TZP decreased greatly, when combined with alumina. However, the TZP/Al_2O_3 composite containing 60wt% of alumina had a relatively higher dielectric constant of 16.5 compared to that of high-purity (99.5% or more) alumina of 9 to 10.[14] The (Y, Ce)-TZP system had a slightly higher dielectric constant than the Y-TZP system. Okazaki proposes the following equation for a composite consisting of two components of different dielectric constants:

$$\log \varepsilon S=(1-V)\log \varepsilon S_a + V\log \varepsilon S_b$$

where

- εS: synthesized dielectric constant of a composite,
- V: packing rate of the crystals,
- εS_a: dielectric constant of the component filling the space around the crystals,
- εS_b: dielectric constant of the complete sinter.

Dielectric constant of the (Y, Ce)-TZP/Al_2O_3 system prepared in this study may be given by the following equation, knowing that dielectric constant ε of polycrystalline alumina is approximately 9.5 and assuming that dielectric constant ε of the (Y, Ce)-TZP system is 36.5, according to the Okazaki equation:

$$\log \varepsilon = (1-V_1-V_2) \log 36.5 + V_1 \log 9.5$$

where ε is relative dielectric constant of the (Y, Ce)-TZP/Al_2O_3, V_1 is volumetric packing rate of alumina, and V_2 is porosity of the (Y, Ce)-TZP/Al_2O_3 composition.

Table 4 shows the observed and calculated dielectric constant values of the (Y, Ce)-TZP/Al_2O_3 compositions, relative to alumina content. Both observed and calculated val-

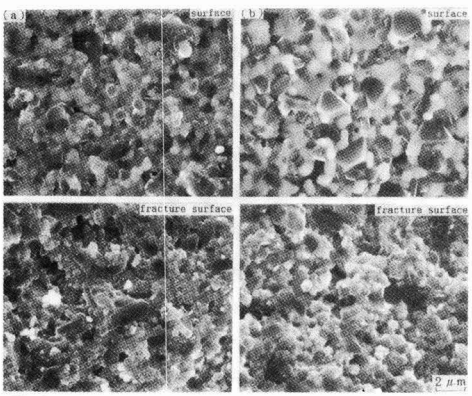

Fig.4. SEM photographs of the surface and the fracture surface of (4Y, 4Ce)-TZP/25wt%Al_2O_3 substrates sintered at (a) 1500°C and (b) 1550°C

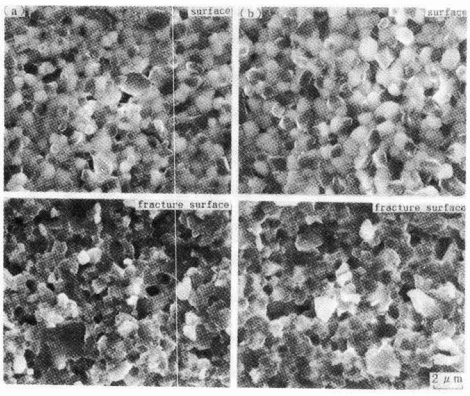

Fig.5. SEM photographs of the surface and the fracture surface of 3Y-TZP/25wt%Al_2O_3 substrates sintered at (a) 1500°C and (b) 1550°C.

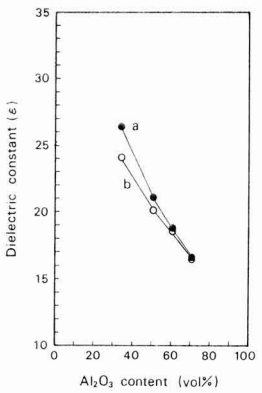

Fig.6. Relation between alumina content and dielectric constant of (a) (4Y, 4Ce)-TZP/Al_2O_3 and (b)3Y-TZP/Al_2O_3 substrates.

Table 4. Dielectric constants of (4Y, 4Ce)-TZP/Al_2O_3 substrates.

Alumina contents (wt%)	Alumina contents (vol%)	Dielectric constant (ε) Observed value	Calculated value
25	33.89	26.2	23.1
40	50.62	21.3	18.5
50	60.59	18.9	16.1
60	69.76	16.7	14.3

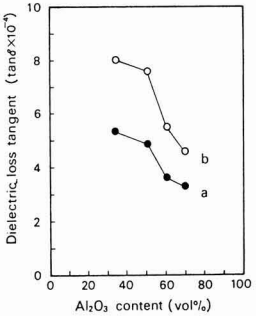

Fig.7. Relation between alumina content and dielectric loss tangent of (a) (4Y, 4Ce)-TZP/Al_2O_3 and (b) 3Y-TZP/Al_2O_3 substrates.

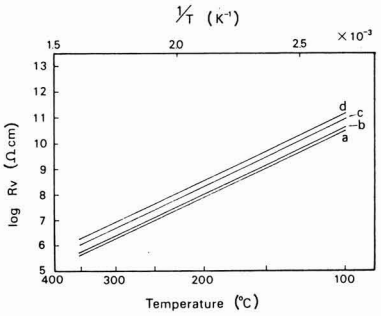

Fig.8. Relation between temperature and volume resistivity of (Y, Ce)-TZP/Al_2O_3 substrates.
(a) C25A, (b) C40A, (c) C50A and (d) C60A

ues decreased as alumina content increased, though the observed values were larger than the calculated ones. The discrepancy between the observed and calculated values is possibly the result of the effect of grain boundaries, because dielectric constant ε of alumina is the average of the two ε components, parallel and perpendicular to the c-axis: 10.55 and 8.6, respectively.

Figure 7 shows the effects of Al_2O_3 content on dielectric loss tangent (tanδ) of the TZP/Al_2O_3. It was observed that tanδ of the composites decreased as Al_2O_3 content increased (tanδ of Al_2O_3 is 1 to 2×10^{-4}).[14] The Y-TZP system had a slightly higher tanδ value than the (Y, Ce)-TZP system. The TZP/Al_2O_3 sample consisted of tetragonal zirconia and α-Al_2O_3 crystal phases, and the electrical properties of the composite were considered to lie between those of TZP and alumina.

Figures 8 and **9** show the effects of temperature on volumetric resistivity of the Y-TZP/Al_2O_3 and (Y, Ce)-TZP/Al_2O_3 compositions, respectively, and **Fig.10** displays the effects of Al_2O_3 content on volumetric resistivity. Kawamura et al. report that resistivity at room temperature of the zirconia composites is 4 to 6×10^{12}Ωcm at a zirconia content of 85wt%, and 2 to 4×10^{12}Ωcm at 90wt%.[12] In this study, the TZP/Al_2O_3 were found to have a volume resistivity of 10^6 to 10^7Ωcm at 300°C, lower than that of 99.5% of pure alumina 10^{14}Ωcm or more;[6] as shown in Fig.10, alumina lost resistivity sharply, when mixed with TZP; addition of approximately 30vol% TZP to alumina decreased logRV at 200°C to 8.6. Volumetric resistivity of the TZP/Al_2O_3 composites were greatly governed by TZP, though they exhibited a dependence on composition to some extent. This means that, even in a composite where alumina is the major component to form the matrix, its volumetric resistivity is determined by the amount of TZP dispersed in the matrix. It is therefore apparent that significant improvement in resistivity of a TZP/Al_2O_3 composite is not expected, because resistivity of TZP will increase only marginally.

3.3. Thermal Properties

Figure 11 shows the effects of Al_2O_3 content on thermal expansion coefficient of the (Y, Ce)-TZP/Al_2O_3 composition. The (4Y, 4Ce)-TZP/Al_2O_3 composition had a slightly lower thermal expansion coefficient than the 2.5Y-

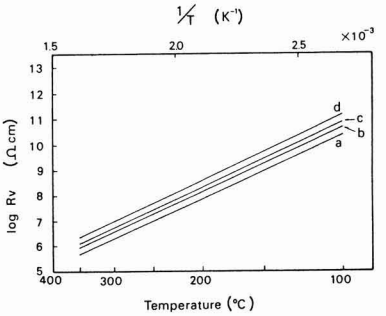

Fig.9. Relation between temperature and volume resistivity of Y-TZP/Al_2O_3 substrates.
(a) 3Y25A, (b) 3Y40A, (c) 3Y50A and (d) 3Y60A

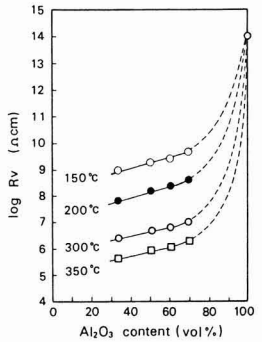

Fig.10. Relation between alumina content and volume resistivity of (Y, Ce)-TZP/Al_2O_3 substrates.

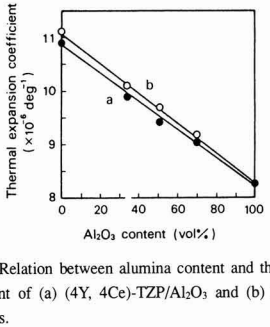

Fig.11. Relation between alumina content and thermal expantion coefficient of (a) (4Y, 4Ce)-TZP/Al_2O_3 and (b) 2.5Y-TZP/Al_2O_3 substrates.

Table 5. Thermal conductivity of (4Y, 4Ce)-TZP/Al_2O_3 substrates.

Specimen	Thermal conductivity (W/mK)	
	25℃	800 ℃
C12.5A	4.7	4.3
C25A	6.1	5.0

TZP/Al_2O_3 composition. Tsukuma et al. reported that thermal expansion coefficient of the Y-TZP composition decreased as content of Y_2O_3 as the stabilizing agent increased,[4] and the results of this study are in good agreement with Tsukuma et al.'s, because the (4Y, 4Ce)-TZP/Al_2O_3 composition contained a larger quantity of stabilizing agent. All samples showed linear expansion curves. **Table 5** gives the thermal conductivity results. Thermal expansion coefficient of the composite were on the line connecting those of the single-phase TZP and alumina sinters, and the same was true for thermal conductivity; thermal expansion coefficient decreased, while thermal conductivity increased as alumina content increased.

4. Conclusions

The effects of alumina content and zirconia composition on electrical and thermal properties of the (Y, Ce)-TZP/Al_2O_3 composite substrates were investigated. In addition, the surface conditions and microstructures of the composite substrates, prepared by the "doctor blade" method, were also investigated.

1) Relative dielectric constant (ε) and dielectric loss tangent ($\tan\delta$) of the composite decreased as alumina content increased.
2) No significant increase in volumetric resistivity of the composite was observed when alumina content was increased; resistivity of the composite was determined, even with the composite in which alumina was the major component to form the matrix, by the TZP dispersed in the matrix.
3) Increasing alumina content increased thermal conductivity and decreased thermal expansion coefficient. Comparing the (4Y, 4Ce)-TZP/Al_2O_3 composition with 2.5Y-TZP/Al_2O_3, the former, which contained a larger quantity of stabilizing agent, had a slightly lower thermal expansion coefficient.
4) The substrates of the composites, prepared by the "doctor blade" method, showed the microstructures in which alumina was uniformly dispersed in the zirconia matrix, and had a surface roughness (Ra) of 0.1μm or less.

References:

1) T.K. Guputa, J.H. Bechtold, R.C. Kuznicki, L.H. Cadoff, and B.R. Rossing, J. Mater. Sci., 12, 2421-26 (1977).
2) T.K. Guputa, F.F. Lange, and J.H. Bechtold, J. Mater. Sci., 13, 1464-70 (1978).
3) K. Kobayashi, H. Kuwajima, and T. Masaki, Solid State Ion., 3-4, 489 (1981).
4) K. Tsukuma, Y. Kubota and T. Tsukidate, Yogyo Kyokai-shi, 92, 11-19 (1984).
5) T. Sato, S. Ohtaki, and M. Shimada, J. Mater. Sci., 20, 1466-70 (1985).
6) T. Kawanami and H. Ohnishi, "Zirconia Ceramics 4," Uchida Rokaku-ho,(1985), pp.31-45.
7) T. Watanabe, K. Urabe, H. Igawa and S.Udagawa, The ceramic Society of Japan Annual Meeting Proceedings, (1984), pp.463-64.
8) T. Sato and M. Shimada, Am. Ceram. Soc. Bull., 64, 1382-84 (1985).
9) M. Hirano and H. Inada, Ceramics Ronbun-shi, 99, 124-30 (1991).
10) M.Ueyama, H.Wada and H.Uehara, Powder and Powder Metallurgy, 35, 526-31 (1988).
11) R.C. Garvie and P.S.Nickolson, J. Am. Ceram. Soc., 55, 303 (1972).
12) K. Kawamura, K. Yamanaka and M. Ono, Ceramics Ronbun-shi, 98, 280-84 (1990).
13) "Ceramic Substrates for Functional Circuits," edited by the Society of Electronic Materials, (1985), pp.32.
14) K.Ishibitsu, M.Kawashima and K.Watanabe, "Fine Ceramics," Gakuken-sha, (1981), pp.32.
15) K.Okazaki, "Introduction to Ceramic Dielectric Materials Engineering," Gakuken-sha, (1983), p.167.
16) Y.Hamano, "Fine Ceramics," Gakuken-sha, (1981), pp.27-32.

This article is a full translation of the article which appeared in Nippon Seramikkusu Kyokai Gakujutsu Ronbunshi (Japanese version), Vol.99, No.4, 1991.

Thermal Hysteresis of High Temperature Resistivity in Indium-Tin-Oxide Films

Keiji Adachi*, Toru Hirayama and Hironobu Sakata

Department of Industrial Chemistry, Tokai University 1117, Kitakaname, Hiratsuka-shi, Kanagawa 259-12, Japan
*Nippon Carbide Ind. Co. Inc., Uozu, Toyama 937, Japan

Indium-tin-oxide(ITO) films were prepared by the chemical spray pyrolysis method using $InCl_3 \cdot 6H_2O$ and $SnCl_4 \cdot xH_2O$(x=3-5) as starting materials. The film with a minimum resistivity of $1.23 \times 10^{-3}\Omega$cm was obtained for tin doping, Sn/In=5at.%. Resistivity of 50nm thick films showed hysteresis phenomena in heat cycles repeated at temperatures between 100°C and 500°C in O_2 and Ar gases. The hysteresis results were discussed in terms of desorption of H_2O from In_2O_3-H_2O complexes, superposing desorption of adsorbed O_2 from the films.
[Received July 17, 1990; Accepted December 4, 1990]

Key-words: ITO films, Chemical spray pyrolysis, Electrical resistivity, Thermal hysteresis

1. Introduction

Indium-tin-oxide (ITO) films, known as n-type semiconductors, have been extensively studied because of the wide applicability of this material to opto-electronic devices. However, electrical resistivity of ITO films were found to be highly affected by post-heat treatments in various gas atmospheres: annealing in air [1-4] or in O_2 [1,5] caused increases in the resistivity of the films whilst in N_2 [6,7], Ar [6], or in vacuum [1,3-5,8] it decreased.

Two models have been proposed to explain these phenomena: an oxygen diffusion model and an oxygen adsorption model. According to the former, oxygen diffuses into oxygen vacancies in the oxide film on heating in O_2 gas, resulting in a decrease in carrier concentration. [7,9,10] In the latter model, however, oxygen atoms adsorped onto the film surface highly affect surface conductance. [11,12] Free carriers close to the surface are trapped by the adsorbed oxygen atoms, thus the space charge due to the trapped electrons extends electron deficient layer, which causes a decrease in carrier concentration in the film surface.

Our previous work [13] on a post-heat treatment (500°C) effect in different gases on the resistivity of 52nm thick ITO films made by spray pyrolysis deposition revealed that monolayer isothermal adsorption of oxygen atoms brought forth variations in the resistivity. The present report describes, in this connection, thermal hysteresis phenomena found in measuring the resistivity of ITO films at high temperatures in oxygen and argon gases.

2. Experimental details

ITO films were prepared by chemical spray deposition technique. [14] The films can be formed by following thermal hydrolysis reactions [5] at high temperature.

$$2InCl_3 + 3H_2O \rightarrow In_2O_3 + 6HCl \quad \ldots\ldots\ldots (1)$$

$$SnCl_4 + 2H_2O \rightarrow SnO_2 + 4HCl \quad \ldots\ldots\ldots (2)$$

We prepared two methanol solutions of $0.1g/cm^3$ of $InCl_3 \cdot 6H_2O$ and $0.1g/cm^3$ of $SnCl_4 \cdot xH_2O$(x=3~5) respectively. For spraying, mixtures with different tin contents of these methanol solutions were used for preparing ITO films with defferent Sn/In ratio. Substrate material was polished PYREX glass. After the substrate was heated up to 600°C, it was then drawn vertically from an electric furnace and the solution was immediately sprayed normally to its surface in air using a spray gun unit with N_2 carrier gas. The flow rate of the carrier gas and the volume of solution sprayed were 10l/min and $3cm^3$, respectively. The spray time was about 3sec. Thus 52nm thick ITO films were obtained for experiments.

The electrical resistance measurements were due to the four probe technique at various temperatures in the electrical furnace shown in **Fig.1** which was the same as that in the previous study. [13] Dried atmospheric gas was flowed into the furnance 3a at a constant flow rate of 1.0l/min. The gas then flowed into furnace 3b for monitoring oxygen which was kept at 500°C and flowed out.

3. Results and Discussion

The ITO films were confirmed by XRD to be poly-crystalline. Their resistivity lowered with an increase in tin doping, and we obtained ITO films with a minimum resistivity of $1.23 \times 10^{-3}\Omega$cm for Sn/In=5at.%. [13,14] Hereafter we used these films (Sn/In=5at.%) throughout present experiments. Further, the resistivity of the films increased gradually up to saturated values on exposure to O_2 gas for about 60min at high temperatures in the furnace. Hence, we took the saturated values as the high temperature resistivity in this work.

Figure 2 shows the variation of the resistivity for a 50nm

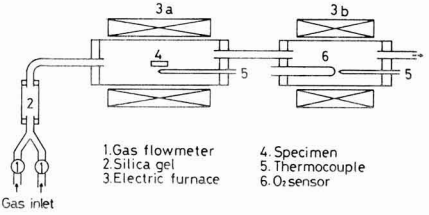

Fig. 1. Schematic diagram for post-heat treatment.

thick ITO film at temperatures ranging from 100°C to 500°C in O_2 atmosphere (1atm). A clear thermal hysteresis is seen throughout one heat cycle experiment. The arrows on the curves indicate order of the experiment. For a repeated heat cycle, the thermal hysteresis was found to be nearly same as that in Fig.2.

Figure 3 exhibits results of the same experiments in Ar gas (1atm), also giving a thermal hysteresis in the resistivity of the same type as in Fig.2. In these two cases, the resistivity initially dropped upon heating and showed a minimum value at 300°C, then it rose at higher temperatures. On the other hand, no minimum resistivity was found in the cooling process. Furthermore in Ar gas (Fig.3), the resistivity at temperatures around 300°C increased gradually as the heat cycle experiment was repeated.

Figure 4 gives XRD results on the films heat-treated in O_2 and Ar gases for 20h at 500°C, together with reference data before the heat treatment. No structural changes due to baking in these gases were seen. Therefore, the hysteresis in Figs.2 and 3 is not considered to be due to any possible structural changes that occured during the heat cycle experiments. Similar thermal hysteresis was reported for ZnO films deposited by spray pyrolysis.[16]

The hysteresis in resistivity-temperature relationship for oxide semiconductors was interpreted as follows.[17,18] Adsorbed oxygen is desorbed on increasing in temperature, causing the liberation of carrier electrons, then high temperature adsorption occurs in passing a temperature range that gives a minimum resistivity. This captures electrons from the solids, resulting in an increase in the resistivity. Takata and Yanagida[12] stated that the adsorped oxygen spacies were transformed as follows with increasing temperature.

$$1/2O_4^- \rightarrow O_2^- \rightarrow 2O^- \rightarrow 2O^{2-} \quad \ldots\ldots\ldots (3)$$

However, this model does not fully explain the phenomena in the present cases because the hysteresis was found not only in O_2 atmosphere but also in Ar (Figs.2 and 3). Therefore, we considered the hysteresis to be mainly due to desorption of H_2O molecules from the film during baking, which had been incorporated prior to the heat treatment. The present ITO films made by the chemical spray pyrolysis probably contain H_2O molecules in grain boundaries and/or surface of the crystallites because we used starting materials containing water of crystallization ($InCl_3 \cdot 6H_2O$ and $SnCl_4 \cdot xH_2O$(x=3~5)). The H_2O molecules probably could not be completely eliminated from the films during the deposition. Therefore, when the films are formed, the following stable complexes can be produced referring to the case of ZnO films.[16]

$$In_2^+O_3^- + H_2O \rightarrow In_2H_2O_4 \quad \ldots\ldots\ldots (4)$$

$$In_2^+O_3^{2-} + H_2O \rightarrow In_2H_2O_4^- \quad \ldots\ldots\ldots (5)$$

$$In_2^{2+}O_3^{2-} + H_2O \rightarrow In_2H_2O_4 \quad \ldots\ldots\ldots (6)$$

On heating the films in O_2 or in Ar gas, the adsorbed H_2O molecules are desorbed from the complexes.

$$In_2H_2O_4 \rightarrow 2In_{In}^{\cdot} + 3O_O^{\cdot} + H_2O \quad \ldots\ldots (7)$$

$$In_2H_2O_4^- \rightarrow 2In_{In}^{\cdot} + 3O_O^{\cdot} + H_2O + e^- \quad \ldots\ldots (8)$$

The reaction (8) is electron-donating, resulting in a decrease in the resistivity as seen in Figs.2 and 3. The desorption of the adsorped H_2O molecules causes a gradual recovery of the film resistivity to its original value for heating to temperatures higher than 300°C. Also the decrease in the difference between the resistivity values at 500°C and 300°C found in the heat cycle experiments in Ar gas explains the desorption of H_2O molecules that gradually proceeds. During cooling, on the other hand, the resistivity decreases without donating carrier electrons by adsorption of H_2O molecules because the desorbed molecules flowed out to-

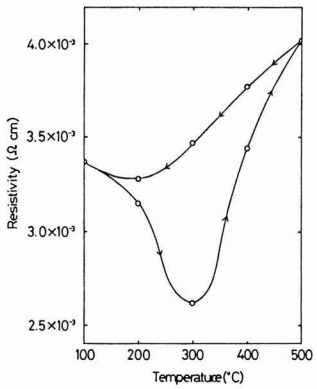

Fig. 2. Resistivity of ITO film in O_2 gas against temperature. Film thickness: 50nm, Sn/In=50at.%.

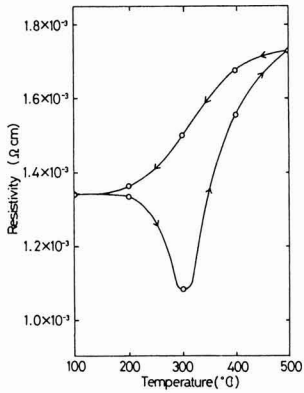

Fig. 3. Resistivity of ITO film in Ar gas against temperature. Film thickness: 50nm, Sn/In=50at.%.

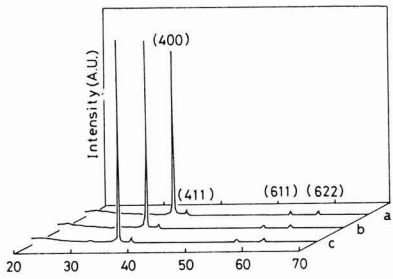

Fig. 4. XRD diagram for ITO films. Sn/In=50at.%. a: before heat treatment, b: heated in Ar (500°C, 20h), c: heated in O_2 (500°C, 20h).

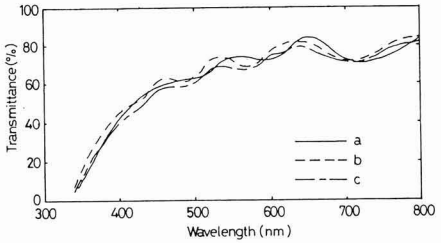

Fig. 5. Spectral transmittance of ITO films. Film thickness: 640nm, Sn/In=50at.%. a: before heat treatment, b: heated in Ar (500°C, 20h), c: heated in O_2 (500°C, 20h).

gether with the carrier gas in the present experiments. This resistivity decrease is due to the degeneracy of tin-doped In_2O_3 films causing metalic conduction.[19]

No thermal hysteresis in resistivity was found in vacuum-evaporated ITO films on baking in dry air.[20] This supports the present interpretation of the phenomena. However, on baking in O_2 gas (Fig.2), desorption of oxygen adsorbed onto the films in air can also be valid, which superposes the H_2O desorption, because the fact that the resistivity values on exposure to O_2 gas were high at any temperatures in comparison with the resistivity on baking in Ar gas explains the O_2 adsorption. Thus in Fig.3, O_2 molecules adsorbed onto the films in air prior to heating can also be desorbed and flow out with increasing temperature.

Another suggestive result is the changes in spectral transmittance of a 640nm thick ITO film before and after baking in O_2 and Ar gases (**Fig.5**), in which optical interference of the film is clearly seen. The theory of interference for a single layer with the refractive index higher than that of substrate shows that minimum and maximum transmittances occur for $nd=(2m+1)\lambda/4$ and $nd=2m'\lambda/4$, respectively, where n and d are refractive index and thickness of the film, m and m′, integers respectively. Assuming that $n=2$[21] for the ITO film with d=640nm, and m=3 and m′=4, we obtain λ=640nm for the maximum transmittance and λ=731nm for the minimum. These results agree with the experimental data (λ=650nm and 725nm) in Fig.5. For wavelengths shorter than 640nm, we calculated wavelengths corresponding to minimun and maximum transmittances for m=4 and m′=5 respectively, with n=2.12 taking account of the refractive index dispersion. The calculated results, λ=603nm and 542nm, also agreed with the experimental data, λ=600nm and 542nm, respectively. It should be noted that the wavelengths corresponding to the maximum and minimum transmittances for the film baked in O_2 and Ar gases shifted respectively to a wavelength 25nm shorter than the initial values (before baking), i.e., these heat treatments produced a decrease in optical thickness, $\Delta(nd)$=25nm, corresponding to a decrease in the film refractive index Δn=0.04 for d=640nm. Hence, providing that the film thickness is kept constant during baking, this result also supports the desorption of H_2O molecules together with desorption of adsorbed O_2 molecules from the film.

References:

1) A. Gupta, P. Gupta and V.K. Srivastava, Thin Solid Films, 123, 325-31, (1985).
2) O.P. Agnigotri, A.K. Sharma, B.K. Gupta and R.Thangaraj., J. Phys. D: Appl. Phys., 11, 643-7 (1978).
3) H.B. Saim and D.S. Campbell, and J. A. Avaritsiotis, Solar Energy Mater. 13, 85-96, (1986).
4) J. Bhattacharya, S. Chaudhuri, D.De and A.K. Pal, Thin Solid Films, 128, 231-39 (1985).
5) H. Hoffman, A. Dietrich and J. Pickl, Appl. Phys., 16, 381-90 (1978).
6) W.G. Haines and R.H. Bube, J. Appl. Phys., 49, 304-7 (1978).
7) S. Ogihara and K. Kinugawa, Yogyo Kyokai Shi, 90, 157-63 (1982).
8) L. Assadourian and L. Herczeg, Appl. Opt., 23, 1452-53 (1984).
9) M. Mizuhashi, Jpn. J. Appl. Phys., 22, 615-20 (1983).
10) Y. Ohhata and S. Yoshida, Oyo Buturi, 46, 43-50 (1977).
11) J.B. Webb, B.F. Williams and R. Adsett, J. Canad. Ceram. Soc., 52, 33-36 (1983).
12) M. Takata and H. Yanagida, Yogyo Kyokai Shi, 87, 13-21 (1979).
13) K. Adachi, T. Hirayama and H. Sakata, J. Mater. Sci., 25, 1403-6 (1990).
14) K.Kaneyasu, K. Adachi, T. Hirayama and H. Sakata, Denki Kagaku, 55, 245-50 (1987).
15) J.C. Manifacier, L.Szepessy, J.F. Bresse and M.Perotin, Mater. Res. Bull., 14, 109-19 (1979).
16) S.D.Sathaye and A.P.B.Sinda, Thin Solid Films, 44, 57-63 (1977).
17) P. Chandora, V.P. Tare and A.P.B. Sinda, Indian J. Appl. Phys., 5, 313 (1967).
18) Y. Fujita and T. Suge, J. Res. Inst. Catalysis, Hokkaido Univ., 15, 21 (1958).
19) S. Noguchi and H Sakata, Thin Solid Films, 157, 181-188 (1988).
20) Y. Katsube and S. Katsube, Oyo Buturi, 49, 2-16 (1980).
21) S. Noguchi, M. Mizuhashi and H. Sakata, Rept. Res. Lab. Asahi Glass Co. Ltd., 28, 25-33 (1978).

This article appeared in English in Nippon Seramikkusu Kyokai Gakujutsu Ronbunshi (Japanese version), Vol.99, No.4, 1991.

Synthesis of a New Compound $NaGaTi_5O_{12}$

Yoshinori Fujiki, Yuichi Michiue and Mamoru Watanabe

National Institute for Researchon on Inorganic Materials
1-1, Namiki, Tsukuba-shi, Ibaraki 305, Japan

Single crystals of a new compound $NaGaTi_5O_{12}$ were synthesized by the flux method. This crystal always occurred in coexistence with $Na_{1-x}Ti_xGa_{5-x}O_8$ crystals. The best crystal was obtained by slow-cooling after keeping at 1350°C for 10h using a mixture of 35mol% crystal composition of $(Na_2O)_1(Ga_2O_3)_1(TiO_2)_1$ and 65mol% flux composition of $(Na_2O)_1(MoO_3)_{1.5}$ as a compositional condition in the flux melt. This crystal structure consists of peculiar framework with one-dimensional tunnel structure of a new type which is a monoclinic system with a=15.202(), b=3.732(), c=9.317() and β-122.04. This compound was identified as a high temperature phase of Na-Ga-freudenbergite ($Na_{0.7}Ga_{0.7}Ti_{3.3}O_8$) which transformed at 1238°C, and melted at 1336°C.

[Received September 17, 1990; Accepted December 14, 1990]

Key-words: New tunnel structure, Sodium gallotitanate, $NaGaTi_5O_{12}$, Flux growth

1. Introduction

A new compound $NaGaTi_5O_{12}$ (hereafter NGTO) was synthesized by the flux method. This crystal structure was coincident with that predicted as a possible structure in alkali-metal titanates by Andersson and Wadsley (1962)[1] and the hypothetical substance has been given to have a composition $A_2Ti_6O_{12}$ (A=alkali-metals).

We succeeded in synthesizing the NGTO crystals by replacing Ti sites in the $Na_2Ti_6O_{12}$ with Ga. In this paper, the growth conditions, chemical composition, structure and thermal stability of single crystals are described.

2. Experimental Procedure

Starting materials were TiO_2, Ga_2O_3 and MoO_3 powders of 99.99% purity and N_2CO_3 powder of 99.9%. The flux employed was a mixture of Na_2CO_3 and MoO_3 powders. A 100ml Pt-crucible which was tightly covered with a fitted lid was used in this work. The grown crystals were taken out from the crucible by dissolving the flux in hot water. The chemical compositions of single crystals were determined by the EPMA method.

3. Results and Discussion

3.1. Single Crystal Synthesis

Table 1 exhibits the compositional conditions in the flux melts and the obtained results for the single crystal growth of NGTO. In the compositional conditions of the flux melts shown in Table 1, the crystal composition is the composition of the mixture of crystal components and the flux composition is that of the mixture of flux components using as the solvent. The NGTO single crystals were synthesized by slow-cooling after keeping at 1350°C for 10h using a mixture of a crystal composition of $(Na_2O)_1(Ga_2O_3)_1(TiO_2)_1$ in 30-35mol% and a flux composition of $(Na_2O)_1(MoO_3)_{1.5}$ in 65-70mol%. The slow-cooling operation was carried out to 1000°C with a rate of 4°C/h. The weight loss of the bulk composition during a growth process was below 1wt%. However, the NGTO crystals always occurred in coexistence with $Na_{1-x}Ti_xGa_{5-x}O_8$ crystals.[2] The NGTO crystals could not be synthesized when the crystal composition in a flux melt was stoichiometrical with that of NGTO, and rutile and $Na_{1-x}Ti_xGa_{5-x}O_8$ crystals were always prepared. Especially, rutile was very predominant with an acicular form. The NGTO crystals were synthesized under conditions where $Na_{1-x}Ti_xGa_{5-x}O_8$ crystals occurred predominantly instead of rutile. Consequently, the monophase of NGTO

Table 1. The compositional conditions in flux melts and the obtained results for the growth of $NaGaTi_5O_{12}$ compared with that of $K_2Ti_6O_{13}$.

Temperature High⟶Low (°C)	Crystal composition(C) (Na_2O)-(Ga_2O_3)-(TiO_2) (Molar ratio)			Flux comp.(F) (Na_2O)-(MoO_3) (Molar ratio)		Melt cmpo. C/F (Mol%)	Crystals*
1350⟶1000	0.5	0.5	5.0	1.0	1.5	30/70	TiO_2, NTGO
1350⟶1000	0.5	0.5	3.5	1.0	1.5	20/80	TiO_2, NTGO
1350⟶1000	0.75	0.5	1.5	1.0	1.5	20/80	TiO_2, NTGO
1300⟶1000	1.0	1.0	1.0	1.0	1.5	30/70	NTGO, NGTO, (TiO_2)
1350⟶1000	1.0	1.0	1.0	1.0	1.5	35/65	NTGO, NGTO
1350⟶1000	2.0	1.0	1.0	1.0	1.5	30/70	NTGO, $Na_2Ti_3O_7$
1350⟶1000	1.0	1.0	1.0	1.0	1.25	30/70	NTGO, $Na_2Ti_3O_7$

* NGTO=$NaGaTi_5O_{12}$, NTGO=$Na_{1-x}Ti_xGa_{5-x}O_8$, TiO_2=rutile, ( )=small amount

crystals is not yet obtained. **Figure 1** shows the NGTO single crystals grown by the flux method. Those crystals are obtained in an acicular form elongating along the c-axis (or the tunnel axis) with transparence or translucence. **Figure 2** shows crystal structure projected on the (010) plane of NGTO, and the crystallographical properties are exhibited in **Table 2**. The crystal structure is characterized by a new type of tunnel framework consisting of treble (Ga, Ti)O_6 octahedral ribbon. This tunnel framework and the crystallographical properties resemble that of sodium hexatitanate $Na_2Ti_6O_{13}$ which has been reported by Andersson and Wedsley[1] except that the β angle is different. An only Na ion is able to occupy in a unit tunnel. The detail of structure analysis is to be published by Michiue et al.[3] **Table 3** shows the chemical compositions of NGTO single crystals analyzed by the EPMA method. The formula was calculated on the basis of atomic ratio as O_{12} in a chemical composition. As a result, the general formula indicated to be $NaGaTi_5O_{12}$ as a stoichiometrical composition.

3.2. Polycrystal Synthesis

The NGTO polycrystal was also prepared by the solid reactions. It was found that the polycrystal was synthesized at temperatures of 1250°C or above. At temperatures of 1200°C or below, only Nag-Ga-freudenbergite, $Na_{0.7}Ga_{0.7}Ti_{3.3}O_8$, was always synthesized using the same starting composition. The Na-Ga-freudenbergite, obtained was transformed into a NGTO phase by reheating at 1250°C. **Figure 3** shows a DTA curve of Na-Ga-freudenbergite which was prepared at 1200°C for 25h with a stoichiometrical $NaGaTio_5O_{12}$ composition. It indicates that the freudenbergite transforms irreversibly to a NGTO phase at 1238°C and melts at 1336°C. This phase transformation is represented by no change of composition as follows:

$$1.5Na_{0.7}Ga_{0.7}Ti_{3.3}O_8 \xrightarrow{1238°X} NaGaTi_5O_{12}$$

We also tried to synthesize $KGaTi_5O_{1.2}$ and $LiGaTi_5O_{12}$ compounds which replaced Na ion in the NGTO with K or Li ions at 1250°C for 25h. As a result, it was unsuccessful, and rutile and priderite, $K_2Ga_2Ti_6O_{16}$, were obtained in the former, and in the latter, rutile and $LiGaTiO_4$[4] Furthermore, we tried to prepare a $NaA1Ti_5O_{12}$ compound as the analogue of NGTO at 1200°C and 1250°C for 20h. However, only Na-Al-freudenbergite, $Na_{0.7}Al_{0.7}Ti_{3.3}O_8$, was obtained. This freudenbergite decomposed into feudenbergite (perhaps $Na_{0.7-x}Al_{0.7-x}Ti_{3.3+x}O_8$) and Na-β-$Al_2O_3$ phases at 1350°C for 20h.

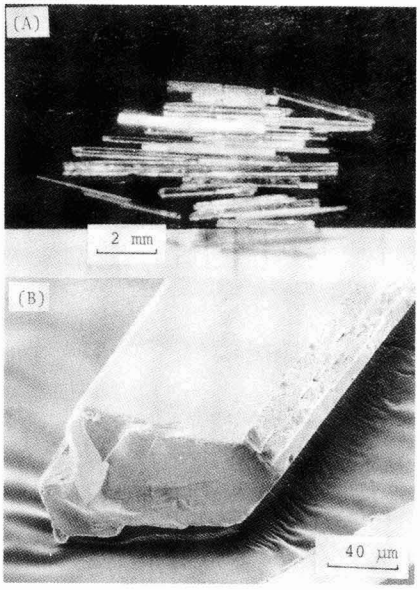

Fig. 1. $NaGaTi_5O_{12}$ Single crystals grown by the flux method; (A) Stereoscopic photomicrograph and (B) SEM image.

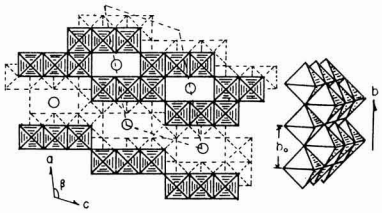

Fig. 2. The crystal structure projected on the (010) plane of $NaGaTi_5O_{12}$ crystal.

Table 2. The crystallographical properties of $NaGaTi_5O_{12}$ comparing with that of $K_2Ti_6O_{13}$.

	$NaGaTi_5O_{12}$ (NGTO)	$K_2Ti_6O_{13}$ (KTO)
	Monoclinic, (C2/m)	Monoclinic, (C2/m)
a(Å)=	15.202	15.131
b(Å)=	3.732	3.745
c(Å)=	9.317	9.159
β° =	122.04	99.3
V(Å^3) =	448.1	512.1
D(g·cm^{-3})=	3.88	3.51
z=	2	2

Table 3. The chemical compositions of $NaGaTi_5O_{12}$ single crystals analyzed by the EPMA method.

No.	(Na_2O)	(Ga_2O_3) (wt%)	(TiO_2)	Total	Chemical compositions
1	6.245	17.522	77.751	105.518	$Na_{1.04}Ga_{0.96}Ti_{5.01}O_{12.00}$
	(6.152)	(17.260)	(76.588)	(100.000)	
2	6.396	17.182	77.328	100.898	$Na_{1.07}Ga_{0.95}Ti_{5.02}O_{12.00}$
	(6.339)	(17.029)	(76.640)	(100.000)	
3	6.328	19.147	76.403	101.870	$Na_{1.05}Ga_{1.05}Ti_{4.94}O_{12.00}$
	(6.211)	(18.795)	(75.00)	(100.000)	

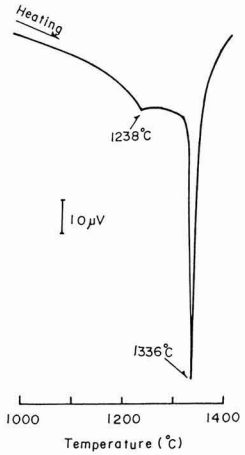

Fig. 3. A DTA curve of Na-Ga-freudenbergite polycrystal prepared at 1200°C for 25h with a $NaGaTi_5O_{12}$ composition.

Acknowledgements

The authors with to thank Mr. Kosoda in NIRIM for his kindness during EPMA analysis of the single crystal.

References:

1) S. Andersson and A.D. Wadsley, Acta Cryst., 15, 149-201 (1962).
2) G.V. Chandrashekhar, B. Bednowitz and S.J. Laplaca, Fast Ion Transport in Solids, eds. Vashista, Mundy and Shenoy, Elsevier North Holland Inc., 447-450 (1979).
3) U. Michiue, Y. Fujiki and M. Watanabe, to be published in Acta Cryst.
4) E.F. Bertaut and G. Patrat, Bull. Soc. Franc. Miner. Cryst., 88, 586-589 (1965).

This article appeared in English in Nippon Seramikkusu Kyokai Gakujutsu Ronbunshi (Japanese version), Vol.99, No.4, 1991.

The Effect of Adding Alkali-Earth Metal Oxides to Mother Glass of Alkali Durable Porous Glass

Tetsuo Yazawa, Hiroshi Tanaka, Kiyohisa Eguchi* and Takashi Arai**

Government Industrial Research Institute
Osaka, 1-8-31 Midorigaoka, Ikeda-Shi, 563 Japan
* Consulting Engineer, 2-1-72, Seiwadai-nichi Kawanishi-shi, 666-01, Japan
** Akagawa Koshitsu Glass Kogyosyo Co., Ltd.
1-2-20, Ikue, Asahi-ku, Osaka-shi, 535 Japan

The effect of adding alkali-earth metal oxides to the mother glass of alkali durable porous glass has been experimentally examined with the following results. The composition of the mother glass employed in this report was $57.2SiO_2{\cdot}22.8B_2O_3{\cdot}5.7Na_2O{\cdot}9.2RO$ (R=Mg, Ca, Sr, Ba)$\cdot 3.2ZrO_2{\cdot}1.9Al_2O_3$ (mol%). (1) The effect of adding alkali-earth metal oxides on the phase separation rate of mother glass was largest for MgO, followed in decreasing order by CaO, SrO and BaO. (2) The effect of adding alkali-earth metal oxides on ZrO_2 content in the skeleton of porous glass remains unclear, but it may be closely associated with the phase separation rate of mother galss. (3) The addition of alkali-earth metal oxide was effective for retaining ZrO_2 in the skeleton of porous glass.

[Received Sepember 14, 1990; Accepted January 24, 1990]

Key-words: Porous glass, Alkali durability, Zirconia, Spinodal decomposition, Alkali-earth metal oxide

1. Introduction

It is essential to obtain porous glasses with alkali resistance. When treated with acids, gelated SiO_2 is deposited in micropores of phase-separated borosilicate glass.[1] If this deposit of SiO_2 is to be eliminated, an acid volume (bath ratio) against glass, for instance, in a pipe-shaped sample of 0.5mm in thickness, has to be more than $1dm^3/g$, thereby requring large volumes of acids and the complicated elimination process.[2] In addition, more careful operations are required since cracks occur in the manufacruring process of formed products such as rods, pipes, and plates.[3] However, porous glass with alkali resistance can be processed with a relatively small volume of alkaline solution, to remove SiO_2 accumulated in a gel state due to phase separation, thereby eliminating troublesome processing with acids and the resultant formation of cracks.

Since amorphous SiO_2 has water solubility of about 100ppm at room temperature,[4] it is difficult to use porous glass containing SiO_2 gel in aqueous solution for long time; this is a major barrier when porous glass is used as membrane. Thus, this problem can also be solved when alkali durable porous glass materials are obtained.

It has been clarified by research and development on glass-fiber reinforced cement (GRC) that alkali resistance can be markedly improved when ZrO_2 is added to the composition of glass.[5] We have so far been successful in retaining ZrO_2 in the skeleton of porous glass by adding CaO in the mother glass.[6] This paper deals more widely with the effects of added alkali-earth oxides.

2. Experiment

2.1. Preparation of Porous Glass Samples

Porous glasses were obtained by phase separation at 700°C-800°C after the various types of mother glass were melted at 1300°C-1500°C for 3h. The mother glass compositions used for the current experiment are shown in **Tables 1** and **2**. Mother glass samples A-1~4 represent the groups whose amounts of added CaO were changed from 6.9mol% to 9.2mol% for the purpose of studying the effects of additing CaO, while motherglass samples G-0~4 consisted of one with no alkali-earth oxides and mothers alkali-earth metal oxides such as MgO, CaO, SrO and BaO added in an amount of 9.2mol% each, for the purpose of studying the effects of addition of alkali-earth oxides. The boric acid phase was eluted after the phase-separated glass was

Table 1. Composition of mother glass and pore characteristics of the porous glasses A-1, A-2, A-3 and A-4.

Composition	SiO_2	B_2O_3	Na_2O	CaO	ZrO_2	Al_2O_3 (mol%)
A-1	59.3	22.8	5.7	6.9	3.2	1.9
A-2	58.8	22.8	5.7	7.5	3.2	1.9
A-3	58.3	22.8	5.7	8.1	3.2	1.9
A-4	57.2	22.8	5.7	9.2	3.2	1.9

Pore characteristics	Median diameter (nm)	Pore volume (cm^3/g)
A-1	153	0.58
A-2	185	0.49
A-3	260	0.48
A-4	405	0.32

Table 2. Composition of mother glass and pore characteristics of the porous glasses G-0, G-1, G-2, G-3 and G-4.

Composition	SiO_2	B_2O_3	Na_2O	R O R =	ZrO_2	Al_2O_3 (mol%)
G-0	66.4	22.8	5.7	0.0	3.2	1.9
G-1	57.2	22.8	5.7	MgO 9.2	3.2	1.9
G-2	57.2	22.8	5.7	CaO 9.2	3.2	1.9
G-3	57.2	22.8	5.7	SrO 9.2	3.2	1.9
G-4	57.2	22.8	5.7	BaO 9.2	3.2	1.9

Pore characteristics	Median diameter (nm)	Pore volume (cm^3/g)	ZrO_2 content in porous glass skeletons (wt%)
G-1	Droplet decomposition	see Fig.1	6.7
G-2	405	0.32	3.0
G-3	217	0.85	1.3

immersed in 1mol/dm^3 of HNO_3 at 98°C for 48h to obtain porous glass. Thereafter samples were immersed in 1.5m/ / dm^3 – H_2SO_4 again at 98°C for 48h, to elute out gel state ZrO_2 deposited in the pores. HNO_3 was primarily used to avoid the sedimentation of sulfate because of the poor solubility of all alkal: earth sulphates but $MgSO_4$.

The above glass samples were further immersed in a solution of 0.4mol/dm^3 of NaOH at 30°C for 5h to remove innerpore SiO_2 in a gel state caused by phase separation and finally porous glass samples were obtained.

2.2. Measurement of Pore Characteristics

The pore size distribution of porous galss was measured by the mercury penetrating method (Porosi Meter, Model 200 manufactured by Carlo Erba Co., Ltd.). Porous glass pores were observed using SEM (Nihon Electron K.K., Model JSM-T100) after the samples were gold-deposited.

2.3. Analysis of Porous Glass Constituents

ZrO_2 was analyzed by adding 2cm^3 of hydrofluoric acid to 1g of a sample glass, heated in a platinum crucible and evaporated to dryness. Then, 4cm^3 of 2% HCI was added and dissolved for analytical studies by a inductively coupled plasma analyzer (ICP Emission Spectrochemical Analyzer, Model SPS 1200 A) levelled up to 1dm^3.

3. Results and Discussion

3.1. Effects of CaO on Phase Separation

Table 1 shows the porous glass pore characteristics confirmed when an amount of CaO added to the mother glass samples was allowed to be changed from 6.9mol% to 9.2mol% for the phase separation at 750°C for 10h. It is clear from this table that CaO is effective in promoting phase separation since the pore diameter of porous glass materials is conceivably increased when a larger amount is contained in the mother glass.

3.2. Effects of Added Alkali-Earth Oxides

Table 2 shows the pore characteristics which were determined when an additional amount of alkali-earth oxides in the mother glass was fixed to 9.2mol% with phase separation at 750°C for 10h. As shown in the SEM photograph (**Fig.1**), droplet phase separation was recognized in G-1 with MgO, while no phase separation was observed in G-4 with BaO. As for G-1, porous glass samples of 73nm in pore diameter could be obtained when phase-separated at 700°C for 10h. This indicates that G-1 containing MgO has presumably passed a spinodal stage to become a droplet because of its faster rate of phase separation. On the other hand, since no phase separation was observed in G-4 treated at 800°C for 10h, it is conceivable that a phase separation rate of G-4 containing BaO is extremely slower.

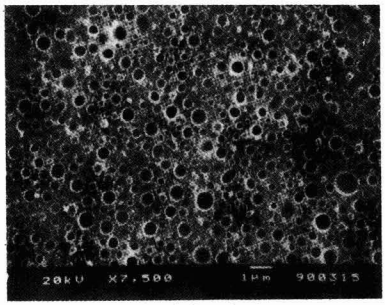

Fig. 1. SEM photograph of G-1 after heat treament.

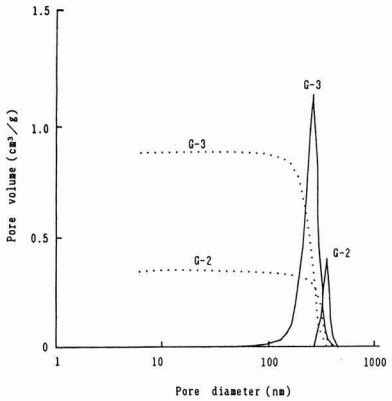

Fig. 2. Pore size distribution of porous glass G-2 and G-3.

In view of Table 2 and the above fact, the effects of alkali-earth oxides on the phase separation are rated in the order of MgO>CaO>SrO>BaO, and as it is known from the SiO_2-RO system and SiO_2-B_2O_3-RO system,[7,8] the phase separation rate tended to increase when the cation field of alkali-earth metal ($F=Z/r^2$ Z:ion charge, namely 2, r:ion radius) was stronger.[9]

It is also clear from Table 2 that the pore volume of porous glass G-3 is considerably larger than that of G-2. This may be explained by the fact that the skeleton of porous

glass samples treated with acid and alkali was eroded while the difference between the compositions of both phases was still smaller, as the skeleton of porous glass was not sufficiently grown, due to a slower phase separation rate than that of G-2. In fact, the above hypothesis is supported by the pore size distribution of G-3, which is much broader than that of G-2, as shown in **Fig.2**.

3.3. ZrO_2 Contents in the Skeleton of Porous Glass Samples

The contents of ZrO_2 contained in the skeleton of porous glass samples are also shown in Table 2. The ZrO_2 contents of G-1 with MgO as large as 6.7wt% is conceivably attributable to the following reasons.

As shown in the SEM photograph in Fig.1, the separated phases are being dispersed as droplets, while the ZrO_2 contents in the mother glass samples of G-1 are 6.2wt%, and the pore volume after acid and alkali treatment is so small (~0.01cm^3/g) that it can barely be measured. Thus, the soluble phase in the inner part of glasses is not eluted during the process of acid and alkali treatment as it is being isolated as droplets, resulting in such a large content of ZrO_2. As mentioned earlier in 3-2, the ZrO_2 content of G-2 larger than that of G-3 may be closely related with the poor development of the skeleton of porous glass samples, and also with the phase separation rate. However, since the effects of alkali-earth oxides on the distribution of ZrO_2 to the skeleton of porous glass materials are not yet clear, further investigations may be required in the future.

G-O not containing alkali-earth oxides in the mother glass is presumably phase-separated because of the white turbidity of mother glass materials heat-treated for phase separation, but the glass structure is disintegrated during the process of alkali treatment to obtain porous glasses. In view of such a phenomenon, it may be effective to add alkali-earth metal oxides to the mother glass in order to retain ZrO_2 in the skeleton of porous glass materials.

4. Conclusion

The following findings were obtained when the effects of alkali-earth metal oxides added to the mother glass in the preparation of alkali durable porous glass materials containing ZrO_2 in the skeleton were investigated.

1) The effects of adding alkali-earth oxides on the phase separation rate of mother glass materials were evaluated in the order of MgO>CaO>SrO>BaO.
2) Although the effects of alkali-earth oxides on the ZrO_2 content in the skeleton of porous glass materials are not yet clarified, they are considered to be closely related with the phase separation rates.
3) It is effective to add alkali-earth oxides to the mother glass to retain ZrO_2 in the skeleton of porous glass materials.

References:

1) H. Tanaka, T. Yazawa, K. Eguchi, H. Nagasawa, N. Matsuda and T. Einishi, J. Non-Crys. Solids, 65, 301 (1984).
2) H. Tanaka, T. Yazawa, K. Eguchi, T. Yamaguro, Ceramics Asso., 92, 492 (1984).
3) K. Eguchi, Report published by Government Industrial Research Institute, Osaka, No.355 (1979), p.3-38.
4) R.K. Iler, "The Chemistry of Silica," John Wiley & Sons (1976), p.31.
5) S. Dobashi, "Physical-chemistry of Glass Surface," Kodansha (1979) p.188.
6) T. Yazawa, Government Industrial Research Institute, Osaka, Report No.377 (1989).
7) Y. Kawamoto and M. Tomozawa, Physics Chem. Glasses, 22, 1 (1981).
8) O.V. Mazurin and E.A. Porai Koshits, "Phase Separation in Glass," Elisevier Science Publishers (1984) p.134.
9) Y. Moriya, "Inorganic Amorphous Materials, General Remarks of Chemistry, No.41" Publishing Center, Japan Chemical Society (1989), p.191-109.

This article is a full translation of the article which appeared in Nippon Seramikkusu Kyokai Gakujutsu Ronbunshi (Japanese version), Vol.99, No.4, 1991

Information & Communications

News

Common Alumina Sinter

The Fine Ceramic Center has started selling common alumina sinter as a standard specimen with clarified production schemes. Its qualities are uniformity and scarce scattering. A number of researchers are attempting to machine fine ceramic materials, but their results have been rarely compared directly due to the lack of a standard specimen (common specimen). This has led the center to produce the "common sinter." It is of an alumina shape (purity: 99.7% or more), 10cm square and 1cm thick, having a density of 3.92g/cm^3, bending strength of 350MPa and fracture toughness of 4.3. Sumitomo Chemical Industry supplies the starting powder, and Asahi Glass produces 1000 specimens annually. The standard price is 24,000 yen for 1 sheet. The center plans to produce silicon nitride, zirconia and silicon carbide sinters in that order.

CBN Light-Emitting Phenomenon

The Science and Technology Agency's National Institute for Research on Inorganic Materials plans to develop an apparatus to analyze the excited conditions within crystals with an eximer dye laser to elucidate the light-emitting phenomena of cubic boron nitride (CBN), which has been attracting attention as a material for ultraviolet-emitting diodes. The apparatus will analyze light produced as a result of irradiation of ultraviolet rays onto single-crystalline CBN, for various purposes such as determination of impurity quantities. Investigation will also be carried out of emission-related items including crystal defects, electron structures and transition, band structures (band gaps and constants), and carrier concentration and mobility. Ultraviolet to visible violet rays (wavelength: 1,700 to 400nm) can be irradiated. The apparatus will be of great help in the development of high-quality, single crystal production techniques.

Synthesis of High-Purity Alumina

The Agency of Industrial Science and Technology's Industrial Research Institute (Nagoya) has succeeded in the production of high-strength, high-transparency alumina ceramic by HIP treatment conducted at 1,200° to 1,400°C. The new process consists of several steps: (1) crushing of the starting alumina material (supplied by Daimei Kagaku) into fine particles of 0.1μm; (2) slip casting of the fine particles in the presence of water into a shape; (3) densification of the shape by preliminary sintering conducted at 1,240°C to a relative density of 98%; and (4) HIP treatment at 1,200° to 1,400°C. The sinter will have an almost theoretical density. The process uses no resin for the slip casting step (to eliminate the digressing step), nor any additives (such as magnesia). As a result, high-strength, high-transparency sinter is produced at a greatly reduced cost. It can be applied to other ceramic materials, and will be very useful for the commercial production of fine ceramic materials.

Controlling Crystalline Structures of Thin Titania Films

Nissan Motor and the National Chemical Laboratory for Industry have jointly developed a method for controlling the crystalline structures of thin titania films. Titania has three crystalline structure types: rutile, brucite and anatase. A titanium alkoxide (titanium tetraisopropoxide) gives a complex upon reaction with diethylene glycol monomethyl ether at 80°C for 90min, to which water is added to form a titanium sol. It is heated at around 80°C, after being spread over a glass or silicon substrate to form a 0.1μm thick anatase type film. A rutile type thin film results when hexylene glycol is used in place of diethylene glycol monomethyl ether. The thin film will be completely of anatase when the sol-coated substrate is heated at a lower temperature.

The results were presented to the Ceramic Basic Seminar held in Nagaoka City.

Ceria-Stabilized Zirconia

Nisshin Flour Milling and Prof. S. Hirano of Nagoya University have jointly developed ceria-stabilized zirconia ceramic materials with greatly improved strength. Ceria-stabilized zirconia is higher in toughness but lower in strength than the leading yttria-stabilized type. This problem has been solved by adding alumina as a reinforcing agent to the composite material. Zirconia, after being mixed with lanthanum b alumina (LBA), is fired at 1,600° to 1,650°C. LBA, tending to expand in columnar shapes at high temperature, works in the composite structures to increase toughness and, at the same time, to relax the effects of external pressure. The company has succeeded, based on proprietary flour-mixing techniques, in dispersing LBA almost uniformly. Samples are already being sent to prospective users for eventual commercialization; initial sales are expected to reach 200 million yen. The new ceramic materials are expected to find wide applications (e.g. as blades) for ceria-stabilized products which have only limited applications at present.

PZT Piezoelectric Ceramics

Matsushita Electric has developed a PZT-base piezoelectric material which is 2.5 times higher in strength than conventional ones and can be produced at a firing temperature 150°C lower. The basis of the development is a proprietary nanopowder process, a mechanical alloying process in which a larger quantity of starting powder is milled with smaller balls. It mills a mixture of lead oxide, zirconia and titania particles having an average size of 2.2μm, reducing their size to 0.2μm in minutes. The mixed powder is fired at 1,140°C into a sinter having a strength of 50MPa.

Piezoelectric ceramics are functional materials which expand and shrink upon application of voltage. They are finding uses in car shock absorbers, shutter-driving devices for cameras, and AF-driving devices for video-cameras, with applications growing at an annual rate of around 5%. The latest development is expected to lead to the production of more reliable PZT ceramics at a reduced cost.

Production of Porous Glass Particles

Assist. Prof. N. Takai of the Institute of Industrial Science, Tokyo University and Ise Kagaku Kogyo have jointly developed a process to produce porous glass particles stably for superhigh-speed liquid chromatography. Sirasu, a mineral matter mainly consisting of silicon dioxide (abundant in Miyazaki Pref.), is heated with boric acid at 600°C for a week to produce the Sirasu sinter in which boric acid is dispersed. The dispersed boric acid is then removed by treating the sinter with hydrochloric acid to leave behind the pores. Repeating this process under different conditions produces porous glass particles of desired pore size in high yield. The porous glass particles have more uniformly sized pores than silica gel. For the particles thus produced to have an average pore size of 500, sizes of all of the pores are within several angstroms on average. When used as the separation medium for liquid gas chromatography, the pores allow liquid to pass through 5 times faster than silica gel.

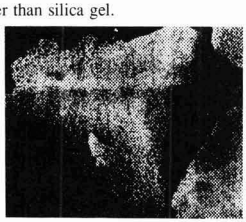

Epitaxial Growth of Diamond Film on Ni Substrate

The Science and Technology Agency's National Institute for Research in Inorganic Material and Onoda Cement Co., Ltd. have jointly succeeded in epitaxially growing diamond on an Ni substrate. When 0.5% of methane was treated at 880°C over the single crystalline nickel as the substrate, it was found that the diamond crystals were epitaxially grown in the direction of the substrate crystals. Raman spectral analysis identified that the substance grown on the substrate was diamond. It is the first attempt to grow diamond heteroepitaxially on a substrate other than that of CBN, though the single crystalline film has not been produced yet.

Moreover, the Institute has confirmed the epitaxial growth on a substrate of single crystalline cobalt. Researchers think that it may occur on single crystalline copper due to its crystalline structures. The discovery may lead to the realization of diamond elements.

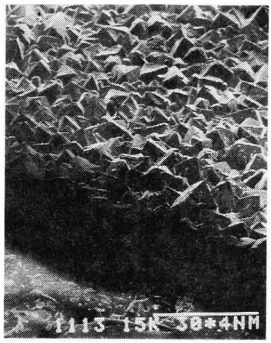

New Method for Synthesizing CBN

A research group at Tokyo Institute of Technology's Faculty of Engineering, headed by Prof. O. Fukunaga, has developed a new method which enables the synthesis of high-quality cubic boron nitride (CBN) at a pressure 10,000 atm lower than the conventional process. It produces CBN particles (of 10 to 20μm) and boron nitride magnesium particles simultaneously at 40,000 atm and 1,200°C or more, these products being easily separated. The separated CBN particles are comparable in quality to those produced by the conventional method, which uses hexagonal boron nitride (HBN) powder as the starting material. The HBN structure is so stable that it can be produced only under very severe conditions of 50,000 atm and 1,500°C or more. CBN, being the hardest material after diamond, has been used for grinders. The new method could reduce the current CBN production cost (around 2,000 yen/g) by 90%.

Corrosion Rate of Natural Glass

The Power Reactor and Nuclear Fuel Development Corp. has confirmed the phenomena of the degradation of natural glass under natural conditions and estimated the rate of corrosion. The corporation is studying

the treatment of strata for the disposal of high-level radioactive waste. Such waste is packed in a stainless container, after being solidified with glass, and then shielded with bentonite and sand in the ground. However, it has not yet been determined how well these materials degrade in the ground. As part of the research program on the underground behavior of these materials, various types of natural volcanic glass such as obsidian have been investigated. Electron microscopic analysis of micropoarticles of basalt-based glass believed

to be formed some 9000 years ago (collected from the stratum on the Izu Ohshima Is.) has indicated that it is degradable to a thickness of 5μm from the surface into the three layers of somectite,

iron hydroxides and amorphous hydrates. Similar results have been observed in samples around Mt. Fuji. The estimated degradation rate is 1μm per 2000 years. The glassy materials used for solidifying the radioactive waste corrode at a similar rate. These results will provide useful information with respect to the reliability of glass solidification of radioactive waste.

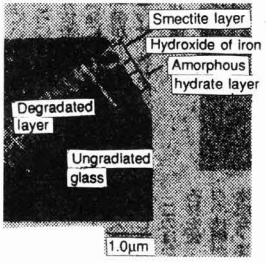

Sound Footing for Superconducting Generator HTC

The Superconducting Generator-Related Equipment and Material R&D Association has, jointly with Toshiba, developed an HTC to be used for a 70,000kW superconducting generator now under development. The success of the development of HTC is thanks to the use of magnetic fluid as a shielding material. HTC is a device to supply liquid helium in a generator to keep internal temperature at the cryogenic level. The newly developed HTC applied magnetic fluid in the part which discharges helium gas. With this success, the Association has established a sound footing for HTC development. Next year the association will test the HTC for eventual operation in 1994.

The new HTC is cylindrical and 30cm in diameter. It uses magnetic fluid as shielding material which is kept by a permanent magnet at a clearance of several micrometers between the rotating shaft and HTC.

During experiments, the HTC could shield helium gas without problems at a rotational speed of 3600 rpm. Shielding capacity was maintained even when differences in interval and atmospheric pressure were over 2 to 3kg/cm^2.

Synthesis of Y System Superconductor under Microgravity

Hitachi Ltd. has synthesized a Y system superconductor under a microgravity environment using a rocket. Microgram analysis has proven the superconductor fabricated in microgravity environment had uniform structure, although Jc was not improved. The experiment was carried out as a part of MASER, a Swedish project, in March 1990. The specimen cartridge was heated to 800°C prior to launch, and then heated to 1100°C under a microgravity environment. Four minutes after heating in the microgravity environment, the specimen quickly cooled.

Automatic Synthesizing of HT Superconductor

The Superconductivity Research Laboratory has, jointly with Toyo Engineering Co. developed equipment which can automatically synthesize a superconducting specimen for experiments. It was developed as part of a next generation key technology development system.

The equipment was installed in a room 10m long, 14m wide and 2.5m high, and composed of weighing mixing, drying, molding and sintering units. It is controlled by 6 personal computers. It can fabricate 80 pieces of specimens having size of 1.5cm in diameter and 1cm thick with 8 different elements. Control of specimen composition is sample.

The facility, which cost 300 million yen excluding development costs, can be applied to ordinary ceramic specimen preparation.

Analysis Method for HT Superconductors

The National Research Institute for Metals has developed analysis equipment to analyze superconductor composition even when the quantity of specimen is very small.

The equipment melts superconductors with agents optimized for each different superconductor system. For instance, the melt-

ing agent for Bismuth system superconductor is natrium borate with lithium hydroxide added. Bismuth system substance is melted in a crucible to make a glassy specimen; X-rays are irradiated on the prepared specimen to measure the intensity of fluorescent x-rays and analyze element content.

This method permits the analysis of superconductors of 10mg (the conventional method required at least 100mg).

Operational High Temperature Superconductors

Efforts to discover new types of superconductor have subsided and trends to apply high temperature superconductors to practical use are now increasing. It is expected that high temperature superconductors will be applied to electronic elements prior to application to electric power components.

The Ministry of International Trade and Industry formulated a next generation Key Technology Development project on the application of high temperature superconductors as electronic elements 2 years ago. Entering the 3rd year of R&D, hopeful signs have appeared for practical applications. In this project, 3 types of elements are under development; 1) approach effects type (Hitachi, Toshiba); (2) superconductivity base types (Sangyo, Oki); and new function types (NEC, Fujitsu).

The approach type element has a gate, source and drain on the same plane, similar to the structure of an FET.

Hitachi confirmed that a current ran between electrodes with holmium system superconductors at 70K – 10 mA when the distance between the electrodes was 0.2μm. The company declared that 3 terminal elements would be possible.

Superconductivity base elements have a high switching speed of several picoseconds, with small power consumption of several milliwatts. Oki Electric has succeeded in the fabrication of bismuth system superconductor thin film on a silicon substrate. If a semiconductor can be placed thereon, an element composed of emitter, base and collector can be fabricated. Some have succeeded in fabricating superconductor thin films on silicon substrate, however, ceramic films must be placed between the silicon and superconductor to prevent mutual defection; thus such thin film cannot be used for transistors. Oki discovered that when 2 to 3 layers of copper atoms are laminated, superconductor thin film can be fabricated on silicon. The critical point is now 20K, but response speed is on the order of picoseconds. Sanyo Electric confirmed that it could form semiconductors and superconductors independently in a bismuth system superconductor.

For new functional devices, Fujitsu is aiming to develop a resonance tunnel diode. Some progress has been made.

Generation of 2800 Gauss Magnetic Field Using High Temperature

Showa Electric Wire & Cable Co., Ltd. has, jointly with Toshiba, developed a high temperature superconductor coil which can generate a magnetic field of 2800 Gauss in liquid helium. It generates a 600 Gauss field in liquid nitrogen. The coil uses superconducting tape made of Bismuth system high temperature superconductor. A silver tube is filled with the superconductor powder to be processed into wire. Until now, the largest value had been Furukawa Electric Industry's 1600 Gauss in liquid helium, and Hitachi Cable's 510 Gauss in liquid nitrogen.

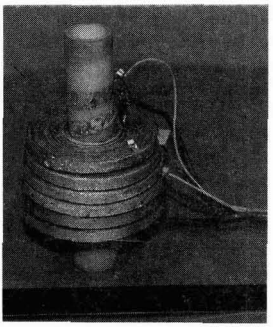

Photo 1. Apparence of superconducting coil which generated 2800 gauss magnetic field perimental facility

Diamond Tool Cutting-Edge Measurement

A measuring method for diamond tool sharpness has been developed by S. Asai (Toshiba Machine Co., Ltd.) and others.

The basic configuration for the newly developed SEM is shown in **Fig.1**. It features a pair of secondary electron detectors, A and B. The dotted line encloses the configuration for a conventional SEM. The image created by summing up the signals from the two detectors is the same as that of a conventional SEM. The image created by the difference in signals emphasizes the convexity and concavity of a sample surface.

To obtain a sectional curve for a diamond tool, a focused electron beam digitally scans the line perpendicular to the edge of a tool which is formed by rake and flank surfaces. When each detected output signal is input to a micro computer through an AD converter, the angle of inclination on the reflection point of the electron beam is calculated and integrated and the sectional curve for the tool is obtained and displayed on the CRT.

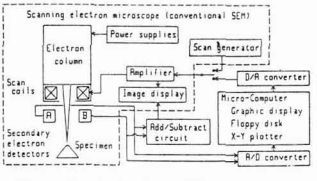

Fig. 1. Newly developed SEM system configuration

Figure 2 shows an SEM image and the sectional curve for a diamond tool with chipping on the edge. Fine convexities and concavities on the chipped conchoidal cleavage surface are accurately identified by the sectional curve.

In **Fig.3**, the edge of the sectional curve was enlarged and 15 measured points were approximated by a circle and a parabola, using the least squares method. The centers of each cutting edge radius are shown to be identical and the cutting edge radius is taken as the radius of the circle and as the radius of curvature at the parabola apex. The cutting edge radius becomes smaller when approximated by the parabola compared with that of the circle. Additionally, variance by parabola approximation is 1/26 that of circle approximation.

Thus, parabola approximation is more suitable than circle approximation in calculating cutting edge radius.

Table 1 shows the cutting edge radius ρ, figured by measuring a total of 24 points on the four tools and the ratio of variance. The cutting edge average value is 60nm or 50nm when approximated by a circle or parabola, respectively. In parabola approximation, variance is smaller and the ratio of variance is 5.8 on an average. These results prove that

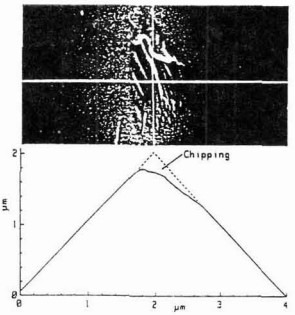

Fig. 2. SEM image and sectional curve for chipped cutting edge

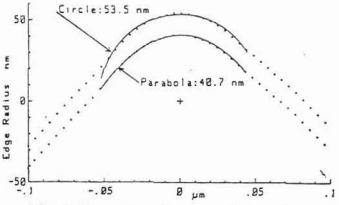

Fig. 3. Comparison between circle and parabolas

Table 1. Measurement results

	Circle	Parabola	Ratio of	Simplex	
Variance	Vc	Vp	variance		method
Sample	P nm	P nm	Vc/Vp	P nm	p
No.1-1	61	50	6.2	44	0.66
-2	58	47	12.0	40	0.72
-3	60	49	1.3	52	0.71
-4	61	51	5.8	64	0.61
-5	56	46	4.1	36	0.73
-6	57	46	11.4	39	0.71
No.2-1	59	48	6.9	47	0.52
-2	63	53	.7	60	0.48
-3	60	50	4.5	48	0.64
-4	58	46	12.5	49	0.62
-5	58	47	3.3	43	0.58
-6	59	48	.9	47	0.47
-7	60	49	.3	52	0.45
No.3-1	54	41	26.3	42	0.79
-2	60	49	9.3	45	0.58
-3	57	46	8.8	45	0.70
-4	60	49	2.0	50	0.66
No.4-1	62	53	3.7	47	0.67
-2	66	57	3.8	51	0.64
-3	65	57	2.4	56	0.52
-4	66	58	4.3	53	0.61
-5	65	54	1.5	48	0.73
-6	60	50	6.5	44	0.66
-7	63	54	1.7	48	0.75
Mean ±	60	50	5.8	48	0.63

parabola approximation is superior to circle approximation in calculating the cutting edge radius.

The edge shape for sectional curves obtained by measuring the diamond tool is not always symmetrical. Additionally, it is difficult to accurately set the tool in symmetry at measurement. If the setting of the tool is inclined, the measured sectional curve is also inclined. When a conic expressed by an explicit function is applied to the edge shape of such an inclined sectional curve, the inclination of the sectional curve is contained in the calculation error. As the parametric-represented conic by parameters t and p can express an inclined curve, the parametric-represented conic was applied to the edge shape of the sectional curve. Assuming that the sectional shape consists of a conic and its tangent and expresses the points of contact as $S(Q_{sx}, Q_{sy})$ and $T(Q_{tx}, Q_{ty})$, and the intersection of two straight lines passing each point of contact as $O(Q_{ox}, Q_{oy})$, the parametric-represented conic can be expressed by the following formula:

$$\begin{cases} x(t,p) = \dfrac{X(t,p)}{W(t,p)} \\ y(t,p) = \dfrac{Y(t,p)}{W(t,p)} \end{cases}$$

$$\begin{cases} X(t,p) = \{(1-p)Q_{sx} - 2pQ_{ox} + (1-p)Q_{tx}\}t^2 - 2\{(1-p)Q_{sx} - pQ_{ox}\}t + (1-p)Q_{sx} \\ Y(t,p) = \{(1-p)Q_{sy} - 2pQ_{oy} + (1-p)Q_{ty}\}t^2 - 2\{(1-p)Q_{sy} - pQ_{oy}\}t + (1-p)Q_{sy} \\ W(t,p) = 2(1-2p)t^2 - 2(1-2p)t + 1-p \end{cases}$$

(1)

where parameter t signifies a coordinate position for the conic. When t=0, it becomes point S. When t=1, it becomes point T. When t=0.5, the coordinate position is a point of intersection for the bisector of straight line ST and the conic. The conic is classified by the other parameter t. That is, when 0, it becomes an ellipse (or a circle under special conditions). When p=0.5, it becomes a parabola. When 0.5, it becomes a hyperbola.

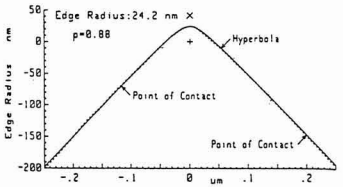

Fig. 4. Approximate hyperbola obtained by parametric representation simplex method

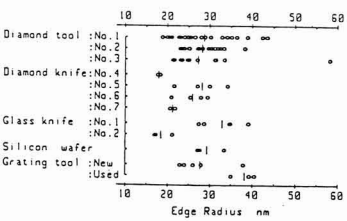

Fig. 5. Measurement of various samples.

Next, the calculating procedures for obtaining the optimal conic are described. First of all, a straight line of the sectional curve is approximated by a linear expression using the least squares method to figure out two straight lines of the left and right inclined planes corresponding to the rake and flank surfaces. Taking these two straight lines as the tangents of the conic, the point of intersection (point 0) is determined. Then the conic is established using two contact coordinates Q_{sx} and Q_{sy}, parameter p as the variable, and the simplex method as an optimization method. Taking variance for the objective function, parameter p and contact position are obtained by the simplex method where the objective function is minimized. The conic obtained by substituting parameter p and contact position in formula (1) becomes the optimal conic. The radius of curvature at the point where the bisector of the angle formed by the two tangents intersects the optimal conic was taken as the cutting edge radius ρ.

Figure 4 shows an example of the edge obtained as described above. Mark "X" signifies a point of intersection of the tangent and mark "+" is a center of the curvature. A conic is covered from one point of contact to the other point of contact. Since p=0.88, this conic is a hyperbola. The cutting edge radius was 24.2mm.

The measured data for 24 points used for the comparison of circle and parabola approximation were calculated again by this simplex method, shown in Table 1. The average cutting edge radius was 50nm when approximated by the parabola and 48nm when calculated by the simplex method. The values obtained were almost identical. Variation of measured results is ±12nm which includes not only shape error but also approximation error. The p value for the data

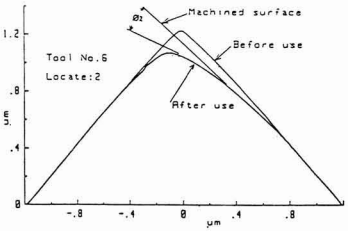

Fig. 6. Comparison of edge shape before and after use of tool & shear angle φ2

of the 21 points was larger than 0.5 with the cutting edge forming a hyperbola but the p value for the remaining three points data was smaller than 0.5, showing it to be an ellipse.

Figure 5 shows the measured results obtained for diamond tools put to practical use, as well as other samples with sharp edges. The measured values and the average are shown for each tool. Tools No.1 and No.2 represent the measured results obtained from seven tools which were ground by two different diamond tool makers. Tool No.3 is the measured result for the five No.1 tools which were ground in addition to the original seven. Individual tool angles (the angle for each cutting edge) were 85 degrees.

Diamond knives are sharpened by ion sputter machining. The tool angle was 55 degrees for Tool No.4 and 85 degrees for Tools No.5, 6 and 7. The tool angle of the glass knives is 43 degrees. The silicon wafer has an edge line obtained by crossing the ground surface and cleavage surface (111). A grating tool was used for engraving the diffraction grating. The tool angle was 90 degrees. The cutting edge radius was 28nm before use. It increased to 38nm after use. In addition, the p value before the use of the tool was over 0.9, which was higher than that for diamond tools. After the grating tool was used, the edge shape was almost symmetrical, with a p value of 0.82.

A comparison of tools with closer tool angles revealed that the cutting edge radius for the ion-sputter etched diamond knife was a little smaller than that for the ground diamond and grating tools. In addition, the silicon wafer was almost the same as the diamond tool in cutting edge radius.

Figure 6 shows a comparison between edge shapes for a rounded corner tool before and after aluminum alloy machining. The flank surface was worn more heavily than the rake surface, and the wear shape for flank surface was parallel with the machined surface. The wear develops at an angle almost identical with the shear angle Φ_2 of the chip.

Abstracts of Articles on Ceramics from the Selected Journals of the Academic Societies

Membrane
Vol.15, No.5, 1990
p.258–262

Ceramic Membranes for High Temperature Fuel Cells

Yohtaro Yamazaki

Department of Electronic Chemistry, Tokyo Institute of Technology at Nagatsuta, 4259 Nagatsuta, Midori-ku Yokohama 227

Ceramic thin films used in high temperature fuel cells are summarized and their peculiarities are described by comparing with organic membranes which are widely used in ambient temperature. Thin films of solid electrolyte separate the ionic current of O^{2-} or H^+ from other flows of charged particles in the fuel cells operated at high temperatures near 1,000°C. Materials of the solid electrolyte have been explored for many years and it is concluded that stabilized zirconia is the candidate for the practical energy conversion systems. To prepare continuous and high-quality solid electrolyte films on porous ceramic substrates are the key technology to develop the high temperature fuel cells, and a number of physical and chemical processes are studied for this purpose. The most well known method to prepare the films is the EVD process which had been developed in Westinghouse Co.. Other processes such as electron beam evaporation and low-pressure plasma spraying method are also being developed. In order to reduce the thermal stresses in the interfaces between the elements of the cells, the thermal expansion coefficients of solid electrolyte, electrodes and supporting materials must be considered. Polymer solid electrolyte (Nafion membrane) is also mentioned as a flexible solid electrolyte which is used in low-temperature fuel cells.

Key words : fuel cell, thin film, zirconia, solid electrolyte

Japanese Journal of Applied Physics
Vol.29, No.11, Nov., 1990
p.2381-2385

Influence of Effective Masses on the Oscillation of Fowler-Nordheim Tunneling in Thin SiO_2 MOS Capacitors

Yukinori ONO and Takahiro MAKINO

NTT LSI Laboratories, Nippon Telegraph and Telephone Corporation, 3-1, Morinosato Wakamiya, Atugi-shi, Kanagawa, 243-01

The influence of effective masses on the oscillation of Fowler-Nordheim tunneling has been investigated by calculating the transmission probability of electrons through thin SiO_2 film assuming effective mass approximation. As a result, the amplitude of the oscillation was found to depend on the ratio of the anode effective mass to the SiO_2 conduction band effective mass. The amplitude has a minimal valley when the anode effective mass is about unity, or when the metal layer works as an anode. This result agrees well with a previous experimental report that the oscillation is strongly reduced when electrons flow into an Al electrode. The period of the oscillation depends on the effective mass of the SiO_2 conduction band, whereas neither cathode nor anode effective mass dependence was found. The present calculations of the period are consistent with the previous experiment.

KEYWORDS: MOS capacitor, thin SiO_2 film, Fowler-Nordheim tunneling, quantum interference effect, multistep potential approximation, effective mass

Japanese Journal of Applied Physics
Vol.29, No.11, Nov., 1990
p.2388-2402

New Classification Method for Layered Copper Oxide Compounds and Its Application to Design of New High T_c Superconductors

Yoshinori TOKURA and Takahisa ARIMA

Department of Physics, University of Tokyo, Tokyo 113

Structures of layered copper oxide compounds and relating high-temperature superconductors are classified by using the concept of the block layer which can isolate each CuO_2-sheet and control carrier density within the Cu-O plane. Particular emphasis is laid on the Cu-O network dependent physico-chemical properties which are entirely governed by ordering and combination of constituent block layers. By the new classification method, structures and carrier-doping characteristics are predicted for prospective but hitherto unknown CuO_2-layered superconductors. Possible importance of the concept of the block layer is pointed out in epitaxial growth of superconducting structures.

KEYWORDS: high-T_c superconductor, material design, Cu-O network, layered copper oxide compound, block layer, structural classification

Japanese Journal of Applied Physics
Vol.29, No.11, Nov., 1990
p.2403-2406

Magnetic Shielding Effect of $Ba_2YCu_3O_{7-\delta}$ Plates

Shigetoshi OHSHIMA and Katsuro OKUYAMA

Electronic and Information Engineering, Faculty of Engineering, Yamagata University, Yonezawa 992

The magnetic shielding effect of $Ba_2YCu_3O_{7-\delta}$, Cu and Fe-Ni plates was examined as a function of the frequency of applied ac magnetic field using magnetic heads. The effect of $Ba_2YCu_3O_{7-\delta}$ plates was superior to that of Cu and Fe-Ni plates in the low-frequency (<5 kHz) region at 77 K, while in the high-frequency (>10 kHz) region, the effect of $Ba_2YCu_3O_{7-\delta}$ plates was almost the same or slightly inferior to that of Cu plates. The shielding effect of $Ba_2YCu_3O_{7-\delta}$ plates was strongly affected by the micro cracks and porosity of the samples. The magnetic shielding effect of $Ba_2YCu_3O_{7-\delta}$ plates decreased rapidly with applied dc magnetic field, while the effect of Cu and Fe-Ni plates did not change with the application of dc magnetic field.

KEYWORDS: magnetic shielding, $Ba_2YCu_3O_{7-\delta}$, Meissner effect

Japanese Journal of Applied Physics
Vol.29, No.11, Nov., 1990
p.2407-2410

Microwave Properties of Inhomogeneous $YBa_2Cu_3O_7$

Jun TATENO and Norio MASAKI

Japan Atomic Energy Research Institute, Tokai-mura, Naka-gun, Ibaraki-ken, 319-11

Microwave properties of the powder specimen of high-T_c superconductor $YBa_2Cu_3O_7$ were examined with the standing-wave method at 9.12 GHz. From the analysis based on the coexistence of superconductivity and dielectricity, the phenomenological penetration depth is found to be as large as 0.3 cm in the powder specimen. The temperature dependence of the penetration depth in the powder specimen resembles that of London penetration depth in the compact material. The imaginary part of the dielectric permittivity diverges at the superconducting phase transition, the origin of which can be attributed to either fluctuations or the Josephson effect.

KEYWORDS: high-T_c superconductor, $YBa_2Cu_3O_7$, microwave properties, phenomenological penentration depth, dielectric permittivity, fluctuations, Josephson effect

Japanese Journal of Applied Physics
Vol.29, No.11, Nov., 1990
p.2411-2412

Flux Line Dynamics Crossover in the Tl-Ba-Ca-Cu-O Thin Film

Chungyung WANG, Hung-Lun CHANG, Ming-Lee CHU, Jenh-Yih JUANG†, Yih-Shun GOU† and Tzeng-Ming UEN†

Institute of Electro-optical Engineering,
†Institute of Electrophysics, National Chiao Tung Univ., Hsinchu, Taiwan 30050, R.O.C.

By extending the observation of the current-voltage characteristics to a much higher dissipative state, the flux-line motion experiences at least two stages of crossover, namely, from glassy hopping to creep-dominating, and finally an abrupt transition into the flow regime.

KEYWORDS: Tl-Ba-Ca-Cu-O thin film, glassy state, flux creep, flux flow

Japanese Journal of Applied Physics
Vol.29, No.11, Nov., 1990
p.2413-2414

Growth and Characterization of $Bi_2(Sr_{1-x}Ca_x)_3Cu_2O_y$ Single Crystals Extracted from KBr Flux

Toetsu SHISHIDO, Naoki TOYOTA, Daisuke SHINDO and Tsuguo FUKUDA

Institute for Materials Research (IMR), Tohoku University, Sendai 980

Single crystals of Bi-based compounds were obtained by the high-temperature solution growth method using KBr as the flux. The compositions of two typical compounds were determined as $Bi_{2.2}Sr_{1.8}Ca_{1.1}Cu_2O_y$ and $Bi_{2.1}Sr_{1.1}Ca_{1.8}Cu_2O_y$, which are close to the chemical formula $Bi_2(Sr_{1-x}Ca_x)_3Cu_2O_y$. The magnetization experiment shows that the onset temperatures of T_c of the two compounds are 98 K and 83 K, respectively.

KEYWORDS: Bi-Sr-Ca-Cu-O superconductor, single crystal growth, KBr flux

Japanese Journal of Applied Physics
Vol.29, No.11, Nov., 1990
p.2415-2416

Polarized Electromagnetic Detections by High T_c Superconducting Antenna

Toshiro OHNUMA

Department of Electrical Engineering, Tohoku University, Sendai 980

Detections of polarized electromagnetic waves (f=9.55 GHz) by high T_c superconducting antenna were confirmed experimentally. New results on polarization effects and the directivity of the high T_c superconducting antenna were observed.

KEYWORDS: superconducting antenna, high T_c superconductor, electromagnetic waves, polarization, detector

Japanese Journal of Applied Physics
Vol.29, No.11, Nov., 1990
p.L2089-L2090

Thermal Expansion of Sol-Gel SiO_2 Glass Fibers

Hiroshi KOBAYASHI and Yukio YAMAGUCHI

National Research Laboratory of Metrology, 1-1-4, Umezono, Tsukuba, Ibaraki 305

The thermal expansion of SiO_2 glass fibers synthesized by the sol-gel method was measured in the temperature range of 100 to 300°C using a laser interferometer developed at NRLM. Fibers as grown represent shirinkage of length, but after annealing, thery represent low thermal expansion as is seen in the usual sol-gel SiO_2 glasses. It is believed that the former is in a sintering process and the latter is a true glass.

KEYWORDS: thermal expansion, sol-gel, glass, annealing, sintering

Japanese Journal of Applied Physics
Vol.29, No.11, Nov., 1990
p.2435-2439

Effect of La Content on the Thermal Volume Change of $Ba_{4.22}Na_{1.44}Nb_{10.12}O_{30.24}$–$Ba_3NaLaNb_{10}O_{30}$ Solid Solutions at Ferroelectric Transition Temperature

Masaji SHIMAZU†, Hirokazu SHINYA, Shinichiro KUROIWA, Masayuki TSUKIOKA† and Sadao TSUTSUMI

†*National Institute for Research in Inorganic Materials, Namiki, Tsukuba-shi, Ibaraki 305*
School of Science and Engineering, Waseda University, Ookubo, Shinjuku-ku, ToKyo 106

Sintered solid solutions in the $Ba_{4.22}Na_{1.44}Nb_{10.12}O_{30.24}$ (BNN–B)–$Ba_3NaLaNb_{10}O_{30}$ (BNLN) system have been synthesized and examined by X-ray powder diffraction and differential scanning calorimeter (DSC) analysis. The BNN(–B)–BNLN system has continuous solid solutions over the whole range, which have a tungsten bronze type of structure with pseudotetragonal symmetry. At room temperature, the *a*-axis increases slightly with increasing La content while the *c*-axis markedly decreases. The temperature dependence of the axes is characteristic in the *c*-axis. The thermal contraction of the *c*-axis occurring at the ferroelectric transition temperature is depressed with increasing La content, and in an intermediate composition, the contraction is reduced to nearly zero. The DSC analysis showed that both the transition enthalpy (ΔH_t) and the transition temperature (T_t) decrease with increasing La content.

KEYWORDS: barium sodium-lanthanum niobate solid solutions, X-ray powder diffraction, differential scanning calorimeter analysis, ferroelectric phase transition, thermal volume change

Japanese Journal of Applied Physics
Vol.29, No.11, Nov., 1990
p.2481-2486

Quantum Size Effect and HRTEM Observation of CdSe Microcrystallites Doped into SiO_2-Glass Films Prepared by Rf-Sputtering

Keiji TSUNETOMO, Akira KAWABUCHI, Haruyuki KITAYAMA, Yukio OSAKA and Hiroyuki NASU†

Department of Electrical Engineering, Faculty of Engineering, Hiroshima University, Higashi-Hiroshima, Saijo 724
†*Department of Industrial Chemistry, Faculty of Engineering, Mie University, Tsu, Kamihama 514*

CdSe microcrystallite-doped SiO_2 glass films were prepared by the magnetron rf-sputtering technique. High resolution transmission electron microscopy (HRTEM) observation was carried out to determine the shape and the average size of the microcrystallites. The microcrystallites had a spherical configuration and they seemed to have a wurtzite structure. The optical band gap of the films clearly exhibited the blue shift compared to bulk CdSe. The shape of optical absorption spectra also changed as the microcrystallite size decreased. A simple model of the size quantization on interband absorption in a semiconductor sphere was used to explain the change of the optical absorption spectra. Taking into account the particle size distribution, the calculated absorption spectra successfully agreed with the real absorption spectra. The observed blue shifts of optical absorption were consistent with theoretical values calculated using the mean microcrystallite radii estimated from the HRTEM observations.

KEYWORDS: semiconductor-microcrystallite-doped glass films, rf sputtering, thin film, quantum dots, optical absorption spectrum, quantum size effect, transmission electron microscopy, lattice image

Japanese Journal of Applied Physics
Vol.29, No.11, Nov., 1990
p.L1987-L1990

Bond-Valence-Sum Study on Possible Candidates for High-T_c Oxide Superconductors

Shigenori TANAKA, Noburu FUKUSHIMA, Hiromi NIU and Ken ANDO

Advanced Research Laboratory, Research and Development Center, Toshiba Corporation, Komukai Toshiba-cho, Saiwai-ku, Kawasaki 210

We have analyzed relationships between crystal structures and electronic states of layered transition-metal oxides in the light of bond valence sums. We introduce parameters representing excess charge and internal strain in the central MO_2 planes (M=3d transition metal) and thereby characterize the electronic states of those oxides. Correlations between the superconducting transition temperature and those bond-valence-sum parameters are investigated for the high-T_c cuprate compounds and the possibility of making nonsuperconducting oxides superconducting is discussed.

KEYWORDS: high-T_c superconductor, 3d transition-metal oxide, layered structure, bond valence sum, crystal structure, superconducting transition temperature

Japanese Journal of Applied Physics
Vol.29, No.11, Nov., 1990
p.L1991-L1994

Large Levitation Force due to Flux Pinning in YBaCuO Superconductors Fabricated by Melt-Powder-Melt-Growth Process

Masato MURAKAMI, Terutugu OYAMA, Hiroyuki FUJIMOTO, Takahiro TAGUCHI, Satoshi GOTOH, Yuh SHIOHARA, Naoki KOSHIZUKA and Shoji TANAKA

ISTEC, Superconductivity Research Laboratory 1-10-13, Shinonome, Koto-ku, Tokyo 135

An extremely large levitation force of as high as 30 N at a height of 1 mm was achieved in Ag-doped YBaCuO fabricated by the Melt-Powder-Melt-Growth process using a repulsive force against a 0.4 T rare-earth magnet at 77 K. The combination of a large J_c value and large shielding current loop is the source of such a large levitation force.

KEYWORDS: levitation force, YBaCuO, Melt-Powder-Melt-Growth process, Ag doping, flux pinning

Japanese Journal of Applied Physics
Vol.29, No.11, Nov., 1990
p.L1995-L1998

Anomalous Electrical Resistivity of Bi-Sr-Ca-Cu-O System at High Temperature

Hiroshi NAGAI, Masahiro KAKUZEN†, Masaru YOKOTA and Kazuhiko MAJIMA

Department of Materials Science and Engineering, Faculty of Engineering, Osaka University, Suita, Osaka 565
†Graduate Student of Osaka University, Suita, Osaka 565

The electrical resistivity of Bi-Sr-Ca-Cu-O and Bi(Pb)-Sr-Ca-Cu-O superconductors at high temperatures was studied in relation to superconducting properties. The resistivity of the samples with a low-T_c phase showed hysteresis around 300 and 650°C between the heating and cooling processes. No hysteresis was detected for nearly single phase high T_c. For the low-T_c samples, it was confirmed that the T_c, the material resistivity and the high temperature resistivity were strongly dependent on the quenching temperature. Weight loss was detected around 300°C in the heating process, but it was not detected in the cooling process.

KEYWORDS: Bi-Sr-Ca-Cu-O system, high-T_c phase, low-T_c phase, high temperature electrical resistivity, hysteresis, quenching temperature

Japanese Journal of Applied Physics
Vol.29, No.11, Nov., 1990
p.L1999-L2001

Addition of New Pinning Center to Unidirectionally Melt Solidified Y-Ba-Cu-O Superconductor

Jun-ichi SHIMOYAMA, Jun-ichiro KASE, Shinji KONDOH, Eiji YANAGISAWA, Toshiya MATSUBARA, Mitsuru SUZUKI and Takeshi MORIMOTO

Research Center, Asahi Glass Co., Ltd., Hazawa-cho, Kanagawa-ku, Yokohama 221

Y-Ba-Cu-O bulk superconductor including small particles of $BaSnO_3$ was synthesized by the unidirectional melt solidification method. Finely dispersed Y_2BaCuO_5 precipitates and $BaSnO_3$ particles were observed in $YBa_2Cu_3O_x$ matrix. The critical current density at 77 K in 8 kOe was 1.8×10^4 A/cm^2, which was about four times higher than that of the $BaSnO_3$-free specimen. Fine particles of $BaSnO_3$ (0.1–1 μm) can act as effective flux pinning centers in the specimen and result in an increase of the critical current density.

KEYWORDS: superconductor, Y-Ba-Cu-O, unidirectional melt solidification, $BaSnO_3$, pinning center, critical current density

Journal of the Chemical Society of Japan
No.12, 1990
p.1329-1335

Synthetic Conditions of High-T_c (2223) Phase of Bi—Pb—Sr—Ca—Cu—O Superconductor

Yuichi DESHIMARU, Tetsuya OTANI, Youichi SHIMIZU, Norio MIURA and Noboru YAMAZOE

Department of Materials Science and Technology, Graduate School of Engineering Sciences, Kyushu University; Kasuga-shi 816 Japan

The synthetic conditions were investigated for preparing the high-T_c (2223) phase of Bi-Pb-Sr-Ca-Cu-O superconductor. The high-T_c phase could be synthesized with good reproducibility from a mixed solution of nitrates of constituent metals, by evaporation, calcination, and sintering, the optimum temperatures of which were found to be 350°C, 820°C (12 h), and 845°C (60 h), respectively (Figs. 1, 3, 4, 5). Mixing of the solution at the evaporation as well as the repetition of the calcination were also important for obtaining the high-T_c phase (Figs. 2, 8). As suggested from XRD analysis, the low-T_c (2212) phase was first produced at the calcination stage (820°C) and then changed into the high-T_c phase at the sintering stage (845°C) (Figs. 3, 4, 8). It was also suggested that the (2223) phase could be derived more easily, as the (2212) phase was produced in a purer and better grown form at the calcining stage (Figs. 8, 9, 10). Pressing and re-sintering of the obtained (2223) phase increased the packing and orientation of planer crystals (Figs. 11, 12).

Journal of the Chemical Society of Japan
No.12, 1990
p.1395-1401

Preparation of TiO_2-ZrO_2 Films by MOCVD

Katsuhiro IMASHITA, Hiroshi FUNAKUBO, Nobuo KIEDA, Masanori KATO and Nobuyasu MIZUTANI*

Department of Inorganic Materials, Faculty of Engineering, Tokyo Institute of Technology; O-okayama, Meguro-ku, Tokyo 152 Japan

TiO_2-ZrO_2 films were prepared by CVD using $Ti(O\,i\text{-}C_3H_7)_4$, $Zr(O\,t\text{-}C_4H_9)_4$ and O_2 as starting materials under an atmospheric pressure. The effects of deposition temperature and input gas composition on the deposition rate, constituent phase, chemical composition and microstructures of TiO_2-ZrO_2 films were investigated comparing with that of TiO_2 and ZrO_2 films. Deposition rate of TiO_2-ZrO_2 films was lowered with respect to the expectations based on each deposition behavior of TiO_2 and ZrO_2 films at any deposition temperature. Though Ti/(Ti+Zr) in TiO_2-ZrO_2 films was in good agreement with expectations from TiO_2 and ZrO_2 films at 350°C, it was surplus in Ti at 550°C. TiO_2-ZrO_2 films were consisted of finer particles comparing with TiO_2 and ZrO_2 films.

Taikabutu
Vol.42, No.12, 1990
p.710-719

The Mechanism and the Countermeasure of the Local Corrosion of Immersion Nozzles at Slag Metal Interface

Kusuhiro Mukai,* Hiroshi Iwasaki,** Tadataka Eguchi,*** Shoji Iizuka,*** and J. M. Toguri.****

*Faculty of Engineering, Kyushute of Technolgy,

**Graduate student, Faculty of Engineering, Kyushu Institute of Technology,

***Kurosaki Refractories Co, Ltd.

****Department of Metallurgy and Material Science, University of Toronto

Kinematic immersion tests were conducted in order to substantiate quantitatively a mechanism for the local corrosion of immersion nozzles at the slag-metal interface. Based on the mechanism, then, experiments were designed to find out effective countermeasures for preventing the local corrosion.

The results obtained are summarized as follows :

For steels containing low carbon levels (e. g., steel for continuous casting), the dissolution of oxides from the nozzle into the slag film is the rate controlling step of the local corrosion process. For metals containing high carbon content (e. g., in the vicinity of carbon saturation), dissolution of graphite from the nozzle into the metal is rate controlling.

If the nozzle :

1) has a high resistance to corrosion by liquid slags, and

2) is easily wetted by the slag,

then it will exhibit a good resistance to local corrosion at the slag-metal interface.

Zirconia-graphite nozzle containing ZrO_2 which has a high resistance to corrosion by the slag much reduces its dissolution rate into the slag film. This mainly results in a remarkable lowering of the local corrosion rate.

Alumina-graphite nozzle containing BN and zirconia-graphite nozzle containing SiC show good resistances to the local corrosion, which can be attributed to the fact that BN and SiC have good resistences to corrosion by the slag and are easily wetted by the slag.

The apparatus used for present immersion test is feasible for evaluating the local corrosion rate of zirconia-qraphite nozzles for the condition of practical use.

Key words : Immersion nozzle, Local corrosion, Slag-metal interface, Mechanism, Countermeasure

Taikabutu
Vol.42, No.12, 1990
p.720-727

Behaviour of Boric Compounds Added in MgO–C Bricks

Satoshi Hayashi, Shigeyuki Takanaga,
Hirokuni Takahashi and Akira Watanabe

Kyushu Refractories Co., Ltd.

B_2O_3–MgO and B_2O_3–CaO compound oxides were added in MgO–C bricks and changes in weight, mineral, strength and resistance to oxidation were investigated after heating at various temperatures ranging from 600℃ to 1400℃.

Adding only B_2O_3 compound, B_2O_3 reacted with C at temperature over 1200℃ and accordingly CO gas and boric vapors diffused to outside. However , the addition of Al powder in MgO–C brick containing B_2O_3 compound controlled the diffusion and then the contribution to oxidation resistance and strength were developed.

Boric compounds function as both accelerator and inhibitor for oxidation depending on temperature and atmosphere. Therefore, when MgO–C brick containing boric compound is practically used, it is necessary to use it in combination with metalic powder and to carefully study the proper amounts of additives.

Key words : MgO – C brick, Boric compound, B_4C, Strength, Oxidation

Journal of the Physical Society of Japan
Vol.59, No.12, Dec., 1990
p.4376-4383

Effect of Hole Itinerancy on XAS and XPS Spectra of the High-T_c Compounds

Tomotoshi NISHINO

Department of Physics, Faculty of Science, Osaka University, Machikaneyama 1-1, Toyonaka, Osaka 560

Spectra of Cu 2*p* XPS, XAS, valence band XPS and BIS of the high-T_c compounds are calculated for Cu_nO_m ($n>1$) clusters. Effects of the hole itinerancy as well as those of the hole correlation on these spectra are investigated. Size dependence of the spectra including the valence band XPS and BIS as well is examined by extending the calculation to linear clusters containing up to seven Cu atoms. It is concluded that the Cu 2*p* XPS spectra consist generally of three groups of peaks which are assigned to $|\underline{c}d^{10}\underline{L}\rangle$, $|\underline{c}d^{9}\rangle$ and $|\underline{c}d^{10}\underline{L}^2\rangle$ final states. The last one which was not obtained by use of either a single Cu atom cluster or the impurity Anderson model appears in between the first two in energy. The main peak corresponding to the $|\underline{c}d^{10}\underline{L}\rangle$ state shifts with concentration of additional holes consistently with experimental data on Y-Ba-Cu oxides.

Journal of the Physical Society
of Japan
Vol.59, No.12, Dec., 1990
p.4419-4427

Correlation of the Infrared Anomaly and Superconductivity in $YBa_2(Cu_{1-x}Co_x)_3O_{7-\delta}$

Kohji OHBAYASHI, Hideaki TUKAMOTO, Norio OGITA, Masayuki UDAGAWA, Yuji AOKI† and Toshizo FUJITA†

Faculty of Integrated Arts and Sciences, Hiroshima University, Hiroshima 730
†Department of Physics, Faculty of Sciences, Hiroshima University, Hiroshima 730

For $YBa_2Cu_3O_{7-\delta}$ oxides sintered at various temperatures, the infrared absorption mode of in-plan Cu(2)-O(2, 3) stretching motions shows the anomalous behavior to disappear for superconducting samples although it is allowed by the selection rule. The correlation between the infrared anomaly and superconductivity has been confirmed systematically for $YBa_2(Cu_{1-x}Co_x)_3O_{7-\delta}$ system in the Co concentration region of $0 \leq x \leq 0.3$ for samples quenched from sintering temperatures of 400, 500, 600, 700 and 800°C.

[lattice vibrations, infrared absorption, high-T_c oxides superconductor, $YBa_2Cu_3O_{7-\delta}$]

Journal of the Physical Society
of Japan
Vol.59, No.12, Dec., 1990
p.4488-4493

Phase Transition of $(NH_4)_2SO_4$–K_2SO_4 Mixed Crystal

Katsuhiko FUJII, Hiroshi MORI and Takeo MATSUBARA

Department of Applied Physics, Okayama University of Science, 1-1 Ridaichou, Okayama 700

The peculiar temperature dependence of a remanent polarization in $(NH_4)_2SO_4$–K_2SO_4 mixed crystal which changes the sign at low temperature has been studied by extending the unified model in the ferroelectric crystals to the ferrielectric crystals consisting of two sublattices. The phase transition in this crystal system has been analyzed on the basis of an idea that two kinds of NH_4^+ ions, NH_4^+(I) and NH_4^+(II), with different dipole moments form two sublattices. In the mixed crystal, NH_4^+(II) with larger dipole moment than NH_4^+(I) is replaced preferentially by K^+ ion with no dipole moment. We consider that the replacement of ions produces modifications in the two kinds of potential in each sublattice, two kinds of ferroelectric intrasublattice interactions and weak antiferroelectric intersublattice interaction, leading to the peculiar thermal property of the ferrielectric phase.

[ammonium sulfate, ferrielectrics, phase transition, two sublattices, unified model]

Journal of the Physical Society
of Japan
Vol.59, No.12, Dec., 1990
p.4554-4559

Valence Electronic Structure of Thallium-Compound High-Temperature Superconductors

Y. HWU,* M. MARSI, A. TERRASI, M. ONELLION, D. L. HUBER, G. MARGARITONDO,† J. H. WANG,†† Z. Z. SHENG†† and A. M. HERMANN††

Department of Physics and Synchrotron Radiation Center, Univeristy of Wisconsin, Madison, WI 53706.
†Institut de Physique Appliquée, Ecole Polytechinique Fédérale de Lausanne, Ecublens, Switzerland
††Department of Physics, University of Colorado, Golden, Colorado

We used photoemission spectroscopy with synchrotron radiation to investigate the electronic structure of eight different thallium cuprates: pure $Tl_{2.2}Ba_2CuO_y$, Ce-doped $Tl_{2.2}Ba_{2-x}Ce_xCuO_y$ (x=0.1, 0.15, 0.2) and $Tl_2Ba_2CeCu_3O_y$, and Zr-doped $Tl_2Ba_{2-x}Zr_xCuO_y$ (x=0.005, 0.05). The material are high-temperature superconductors, except one of the $Tl_{2.2}Ba_2CuO_y$ samples. The study included an investigation of the valence-electron density of states, and a detailed analysis of the Fermi edge at room temperature. No departures from the Fermi-liquid picture were observed.

Japanese Journal of Advanced Automation Technology Vol.2 No.4 July 1990

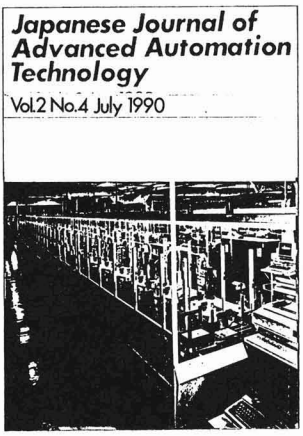

Contents

What is the English Monthly Journal TECHNO JAPAN?

It is a professional international periodical designed to cater to people in a wide variety of key industrial and government positions. Its carefully selected contents, including complete reports, for example, on the current status and new developments in Japanese industry and technology, are tailored to meet the information needs of specialists all over the world. Each news article includes an expert's commentary based on in-depth data analysis and also incorporates sufficient data to enable readers to make their own independent judgements on various issues and topics. Techno Japan is a monthly journal whose reports contain information indispensable for those overseas specialists who keep track of current conditions and must project future Japanese and international economic and industrial trends. It is the most authoritative source of information about the most recent technological advances in virtually all fields of industry.

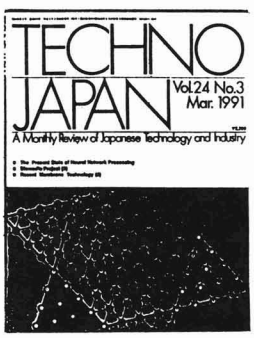

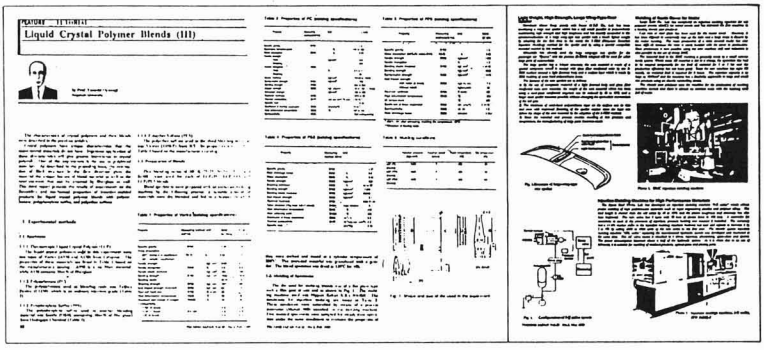

Contents of TECHNO JAPAN

Industrial & TechnoJogical News Articles

Every issue of Techno Japan contains more than 300 pieces of information.

News articles are classified as follows:

Basic Industries:	*Energy, Steels & Metals, Ceramics & Materials Science, Superconductivity*
Machinery Industries:	*Miscellaneous Machines, Precision Engineering & Fine Finishing, Factory Automation, Transportation & Materials Handling*
Electronics Industries:	*Electronic Devices, Telecommunications, Information Processing, Home Automation & Broadcasting, Electronics Instruments, Medical Engineering, Electronic Machine Manufacturing & Assembly*
Chemical Industries:	*Chemicals, Polymers, Biotechnology*
Disaster Prevention, Agribusiness Systems Industries:	

Feature Articles

Long, highly informative feature articles of crucial interest to overseas governments and industries appear each month. As many as 55 pages in one issue may be devoted to such important and fascinating articles which enlarge the depth and breadth of readers' knowledge about subjects of current interest. Such high news value feature articles are carried individually or in a series.

Economic Report and Statistics

Techno Japan's economic report and statistics is officially provided by the Economic Planning Agency. These reports help to promote mutual understanding among various nations.

Research Institutes in Japan

TECHNO JAPAN *FUJI TECHNOLOGY PRESS LTD.*
Daini Bunsei Bldg., 11-7, Toranomon 1-chome, Minato-ku, Tokyo 105, Japan